

FORSCHUNGSZENTRUM ROSSENDORF

WISSENSCHAFTLICH-TECHNISCHE BERICHTE

**FZR-268**

Juli 1999



# **Annual Report 1998**

**Institute of Safety Research**

**Editors:**

Prof. Dr. F.-P. Weiß

Dr. U. Rindelhardt

# CONTENTS

## Preface

## Selected Reports

Investigation of Coolant Mixing in Pressurized Water Reactors at the Rossendorf Mixing Test Facility ROCOM G. Grunwald, T. Höhne, H.-M. Prasser, K. Richter, F.-P. Weiß	1
A Benchmark for Coupled Thermohydraulics System/Three-Dimensional Neutron Kinetics Core Models S. Kliem	7
New 3D Nodal Method HEXNEM for Improving the Accuracy of the Hexagonal Version of the Code DYN3D U. Grundmann	11
Improvement of the Verification of Coupled Thermohydraulics/Neutron Kinetic Codes: DYN3D Burnup and Steady Calculations S. Kliem, S. Mittag, U. Rohde, A. Seidel, F.-P. Weiß	17
Wire-Mesh Sensors for Two-Phase Flow Investigations H.-M. Prasser	23
A New Criterion for the Bubble Slug Transition in Vertical Tubes A. Schaffrath, A.-K. Krüssenberg, H.-M. Prasser	29
Prevention of Water Hammers Behind Fast Acting Shut-Off Valves A. Dudlik, H.-M. Prasser, S. Schlüter	37
Fluiddynamic Waterhammer Simulations with Consideration of Fluid-Structure Interaction T. Repp	41
Solution of a Mixed Convection Flow Benchmark Using Computational Fluid Dynamic Codes E. Krepper, H.-G. Willschütz, F.-P. Weiß	47
Investigation of Heating up and Evaporation of Fluids in Storage Tank-Experiments and Numerical Simulation A. Aszodi, E. Krepper, H.-M. Prasser	56
BRICK - a One-Dimensional Model for Transient Simulation of Pressure Relief from Batch Reactors D. Lucas	65

Characterizing the Kinetics of Heterogeneous Exothermic Reactions K. Biskup, H. Bothe, G. Hessel, G. Hulzer, H. Kryk, W. Schmitt, N. Tefera	71
Plume and Finger Regimes Driven by an Exothermic Interfacial Reaction A. Grahn, K. Eckert	81
Finite Element Based Vibration Modelling of VVER-1000 Type Reactors M. Werner, E. Altstadt, S. Perov	85
Finite Element Analysis of a BWR Feed Water Distributor Under Extreme Transient Pressure Load E. Altstadt, H. Ohlmeyer, F. Otremba, F.-P. Weiß	91
Calculations with ANSYS/FLOTRAN to a Cdore Catcher Benchmark H.-G. Willschütz	99
Materials Testing at the Hot Cell Laboratory of the Institute for Safety Research H.-W. Viehrig	105
Small Angle Scattering Experiments at VVER 440-Type Weld Metal Sv-10KhMFT M. Grosse, J. Böhmert V. Denner	115
Composition Effects on the Irradiation Embrittlement of VVER Reactor Pressure Vessels J. Böhmert, A. Kryukov, Y. Nikolaev, D. Erak	121
Increasing the Accuracy of Neutron Load Determination for WWER Reactor Components B. Böhmer, G. Borodkin, E. Brodtkin, V. Gorbunov, G. Manturov, A. Tsiboulia, S. Zaritsky	127
Influence of the Number of Energy Groups on the Accuracy of Neutron Fluence Calculations H.-U. Barz, J. Konheiser	133
Reactive Transport Modelling of a Mixed Equilibrium-Kinetic System R. Küchler, K. Noack	139
Electromagnetic Control of Flow Separation T. Weier, G. Mutschke, U. Fey, V. Avilov, G. Gerbeth	147
Si-Czochralski Crystal Growth Melt Flow Control by Means of Magnetic Fields	

V. Galindo, G. Gerbeth	155
Contributions to the Riga Dynamo Experiment F. Stefani, G. Gerbeth	161
<b>Short Contributions</b>	165
<b>Publications</b>	179
Publications in scientific and technical journals and in conference proceedings	181
Oral conference contributions	189
FZR-reports and other publications	193
<b>Meetings and Workshops</b>	197
<b>Patents</b>	201
<b>Seminars of the Institute</b>	205
<b>Lecture Courses</b>	211
<b>Departments of the Institute</b>	215
<b>Personnel</b>	219



## Preface

The Institute of Safety Research is one of the five scientific institutes of Forschungszentrum Rossendorf e.V. The Forschungszentrum Rossendorf is a member of the "Wissenschaftsgemeinschaft Gottfried Wilhelm Leibniz" and is funded by the Federal Ministry of Education and Research and by the Saxon Ministry of Science and Arts with 50 % each.

The research work of the institute aims at the assessment and increase of the safety and environmental sustainability of technical plants. The emphasis is put on the development and validation of mathematical and physical models for process and plant analysis, and of techniques for process and components monitoring. Subject of investigations are equally nuclear plants and installations of process industries.

To analyse the thermo-fluid dynamics of normal plant operation and of the behaviour during accidents, physical models and computer codes are developed for multi-phase and multi-component flows, and for the space and time dependent heat release (neutron kinetics, chemical kinetics).

The theoretical work is based on experimental investigations on chemical process kinetics and on transient two-phase flows. In the years to come, the institute will construct a multi-purpose test facility (TOPFLOW) to study transient flow phenomena. To better characterize the momentum, mass, and energy transfer between the phases and components sophisticated two-phase measuring equipment is developed.

Magneto-hydrodynamics (MHD) is a particular branch of the thermohydraulics research of the institute dealing with the control of electrically conducting fluids by external electromagnetic fields. MHD offers technological and safety relevant applications in semiconductor materials, metallurgy, and e.g. electrochemistry. The work is constitutional part of a common Innovationskolleg (innovative research activity) of the Technical University of Dresden and Forschungszentrum Rossendorf that is funded by Deutsche Forschungsgemeinschaft.

The efforts in materials safety are devoted to the behaviour of materials under neutron and gamma radiation. The susceptibility to irradiation induced embrittlement and the state after thermal annealing is assessed by fracture mechanical tests in dependence on the materials composition. The institute is specialized to the investigation of irradiated, radioactive material. Recently licensed laboratories are available to prepare and test radioactive specimens. The microstructural mechanisms of ductility reduction are revealed by highly resolving methods of structural analyses. Monte Carlo methods for radiation field calculation are developed and validated to get information about the irradiation fluences to which the components have been exposed. Starting from the estimated accident loads (pressure and temperature) and from the mechanical and thermal properties of the relevant components, the integrity of the plants and components is assessed by structural dynamic calculations. These calculations consider the thermal and mechanical interactions between the fluids and the components.

Together with the Institute of Radiochemistry, the institute investigates the chemical and physical phenomena ruling the transport of radionuclides in unsaturated zones of soil. The relevance of this topic is due to the wastes from Uranium mining in Saxony and Thuringia till

the end of the eighties.

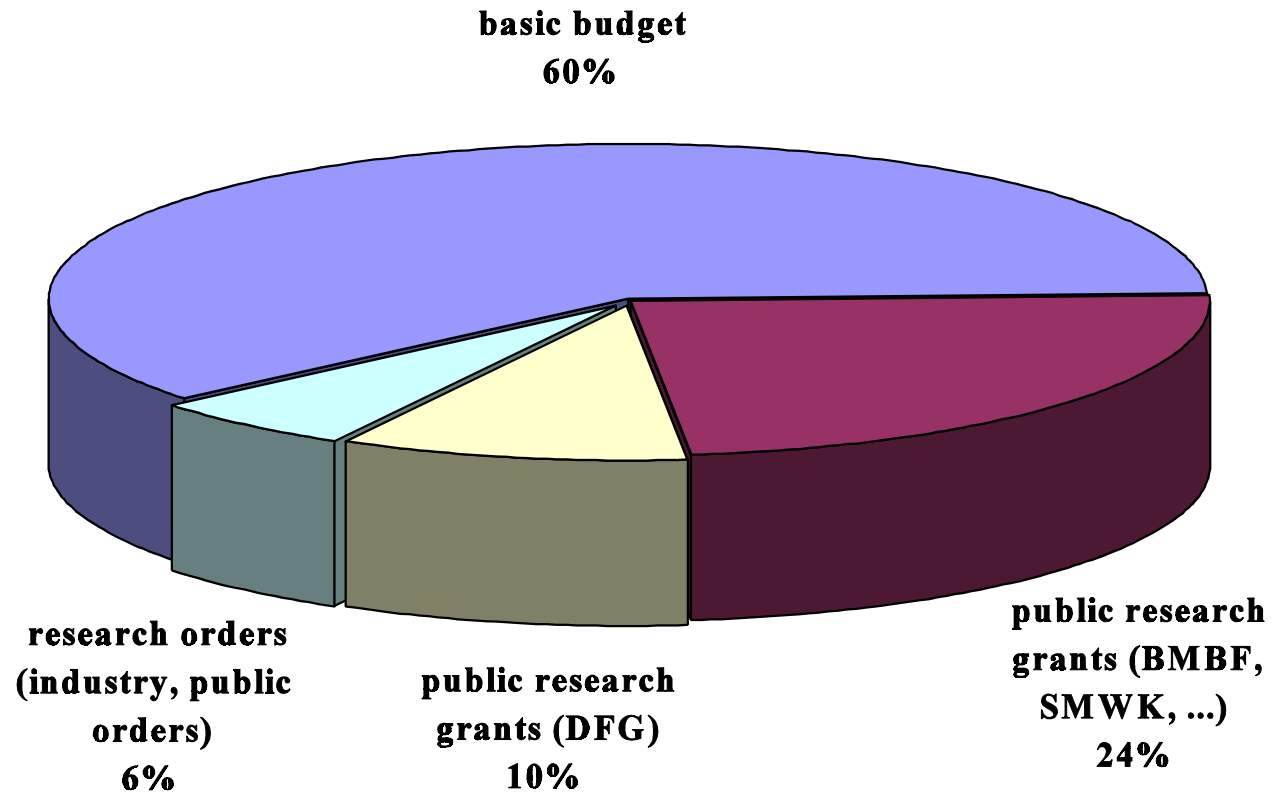
The work on decision analysis to support strategy finding for the environmental remediation from wastes were concluded. That topic could not satisfyingly be embedded into the research profile of the institute.

Together with the Technical University of Dresden and Hochschule für Technik, Wirtschaft und Sozialwesen (HTWS) Zittau/Görlitz the Institute of Safety Research constitutes one of the four remaining centres of competence for nuclear energy and nuclear safety research in Germany. It is the only one in East Germany and regionally takes care for the conservation of the nuclear science and engineering competence. There are vital scientific links to the other centres of competence, particularly to the Gesellschaft für Anlagen- und Reaktorsicherheit and the Munich Technical University.

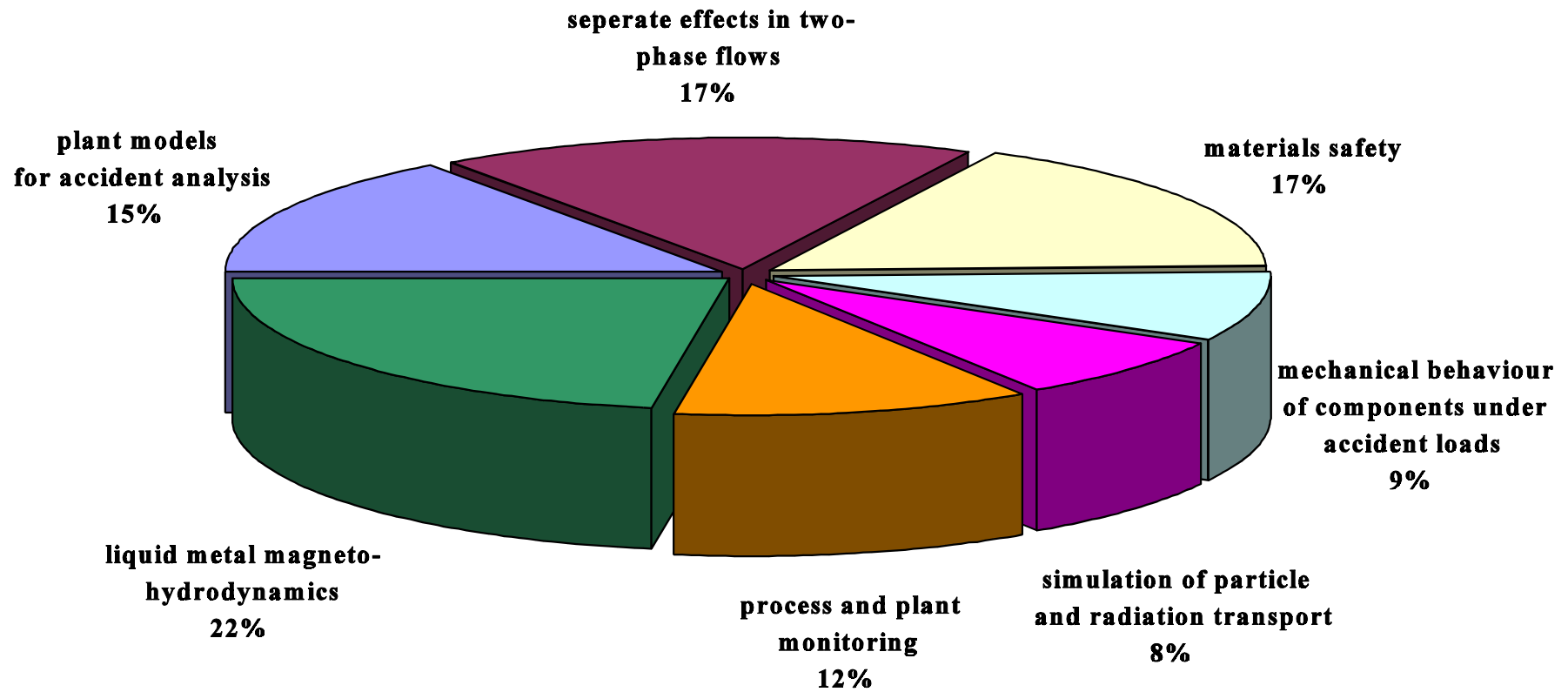
The institute takes part in coordinated research activities of the EU and in the German nuclear safety research programm of BMBF/BMWi. Among others we act as the leader of the western consortium in the safety research related TACIS project on the "Improvement of the Validation of Coupled Thermohydraulics, Neutron-Kinetics Code". Moreover, we are a member of the EU concerted action on the investigation of boron dilution transients in pressurized water reactors. The related research project is funded by BMWi. In this context, the institute constructed a 1:5 scaled model of a German pressurized water reactor for coolant mixing studies (ROCOM). This work is cofinanced by Vereinigung der Großkraftwerksbetreiber (VGB).

The following graphs give an overview about the sources and deployment of funding amongst the different research tasks. In 1998, nearly 40 % of the total budget came from external sources with 34 % from public research grants and with 6 % from research orders mainly by the industry.

## Distribution of funding sources 1998



### Deployment of funding on the various tasks/projects 1998



# INVESTIGATION OF COOLANT MIXING IN PRESSURIZED WATER REACTORS AT THE ROSSENDORF MIXING TEST FACILITY ROCOM

Gerhard Grunwald, Thomas Höhne, Horst-Michael Prasser, Karlheinz Richter,  
Frank-Peter Weiß

## 1. Introduction

During the so called boron dilution or cold water transients at pressurized water reactors too weakly borated water or too cold water, respectively might enter the reactor core. This results in the insertion of positive reactivity and possibly leads to a power excursion. If the source of unborated or subcooled water is not located in all coolant loops but in selected ones only, the amount of reactivity insertion depends on the coolant mixing in the downcomer and lower plenum of the reactor pressure vessel (RPV). Such asymmetric disturbances of the coolant temperature or boron concentration might e.g. be the result of a failure of the chemical and volume control system (CVCS) or of a main steam line break (MSLB) that does only affect selected steam generators (SG) [1-3]. For the analysis of boron dilution or MSLB accidents coupled neutron kinetics/thermo-hydraulic system codes have been used. To take into account coolant mixing phenomena in these codes in a realistic manner, analytical mixing models might be included. These models must be simple and fast running on the one hand, but must well describe the real mixing conditions on the other hand. One possibility is to use pre-determined mixing matrices mapping the contribution of each cold leg to each fuel assembly at the reactor core inlet [2]. The coolant mixing in the downcomer and lower plenum depends

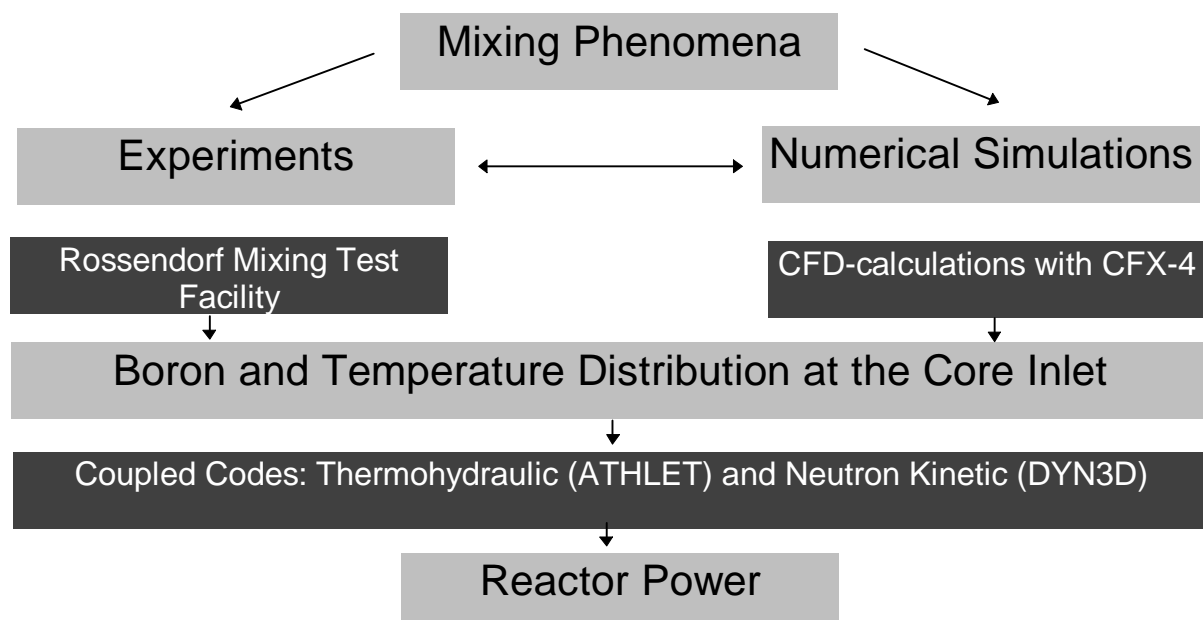


Fig. 1: Systematic of investigations in mixing phenomena

significantly on the construction of the reactor vessel and on the instantaneous flow conditions. The models and assumptions for coolant mixing description to be used in the coupled codes must be validated against experimental data and detailed computational fluid dynamics (CFD) calculations. Therefore the Institute for Safety Research of Forschungszentrum

Rosendorf has constructed a 1:5 mixing test facility ROCOM (**R**osendorf **C**oolant **M**ixing **M**odel) representing the geometry of the German Konvoi type pressurized water reactor. Later on tests on the future European Pressurized Water Reactor (EPR) are planned. The numerical simulations are based on the CFD-Code CFX-4.2. [4].

The scheme in Figure 1 shows the systematics of transient analyses reaching from mixing tests and numerical simulations of the mixing up to the reactor dynamics calculations providing the reactor power and other safety relevant parameters [5].

## 2. The test facility



Fig. 2: RPV Plexiglas® Model



Fig. 3: Test facility ROCOM

Table 1 compares the relevant parameters of the model with those of the Konvoi type reactor.

Table 1: Comparison original PWR - 1:5 scaled mixing model: coolant medium water, 20°C

Dimension	Unit	Original	Model 1:5
diameter of the pressure vessel	mm	5000	1000
height of the pressure vessel	mm	~12 000	~2400
inlet nozzle diameter.	mm	750	150
downcomer gap	mm	315	63
general mass flow of the coolant	m <sup>3</sup> /h	92 000	1400
mass flow per loop	m <sup>3</sup> /h	23 000	350
speed at inlet nozzle	m/s	14.5	5.5
speed at the downcomer	m/s	5.5	2.1
Re inlet nozzle	-	8.4*10 <sup>7</sup>	8.3*10 <sup>5</sup>
Re downcomer	-	2.7*10 <sup>7</sup>	2.5*10 <sup>5</sup>
Re Original / Re Model	-	1	~100

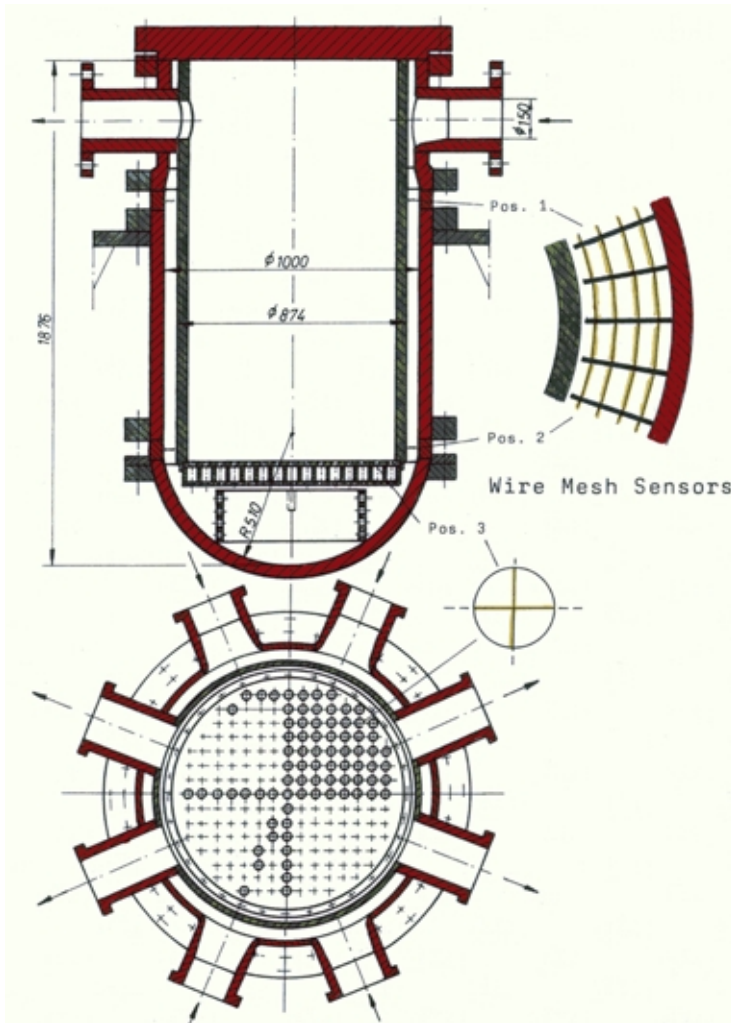


Fig. 4: View of the Plexiglas® model

explained in „Wire-mesh sensors for two-phase flow investigations“ of this annual report and in [6].

There is one sensor at the lower core support structure, two are in the downcomer and one in one cold leg (see Fig. 4). The extensive instrumentation with these sensors permits a high resolution of the concentration field in the RPV in space and time. The sensors are shown in detail in Fig 5-7. The downcomer sensors and those in the cold leg have 16x16 measurement points each. The sensor at the core bottom yields 193 points at the same time. This means, there is one concentration measurement at the bottom of each fuel element.

All sensors provide 200 measurements per second and work in the conductivity range of 10-500  $\mu\text{S}/\text{cm}$ . In the experiments, a time resolution of 20 measurements per second is sufficient, i.e. 10 individual measurements are averaged.

As mixing is less influenced by the absolute temperatures and by the static pressure but by density differences and flow velocity the vessel of the 1:5 scaled test facility could be made of Plexiglas® and is operated at ambient pressure with cold water (Fig. 2) This allows flow visualisation and LDA velocity measurements.

The test facility is furnished with 4 separately controllable coolant pumps (Fig. 3) to be able to simulate different flow conditions from nominal coolant flow rate to natural convection and pump start-up.

To study the mixing phenomena plugs of salt water are injected into deionate in the RPV through one of the cold legs. The salt significantly changes the conductivity of the water what can be measured by conductance methods. In the facility, the so called wire mesh sensors are applied. The working principle of the mesh sensors is

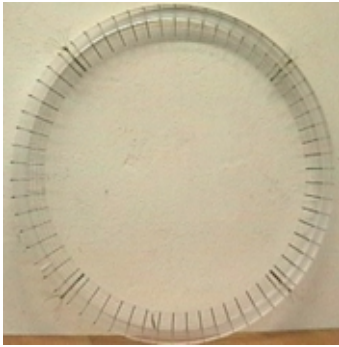


Fig. 5: Sensor DC

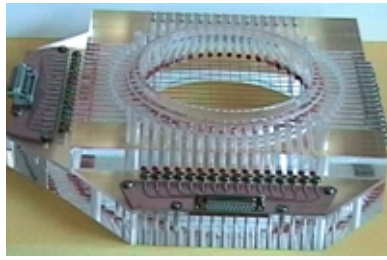


Fig. 6: Sensor inlet nozzle



Fig 7: Sensor core inlet

The mixing measurements in the reactor model are realised by the following steps: First the test facility is filled with low conductivity water (deionat). The wanted flow field is adjusted by controlling the main coolant pumps. After this, the injection pumps forward a plug of salted water continuously or discontinuously to the mixer in one of the cold legs. The concentration profile is measured by the wire mesh sensor in that cold leg. All processes, including the measurement of the mass flow, temperature, pressure, the tracer injection and the water cleaning with ion exchangers are computer controlled.

The screen panels of the computerised process control system is shown in Fig. 8. It is based on the software package DELPHI™ -4.

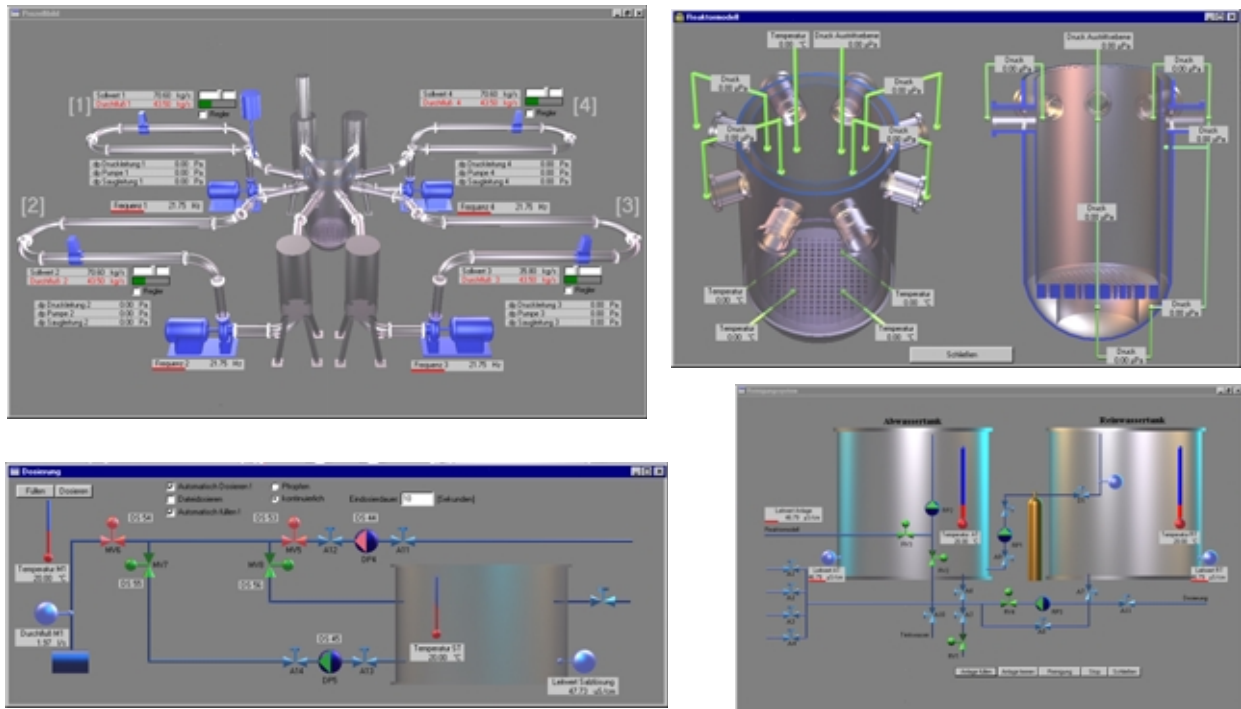


Fig. 8: Process control system of the mixing test facility

## 5. Experimental Results

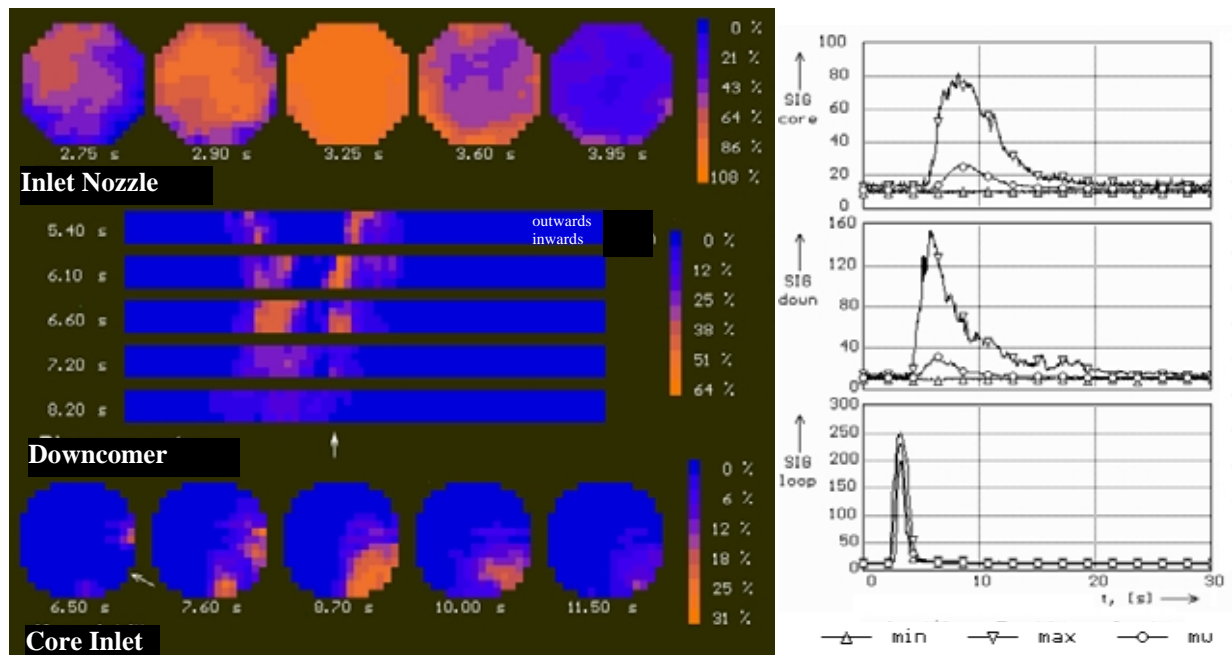


Fig. 9: Injection of a salted water plug into one loop at nominal conditions

Figure 9 shows the concentration distribution in space and time after the injection of a short salted water plug in one loop at nominal conditions, i.e. all four pumps were operating at full speed. Conductivity distributions are shown at the inlet nozzle, at the end of the downcomer and at the core inlet. The arrows are indicating the direction of the injection. The mass flow rate was  $50 \text{ m}^3/\text{h}$  in all 4 loops and the tracer injection lasts 0.7 seconds (1 litre salted water).

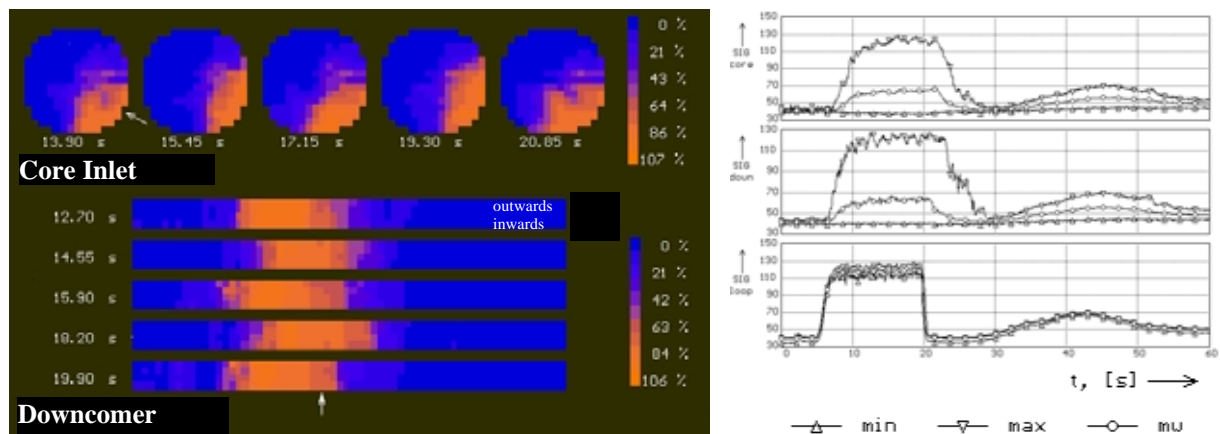


Fig. 10: Constant injection of a salted water plug into one loop at nominal condition

The diagrams show three time dependencies of the conductivity at the wire mesh sensors: instantaneous values of the maximum, the minimum and the averaged conductivity over the measuring planes at the core inlet sensor (core), the downcomer sensor (down) and the inlet nozzle sensor (loop). The sensor in the inlet nozzle confirms the good mixing of the salt water by the injection device. In the downcomer and at the lower plenum, the mixing is incomplete. At the moment when the plug is entering the downcomer sensor and also at the core inlet, two

maxima are clearly to be seen. This phenomenon is caused by a re-circulation area below the inlet nozzle. Later on, these two maxima are merging together. The highest concentration level at the core inlet is found at the periphery. It reaches only 31 % of the concentration at the reactor inlet, which is caused by mixing due to the wide spectrum of travelling times in the vortexes of the downcomer. When the plug is big enough, like in Fig. 10 (injection: 22 liters in 15 seconds, mass flow rate per loop: 100 m<sup>3</sup>/h), the maximum concentration at the core inlet corresponds to the concentration at the inlet nozzle, i.e. there are several fuel element positions, which are supplied with practically unmixed water from the disturbed loop. At the same time, the minimum concentration remains at the initial level, i.e. the majority of the measuring points are not reached by the water from the plug. In the process shown in Fig. 10, the injection conditions were constant for 14 s seconds. Despite of this, the concentration distribution shows characteristic azimuthal oscillations with a period of about four seconds, which are caused by the vortexes in the downcomer. The diagrams also show the second arrival of the plug after one turn around through the loops.

## 6. Outlook

To simulate real accident scenarios and for code validation an extensive test programme is planned. The experimental results will be compared against CFD calculations for analysing the dependencies of the power output of the reactor on the temperature and/or boron distribution. The classification of the tests is shown in Table 2.

Table 2: Classification of the Mixing Experiments

Group	Experimental Objects
A	Mixing under steady state conditions
B	Mixing under quasi-steady state conditions
C	Pump start-up scenarios
D	Steady state or transient flow regimes as an input for an analytical model using transfer functions
E	Start of natural circulation
F	Influence of internals on the flow field

## References

- [1] R. Hertlein, (1998), UPTF TRAM Test Phase C3, 1. EUBORA Project Meeting, 21-23 Oct., Vantaa, Finland
- [2] P. Dräger (1987), Makroskopische Kühlmittelvermischung in Druckwasserreaktoren, Dissertation TH Zittau
- [3] G. Ulrych und E. Weber (1983), Neuere Ergebnisse zur Kühlmittelströmung in Druckwasserreaktoren, Atomkernenergie-Kerntechnik 42, 217
- [4] CFX-4.2 User Manual (1997), AEA Technology
- [5] U. Grundmann, S. Kliem, U. Rohde (1997), The coupled code complex DYN3D/ATHLET- application to main steam line break analysis, Proc. M&C and SNA '97, Saratoga Springs, New York, USA, October 6-9
- [6] H.-M. Prasser, A. Böttger, J. Zschau(1998), A new electrode-mesh tomograph for gas liquid flows, Flow Measurement and Instrumentation 9, 111-119

# **A BENCHMARK FOR COUPLED THERMOHYDRAULICS SYSTEM/ THREE-DIMENSIONAL NEUTRON KINETICS CORE MODELS**

**Sören Kliem**

## **1. Introduction**

During the last years 3D neutron kinetics core models have been coupled to advanced thermo-hydraulics system codes. These coupled codes can be used for the analysis of the whole reactor system. Although the stand-alone versions of the 3D neutron kinetics core models and of the thermo-hydraulics system codes generally have a good verification and validation basis, there is a need for additional validation work. This especially concerns the interaction between the reactor core and the other components of a nuclear power plant (NPP). In the framework of the international „Atomic Energy Research“ (AER) association on VVER Reactor Physics and Reactor Safety, a benchmark for these code systems was defined.

## **2. Definition of the Benchmark**

This benchmark is the first benchmark for coupled thermo-hydraulics system/3D hexagonal neutron kinetics core models. It was defined by the Institute of Safety Research of Forschungszentrum Rossendorf (FZR). The complete definition can be found in [1]. The reference plant for the definition of the benchmark is the VVER-440/213. The VVER-440/213 is a pressurized water reactor with six loops. The nominal power is  $1375\text{MW}_{\text{th}}$ . The NPP has six horizontal steam-generators and two turbines. The reactor core consists of 349 fuel assemblies with hexagonal cross section. In this benchmark the response of the reactor core to a perturbation coming from the secondary side of the NPP is to be investigated. The initiating event of the transient is a break of the main steam header at the end of the first fuel cycle during hot shutdown conditions with one control rod group sticking. Although the main application fields of such coupled code systems are accidents with asymmetrical perturbations, a nearly symmetrical main steam line break was chosen for this first benchmark for these codes. This assumption corresponds to the way: begin with a simple problem and then increase the complexity. This approach led to good results in the previous AER benchmarks.

The following control and safety systems were considered in the benchmark calculation: pressurizer heater, volume control system and high pressure injection system (HPIS) in the primary circuit and one feedwater pump in the secondary circuit. For the calculation each participant had to use own nuclear cross section data. A burnup calculation for the first loading of the core had to be performed by each code. The use of own data bases for the nuclear cross sections leads to the necessity to provide a reference value for some key parameter. It was decided to adjust the subcriticality at the beginning of the transient, so that all participants begin the calculation from the same subcriticality level.

The expected course of the transient is the following: The double ended break of the main steam header causes a depressurization of all six steamgenerators. The set points for the closure of the main steam isolation valves will not be reached, so that this depressurization will not be stopped. For this reason, the main coolant pumps remain in operation, too. The water level in the steam-

generators decreases and the one available feedwater pump begins to work. The secondary side temperature decreases together with the pressure along the saturation line. Pressure and temperature decrease lead to an increasing heat flux from the primary to secondary side. Coolant temperature and primary circuit pressure start to drop. Due to the negative moderator temperature feedback, a positive reactivity is inserted into the core, and the initial subcriticality can be compensated so that recriticality of the reactor is achieved. Due to the further overcooling of the primary circuit, the nuclear power can rise until reactivity compensation by fuel temperature increase. The pressure and temperature decrease in the primary circuit lead to an activation of the HPIS. The injection of highly-borated water terminates the power excursion.

### 3. Results

Five organizations from five different countries took part in the benchmark calculations. Solutions were received from Kurchatov Institute Moscow (Russia) with the code BIPR8/ATHLET, VTT Energy Espoo (Finland) with HEXTRAN/SMABRE, Nuclear Research Institute Rez (Czech Republic) with DYN3D/ATHLET, KFKI AEKI Budapest (Hungary) with KIKO3D/ATHLET and Forschungszentrum Rossendorf (Germany) with the code DYN3D/ATHLET.

Tab. 1: Comparison of Key Parameters

	DYN3D/ ATHLET	BIPR8/ ATHLET	HEXTRAN/ SMABRE	DYN3D/ ATHLET (Rez)	KIKO3D/ ATHLET
recriticality time [s]	48.8	80.4	66.0	56.9	58.2
recriticality temperature [°C]	228.2	218.3	221.2	225.1	222.0
max. core power [MW]	685.7	547.4	534.0	657.6	585.9
integrated leak mass at 400s [t]	169.3	147.5	154.5	165.0	149.3
time of HPIS activation [s]	229.9	230.0	236.0	231.4	224.8
boron concentration at 400s [ppm]	95.5	68.1	129.5	109.5	149.1

All codes predicted the recriticality of the core due to overcooling, but at different times (Tab. 1). The corresponding recriticality temperatures were determined by stationary  $k_{\text{eff}}$ -calculations. For these calculations all boundary conditions were given, so that differences in the results are caused only by the different nuclear libraries used in the calculations. It can be seen, that the recriticality temperatures of the core range from 228.2°C (DYN3D/ATHLET) to 218.3°C (BIPR8/ATHLET). These differences in the nuclear data give the biggest contribution to the deviations in the predicted recriticality time.

Within the first 60s the thermohydraulic quantities in the primary circuit behave very similar in

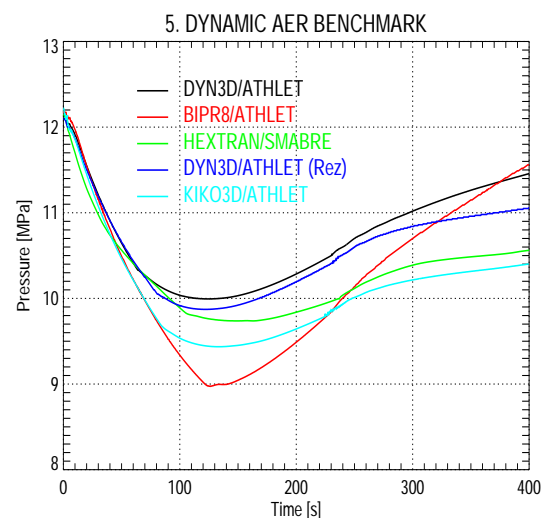


Fig. 1: Upper Plenum Pressure

all calculations. Later on, the influence of the re-established power generation in the core after recriticality can be seen. The minimum pressure reached during the overcooling depends on the time of recriticality. In the later phase of the transient (after  $t=230s$ ) the pressure is dominated by the volume control system and the beginning high pressure injection (Fig. 1).

Fig. 2 shows the behaviour of the core power. The time of remarkable power increase is in the interval from 62s (DYN3D/ATHLET) to 123s (BIPR8/ATHLET). The initial power peak can be seen only in two calculations (DYN3D/ATHLET, DYN3D/ATHLET (Rez)). The sudden power decrease after the beginning of the injection of highly-borated water by the HPIS can be observed in all calculations. The efficiency of the HPIS depends on the primary circuit pressure. Due to the differences in this pressure, the mass of highly-borated water injected by the HPIS differs in the calculations, too. This is expressed also in the boron concentration at core inlet at the end of the transient (Tab. 1). Four calculations show a consistence of the primary circuit pressure and the core inlet boron concentration. An analysis of the pressure behaviour in the BIPR8/ATHLET calculation showed, that the mass of injected highly-borated water should be in the range of the DYN3D/ATHLET and DYN3D/ATHLET (Rez) calculations. For this reason, the boron concentration should be about the same. However, the provided value is lower.

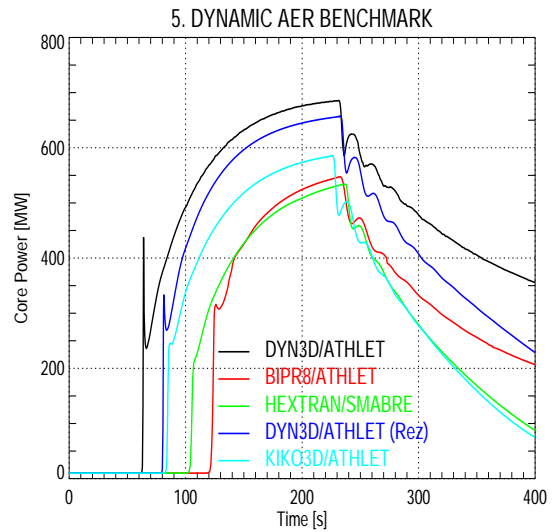


Fig. 2: Total Core Power

In section 2, it was stated, that the selected break causes a nearly symmetrical perturbation of the core. A small asymmetry is introduced by the connection of the pressurizer (to one loop). During the overcooling of the primary circuit the hot coolant coming down from the pressurizer affects the steamgenerator inlet collector temperature. For this reason, differences in the behav-

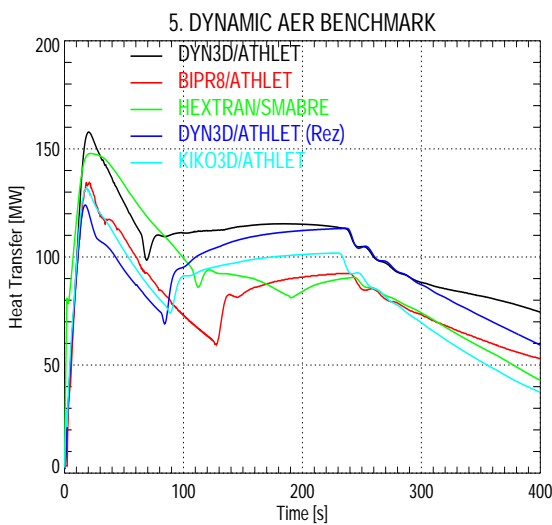


Fig. 3: Heat Transfer in the Steamgenerator of the Loop with the Pressurizer

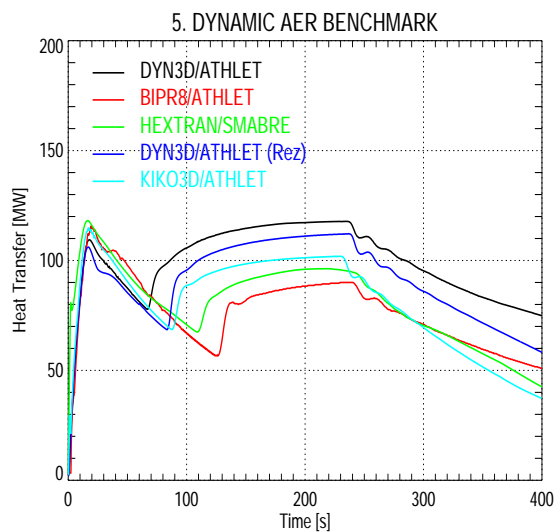


Fig. 4: Averaged Heat Transfer in the Steamgenerators of the Loops without the Pressurizer

four of the loops were expected. Therefore, results for the loop with the pressurizer and averaged over all remaining loops were requested. Fig. 3 and 4 show the heat transfer from the primary to secondary side of the steamgenerators. A direct comparison of the values of one calculation reveals the expected differences in the behaviour of the loops with and without pressurizer. Two calculations (DYN3D/ATHLET and HEXTRAN/SMABRE) provide much higher values of this difference. This is obviously connected with the higher number of loops modeled in the calculations. The influence of the pressurizer is not distributed over several loops like in a calculation with two 3-fold loops (BIPR8/ATHLET, DYN3D/ATHLET (Rez), KIKO3D/ATHLET).

#### 4. Conclusions

A short overview of the results of the first international benchmark for coupled thermohydraulics system/three-dimensional neutron kinetics core models is presented. The complete comparison can be found in [2].

All codes predicted the recriticality of the core due to overcooling, but at different times. Until the time of beginning of remarkable power generation in the core, all effects in the primary circuit observed in the calculations are dominated by the thermohydraulic modules of the codes. The depressurization of the secondary side caused by the break of the main steam header, the heat transfer from the primary to secondary side with the overcooling of the primary circuit are described in good agreement by all codes. The corresponding parameters show a very similar behaviour in all calculations. The recriticality temperature differs by 10K. These differences are caused by the use of different nuclear data libraries. The different nuclear data have an important influence on the further course of the transient. It seems, that this is the main reason for the differences between the solutions.

The realization of such benchmark calculations is very helpful, because different physical models and data can be compared. They contribute to minimize the user effects, too. But all in all it can be stated, that this very complex and complicated benchmark problem was solved by all participants in a very good manner. The considerable experience in calculations of both 3D neutron kinetics core and thermohydraulics NPP behaviour of the reactor type selected for this benchmark was a very good basis for the realization of the benchmark.

#### References

- [1] S. Kliem (1997), Definition of the fifth dynamic AER benchmark problem - a benchmark for coupled thermohydraulic system/ three-dimensional hexagonal neutron kinetic core models, Proceedings of the 7<sup>th</sup> Symposium of AER (pp. 429-438), Budapest, KFKI Atomic Energy Research Institute
- [2] S. Kliem (1998), Comparison of the results of the fifth dynamic AER benchmark - a benchmark for coupled thermohydraulic system/3D hexagonal neutron kinetic core models, Proceedings of the 8<sup>th</sup> Symposium of AER (pp. 429-469), Budapest, KFKI Atomic Energy Research Institute

*The project this paper is based on is funded by the BMBF (Bundesministerium für Bildung, Wissenschaft, Forschung und Technologie) and is registered with No. 150 0925A.*

# NEW 3D NODAL METHOD HEXNEM FOR IMPROVING THE ACCURACY OF THE HEXAGONAL VERSION OF THE CODE DYN3D

Ulrich Grundmann

## 1. Introduction

The nodal expansion method (NEM) used in the hexagonal version of the code DYN3D is based on the node averaged values of fluxes in the node volume and averaged values of fluxes and currents at the interfaces of the nodes [1]. The 3-dimensional diffusion equation is split into a 2-dimensional equation in the hexagonal plane solved with the help of Bessel functions and a 1-dimensional equation in axial direction solved by polynomial expansion. The two equations are coupled by the transversal bucklings. The accuracy of this method is sufficient for the VVER-440 where the assembly pitch is 14.7 cm. The assemblies of the VVER-1000 have a larger pitch of 24.1 cm. Comparisons with mathematical benchmarks for the VVER-1000 show a maximal deviation of powers in the order of 5%. The new nodal expansion method HEXNEM presented here uses a different flux expansion in the nodes. In addition to the averaged values at the interfaces of the hexagon the values at the corner points are included. It is shown that the accuracy is improved particularly for the VVER-1000 problems.

## 2. Description of the Method

Using standard notation the 3-dimensional 2-group neutron diffusion equation in the node n is given by

$$-\nabla D_g^n \nabla \Phi_g(\mathbf{r}) + \Sigma_g^n \Phi_g(\mathbf{r}) = S_g^n(\mathbf{r}) \quad (1)$$

with

$$S_1^n(\mathbf{r}) = \frac{1}{k_{eff}} \sum_{g=1}^2 \nu \Sigma_{f,g}^n \Phi_g^n(\mathbf{r}) \quad \text{and} \quad S_2^n(\mathbf{r}) = \Sigma_{1 \rightarrow 2}^n \Phi_1(\mathbf{r}) \quad (2)$$

The one- and 2-dimensional equations of the node n are obtained by integration over the hexagonal area  $F_{hex}$  or the height  $a_z$  of the box with the volume  $F_{hex} \cdot a_z$ . After integration over the z-direction for each energy group one obtains the 2-dimensional equation (the group index g and node index n are omitted in the following) for the axially averaged flux  $\Phi(x, y)$

$$-D \left( \frac{\partial}{\partial x^2} + \frac{\partial}{\partial y^2} \right) \Phi(x, y) + \Sigma \Phi(x, y) = S(x, y) - L^z(x, y) \quad (3)$$

with the transversal leakage term

$$L^z(x, y) = -\frac{D}{a_z} \int_{z_0}^{z_1} \frac{\partial^2}{\partial z^2} \Phi(x, y, z) dz \quad (4)$$

for any  $z_0$  and  $z_1 = z_0 + a_z$ . The integration over the hexagon  $F_{hex}$  gives the one-dimensional equation for the radially averaged flux  $\Phi(z)$

$$-D \frac{d^2}{dz^2} \Phi(z) + \Sigma \Phi(z) = S(z) - L'(z) \quad (5)$$

The average value of transversal leakage  $L'(z)$  is given by

$$L'(z) = -\frac{D}{F_{hex}} \int_{F_{hex}} \left( \frac{\partial^2}{\partial x^2} + \frac{\partial^2}{\partial y^2} \right) \Phi(x, y, z) dF \quad (6)$$

The solution of the equations (3) and (5) in the nodes is described in the following. The flux in the hexagonal plane is expanded using polynomials  $w_i(x, y)$  up to the 2<sup>nd</sup> order and exponential functions being the solutions of the homogeneous equation (3)

$$\Phi(x, y) \approx \sum_{i=0}^5 c_i w_i(x, y) + \sum_{k=1}^6 a_{s,k} \exp[B(e_{s,k} \mathbf{r})] + \sum_{k=1}^6 a_{c,k} \exp[B(e_{c,k} \mathbf{r})] \quad (7)$$

with  $\mathbf{r} = (x, y)$ . The unity vectors  $\mathbf{e}_{s,k}, \mathbf{e}_{c,k}$  show in the directions of the midpoints of the sides and to the corners (see fig. 1). The buckling  $B$  is given by

$$B = \sqrt{\frac{\Sigma}{D}} \quad (8)$$

The chosen polynomials  $w_i(x, y)$  fulfill the following conditions

$$\frac{1}{F_{hex}} \int_{F_{hex}} w_i w_j dF = N_i^2 \delta_{ij} \quad (9)$$

with Kronecker's symbol  $\delta_{ij}$  and the normali-

zation factors  $N_i$ . The source terms and the transversal leakage terms of (3) are approximated by the polynomials. The coefficients of the leakage terms are obtained from the averaged leakage of the considered box and the values of the neighbouring hexagons. The coefficients of the source are given by the updated coefficients of the fluxes of the last outer iteration. Inserting expansion (7) into the diffusion equation (3) the coefficients  $c_i$  are obtained from the coefficients of polynomial expansions at the right hand side. Defining the partial currents by

$$J^\pm = \frac{1}{2} \left[ \frac{\Phi}{2} \pm (\mathbf{e} \mathbf{J}) \right] \quad \text{with } \mathbf{J} = -D \nabla \Phi \quad (10)$$

for any direction from (7)  $\mathbf{e} = \mathbf{e}_{s,k}, \mathbf{e}_{c,k}$  one obtains the equation system

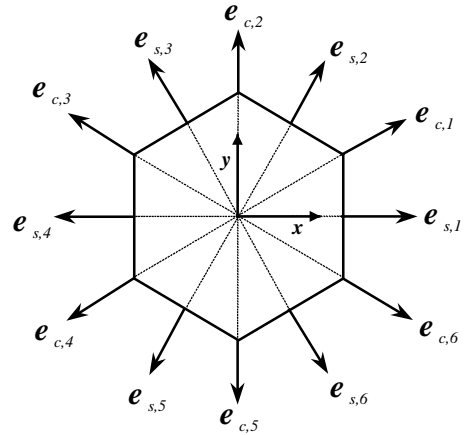


Fig. 1: Vectors  $\mathbf{e}_{s,k}, \mathbf{e}_{c,k}$  of directions

$$\begin{aligned} \mathbf{J}_s^\pm &= \mathbf{P}_s^\pm \mathbf{C} + \mathbf{Q}_{ss}^\pm \mathbf{A}_s + \mathbf{Q}_{sc}^\pm \mathbf{A}_c \\ \mathbf{J}_c^\pm &= \mathbf{P}_c^\pm \mathbf{C} + \mathbf{Q}_{cs}^\pm \mathbf{A}_s + \mathbf{Q}_{cc}^\pm \mathbf{A}_c \end{aligned} \quad (11)$$

where  $\mathbf{C}, \mathbf{A}_s, \mathbf{A}_c$  are the vectors of the coefficients  $c_i, a_{s,k}$  and  $a_{c,k}$ , respectively. The side averaged partial currents and the partial currents at the corners form the vector  $\mathbf{J}_s^\pm$  and  $\mathbf{J}_c^\pm$ , respectively. Caused by the symmetry of the problem each of the 6x6 matrices has only a few different elements. Each of the matrices  $\mathbf{P}_s^\pm, \mathbf{P}_c^\pm$  consist of 6 different elements  $\mathbf{Q}_{ss}^\pm, \mathbf{Q}_{cc}^\pm$  of 4, and  $\mathbf{Q}_{sc}^\pm, \mathbf{Q}_{cs}^\pm$  of 3 elements. The  $\mathbf{A}_s, \mathbf{A}_c$  are determined by a direct calculation of the inverse matrices of the (12x12) equation system (11) for given incoming partial currents  $\mathbf{J}_s^-, \mathbf{J}_c^-$  and  $\mathbf{C}$ . Eliminating the  $\mathbf{A}_s, \mathbf{A}_c$  in the equations (11) for the outgoing partial currents  $\mathbf{J}_s^+, \mathbf{J}_c^+$  it is possible to express the  $\mathbf{J}_s^+, \mathbf{J}_c^+$  by means of the incoming partial currents  $\mathbf{J}_s^-, \mathbf{J}_c^-$ , and the coefficients of the polynomial expansion  $\mathbf{C}$ :

$$\begin{aligned} \mathbf{J}_s^+ &= \mathbf{V}_s \mathbf{C} + \mathbf{W}_{ss} \mathbf{J}_s^- + \mathbf{W}_{sc} \mathbf{J}_c^- \\ \mathbf{J}_c^+ &= \mathbf{V}_c \mathbf{C} + \mathbf{W}_{cs} \mathbf{J}_s^- + \mathbf{W}_{cc} \mathbf{J}_c^- \end{aligned} \quad (12)$$

These matrices have the same structure as the matrices of (11). The different elements can be calculated at beginning of the iteration. At the interface between two hexagons, the incoming partial currents  $\mathbf{J}^-$  are equal to the outgoing currents  $\mathbf{J}^+$ . For the corners of three hexagons 1,2 and 3 (number in parentheses), the following interface condition is derived:

$$\{J_{c,1}^+(1) - J_{c,1}^-(1)\} + \{J_{c,3}^+(2) - J_{c,3}^-(2)\} + \{J_{c,5}^+(3) - J_{c,5}^-(3)\} = 0 \quad (13)$$

The described 2-dimensional method with the zero transversal leakage term in (3) was verified separately in [3] with the help of benchmark solutions obtained by Chao et. al. [2].

A analogous procedure as in the 2-dimensional case above is used for the solution of the equation (5), i. e. the flux is  $\Phi(z)$  expanded into polynomials until second order and exponential functions

$$\Phi(z) \approx \sum_{i=0}^2 c_i^z w_i^z(z) + a_1^z \exp(Bz) + a_2^z \exp(-Bz) \quad (14)$$

A quadratic approximation of the source term and the leakage is used in (14). The coefficients of the radial leakage are calculated from the averaged radial leakage of the box and the values of the upper and lower boxes. The coefficients of the source are given by the updated coefficients of the fluxes from the last outer iteration. Inserting expansion (14) into the diffusion equation (5) the coefficients  $c_i^z$  are obtained. Using a similar procedure as for the 2-dimensional case the outgoing partial currents at the bottom and top of the node are expressed by the  $c_i^z$  and the incoming partial currents in axial direction:

$$\begin{aligned} J_{z_0}^+ &= v_0^z c_0^z - v_1^z c_1^z + v_2^z c_2^z + w_1^z J_{z_1}^- + w_2^z J_{z_0}^- \\ J_{z_1}^+ &= v_0^z c_0^z + v_1^z c_1^z + v_2^z c_2^z + w_2^z J_{z_1}^- + w_1^z J_{z_0}^- \end{aligned} \quad (15)$$

An inner and outer iteration scheme is applied to solve the equation system for all nodes of the core. In the inner iteration process it is assumed that the fission and scattering sources in (3) and (5) are approximated by the polynomials with coefficients given from the last outer iteration. Based on the coefficients of the right hand side source terms and the coefficients of the leakage terms the polynomial coefficients  $c_i$  and  $c_i^z$  of the flux expansions are determined by inserting (7) and (14) into the diffusion equations (3) and (5), respectively. Using these coefficients the outgoing partial currents are calculated for each node by means of the expressions (12) and (15) from the given incoming currents. The incoming currents are determined from the outgoing currents of the neighbouring nodes using the interface conditions between the nodes or the boundary conditions at the core border.

After few (3 - 5) inner iterations the coefficients of the source terms are updated from the flux expansions (7) and (14) by using (9) and equivalent conditions for the polynomials of (14). The new source terms are used for the next outer iteration step. A Chebychev extrapolation scheme is applied to accelerate the outer iteration.

### 3. Results

Two 3D steady state benchmark problems were calculated with one node per assembly in horizontal direction and  $\Delta z = 25$  cm (VVER-440) or  $\Delta z = 35.5$  cm (VVER-1000). The problems have a 30 degree symmetry. Fig. 1 shows the axial configuration of the VVER-440 with the half inserted control rods of bank K6. The calculation was carried out with axial and radial reflector assemblies. The deviations  $\Delta k_{eff}$  of the eigenvalue  $k_{eff}$ , the maximum and averaged value of the relative deviations of nodal powers and assembly powers from reference solution of Maraczy [4] are presented in table 1 for the DYN3D method and the HEXNEM method. The comparison of the HEXNEM assembly powers with the results of reference solution [4] can be seen in fig. 2. The positions of the half inserted control rods of bank K6 are identical by the assemblies with a thicker boundary (no. 1 and 7). In case of the VVER-440 with the smaller assembly pitch of 14.7 cm the accuracy of the DYN3D method is sufficient for practical applications. The HEXNEM method even shows an improvement of the results in this case.

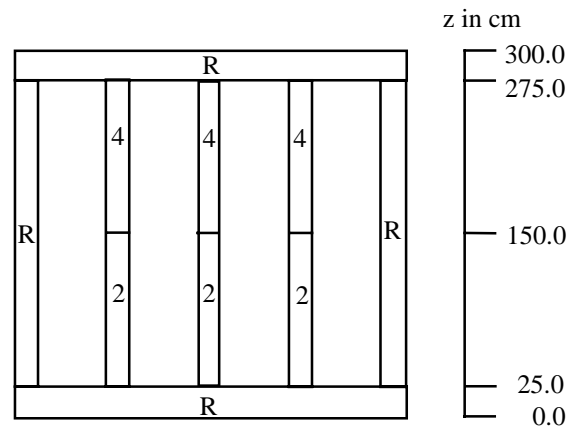


Fig. 2: Axial configuration of the VVER-440 (4 = absorber, R = reflector, 2 = fuel)

Table 1: VVER-440: Comparison of DYN3D and HEXNEM results with the reference:

VVER-440 Benchmark	DYN3D $\Delta k_{eff} = 40$ pcm		HEXNEM $\Delta k_{eff} = 1$ pcm	
	Max. (%)	Av. (%)	Max. (%)	Av. (%)
Nodal powers	2.7	0.93	0.8	0.17
Assembly powers	1.1	0.52	0.4	0.08

6	No. assembly	(k = 1.01132)
0.7758	Reference	
0.7751	HEXNEM	(k = 1.01131)
-0.09	Rel. dev (%)	
1	No. material	

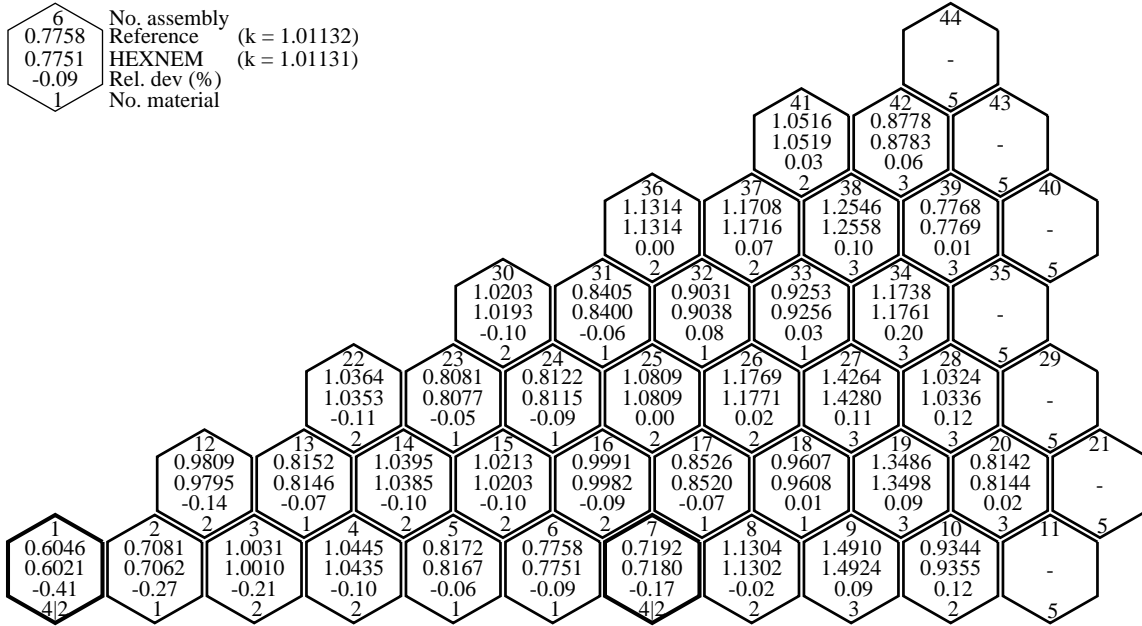


Fig. 3: Comparison of assembly powers for the VVER-440 Benchmark

The accuracy is more improved by the HEXNEM method for the VVER-1000 (pitch 24.1 cm). The 3D AER benchmark for the VVER-1000 is a problem with half inserted cluster and a half cluster in the central fuel assembly. The axial configuration is shown in Fig. 3. The results of the detailed comparison with the reference values published by Kolev in [5] can be seen in table 2. Fig. 4 compares the normalized assembly powers for each assembly. The HEXNEM results for the VVER-1000 problem show a significant improvement of the results compared with the DYN3D method.

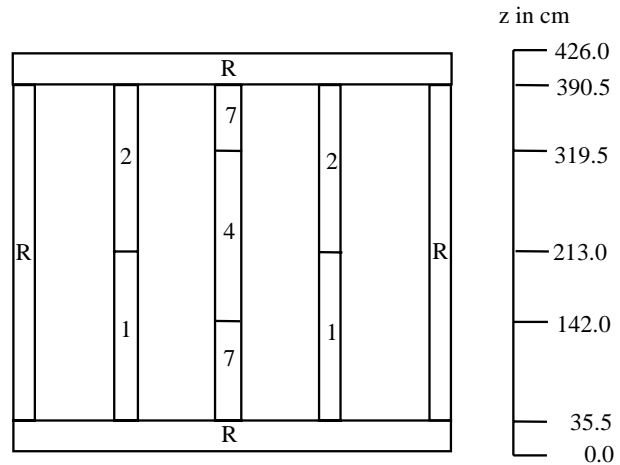


Fig. 4: Axial configuration of the VVER-1000 (1,7 = fuel, 2,4 = fuel with absorber rods, R = reflector)

Table 2: VVER-1000: Comparison of DYN3D and HEXNEM results with the reference:

VVER-1000 Benchmark	DYN3D $\Delta k_{eff} = 62$ pcm		HEXNEM $\Delta k_{eff} = 14$ pcm	
	Max. (%)	Av. (%)	Max. (%)	Av. (%)
Nodal powers	5.2	1.83	2.2	0.60
Assembly powers	3.0	1.53	0.8	0.33

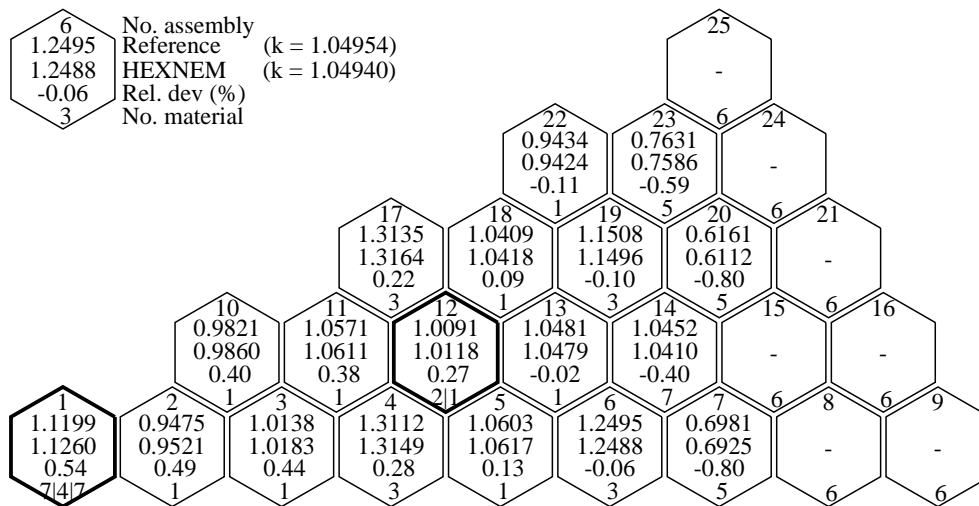


Fig. 5: Comparison of assembly powers for the VVER-1000 Benchmark

#### 4. Conclusions

The new nodal method HEXNEM for hexagonal geometry which includes the corner point fluxes shows a better accuracy for problems with large fuel assembly pitch as in the VVER-1000 reactors. Considering the future implementation of the method into the code DYN3D the use of the corner point fluxes together with the average values on the sides of the hexagon gives the possibility to apply the flux reconstruction method of DYN3D presented in without additional reconstruction of corner fluxes. Concerning the further development of the method the assembly discontinuity factors (ADF) can be taken into account in a simple way. The energy group wise solution scheme combining polynomial expansion and exponential functions can be extended to a larger number of energy groups.

#### References

- [1] U. Grundmann, U. Rohde (1989), DYN3D/M2 - a Code for Calculation of Reactivity Transients in Cores with Hexagonal Geometry, Proceedings of IAEA Technical Committee Meeting on Reactivity Initiated Accidents (pp. 257-302), Wien or Report FZR 93-01, Research Center Rossendorf (1993)
- [2] Y. A. Chao and Y. A. Shatilla (1995), Conformal Mapping and Hexagonal Methods - II: Implementation in the ANC-H Code, Nucl. Sci. Engng., 121, 210
- [3] U. Grundmann, F. Hollstein (1999), A Two-Dimensional Intranodal Flux Expansion Method for Hexagonal Geometry, accepted for publication in Nucl. Sci. Engng.
- [4] Cs. Maraczy (1995), A Solution of Seidel's 3D Benchmark for VVER-440 with the DIF3D-FD Code, Proceedings of 5th Symposium of AER (pp. 287 - 296), KfKI Atomic Energy Research Institute Budapest
- [5] N.P. Kolev, R. Lenain, C. Fedon-Magnaude (1997), Solutions of the AER 3D Benchmark for VVER-1000 by CRONOS, Proceedings of 7th Symposium of AER (pp. 650 - 665), KfKI Atomic Energy Research Institute Budapest.

# **IMPROVEMENT OF THE VERIFICATION OF COUPLED THERMOHYDRAULICS / NEUTRON KINETICS CODES: DYN3D BURNUP AND STEADY STATE CALCULATIONS**

**Sören Kliem, Siegfried Mittag, Ulrich Rohde, André Seidel, Frank-Peter Weiß**

## **1. Introduction**

The Commission of the European Community (CEC) has been funding projects aimed at a long-term collaboration in the field of reactor safety research and technology between the EU member states and East European countries within the PHARE programme. PHARE originally meant: **P**oland and **H**ungary - **A**ssistance in the **R**econstruction of the **E**conomy, but the programme was later extended to assist other East European countries, too.

The principal objective of the **S**afety **R**elated **R**esearch project SRR1/95 is the verification of those coupled thermal-hydraulics - neutron kinetics codes, that are currently used for modelling the behaviour of the Russian pressurized water reactors VVER during transients and accidents. The simulation of transient processes and the comparison of the results obtained by coupled codes with measured transient data is of particular interest. The higher the degree of code validation, the more reliable will be the analyses of possible abnormal states in the NPP, and the better is the safety assessment of these reactors.

This report provides a survey of the project participants, the codes to be validated and the measured NPP data, that have been documented for code validation. Prior to the transient calculations, the stationary core state from which the transient started has to be calculated. The comparison of the measured steady-state parameters to the calculated values is the first step of code validation. Only after that, transient simulations should be carried out.

## **2. International Project Team**

The project work is performed by a Consortium consisting of Forschungszentrum Rossendorf e.V. (FZR) Germany, VTT Energy (Finland), Gesellschaft für Anlagen- und Reaktorsicherheit (GRS) mbH, Germany and AEA Technology, UK, the Contractor FZR being the leading company.

The Nuclear Research Institute (NRI) Rez (Czech Republic), Atomic Energy Research Institute Budapest, (AEKI), Russian Research Center "Kurchatov Institute" Moscow (KI), Scientific & Technical Centre on Nuclear and Radiation Safety Kiev (STCNRS), and the Institute of Nuclear Research and Nuclear Energy Sofia (INRNE) are the East European Subcontractors in the project, Imatran Voima Oy (IVO) Power Engineering Ltd., Finland is a direct Subcontractor of VTT Energy.

The Consortium brings together organisations that have been at the forefront of thermal-hydraulics and neutron kinetics code development and application for many years. The chosen Subcontractors are able to provide transient data measured in operating VVERs.

### 3. Codes

In the Institute for Safety Research of FZR, the code DYN3D has been developed and coupled to the thermal-hydraulics code ATHLET developed by GRS [1]. DYN3D is a three-dimensional two-group nodal neutron kinetics code that is widely used for VVER core analyses in Eastern Europe. The code was transferred to Bulgaria, the Czech Republic, the Slovak Republic, and the Ukraine in the framework of an IAEA project. The coupled code system ATHLET-DYN3D is also being transferred to the countries mentioned.

KI has developed the three-dimensional two-group neutron kinetics code BIPR8 [2]. This code and earlier versions of it are used in Russian NPP operating VVER. KIKO3D [3] is a similar code, developed by AEKI. Both neutron kinetics code have been coupled to ATHLET.

VTT developed the thermal-hydraulics / neutron kinetics (three-dimensional, two groups, nodal expansion method) code system SMABRE / HEXTRAN [4,5]. VTT has been applying the code system to the Finnish VVER-440 reactors.

### 4. NPP transients

The following transients (experiments) have been provided by the Subcontractors and documented for code validation [6]:

VVER-440:

- Drop of the power of one of the two turbo-generators from full power down to house load level (Loviisa-1, documented by IVO),
- Coast-down of three of six working main coolant pumps at 55 % of nominal power (Dukovany-2, documented by NRI),

VVER-1000:

- Failure of one of the two working feed water pumps at nominal power (Balakovo-4, documented by KI),
- Drop of the turbo-generator power from nominal value down to house load level (Zaporyshye-6, documented by STCNRS),
- Coast-down of two from four working main coolant pumps at 90 % of nominal power (Kozloduy-6, documented by INRNE).

For each reactor type, the first-mentioned transient has been chosen for the code validation in the framework of the current project. The remaining transient files are available to later validation work.

## 5. The Loviisa-1 VVER-440 transient

### 5.1 Transient description

The transient was initiated by the load drop of one turbo-generator, i. e. the electric power output of the plant was suddenly reduced by half [7]. At the moment of generator drop, the nuclear power production in the reactor core was still at 100 %. Shortly after transient initiation, the reactor control system started to reduce the reactor power by inserting the group number six of the neutron-absorbing control assemblies. Thus neutron power was reduced down to 60 % within some 100 seconds. As a result of power reduction, the hot leg temperatures of the primary circuit decreased. Moreover, the cooling of the primary circuit by the steam generator is reduced because of the increasing steam pressure at the secondary side. Therefore, the cold leg temperature first increased significantly. Some 20 seconds later this temperature also started decreasing. The primary circuit pressure first increased, too, but was quickly reduced by spraying in the pressurizer. Later on, the reducing nuclear power decreased the pressure, so that the pressurizer heaters were switched on to stabilize pressure at its nominal level. On the secondary side, pressure also started increasing sharply, but was quickly brought back to normal by opening the turbine bypass valves, before the dropping nuclear power took effect here, too.

### 5.2 Burnup and steady-state calculations

The described transient was measured in the 21st cycle of the Loviisa-1 VVER-440. The burnup distribution at the beginning of cycle 19 was provided by IVO together with the shuffle schemes and operation history up to the start of the transient. Each participant in the validation carries out his own burnup calculation to get the actual burnup distribution and the steady-state reactor parameters as an input for the transient calculation. Only FZR (DYN3D) results will be presented in this report.

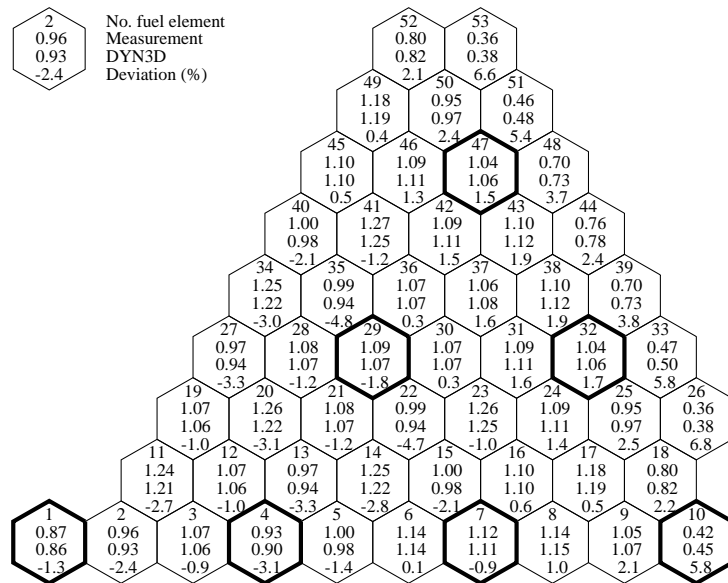


Fig. 1: Normalized power distribution before transient

The critical boron concentration calculated by DYN3D for the state at 71 full power days of cycle 21, i. e. for the burnup state at which the transient started, amounts to 5.60 g/kg (g boric acid per kg water), which is near to the measured value of 5.53 g/kg [7].

The DYN3D burnup distribution for this state was compared to the distribution calculated by IVO applying the Finnish standard fuel cycle lay-out code HEXBU-3D. The mean deviation

of fuel assembly burnup between DYN3D and HEXBU-3D is 0.9 %, the maximum deviation is 3.2 %. This agreement is satisfying.

Self-powered neutron detector measurements were done by IVO [7] in the stationary state prior to the transient to reconstruct the three-dimensional power distribution. Fig. 1 presents the comparison of assembly powers calculated by DYN3D to these experimental values for a 60-degree symmetry sector of the reactor core.

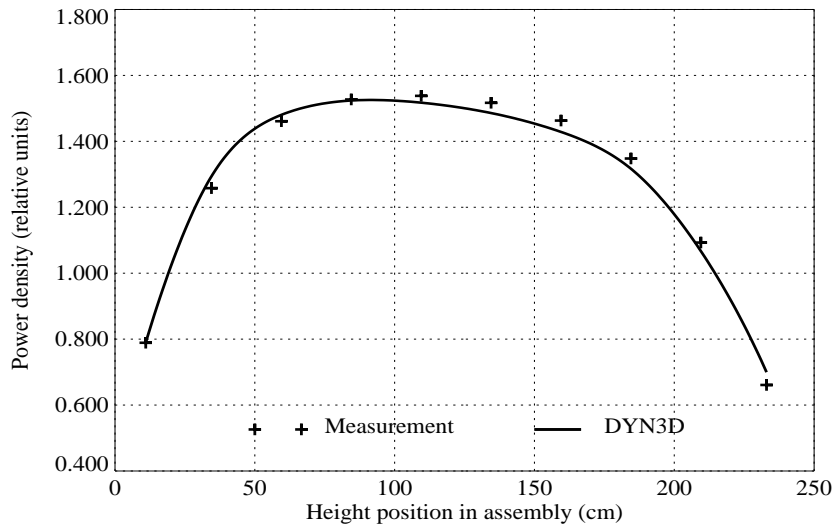


Fig. 2: Axial power distribution in the hottest assembly

Significant deviations are found near the core edges, i. e. in a region of low power densities. Fig. 2 shows the axial power distribution in assembly 41, where the highest assembly power has been measured.

In fig. 3, the fuel assembly outlet temperatures calculated by DYN3D are compared to the values measured in the steady state before the transient start. The core coolant inlet temperature at this state was at 265.5 °C, the thermal power was 1495 MW. The measured outlet temperatures are averages over the six core symmetry sectors. The deviations between calculated and measured temperatures correspond to the differences in the assembly powers (cf. fig. 2). The highest temperature deviation is found in fuel assemblies 22 and 35.

Altogether, there is a satisfying agreement between the DYN3D results and the measured values.

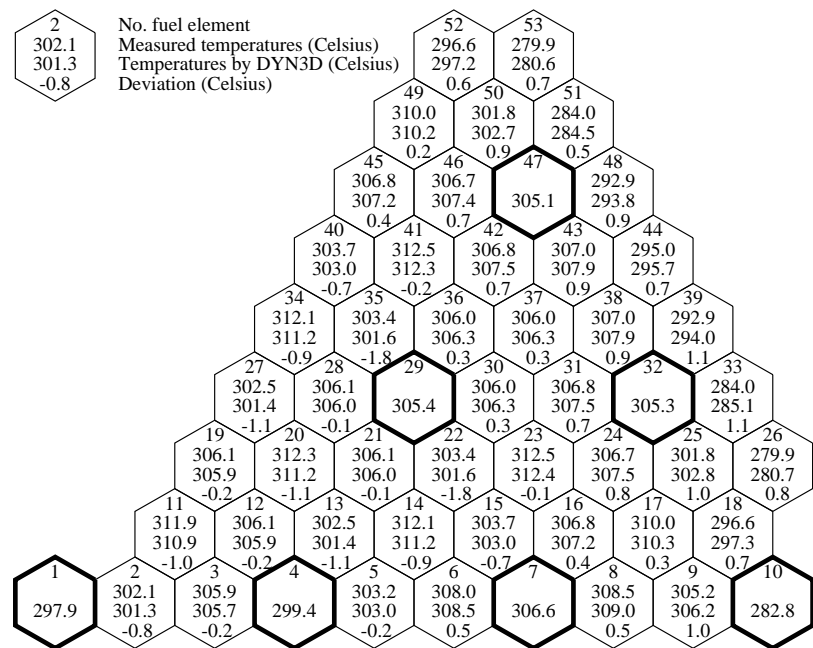


Fig. 3: Fuel assembly outlet temperatures before transient

## 6. The Balakovo-4 VVER-1000 transient

### 6.1 Transient description

The initiating event for the transient was the failure of one of the two working feed water pumps at full power [8]. The power control system responded by dropping the first control rod group from top to bottom within four seconds. Group No. 10, that had been at the axial position of 275 cm, started inserting in at the rate of 2 cm/s. As a result of dropping group No. 1, the neutron power decreased to about 63 % of the nominal value within 10 seconds. The slow insertion of group No. 10 down to a position of 140 cm resulted in a power of about 45 %. The reactor power was stabilized at this level by the automatic power controller.

The thermal power of the primary circuit followed the neutron power decrease with a delay of about 20 seconds. The differences between the temperatures of the hot legs and the corresponding cold legs of the four main coolant pumps decreased proportionally to the thermal power reduction, as all four pumps continued working.

In the secondary circuit, where the transient had been initiated, the flow rate through the second feed water pump that was still in operation, was increased by some 50 % within 16 seconds after the failure of the first pump, in order to partly compensate the deficient feed water flow. In the following, the flow rate of the second pump was reduced again to match the decreasing thermal power of the primary circuit.

### 6.2 Burnup and steady-state calculations

A DYN3D burnup calculation was carried out over 152 full-power days of the 1st cycle. The calculated critical boric acid concentration for the full-power state before the transient amounts to 2.77 g/kg, which underestimates the measured value by 0.23 g/kg [8].

KI provided three-dimensional core power distributions derived from self-powered neutron detector measurements in the stationary states before and after the transient [8]. Fig. 4 shows the assembly-wise normalized power density distribution (before the transient) calculated by DYN3D in comparison with the reference values, that have been given for the assemblies equipped with SPNDs. The maximum deviation is about 3%. In fig. 5, a comparison is presented

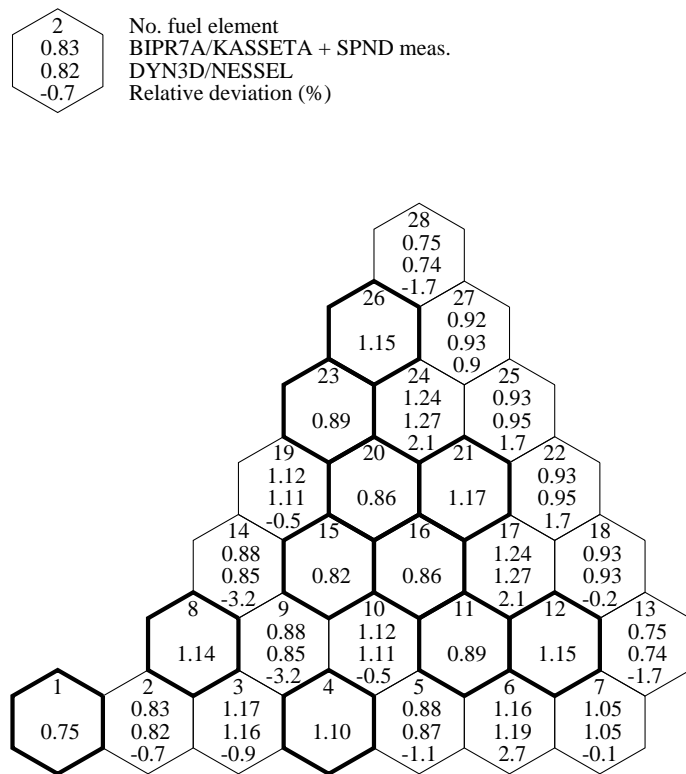


Fig. 4: Normalized power distribution before transient (Balakovo)

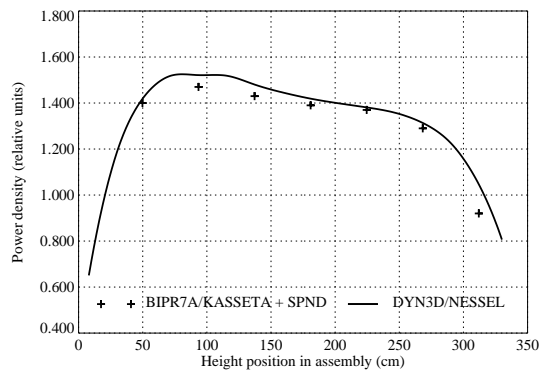


Fig. 5: Axial power distribution in assembly 17

for the axial power distribution within the hottest fuel assembly. In the stationary state after the transient, the agreement is worse. The maximum deviation in the assembly-wise power distribution is 5.3 %. A significant overestimation of the axial power distributions by DYN3D has been observed in the upper core part. But in all, a satisfying agreement between the calculated and measured values has been reached.

## 7. Conclusions

The task of collection, review and documentation of stationary state and transient data measured in VVER reactors has been fulfilled. The comparisons of sections 5.2 and 6.2 can be considered as successful validation of the burnup and steady-state options of DYN3D for VVER-440 and VVER-1000 cores. Corresponding calculations are carried out by the other project participants, applying the neutronics codes HEXTRAN, BIPR8 and KIKO3D. Preliminary comparisons indicate that the agreement to the measurements is roughly the same as that reached by DYN3D. For the transient analyses, the input data sets of the thermal-hydraulics parts of the codes have been prepared and tested. First coupled codes analyses of the selected transients are under way. The validation work including a comprehensive comparison and discussion of all results will be completed until the end of 1999.

## References

- [1] U. Grundmann, D. Lucas, S. Mittag and U. Rohde (1995), Weiterentwicklung und Verifikation eines dreidimensionalen Kernmodells für Reaktoren vom Typ WWER und seine Ankopplung an den Sörfallanalysecode ATHLET, Rossendorf, Report FZR-84
- [2] P. Fomitchenko, M. Lizorkin, L. Gilvanov et al. (1993), Coupling of the thermal-hydraulic system code ATHLET and the 3D-neutronics model BIPR8, RRC KI Moscow, GRS Garching (Germany), Interim report
- [3] G. Hegyi, K. Velkov, I. Trosztel et al. (1998), Kopplung von ATHLET mit dem ungarischen 3D-Kernmodell KIKO3D, Garching (Germany), Report GRS-A-2547
- [4] R. Kyrki-Rajamäki (1995), Three-dimensional reactor dynamics code for VVER type nuclear reactors, Espoo (Finland), VTT Publications 246
- [5] J. Miettinen (1998), SMABRE Code Manual, Volume 1: SMABRE System Models and Numerical Methods, Espoo (Finland), VTT Publications
- [6] R. Kyrki-Rajamäki, S. Mittag (1998), Collection and review of VVER transient measurement data, Rossendorf, Technical Report on CEC PHARE project SRR1-95, FZR/SRR195/RREV1.2
- [7] H. Kantee (1998), Drop of one turbine to house load level experiment on Loviisa-1 NPP, Rossendorf, Technical Report on CEC PHARE project SRR1-95, IVO/SRR195/LOV1.1
- [8] S. Danilin (1998), Experimental data of the transient caused by turning off one feed water pump from working two, Rossendorf, Technical Report on CEC PHARE project SRR1-95, KI/SRR195/ED2.0

# WIRE-MESH SENSORS FOR TWO-PHASE FLOW INVESTIGATIONS

Horst-Michael Prasser

## 1. Introduction

In the annual report 1996 a new wire-mesh sensor for gas-liquid flows was presented [1]. It was used to visualise the cavitation bubble behind a fast acting shut-off valve in a pipeline with a time resolution of over 1000 frames per second for the first time. In the last two years the sensor was applied to an air-water flow in a vertical pipeline (inner diameter  $D=51.2\text{mm}$ ) to study the flow structure in a wide range of superficial velocities. Besides the void fraction distributions, the high resolution of the sensor allows to calculate bubble size distributions from the primary measuring data. It was possible to study the evolution of the bubble size distribution along the flow path with growing distance from the gas injection (inlet length,  $L$ ).

## 2. Working principle of the wire-mesh sensor

The function is based on the measurement of the local instantaneous conductivity of the two-phase mixture. The sensor consists of two electrode grids with 16 electrodes each, placed at an axial distance of 1.5 mm behind each other. The conductivity is measured at the crossing points of the wires of the two grids. This results in  $16 \times 16$  sensitive points, which are equally distributed over the cross section (Fig. 1). In the corners of the rectangular measuring grid some of the sensitive points lie outside the boundary of the circular cross section and cannot be used. Therefore, the number of points taking part in the measurement is 242. The wires have a diameter of  $120\ \mu\text{m}$ .

For the conductivity measurement, one plane of electrode wires is used as transmitter, the other as receiver plane. During the measuring cycle, the transmitter electrodes are activated by a multiplex circuit in a successive order, as illustrated in Fig. 2 for an example of  $2 \times 4$  wires. The time resolution achieved by the signal processing unit is 1200 frames per second. The spatial resolution is given by the pitch of the electrodes and equals 3 mm.

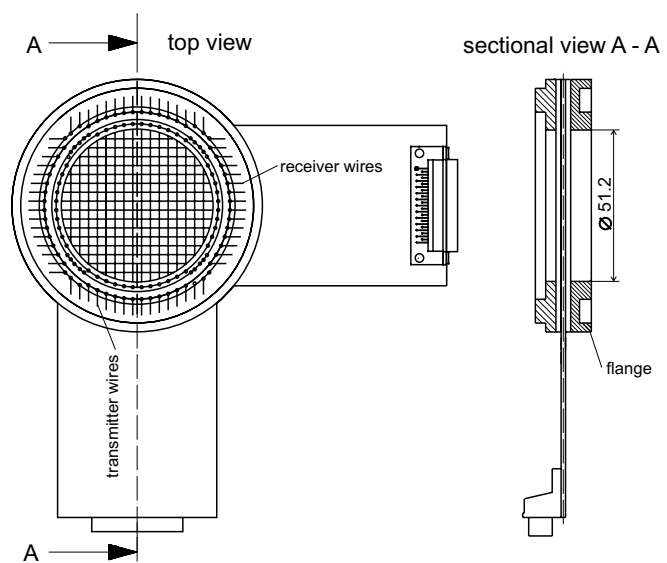


Fig. 1: Wire-mesh sensor ( $2 \times 16$  electrode wires)

The measurement for one row is started by closing one of the switches  $S1-S4$ . The currents arriving at the receiver wires are transformed into voltages by operational amplifiers and sampled by individual sample/hold circuits. After an analogue/digital conversion the signals are recorded by a data acquisition computer and stored for each receiver electrode separately. This procedure is repeated for all transmitter electrodes.

During the activation of a single transmitter electrode all the other electrodes are kept on zero potential. This is done by low impedance input respectively output cascades (see Fig. 2). This special feature prevents a deterioration of the resolution by cross talk between parallel wires. In fact, the current from the activated wire flows towards all the other electrodes, but as the grounded wires cannot depart from zero potential there is no additional current from them to the given receiver wire. The network of grounded wires creates symmetry conditions, which prevent that the conductivity of the fluid far from the given crossing point can influence the locally measured value. In this way, the distribution of the electrical conductivity over the cross section occupied by the sensor is obtained row by row. After the last transmitter electrode has been activated, a two-dimensional matrix of 16 x 16 AD conversion results is available, which are proportional to the conductivity in the control volumes in the vicinity of all crossing points of two perpendicular wires. For more details about the signal acquisition see [2].

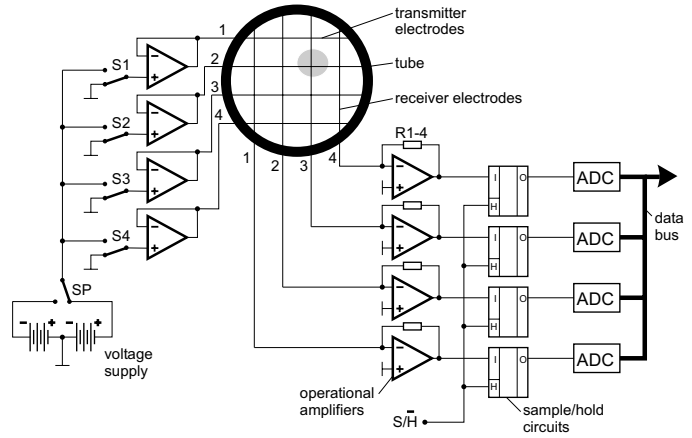


Fig. 2: Simplified scheme of a 2 x 4 wire-mesh sensor with signal acquisition system

### 3. Calculation of void fractions

During a calibration procedure, measurements for the situations "tube completely filled with liquid" and "tube completely filled with gas" are performed and the resulting matrices of AD conversion results are stored. The matrices acquired during the measurement of the two-phase flow are transformed into distributions of the void fraction by relating the individual measured components to the calibration values assuming a proportionality of local void fraction and electrical conductivity. The accuracy of the void fraction was tested by comparing line averages calculated from the wire-mesh data to the readings of a gamma-densitometer, which was located close to the wire-mesh sensor.

For that, the gamma-device (0.13 mCi Cs-137) was operated with an integration time of 120 s. This allowed to achieve a statistical accuracy of better than 1 %. The comparison to the gas fraction measured by the wire-mesh sensor is shown in Fig. 3. The dependency is linear within an error band of  $\pm 5\%$  (related to the final value) in the following range of superficial velocities:  $J_{Air}$  0.0024 - 12 m/s,  $J_{Water}$  0.043 - 4 m/s.

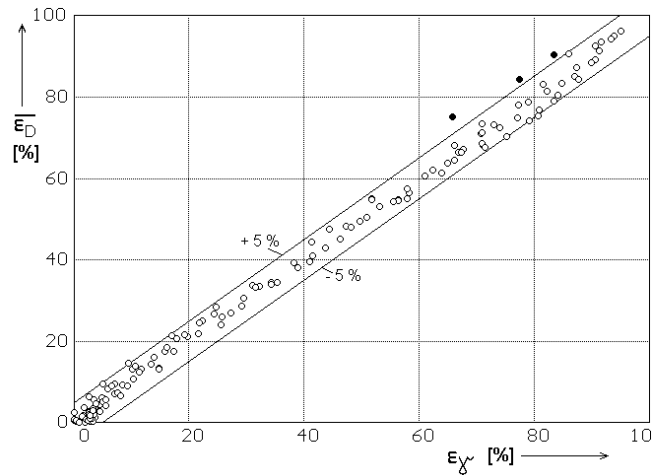


Fig. 3: Comparison between wire-mesh sensor and gamma-densitometer (black filled points:  $J_{Water}$ : 1.6 - 4 m/s;  $J_{Air}$ : 12 m/s)

#### 4. Flow pattern visualisation

The output of the wire-mesh sensor consists of a time sequence of local instantaneous void fractions that characterise the presence of the gaseous phase in a grid of measuring positions in the cross section. These data sets can be used for a visualisation of the two-phase flow. With the help of a special software the individual gas fraction distributions can be displayed as a sequence of frames. Eulerian sectional views (pseudo side views) of the gas fraction distribution in the vertical center plane of the pipe can be obtained, if successive void fraction distributions over the diameter are plotted in a vertical stack, beginning from the top and moving downwards. When we assume that the gas bubbles travel with a constant velocity independently of their location in the cross section (radial velocity gradients are neglected), the phase velocity calculated from the average void fraction and the superficial gas velocity can be used to transform the time axis into a virtual z-axis.

Fig. 4 shows these sectional side views, obtained at different distances between air injection and wire-mesh sensor for a developed slug flow at  $J_{\text{Water}} = 1 \text{ m/s}$  and  $J_{\text{Air}} = 0.48 \text{ m/s}$ . The relation between horizontal and vertical dimensions of the bars in Fig. 4 are kept 1:1 with consideration the phase velocity of the gas, i.e. the shape of the gas bubbles, observed in the flow, is not distorted. In the presented experiment, the air was injected through 8 orifices in the wall of 4 mm diameter each. Therefore, the primary bubbles are therefore quite large. It has to be remarked that the side views represent a “frozen” flow pattern, characteristic for the given measuring position. In reality, the flow pattern continuously changes with growing height, e.g. at the sensor position of  $L = 30 \text{ mm}$  above the injection we must expect the flow pattern of the next measuring position ( $L = 80 \text{ mm}$ ) at  $z=50 \text{ mm}$  in the direction of the virtual z-axis, the flow pattern of the following position ( $L = 130 \text{ mm}$ ) at  $z=100\text{mm}$ , a.s.o..

The large primary bubbles are clearly visible at the distance of  $L = 30 \text{ mm}$ . With growing height, they are more and more shifted towards the center of the pipe. Further, both coalescence and fragmentation occurs, leading to the appearance of bubbles either smaller or larger than the primary bubbles. In the end, slugs are formed. The characteristic shape of the slugs is very well reproduced by the sensor.

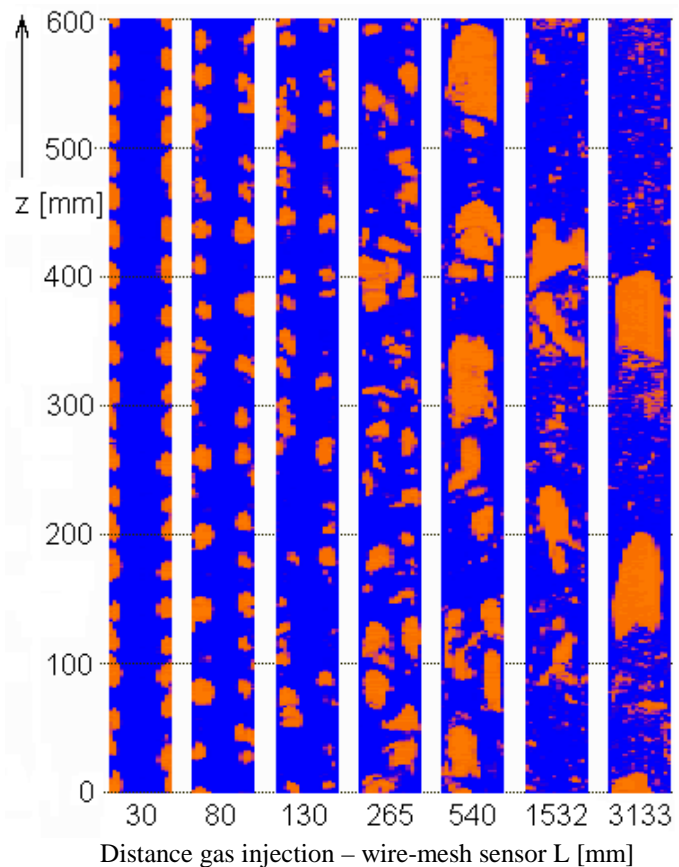


Fig. 4: Evolution of the flow pattern with growing distance from the air injection,  $J_{\text{Water}} = 1 \text{ m/s}$ ,  $J_{\text{Air}} = 0.48 \text{ m/s}$

## 5. Bubble size distributions

The high spatial and time resolution of the wire-mesh sensor allows to calculate bubble size distributions from the measured gas fraction distribution sequence. After the transformation of the time axis into the virtual z-axis, described in the previous section, the measured data can be treated as a three-dimensional instantaneous void fraction distribution  $\epsilon_{x,y,z}$  with a resolution given by the pitch of the electrode wires ( $\Delta x = \Delta y = 3$  mm) in the x and y directions, and given by the phase velocity of

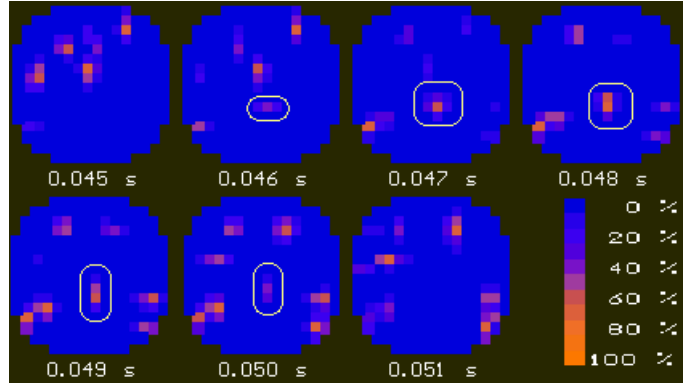


Fig. 5: Image of a selected bubble in a series of successive frames delivered by the sensor

of the gas divided by the framing rate of  $f_{meas} = 1200$  Hz in the z-direction ( $\Delta z = 1.4$  mm in the example shown in Fig. 4). In the consequence, each bubble is mapped in several successive instantaneous void fraction distributions, delivered by the sensor (Fig. 5). The volume of an individual bubble  $V_{bub}$  can then be obtained by adding the local void fractions  $\epsilon_{x,y,z}$  of the grid points belonging to the selected bubble, multiplied by the magnitude of the control volume  $V$ :

$$V_{bub} = V \cdot \sum_{\epsilon > \epsilon_{min}} \epsilon_{x,y,z} = \Delta x \cdot \Delta y \cdot \frac{J_{Air}}{\bar{\epsilon}} \cdot \frac{1}{f_{meas}} \cdot \sum_{\epsilon > \epsilon_{min}} \epsilon_{x,y,z} \quad (1)$$

Here, the phase velocity of the gas is obtained from the superficial air velocity  $J_{Air}$  divided by the average void fraction  $\bar{\epsilon}$ , which is determined by averaging the wire-mesh data. The summation is carried out

by a recursive search procedure that starts at a grid position, where the void fraction is maximal. The summation must be terminated, when the boundary of the bubble is reached. Due to the presence of signal noise a termination threshold  $\epsilon_{min}$  greater than zero must be defined. Otherwise, the recursive search could jump from one bubble to another via a channel of grid elements where the gas fraction is not accurately equal to zero. This would lead to an overestimation of the bubble volume. From the individual bubble volumes  $V_{bub}$ , equivalent bubble diameters  $D_{bub}$  were calculated:

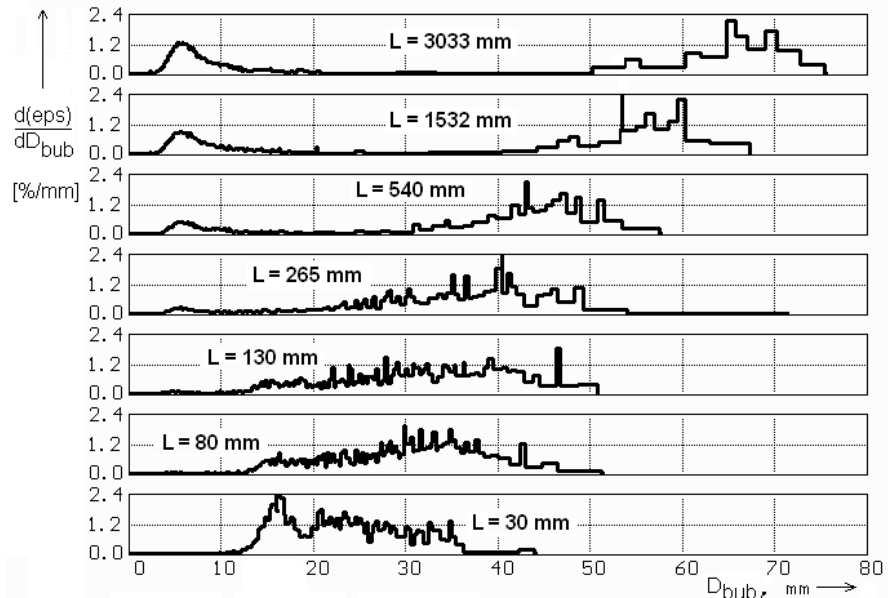


Fig. 6: Evolution of the bubble size distribution with growing distance  $L$  from the air injection,  $J_{Water} = 1$  m/s,  $J_{Air} = 0.13$  m/s

$$D_{bub} = \sqrt[3]{\frac{6}{\pi} \cdot V_{bub}} \quad (2)$$

Bubble size distributions were constructed by summarising the contribution of the bubbles of a given range of diameters to the integral volumetric gas fraction. These partial void fractions are plotted against the equivalent bubble diameter. In Fig. 6 the evolution of the bubble size distribution at the flow conditions of Fig. 4 is shown.

At  $z = 30$  mm the maximum of the bubble size distribution corresponds to the size of the primary bubbles ( $D_0$ ). With growing height, the coalescence leads to the appearance of a second peak at a diameter of  $\sqrt[3]{2} \cdot D_0$ . These are bubbles that origin from coalescence between pairs of primary bubbles. At  $z = 1532$  mm, a characteristic bimodal distribution is observed, which indicates the transition to slug flow. The large bubble fraction is still further developing with increasing height. At the same time, bubbles smaller than the primary bubbles appear due to fragmentation.

## 6. Void fraction profiles

When the instantaneous two-dimensional void fraction distributions are averaged over a long period, void fraction profiles can be obtained. Fig. 7 shows the development of the profiles at the superficial velocities of  $J_{Water} = 1$  m/s,  $J_{Air} = 0.13$  m/s for three different air injection conditions.

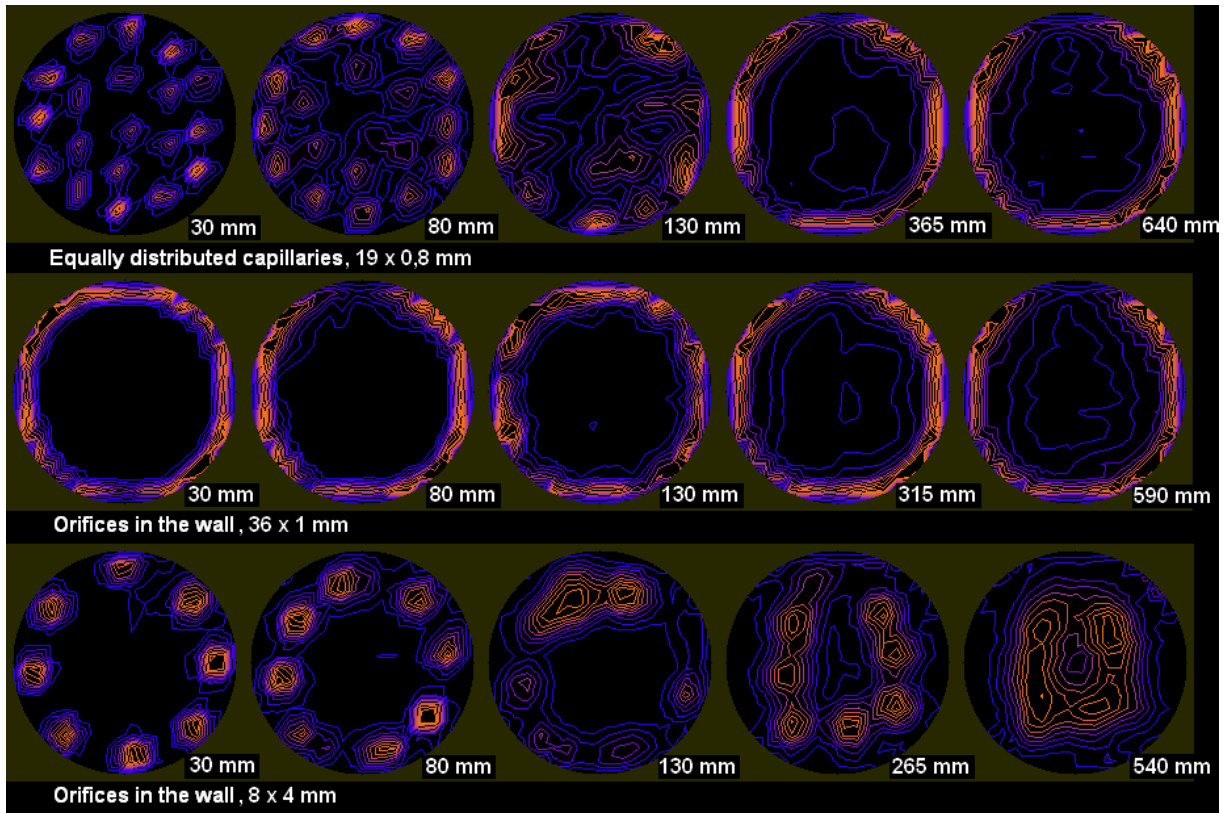


Fig. 7: Void fraction profiles averaged over 10 s for three different air injection conditions at different inlet length  $L$ ,  $J_{Water} = 1$  m/s,  $J_{Air} = 0.13$  m/s

In case of 19 capillaries equally distributed over the cross section, at  $z = 30$  mm a maximum of the void fraction is found at each individual position of an injecting capillary. With growing distance, the gas is pushed towards the wall by the lift force and a wall-peaked profile is formed. When the gas is injected through 36 orifices of 1 mm diameter, the peak at the wall is already formed by the mode of injection. A completely different behaviour is observed, when the gas is injected through large orifices of 4 mm diameter. Here, again each injecting orifice is visible in the void fraction distribution. But in contradiction to the injection by capillaries, the wall-peaking disappears with growing height, despite of the identical superficial velocities. The bubble size distributions are also significantly different even after a related inlet length of a approximately 60  $L/D$ , as shown in Fig. 8.

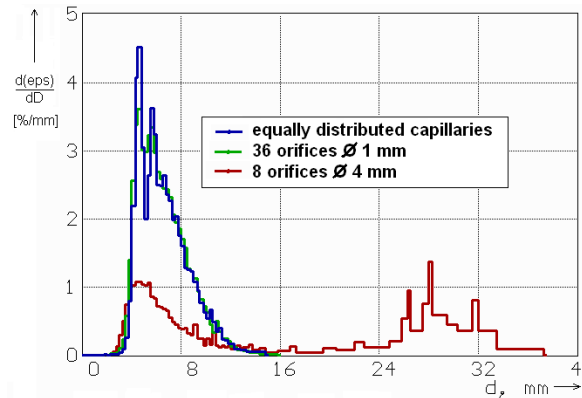


Fig. 8: Bubble size distributions at  $L \cong 3100$  mm ( $L/D \cong 60$ ) for three different air injection devices,  $J_{\text{Water}} = 1$  m/s,  $J_{\text{Air}} = 0.13$  m/s

## 7. Conclusion

The wire-mesh sensor provides detailed information about the structure of the two-phase flow. It is successfully used to visualise the air-water flow in a vertical pipeline. The comparison to gamma-densitometry has shown, that void fractions can be measured with good accuracy. From the primary measuring data it is possible to obtain void fraction profiles as well as bubble size distributions. Experiments were carried out to study the evolution of the flow structure with growing distance from the gas injection. A significant influence of the kind of the gas injection was found. The bubble size distributions clearly show the effect of coalescence and fragmentation. They can therefore be used for the development of bubble population models.

## References

- [1] H.-M. Prasser, A. Böttger, J. Zschau (1997), A New wire-mesh tomograph for gas-liquid flows, in F.-P. Weiß, U. Rindelhardt (Ed.), Annual Report 1996, Institute for Safety Research, FZR-190, 34-37
- [2] H.-M. Prasser, A. Böttger, J. Zschau (1998), A new electrode-mesh tomograph for gas-liquid flows, Flow Measurement and Instrumentation 9, 111-119

# A NEW CRITERION FOR THE BUBBLE SLUG TRANSITION IN VERTICAL TUBES

**Andreas Schaffrath, Anne-Kathrin Krüssenberg, Horst-Michael Prasser**

## 1. Introduction

The use of one dimensional (1D) system codes is very common in the design, optimization and safety analysis of nuclear power or chemical plants. These codes are based on the solution of a complete set of conservation equations for mass, momentum and energy for all phases. In complex structures three dimensional (3D) flow phenomena are often dominating. In this case, the 1D approximation requires constitutive laws, which describe the effect of the 3D processes on the mass, momentum and energy transfer integrated over the nodes of the 1D model. These correlations strongly depend on the geometry. They are found empirically and may have a comparatively narrow region of validity, i.e. they cannot be transferred to other boundary conditions without additional experiments. A particular problem of this kind is for example the scale-up from experimental test facilities up to the scale of the original plants.

The present work is aimed at the investigation of two-phase flow in a vertical pipe. Even under these very simple boundary conditions, strong 3D effects are observed. The distribution of the gas phase over the cross section varies significantly between the different flow patterns, which are known for the vertical two-phase flow. The paper presents experimental void fraction distributions obtained by a wire-mesh sensor in a wide range of superficial velocities of gas and liquid. The high resolution of the measurement allows to perform the analysis of the flow structure on a new qualitative level.

## 2. MTLOOP Test Facility and Test Procedure

For the study of two phase air-water and steam-water flows the MTLOOP test facility was constructed at Forschungszentrum Rossendorf. The facility has maximum operation parameters of 2.5 MPa and 225 °C (see Fig. 1). For the present investigations, the loop was operated with air at atmospheric pressure and 30 °C. The measurements were carried out at a vertical test section of 4 meters height and 51.3 mm inner diameter. Air was injected through systems of capillaries. The ends of these capillaries were equally distributed over the cross section of the pipe. The wire mesh sensor with 16 x 16 wires was located 3.5 m above the injection device, i.e. the inlet length was 70 L/D.

220 experiments were performed with superficial velocities of air between 0.0024 to 12 m/s and from 0.043 to 4 m/s for water respectively. The air flow rate was measured under normal conditions. The superficial velocity was calculated from a flow rate corrected according to the actual temperature and pressure at the location of the wire-mesh sensor. The pressure correction was necessary, because the pressure increasingly departed from atmospheric at higher flow rates due to the pressure drop in the pipeline. At each test point, the loop was operated under steady-state conditions.

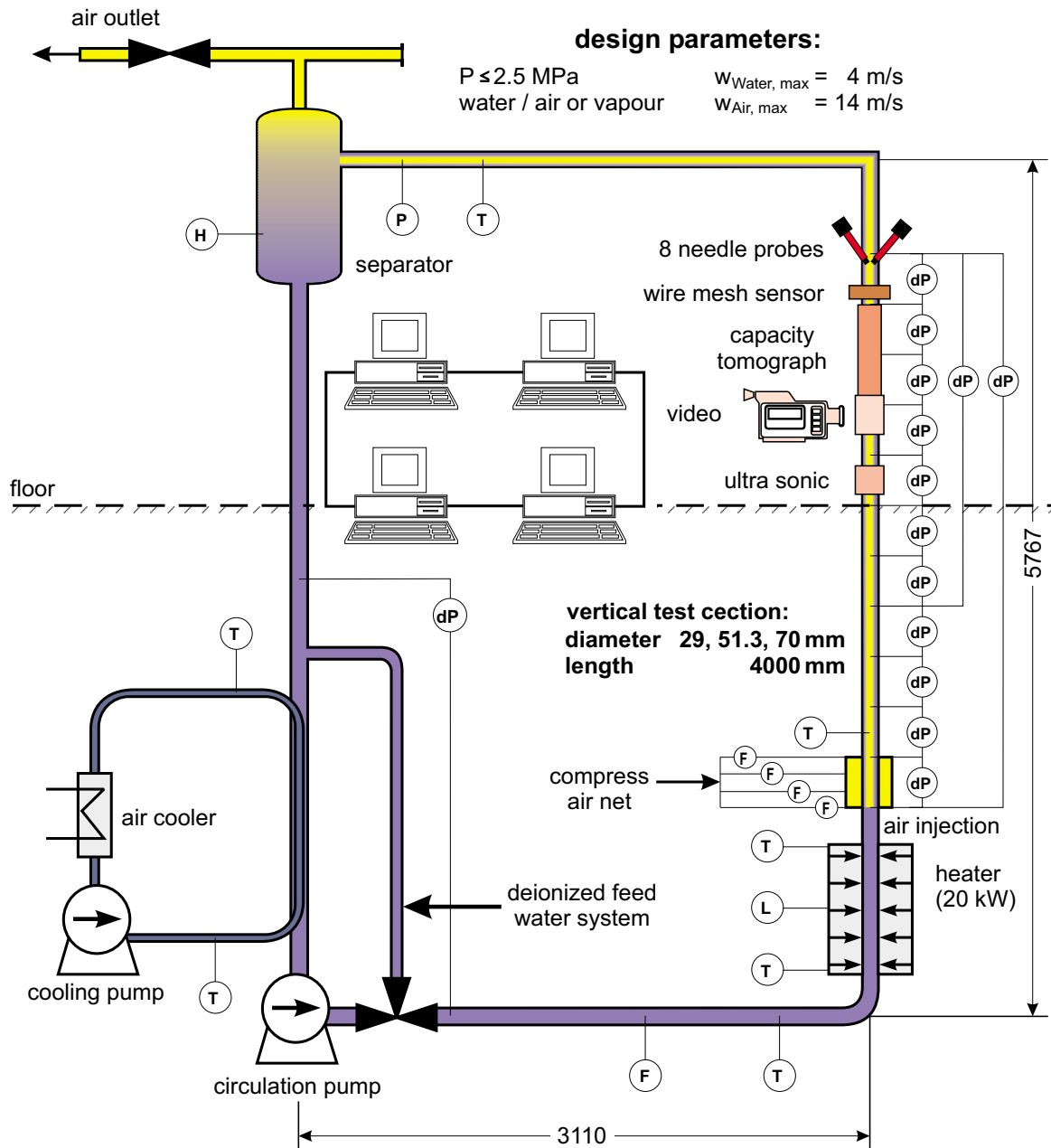


Fig. 1: MTLOOP test facility

The MTLOOP is equipped with several measurement systems (e.g. ultrasonic sensor, video camera, capacity tomography, wire mesh sensor and needle probes). The wire mesh was developed in Rossendorf [1,2]. A time resolution of the signal processing unit of up to 1200 frames per second is achieved. The spatial resolution is given by the pitch of the electrodes and is 3 mm.

### 3. New Criterion for Bubble-Slug Transition

The measuring data of the wire-mesh sensor can be used to create Eulerian sectional views (pseudo side views) of the flow. For this purpose, successive instantaneous void fraction distributions over the diameter are extracted from the measured two-dimensional distributions and plotted as a vertical stack along the time axis. Assuming a constant phase velocity of the

gas, which is given by the superficial gas velocity divided by the average gas fraction, the time axis can be transformed into an imaginary z-axis (see [3]). The result for the region of the transition from bubble to slug and from slug to annular flow is shown in Fig. 2. On the left side of the figure, the relations between the horizontal and the vertical dimensions of the side views is kept 1:1. That means, that the shape of the gas regions observed in the flow is not distorted. On the right side starting from  $J_{\text{Air}} = 0.75$  m/s, the slugs become very long, so that the z-axis was shrunken by factor 5. The side view for  $J_{\text{Air}} = 0.75$  is shown in both presentation modes, for orientation.

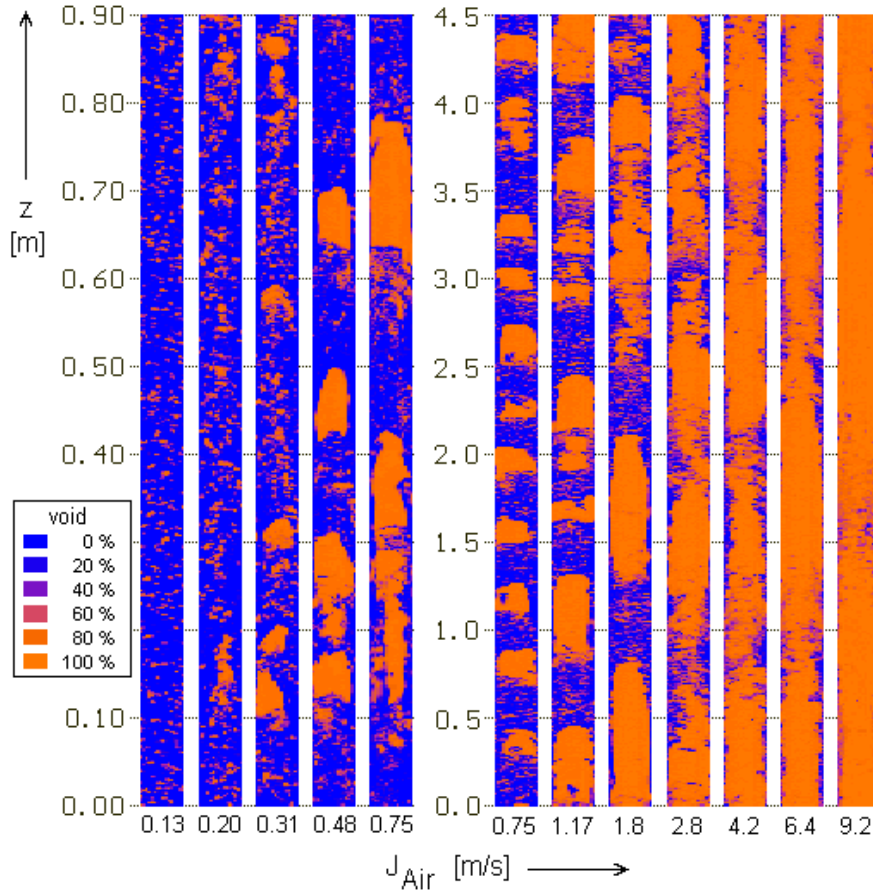


Fig. 2: Sectional side views of the flow pattern at different superficial velocities of air, transition from plug to annular flow,  $J_{\text{Water}} = \text{const.} = 1$  m/s

At a superficial velocity of the water of 1 m/s, the transition to slug flow takes place at a superficial gas velocity between 0.31 and 0.48 m/s. When the gas flow rate is further increased, the transition to annular flow is observed. At the superficial gas velocity of 9.2 m/s, the flow is wispy annular.

The high spatial and time resolution of the wire-mesh sensor allows to calculate particle size distributions from the measured gas fraction distribution sequence. This was carried out for the flow regimes shown in Fig. 2 according to the method, which is described by Prasser in [3].

Fig. 3 shows the results for a stepwise increase of the gas flow rate (threshold  $\min=0.2$ , see [3]). The superficial velocity of the water was kept constant at 1 m/s, while the gas flow was increased from a superficial velocity of 0.033 to 0.75 m/s. It is clearly to be seen that the bubble size distribution changes from a monomodal ( $0.033 \text{ m/s} \leq J_{\text{Air}} \leq 0.08 \text{ m/s}$ ) distribution to a

bimodal one at a superficial gas velocity from 0.08 to 0.13 m/s. The bimodal distribution is characteristic for the transition to heterogeneous bubble flow. At  $J_{Air}=0.31$  m/s the largest bubbles show an equivalent diameter of greater than 50 mm, i.e. they are bigger than the pipe diameter. These large bubbles are identical with the plugs observed in the pseudo side views in Fig. 2.

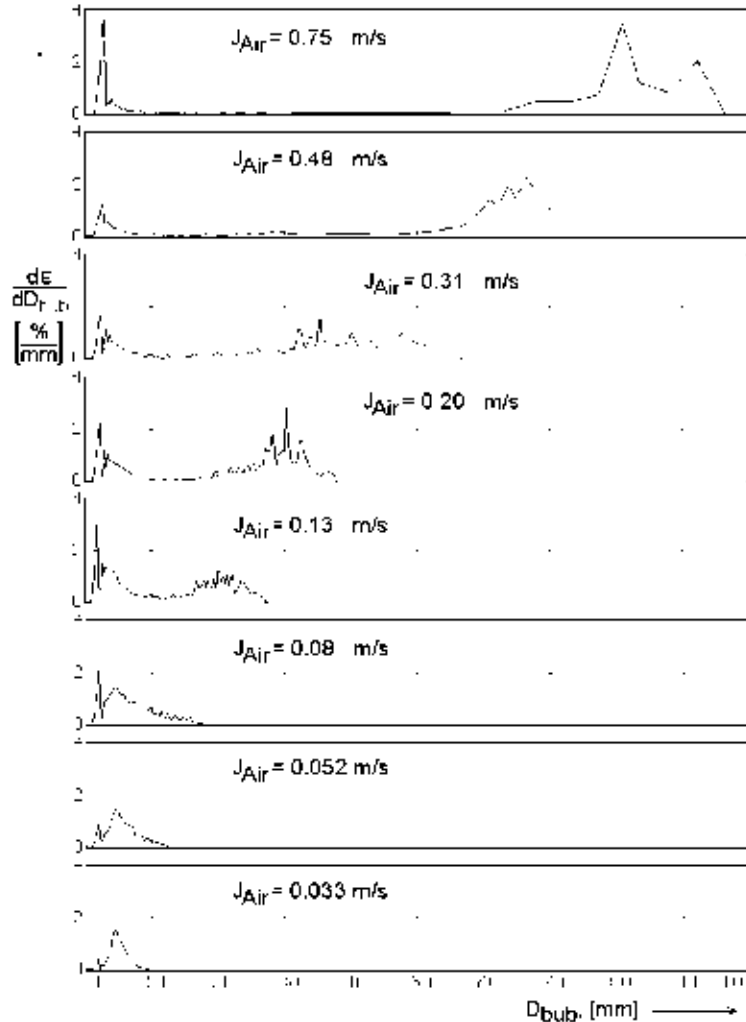


Fig. 3: Bubble size distribution at different superficial air velocities and  $J_{Water} = 1$  m/s const. for a threshold of  $\min=0.2$

From the analysis of the bubble size distribution, the following two criteria for flow pattern changes were formulated:

- the transition from homogeneous to heterogeneous bubble flow can be identified by the appearance of a bimodal bubble size distribution calculated from the wire-mesh data,
- the transition from bubble to plug flow takes place, when the largest bubbles in the bubble size distribution reach an equivalent diameter that is larger than the inner diameter of the pipe.

It is evident that the choice of the threshold has a strong influence on the shape of the bubble size distribution. With higher thresholds the transition from homogeneous to heterogeneous

bubble flow as well as from bubble to slug flow occurs at higher superficial air velocities. Detailed investigations on this subject will be performed in future.

In the left part of some of the curves in Fig. 3 there is a local minimum in the bubble size distribution at a diameter of 2.25 - 2.75 mm. This is an artefact caused by the finite resolution of the sensor. Indications of bubbles with a diameter less than 3 mm appear, if small bubbles do not fill the entire sensitive volume in the vicinity of the measuring point. This results in a higher error for small bubble volumes.

In Fig. 4 the measurements with the wire mesh sensor described in section 2 are plotted as superficial water velocity versus the superficial air velocity. The mentioned three different flow regimes bubble flow (monomodal distribution of bubbles), slug flow (bimodal distribution of bubbles), and the transition regime between these two flow patterns (characterized in fig. 4 as coalescence) are clearly identified.

#### 4. Comparison with Existing Flow Regime Maps

The classification of the own experiments (see Fig. 4) is now compared with existing flow regime maps from literature (see. Tab. 1).

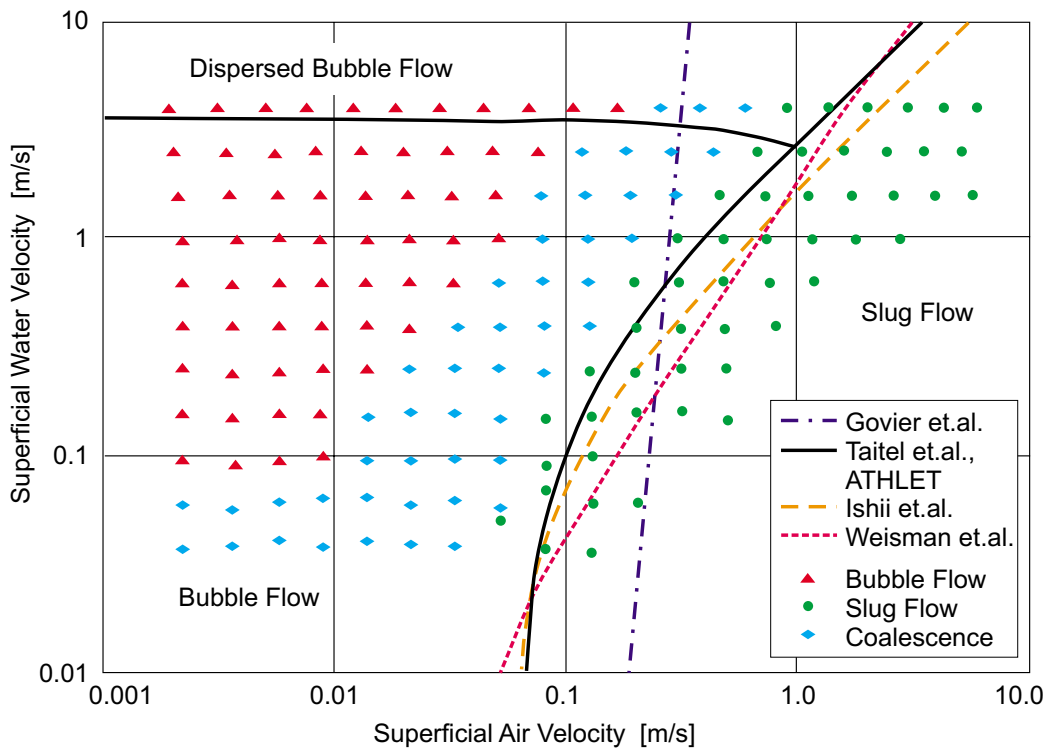


Fig. 4: Classification of own air/water flow experiments and comparison with existing flow pattern maps

The state-of-art in predicting the two-phase flow pattern is characterized by steady state flow-maps presented by different research groups. The flow classification is important, because the flow pattern decisively influences on the transport phenomena (e.g. pressure losses and heat transfer) [4]. Vertical two-phase flow is normally divided into four basic flow regimes and characterized as follows [5]:

- bubbly flow: small, discrete bubbles, which are normally distorted spheres, are surrounded by liquid,
- slug flow: slugs of liquid and bubbles are separated by regions of high vapor content (plug), which appears as large, spherical-capped bubbles and followed by a collection of smaller voids in bubbly form,
- churn flow: highly disordered (chaotic) flow regime in which the vertical motion of the liquid is oscillatory,
- annular flow: gas is flowing in the center of the tube and the liquid partially as a film along the walls and partially as droplets in the central gas bulk.

Table 1: Comparison of criteria for the transition of bubble flow to slug flow respectively bubble flow to intermittent flow transition

Author / Code	Investigated Flow Regimes	Abscissa	Ordinate	Criteria for the transition bubble – slug flow
Govier & Aziz [7]	bubble, plug, slug, churn, annular flow	$V^* = \frac{1-\dot{\varepsilon}}{\dot{\varepsilon}}$	$J_L$	$J_L \leq 0.24 V^{*-1.1}$
Weisman & Kang [8]	bubble, intermittent, annular flow	$J_L/\phi_2$	$J_G/\phi_1$	$\frac{J_G}{\sqrt{gD}} > 0.45 \left( \frac{J_G + J_L}{\sqrt{gD}} \right)^{0.78} \cdot (1 - \cos \Theta)$ $\phi_1 = \left( \frac{D}{0.0254} \right)^{n_w} (1 - 0.65 \cos \Theta)$ $n_w = 0.26 \varepsilon^{-0.17 (J_L/0.305)} \text{ and } \phi_2 = 1$
Taitel, Bornea & Dukler [9]	bubble, dispersed bubble, slug, churn, annular flow	$J_L$	$J_G$	$J_L = 2.34 J_G - 1.07 \cdot \frac{[g(\rho_L - \rho_G)\sigma]^{0.25}}{\rho_L^{0.5}}$
Ishii & Mishima [10]	bubble, slug, annular flow	$\varepsilon$  $J_L$	$J$  $J_G$	$\varepsilon = 0.3$ transition into coordinate system with superficial velocities $J_L = \left( \frac{3.33}{C_0} - 1 \right) J_G - \frac{0.76}{C_0} \left( \frac{g(\rho_L - \rho_G)\sigma}{\rho_L^2} \right)^{0.25}$
ATHLET (Steinhoff, [11])	bubble, churn turbulent bubble, slug, annular drop flow	$\varepsilon$	$J$	$\varepsilon < 0.1$ - bubble flow; $0.1 < \varepsilon < 0.3$ - churn turbulent bubble flow; $0.3 < \varepsilon$ - slug flow

It should be noticed that the transition between the different flow regimes does not occur suddenly and many extensions of this classification can be found in literature (e.g. subdivision of the annular flow regime into a wispy or nonwispy regime). For the prediction of flow patterns empirical and theoretical flow pattern maps have been developed [6].

Empirical flow pattern maps (e.g. Govier & Aziz [7]) are based on experimental investigation for a particular fluid (air-water or water-steam), geometry (in general diameter up to 50 mm) and pressure range (normally atmospheric pressure). The results are presented in different coordinate systems, but none of them is capable of making a proper prediction for all flow regimes. To overcome this problem Weisman and Kang [8] apply scaling parameters to various transitions. Because the classification of the flow regimes is subjective and mostly based on visual observations (and not on measurements) the agreement of the different flow maps is rather poor. Additionally, the application outside the scope is not possible.

Theoretical flow pattern maps (e.g. Taitel, Bornea and Dukler [9], Ishii and Mishima [10]) consider conditions which are necessary for the existence of each flow pattern and postulate mechanisms (e.g. interface friction, pressure gradients) associated with each transition. Therefore the effect of fluid properties and pipe sizes are considered. The result is a set of equations for the transition of the flow regimes. A comparison with experimental data shows a reasonable agreement.

In the present work the main attention was put on the transition from bubble to slug flow. The transition criteria presented in table 1 are transferred into a coordinate system with the superficial velocity of the air as abscissa and the superficial velocity of water as ordinate. The flow regime map of ATHLET [11], a 1D thermohydraulic code, developed by the Gesellschaft für Anlagen und Reaktorsicherheit (GRS) mbH, and own data are added to this comparison.

The flow map of Taitel, Bornea and Dukler and the model of ATHLET show the best agreement with the experiment. Ishii and Mishima indicate the transition at slightly higher superficial gas velocities. The correlation of Weisman and Kang overestimates the critical gas flow rate by a factor of 2 at medium superficial liquid velocities. The largest deviations were found for the correlation of Govier and Aziz, which overestimates the superficial air velocities for the transition at low superficial water velocities ( $J_L < 0.2$  m/s) by a factor of 2 and underestimates it at high superficial water velocities ( $J_L > 0.7$  m/s).

## 5. Summary

Experimental investigations of two phase air water flow were carried out in the MTLOOP facility at environmental conditions in a wide range of superficial velocities. The two-phase flow was studied by a wire-mesh sensor, a new device for high resolution local instantaneous conductivity measurements, which was developed by Forschungszentrum Rossendorf.

The high resolution of the void fraction measurements allows to determine the bubble size distribution by a recursive search procedure. From the individual bubble volumes, the equivalent bubble diameters are determined what allows to derive a bubble size distribution. From this analysis the quantitative criteria for flow pattern transitions were formulated. The transition from homogeneous to heterogeneous bubble flow is indicated by the appearance of a bimodal bubble size distribution. If the equivalent bubble diameter exceeds the tube diameter the transition from bubble to plug flow occurs.

The new criterion for the classification of the bubble slug flow transition were compared to existing flow pattern maps. The best agreement was found with Taitel, Bornea & Dukler and the code ATHLET.

## References

- [1] H.-M. Prasser, A. Böttger and J. Zschau, A new Electrode Tomograph for Gas-Liquid Flows, in F.-P. Weiss et. U. Rindelhardt (Ed.), Institute of Safety Research, Annual Report 1996, FZR-190, 34
- [2] H.-M. Prasser, A. Böttger and J. Zschau (1998), Hochauflösende Gittersensoren für Gas-Flüssig-Strömungen, MSR Magazin 10, 12
- [3] H.-M. Prasser, Wire-mesh sensors for two-phase flow investigations, in F.-P. Weiss et. U. Rindelhardt (Ed.), Institute of Safety Research, Annual Report 1998, FZR-268, 23
- [4] S. Z. Rouhani and M. S. Sohal (1983), Two-Phase Flow Patterns: A Review of Research Results, Progress in Nuclear Energy 11, 219
- [5] M. A. Vince and R. T. Lahey (1982), On the Development of an Objective Flow Regime Indicator, Int. J. Multiphase Flow 8, 94
- [6] K. W. Quillan and P. B. Whalley (1985), Flow Patterns in Vertical Two-Phase Flow, Int. J. Multiphase Flow 11, 161
- [7] G. W. Govier and K. Aziz, K. (1982), The Flow of Complex Mixtures in Pipes, van Nostrand Reinhold Company, New York, Cincinnati, Toronto, London, Melbourne
- [8] J. Weisman and S. Y. Kang (1981). Flow Pattern Transition in Vertical and Upwardly Inclined Lines, Int. J. Multiphase Flow 7, 271
- [9] Y. Taitel, D. Bornea and A. E. Dukler (1980), Modelling Flow Pattern Transitions for Steady Upward Gas-Liquid Flow in Vertical Tubes, AIChE Journal 26, 345
- [10] K. Mishima and M. Ishii (1984), Flow Regime Transition Criteria for Upward Two-Phase Flow in Vertical Tubes, Int. J. Heat Mass Transfer 27, 723
- [11] F. Steinhoff (1989), Thermo- und Fluidodynamikmodelle im Rechenprogramm DRUFAN und im Nachfolgeprogramm ATHLET zur Simulation von Separationsvorgängen und Gemischspiegelbewegungen in vertikalen Strömungskanälen - Teil1: Entwicklung der Modelle, Gesellschaft für Anlagen- und Reaktorsicherheit (GRS) mbH, Report GRS-A-1539

# PREVENTION OF WATER HAMMERS BEHIND FAST ACTING SHUT-OFF VALVES

Andreas Dudlik<sup>1</sup>, Horst-Michael Prasser, Stefan Schlüter<sup>1</sup>

## 1. Introduction

Shut-off valves are often applied for a quick safety shut-down of pipelines for dangerous liquids (Fig. 1). When the valve is suddenly closed at a certain flow rate, the pressure behind the valve decreases due to the momentum of the liquid. This leads to an evaporation and to a formation of a cavitation bubble if the resulting minimum pressure becomes lower than the saturation pressure at the given temperature. The liquid is decelerated by the pressure difference between the counter-pressure at the end of the pipeline and the saturation pressure inside the cavitation bubble. After the velocity has reached zero, the liquid is again accelerated towards the valve, which is now closed. At the end, the column of liquid hits the closed valve, which may cause a strong water hammer.

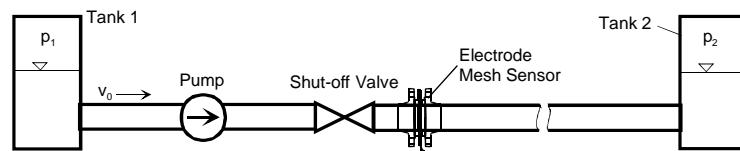


Fig. 1: Scheme of a pipeline with a fast acting flap valve

This type of water hammer was studied at a test facility of Fraunhofer UMSICHT in Oberhausen. The task of FZR was the development of an adequate two-phase flow instrumentation to visualise the cavitation phenomenon [1]. During the project unique digital movie sequences of appearing and condensing cavitation bubbles were recorded, that gave valuable insights into the transient process. In the result, a new method was found to prevent the collapse of the cavitation bubbles and to avoid the corresponding pressure peaks.

## 2. Experiments and measurement instrumentation

The water hammers were studied in a 200 m long pipeline of 100 mm diameter. The tests were carried out with water at room temperature and in the range of initial velocities  $v_0$  between 1 and 6 m/s. The resulting water hammers reached maximum pressures of  $p_{\max} > 75$  bars. An electrode mesh sensor (Fig. 2) was put 0.15 m behind the valve (see Fig. 1) to measure the transient steam fraction distribution. Due to the high resolution of the sensor (2D grid of 5.8 mm pitch, time resolution 1024 frames/s), it was possible to visualise the evolution of the cavitation. For example, Fig. 3 shows the void fraction distribution appearing just after the valve has been closed. The void distribution is asymmetric, because the flap of the valve rotates in a way, that the relative velocity between liquid and flap has its maximum on the left side. Therefore the evaporation is more intensive on this side.

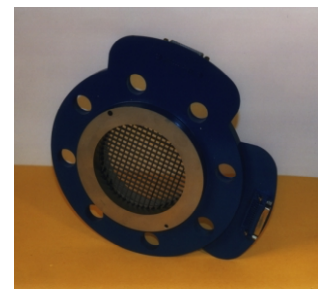


Fig. 2: Mesh sensor

---

<sup>1</sup> Fraunhofer UMSICHT, Oberhausen

The sensor also allowed to obtain courses of the average void fraction at the measuring location. For the tracing of the cavitation bubble in the flow direction, several needle shaped conductivity probes were installed at the pipeline at different distances from the fast acting valve. The probes were mounted 10 mm deep into the top of the cross-section of the pipe.

The experiment was started at a given initial flow velocity  $v_0$  of the water by closing the valve. A fast acting flap valve with closing time of 100 ms was applied.

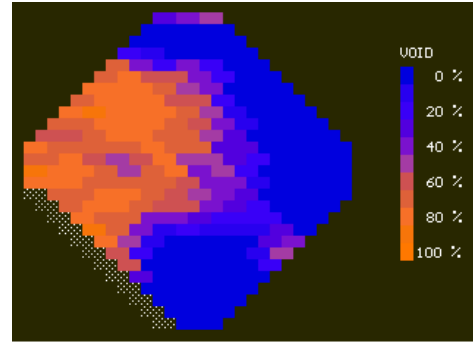


Fig. 3: Void fraction distribution behind the flap valve at  $t=105$  ms,  $v_0=4$  m/s

### 3. Cavitation collapses

Fig. 4 shows an example of the process for an initial liquid velocity of  $v_0 = 4$  m/s. After the valve has been closed, the pressure decreases to saturation pressure, which is close to vacuum. The steam fraction increases and reaches a value of over 95 %, i.e. the tube is always completely empty. The water flows back in a slug, the steam fraction decreases rapidly and, when the steam is completely condensed, the pressure peak is observed. The pressure wave travels through the pipeline. It is reflected at the entrance into tank 2 and returns as a wave of pressure decrease. When this wave reaches the closed shut-off valve, a new cavitation bubble is generated. This process repeats several times and a series of water hammers with decreasing amplitudes is observed.

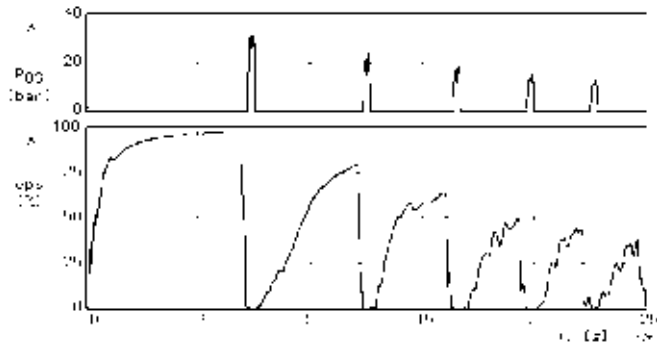


Fig. 4: Average void fraction (eps) and pressure behind the flap valve (p03),  $v_0=4$  m/s

The time behaviour of the length of the cavitation bubble is well described by the momentum equation for the water column:

$$\rho_w \cdot L \cdot \frac{dv}{dt} = p_s - p_2 - \Delta p_{hydr} \quad (1)$$

The difference between the pressure in tank 2,  $p_2$ , and the saturation pressure  $p_s$  plus the total hydraulic pressure losses  $\Delta p_{hydr}$  act at a water column of the length  $L$  and the density  $\rho_w$  against the initial flow direction. By integrating the velocity  $v$  the instantaneous extension of the cavitation bubble  $x$  is obtained. In the experiments, the bubbles were traced by the needle probes (Fig. 5). The theoretic-

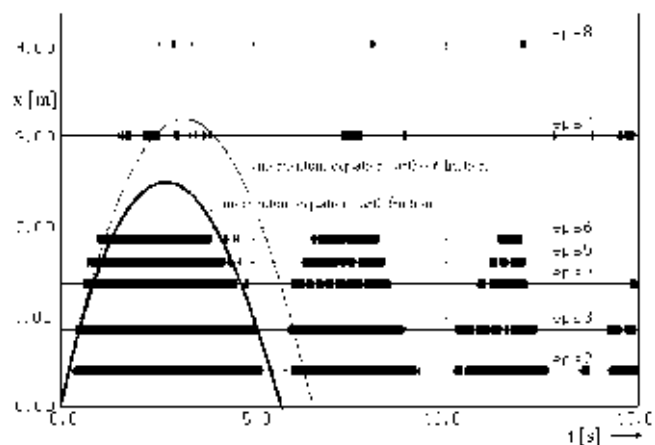


Fig. 5: Axial extension of the cavitation bubble  $x$  as a function of time  $t$ ,  $v_0 = 2$  m/s  
eps2 - eps8: needle probes, thick bar = steam, thin bar = water, location of the bars relative to  $x$  axis corresponds to distance between valve and probe

cal results are in good agreement with the measurements only if the hydraulic pressure losses are considered. In the opposite case, the theory predicts too large cavitation bubbles.

#### 4. Prevention of cavitation collapses

Based on an analysis of the experimental results, a new method to prevent the cavitation caused water hammers was developed. A second so-called auxiliary valve is put behind the fast acting valve. For this purpose, a check valve can be used (Fig 6). The check valve closes, when the liquid is accelerated back to the flap valve, i.e. in the moment of the maximum extension of the cavitation bubble. The bubble remains captured between the two valves and a water hammer cannot occur. It can now be eliminated by slowly supplying liquid into the section between the two valves, e.g. by a slow opening of the shut-off valve. After that, the pipeline can be put into operation again.

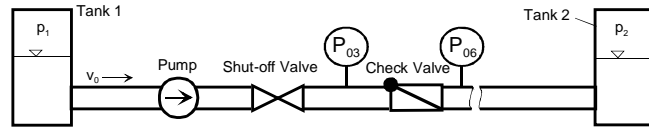


Fig. 6: Method to prevent water hammers caused by collapsing cavitation bubbles

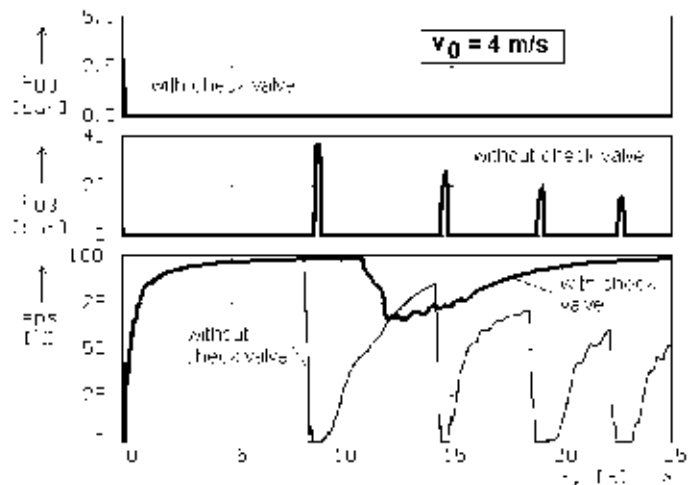


Fig. 7: Effect of the check valve on pressure ( $p_{03}$ ) and void fraction ( $\epsilon_{ps}$ ) behind the shut-off valve

The method was tested at the experimental pipeline in Oberhausen. When the check valve is applied, no pressure peaks can be observed downstream of the flap valve, the pressure remains at the level of saturation (Fig. 7).

Nevertheless, the positive effect can be diminished, if the rules for the right application of the auxiliary valve are not met. A strong secondary water hammer can occur, if the shut-off valve is reopened quickly when the cavitation is still present. At the test facility in Oberhausen pressure peaks of approximately 60 bars were obtained in this case (Fig. 8).

It is necessary to avoid that the cavitation bubble is able to extend into the pipeline behind the check valve. Otherwise a part of the bubble would collapse there causing another type of a secondary water hammer.

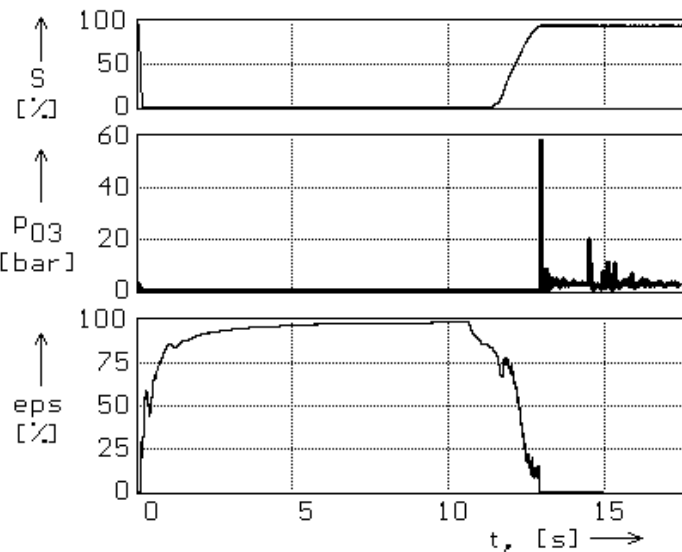


Fig. 8: Secondary water hammer caused by reopening of the shut-off valve ( $S$  – opening of the valve [%])

Another important factor is the hydraulic pressure drop caused by the check valve. In the experiments, a check valve with an opening of 75 mm diameter was installed. In the 100 mm diameter pipeline this means a cross section reduction of almost 50 %. After the closure of the shut-off valve the pressure behind it is close to saturation. In this state even a low pressure drop in the check valve can cause evaporation. In the result, a second cavitation bubble is formed behind the check valve and provides a secondary water hammer, which can only be avoided by reducing the pressure drop.

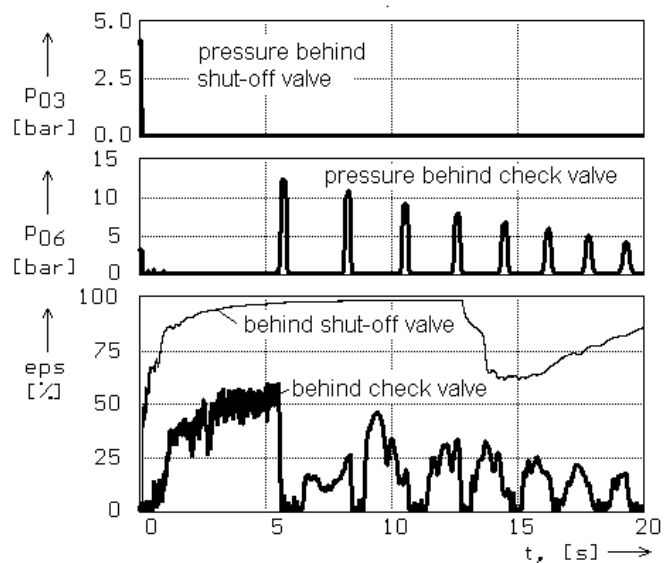


Fig. 9: Secondary cavitation caused by the pressure drop in the check valve,  $v_0=5$  m/s

During the experiments a second mesh sensor was installed behind the check valve in order to visualise the secondary cavitation bubble. The check valve was located 22 m behind the shut-off valve, while the theory predicts a maximum extension of the primary cavitation bubble of approximately 8 m, so that any steam detected at the position behind the check valve must be a result of the pressure drop.

A characteristic result is presented in Fig. 9. The pressure peaks at the measuring position behind the check valve ( $P_{06}$ ) are caused by the collapse of the void in this place. The amplitude is about 12.5 bars. The mesh sensor indicates these voids clearly. Due to the non-optimal design of the check valve, a complete suppression of water hammers was not achieved in the experiments.

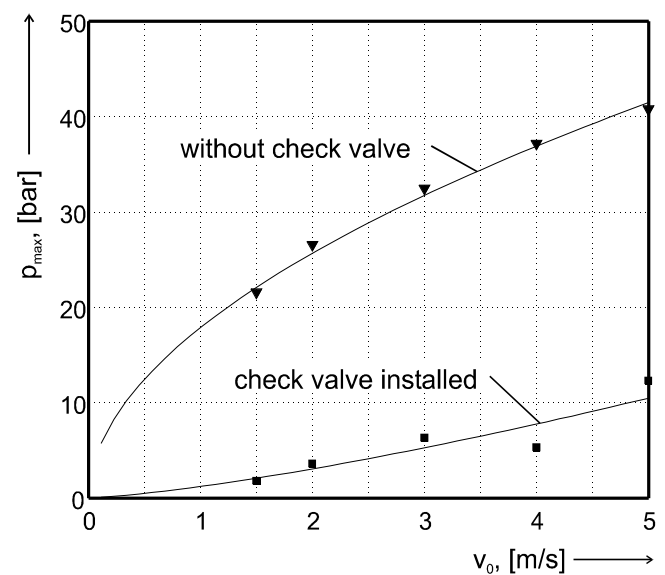


Fig. 10: Water hammer amplitudes  $p_{\max}$

Nevertheless, the reduction of the maximum pressure peaks is significant (Fig. 10). The presented method was therefore taken for the basis of a patent application.

## References

- [1] H.-M. Prasser, A. Böttger, J. Zschau (1998), A new electrode-mesh tomograph for gas-liquid flows, *Flow Measurement and Instrumentation*, 9, 111-119
- [2] A. Dudlik, S. Schlüter, H.-M. Prasser (1997), *Transiente Strömungsvorgänge in Rohrleitungen, Messung und Berechnung von Druckstößen und Kavitationsschlägen in Rohrleitungen*, Tagung: Monitoring und Diagnostik in energietechnischen Anlagen, Braunschweig 8.-9.10.1997, VDI-Bericht 1359 (pp 353-367), ISDN 3-18-091359-2

# FLUIDDYNAMIC WATERHAMMER SIMULATIONS WITH CONSIDERATION OF FLUID-STRUCTURE INTERACTION

Thomas Repp

## 1. Introduction

The design rules for pipe systems of nuclear installations require that also fluid dynamic loads have to be examined (KTA 3201 and 3211 [1], RSK-L. 4.1.1-3,4 [2]). These loads are the result of transient pressure changes, developing due to the acceleration and slow down of the fluid masses. In the past, results were obtained only from fluid dynamic calculations or simulations without consideration of the fluid-structure interaction (FSI) or only by considering the structural influence to the fluid. In the last decade, one-dimensional programs were introduced to simulate the influence of the structure to the fluid but not to explore the feedback from the fluid to the structure (Borchsenius and Bornemann [3]). The topic of this project is to investigate the influence of the dynamic fluid-structure interaction in pipes on the pressure in the fluid and on the reaction loads on the structure to show whether the commonly used formula are conservative or not and when it is necessary to consider the FSI especially with fully-coupled 3D-Codes. The project this report is based on is included in the initiative for competence maintenance in nuclear technology which is carried by the Verein Deutscher Elektrizitätswerke e.V. (VDEW e.V.) and the German Ministry of Research (BMBF).

## 2. Theoretical Background

A pressure wave may arise when a valve is closed very fast. Before the valve the fluid masses are slowed down and because of this acceleration a pressure wave occurs which propagates in the pipe with sound velocity (see Fig. 1). It is reflected at the open end of the pipe (change of sign but not of the amplitude) or at a wall or a closed pipe end (no change of sign and same amplitude). When the wave hits a wall considerable mechanical loads may occur. This phenomenon is called a waterhammer.

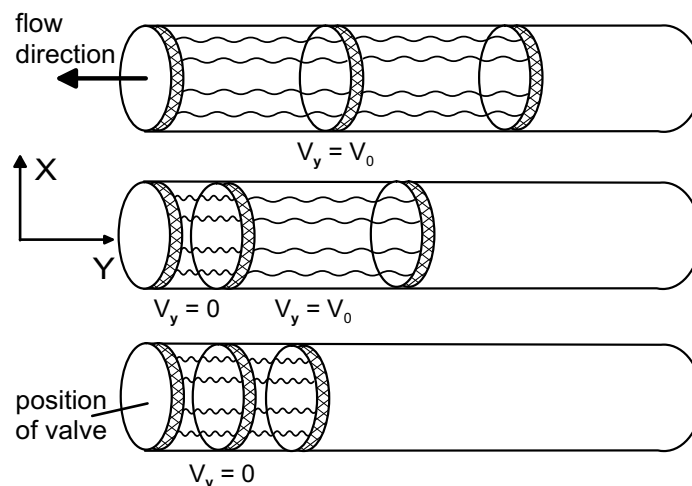


Fig. 1: Fluid compression

Commonly the Joukowsky equation is used to determine the amplitude of the pressure wave.

$$\Delta p = \rho c \Delta v \quad (1)$$

The Joukowsky equation (1) shows that the pressure change  $\Delta p$  only depends on the density  $\rho$ , the sound velocity  $c$ , and the change of the fluid velocity  $\Delta v$ . For rigid pipe walls, the sound velocity can be calculated by

$$c_{rigid} = \sqrt{\frac{E_F}{\rho}} \quad (2)$$

with the bulk modulus  $E_F$ , being the elasticity of the fluid which is in the range of  $2,1 \cdot 10^9 \text{ N/m}^2$ , and the density  $\rho$  in the range of  $1000 \text{ kg/m}^3$ . To consider the influence of the elastic walls upon the propagating pressure wave in the Joukowsky approximation, the sound velocity is modified according to

$$c_{elastic} = \sqrt{\frac{\frac{E_F}{\rho}}{1 + \frac{E_F}{E_M} \frac{d}{s} K}} \quad (3)$$

Eq. (3) is called the extended Joukowsky formula, which includes also material properties of the structure, like the Young's modulus  $E_M$ , the inner diameter  $d$ , the thickness of the pipe  $s$  and additionally the factor  $K$  ( $0 \leq K \leq 1$ ), which depends on the geometry and the fixing of the pipe structure. The  $K$  factor is clearly defined only for certain kinds of fixing and in general only for straight pipes (Tijsseling [4]). It is not clear whether the pressure amplitude can be described for pipes with high ratios of the pipe diameter to the pipe wall thickness and with build-ins like pipe bends. It is also unknown whether the maximum pressure amplitude gives enough information to exactly predict the stresses and strains in the pipe structure. But is clear that the locations of the maximum stress and strain cannot be predicted by equations (1) - (3). For that a 3-dimensional simulation is needed.

### 3. 3D-modeling using ADINA

The simulations are performed using the program system ADINA<sup>®</sup>, which is a fully coupled fluid and structure code. It is possible to perform transient 1- and 2-phase flow simulations under consideration of dynamic fluid-structure interaction. For the simulation of a waterhammer only 1-phase flow simulation is needed. Even if cavitation occurs, the pressure wave is induced after the condensation of the vapor phase. The interface between the fluid and the structure is modeled with FSI-elements at the structure and special FSI-boundary conditions at the fluid wall. Both together transfer the fluid pressure as load to the structure and the new structural geometry to the fluid within every iteration of every time step. As convergence criteria the relative displacement and stress residuals are used (ADINA R&D [5]). With a fully incompressible fluid it is not possible to simulate pressure waves with a finite sound velocity. Therefore, ADINA<sup>®</sup> offers the special feature to model slightly compressible fluids. Up to now straight pipes and pipe bends with water flow have been examined with regard to pressure and stress changes within a certain time after the valve closure.

The pressure amplitude, the stress and the strain of the pipe were calculated depending on the ratio of the wall thickness to the diameter and of the diameter to the bend radius. In case of the straight pipe the initial conditions are the pressure level and the axial fluid velocity in the whole volume. In case of the pipe bend the pressure and the fluid velocity obtained from a transient calculation is used as initial condition. The valve closure is simulated by a transient slow down of the fluid velocity at the position of the valve. As boundary condition for the pipe wall it is assumed that the fluid velocity normal to the wall is equal to the local structural velocity. In general, the structural motion causes a change of the pressure in the fluid and due to the fluid reaction forces stresses and strains in the elastic pipe wall. At the location of the valve no translational motion is permitted. The model of the bended pipe consists of the bend and two short straight pipes at its ends. The model is axially fixed at the open ends. The straight pipes are only added to minimize the influence of the support onto the stresses. Therefore, the pressures and stresses are only analyzed at the curved part.

#### 4. Results of the simulations

Figure 2 shows the pressure amplitude over the time for a straight pipe (initial fluid velocity 5 m/s, time of slow down 0,005 ms, inner diameter 0,1 m, wall thickness 3 mm, length 1m) at defined locations of the pipe (see right side of Fig. 2). The extended Joukowsky equation yields  $\Delta p = 6,275$  MPa (see straight horizontal line in Fig. 2). The maximum pressure is more than 10 % higher than the value predicted with the extended Joukowsky equation. The difference between the averaged pressure amplitude (disregarding the over oscillations) and the analytical solution is smaller than 2,5 %. It can be stated that the average pressure amplitude agrees well with the result of the extended Joukowsky equation.

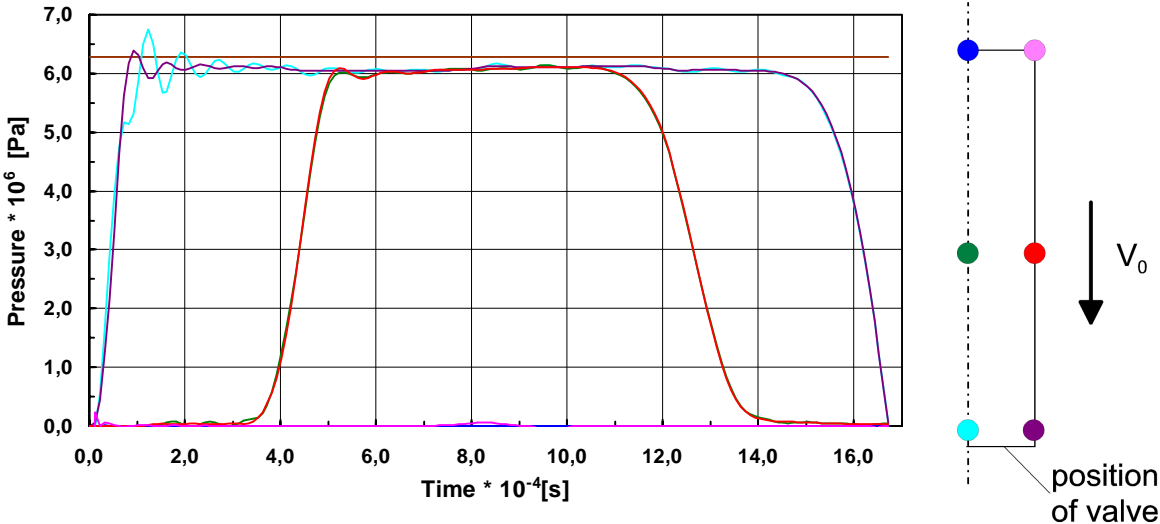


Fig. 2: Pressure over time on the pipe axis and pipe wall (with FSI)

Figure 3 shows the von-Mises-stress for the straight pipe under dynamic pressure load. The static stress because of the static pressure level is not regarded in the simulations and therefore generally needs to be added. Neglecting the oscillations the local maximum stress amplitude is at the same level as the static stress in the same pipe if it was exposed to a static pressure as predicted with the extended Joukowsky equation (straight line at 109 MPa). At maximum pressure (at 0,1 ms) also the maximum von-Mises-stress is found (see Fig. 2 and 3).

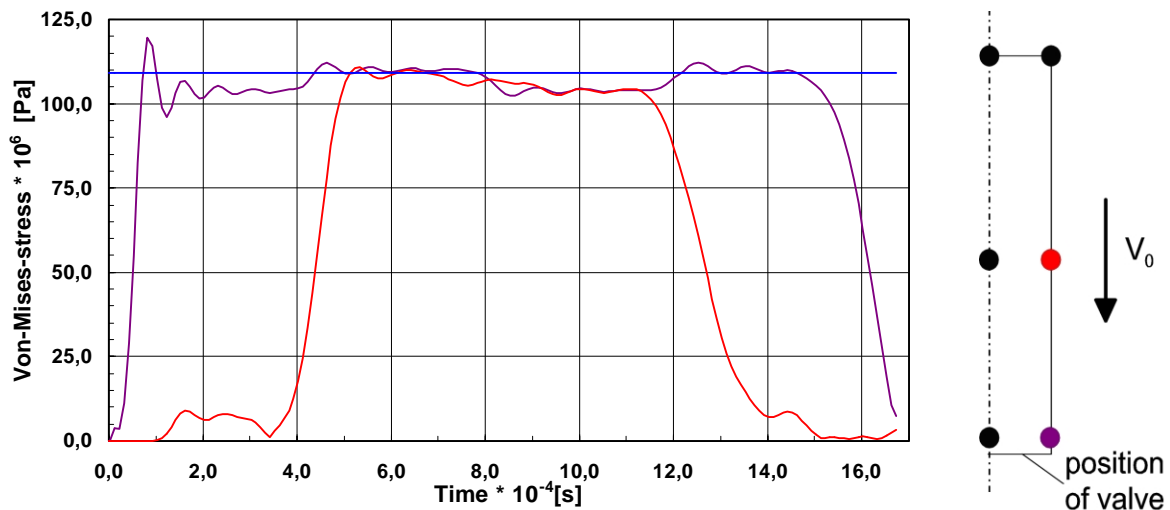


Fig. 3: Von-Mises-stress over time at the inner pipe wall

The response of a pipe bend to a waterhammer differs significantly from that of a straight pipe. Figure 4 shows the pressure amplitude in a pipe bend (initial fluid velocity 5 m/s, slow down time 0,05 ms, inner diameter 0,1 m, wall thickness 2,6 mm, bending radius 0,27 m, bend length 0,424 m) at the inner and outer bend radius under 0°, 45°, and 90°. Additionally the pressure amplitude predicted with the extended Joukowsky equation (horizontal line) is shown. The analytical result is conservative compared with the simulation. But there are unneglectable differences comparing the pressure at the inner and outer bend radius.

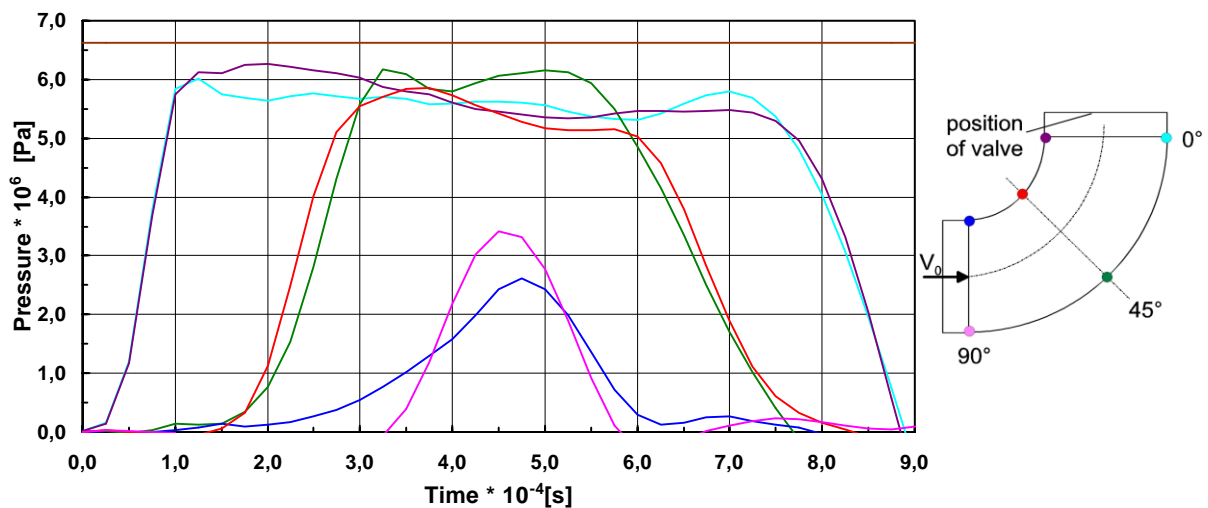


Fig. 4: Pressure over time at specified locations in a pipe bend

Figures 5 and 6 show the maximum Von-Mises-stress for the same pipe bend under dynamic load and under static load (equal to the maximum pressure amplitude predicted with extended Joukowsky). The maximum equivalent static stress is more than 50 % lower than the maximum dynamic stress within the investigated time range. The maximum stress is found at the end of the pipe bend.

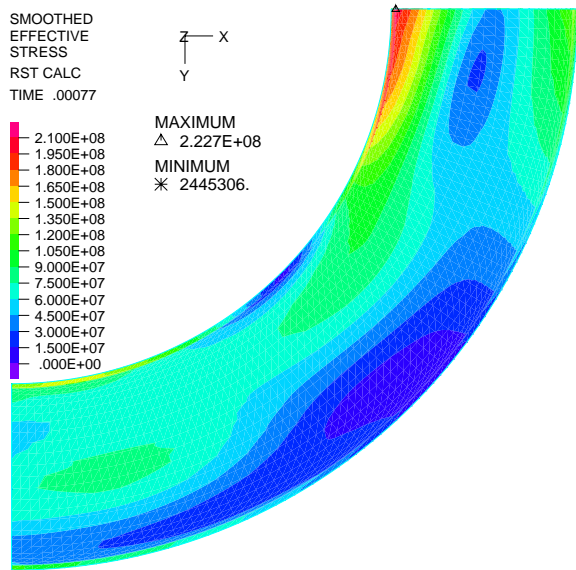


Fig. 5: Maximum von-Mises-stress [Pa] for a calculated pressure wave (accord. to Fig. 4)

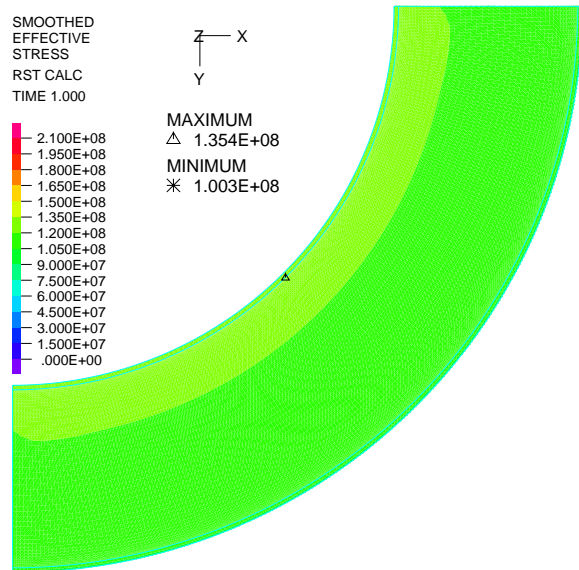


Fig. 6: Von-Mises-stress [Pa] for a static internal pressure according to eq. (1)

Figure 7 shows the decrease of the pressure amplitude (maximum pressure minus static pressure) in dependence on the slow down in a straight pipe for two selected fluid velocities. The maximum pressure, in this case regarded without FSI, is proportional to the initial fluid velocity and strongly decreases with increasing closure time. The start of the decrease is proportional to  $L$  ( $L$  = length of pipe). For  $L = 1$  m a critical valve closure time  $t_{critical} = 1,34$  ms is found.

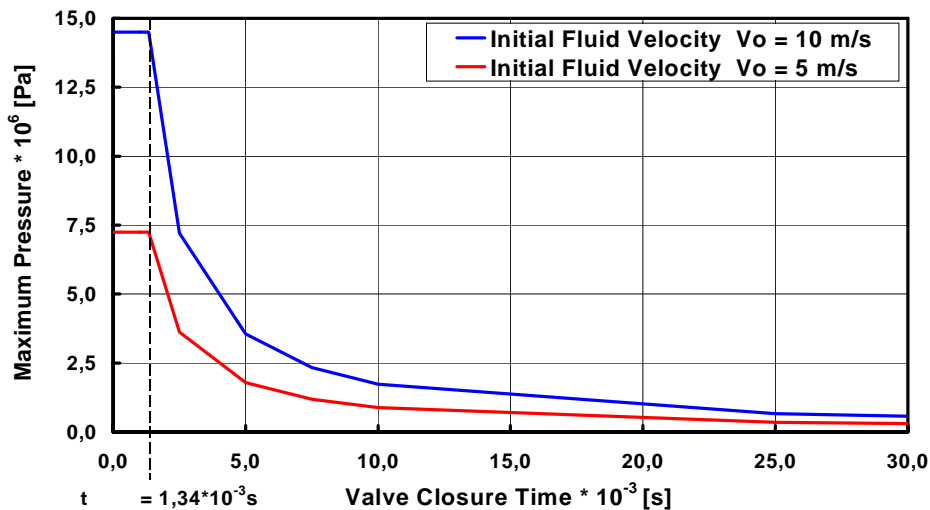


Fig. 7: Pressure versus valve closure time for two initial velocities

## 5. Conclusions

The simulations show that an overall good agreement is found for the average pressure amplitude of a straight pipe in comparison to the analytical results obtained with the extended Joukowsky equation. In case of the bended pipe the pressure amplitude of the extended

Joukowsky equation seems to be too conservative. In general the average pressure decreases with fluid-structure interaction. But sometimes pressure peaks may appear nearly as high as without FSI. Fluid-structure interaction may locally lead to higher stresses than obtained with common calculation methods. In case of the bended pipe the maximum stress is significantly higher than the static stress which is predicted by a static structural simulation using the pressure amplitude obtained by the extended Joukowsky equation as load.

## 6. Outlook

The future work is to investigate how the necessity to consider FSI changes with changing geometric parameters of the pipe (straight and bended). The influence of the wall thickness at higher pressure levels will be analyzed and also nonlinear material behavior shall be considered if large deformations and stresses are predicted. The results of the simulations will be compared to one-dimensional simulations (Krepper [6]). Cavitation simulations with pressure dependent density shall be made. Also the influence of an elastically supported valve on the FSI will be examined. Finally, if possible, the material properties shall be changed from slightly compressible water to a fully compressible medium to simulate waterhammer due to cavitation and sudden condensation, which may occur even at slower closure processes. Such simulations could be compared with measurements performed by UMSICHT and FZR (Dudlik, Schlüter and Prasser [7]).

## References

- [1] Sicherheitstechnische Regeln des Kerntechnischen Ausschusses (KTA) für den Primär- und Sekundärkreislauf, 3200 ff, aktuelle Version
- [2] Handbuch Reaktorsicherheit und Strahlenschutz, Abschnitt 4: Empfehlungen der Reaktorsicherheitskommission, Herausgeber: Der Bundesminister für Umwelt, Naturschutz und Reaktorsicherheit, aktuelle Version
- [3] F. Borchsenius, J.-Th. Bornemann (1998), Entwicklungen bei fluiddynamischen Berechnungen im atomrechtlichen Aufsichts- und Genehmigungsverfahren, Tagungsbericht der Jahrestagung Kerntechnik 1998, München, ISSN 0720-9207
- [4] A. S. Tijsseling (1993), Fluid-structure interaction in case of waterhammer with cavitation, Ph. D. Thesis, Delft University of Technology, Faculty of Civil Engineering, Communications on Hydraulic and Geotechnical Engineering, Report No. 93-6, Delft, The Netherlands, 1993, ISSN 0169-6548
- [5] ADINA R & D Inc. (1997), Theory and Modeling Guide, Volume II: ADINA-T and ADINA-F, Report ARD 97-8
- [6] E. Krepper (1998), Hausmitteilung: Wasserhammer-Simulationen mit Athlet<sup>®</sup>, Forschungszentrum Rossendorf (FZR)
- [7] A. Dudlik, S. Schlüter und H.-M. Prasser (1997), Transiente Strömungsvorgänge in Rohrleitungen, Visualisierung und Berechnung von Kavitation in Rohrleitungen hinter schnell schließenden Regelklappen, Workshop „Meßtechnik für stationäre und transiente Mehrphasenströmungen“, Forschungszentrum Rossendorf (FZR)

# SOLUTION OF A MIXED CONVECTION FLOW BENCHMARK USING COMPUTATIONAL FLUID DYNAMIC CODES

Eckhard Krepper, Hans-Georg Willschütz and Frank-Peter Weiß

## 1. Introduction

For next generation nuclear power plants it is demanded that there are no consequences for the population and environment - even in the closest vicinity of the plant - during and after every possible accident scenario. This may be achieved by passive safety injection systems for decay heat removal. Examples for such components are the emergency condenser or the building condenser in new BWR designs. To control the hypothetical case of a core meltdown and the formation of large corium pools the development and assessment of in- or ex-vessel corium retention facilities are necessary.

For the design, optimisation and safety analysis of nuclear plants, the use of 1D system codes is state of the art. However, for the modelling of passive equipment the range of validity of the 1D-codes is exceeded, because in these structures 3D-flow phenomena are often dominating. The fast progress of the computer technique and of Computational-Fluid-Dynamics (CFD-) codes gives the opportunity, to apply CFD-codes to the assessment of the efficiency of those components. Most of these codes are based either on the finite-volume or the finite-element method.

Integrated simulation of thermo-hydraulic phenomena and the resulting thermo-mechanical loadings for the surrounding structures (e. g. the reactor pressure vessel) can be achieved using a finite-element-code like ANSYS/Multiphysics<sup>®</sup>. The finite volume code CFX<sup>®</sup> has been proven to be an appropriate tool for modelling of 3D single phase fluid phenomena.

The governing mechanism in passive components for decay heat removal and also in corium pools is natural convection and heat transfer with internal heating under high-Rayleigh-number conditions of about  $10^{14}$  to  $10^{17}$  (Theofanus et al. [1] (1997), Dinh et al. [2] (1997)). The main difficulty describing this phenomenon arises from the strong coupling of momentum and heat exchange. Most of the commercial codes use first order turbulence models, which assume an isotropic behaviour of the turbulent diffusivity (e.g. the widely used standard K- $\epsilon$  model). Due to the buoyant force, which in the present task essentially determines the flow field, the flow is anisotropic. Further difficulties arise from the implicit Reynolds assumption, that the transport of the turbulent momentum and energy proceeds according to the same diffusivity coefficient.

To investigate the capability of the widely used commercial CFD-codes ANSYS/FLOTRAN<sup>®</sup> and CFX-4<sup>®</sup> to model natural convection in spite of the weakness of the models, post-test analyse of the 7-th IAHR-Benchmark were performed, which was defined by the working group of advanced nuclear reactor types of IAHR (International Association for Hydraulic Research). The test is well documented and detailed measuring results are available (Kamide et al. [3] (1991)). The Rayleigh-numbers during the experiment were only in the order of  $10^{11}$ , but the calculations can be considered as a validation step towards higher Rayleigh-numbers.

The task for the calculation was the modelling of the forced flow field of a single phase incompressible fluid with consideration of heat transfer and the influence of buoyancy driven flow effects.

## 2. The test

The test arrangement consisted of a flat tank, divided into a long inlet channel from below, a test volume with a cooled wall section and an outlet channel to the top (see Figure 1). The upper wall was inclined. The vertical profiles of the flow field and the temperature distribution in the test volume were measured at four positions (see Figure 1, traverse lines P1 to P4). Moreover, the flow profile in the inlet channel before the entrance into the test volume was measured (see Figure 1: Inlet velocity profile measurement line).

Four tests were documented, which mainly distinguish in the average velocity at the bottom of the inlet channel (see Table 1). The velocity was varied in the order of  $4.1 \cdot 10^{-2}$  m/s to  $11.4 \cdot 10^{-2}$  m/s.

The inlet temperature amounts to about  $50^\circ\text{C}$ . The coolant temperature at the cooled wall was about  $15^\circ\text{C}$ . The corresponding heat flux through the cold wall was given by the authors of the benchmark to be in the region of  $2.1$  to  $2.4 \cdot 10^4$  W/m<sup>2</sup>. The Reynolds numbers of the four tests with different inlet velocities range from the slight turbulent to the turbulent flow regime. As characteristic length for the estimation of the Reynolds number in the inlet channel the hydraulic diameter of the channel was used - for the Rayleigh number at the cooled wall the tank dimension was taken into account.

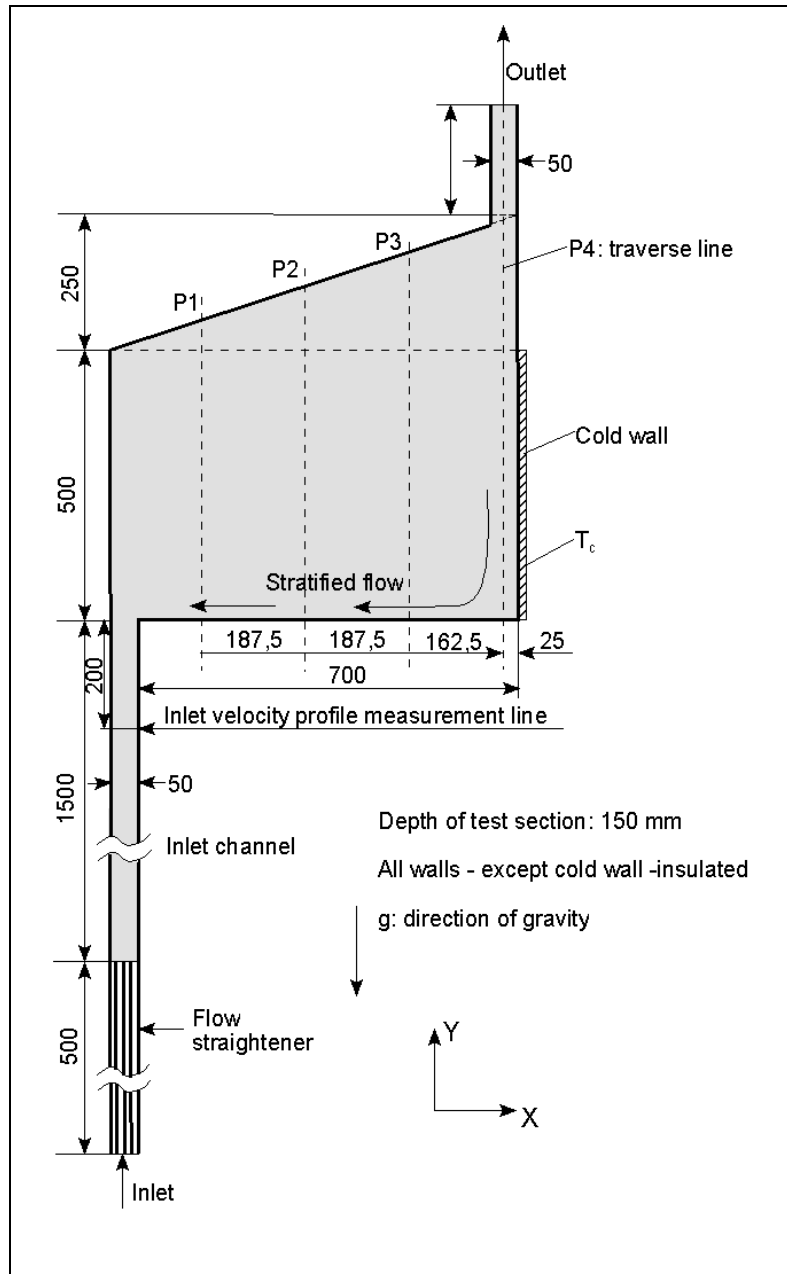


Fig 1: Test arrangement

Table 1: Boundary Conditions of the IAHR-Benchmark Tests

Test No.	1	2	3	4
Inlet temperature [K]	322.05	322.15	322.25	322.25
$\varnothing$ inlet velocity [m/s]	4.15e-2	5.16e-2	6.34e-2	11.4e-2
Temperature at the cold wall [K]	287.95	287.55	287.65	288.55
Heat flux at cold wall [W/m <sup>2</sup> ]	-2.13e+4	-2.24e+4	-2.34e+4	-2.40e+4
Temperature at the bottom of P4 [K]	310.15	309.85	309.55	311.65
Re-Number inlet	$3.4 \cdot 10^3$	$4.3 \cdot 10^3$	$5.2 \cdot 10^3$	$9.4 \cdot 10^3$
Ra-Number cooled wall	$2.8 \cdot 10^{11}$			

### 3. Observed thermo-hydraulic phenomena

During the tests a large vortex established in the test section. The higher the inlet velocity, the stronger the vortex developed. The vortex was overlayed by buoyancy caused temperature stratification at the bottom of the test section. For lower inlet velocities, the stratification and for higher inlet velocities the vortex was predominating. During the experiments a penetration of cold water from the right side of the test section into the inlet channel was observed. This has been clearly seen for test No. 1 but did not occur during test No. 4. For the tests 2 and 3 the penetration has not been clearly recorded. A periodicity was found of the penetration depth of cold fluid back into the inlet channel.

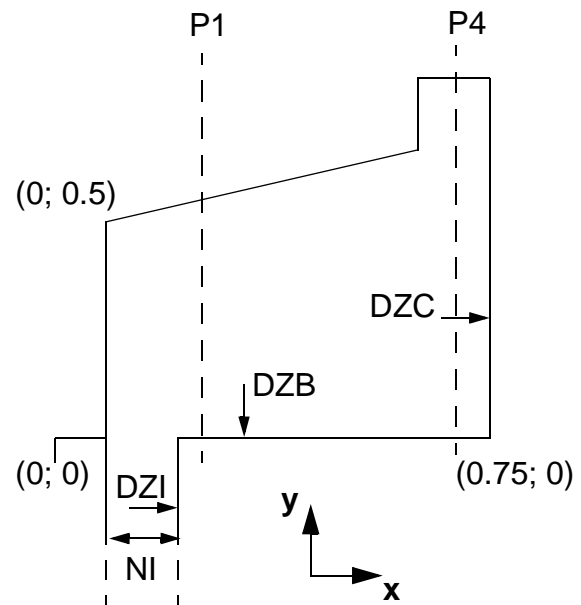


Fig. 2: Cell dimensions of the grid

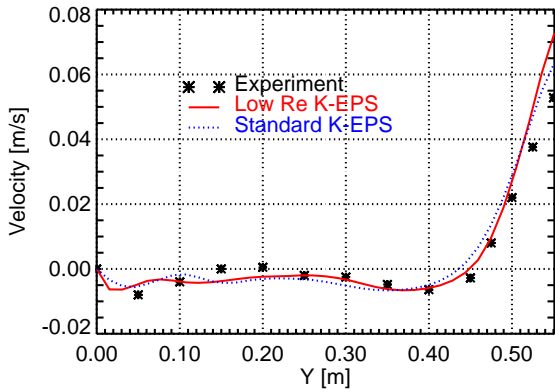
### 4. Modelling aspects

The flow field was predominated by 2-D effects. Therefore, the test was modelled by a 2-D simulation. The boundary conditions are described by an inlet velocity at the end of the flow straightener (see Figure 1), a pressure boundary condition at the outlet and the no-slip condition at the walls. All walls except the cold wall are assumed to be adiabatic. At the cold wall the heat flux

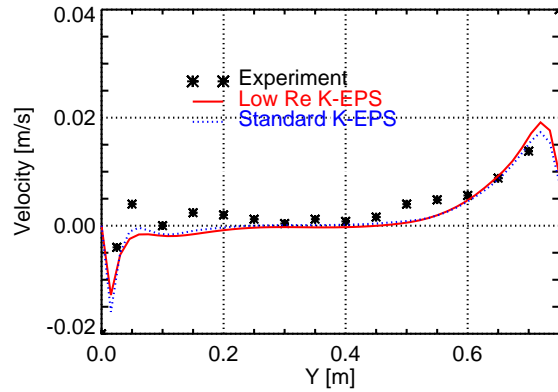
Table 2: Investigated CFX-grids

turbulence model	K-EPS	Low Reynolds number K-EPS
NI	20	40
DZI [m]	$2.0 \cdot 10^{-3}$	$2.0 \cdot 10^{-4}$
DZB [m]	$2.0 \cdot 10^{-3}$	$4.5 \cdot 10^{-4}$
DZC [m]	$5.0 \cdot 10^{-3}$	$2.0 \cdot 10^{-5}$
cell number	8175	12520

### CFX-results for test 1

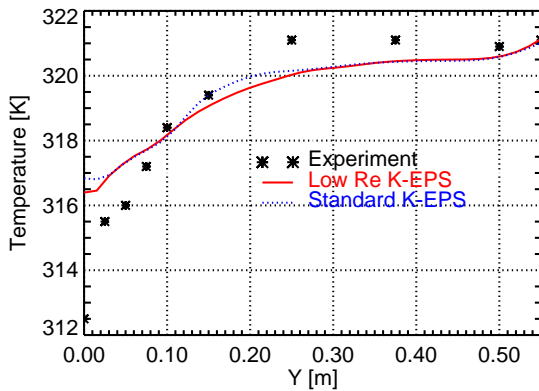


a) P1 ( $x = 0.1875$  m)

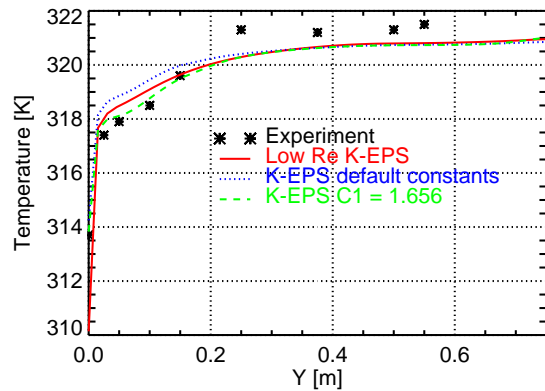


b) P4 ( $x = 0.725$  m)

Fig. 3: Vertical profiles for VX



a) P1 ( $x = 0.1875$  m)



b) P4 ( $x = 0.725$  m)

Fig. 4: Vertical temperature profiles

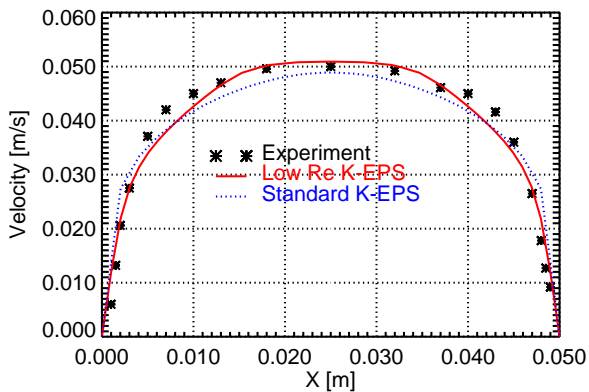


Fig. 5: Inlet velocity profiles

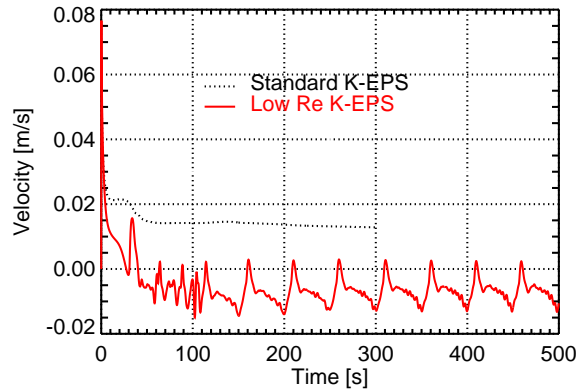


Fig. 6: Local inlet velocity at (0.049; 0.0)

or the temperature were preset. In both codes all calculations were performed as transient with 20 iterations per constant time step.

## 5. Results of the CFX-calculations

### 5.1. Influence of the turbulence model

The CFX-calculations were performed using the code version 4.2, which is based on multiblock grids. The Standard K- $\epsilon$  and the Low Reynolds Number K- $\epsilon$  turbulence model were applied, which requires the adaption of the mesh dimensions (see Table 2). These grids differ particularly in the dimension of the first cells near the wall, here denoted as DZI, DZB and DZC respectively. The mesh subdivisions were unequally distributed, so that the divisions were finer near the walls.

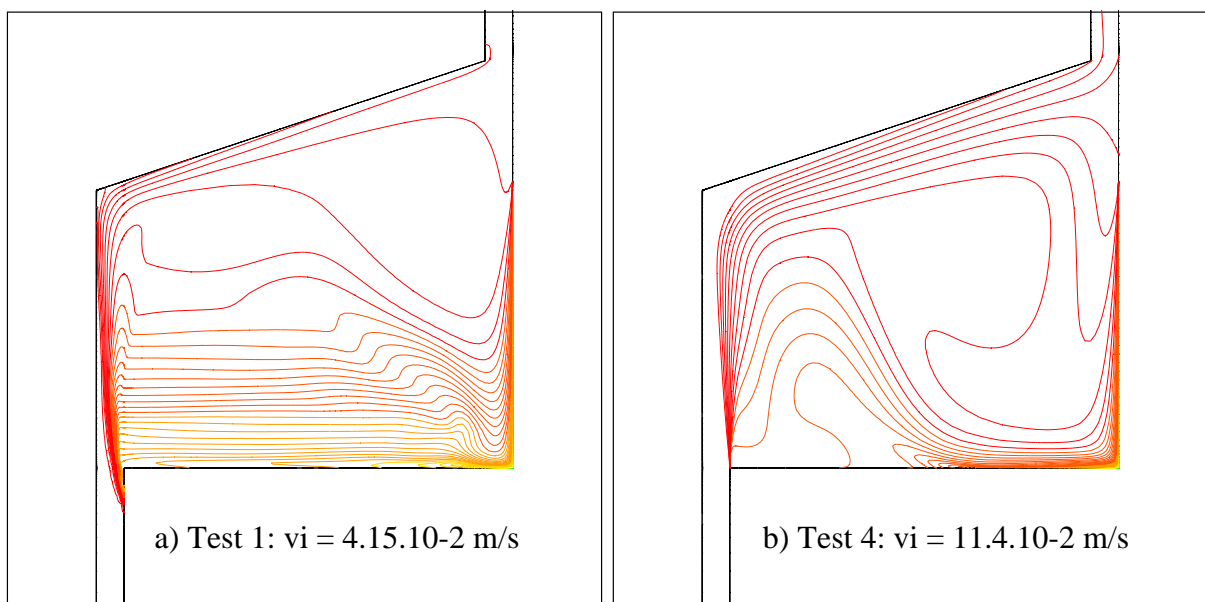


Fig. 7: Temperature distribution contour for different average inlet velocities (CFX, Low Reynolds Nuber K- $\epsilon$  Model; contour distance 0.2 K)

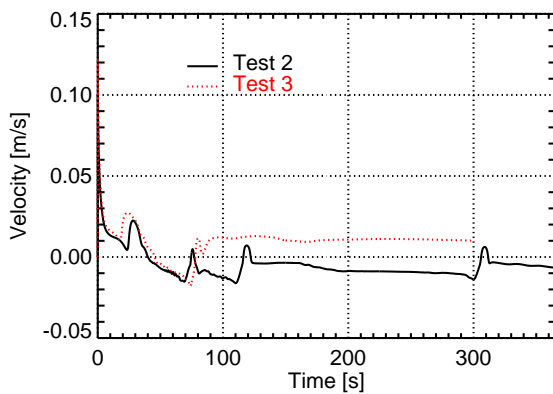


Fig. 8: Local inlet velocity at (0.049; 0.0); Low Re K-EPS turbulence model

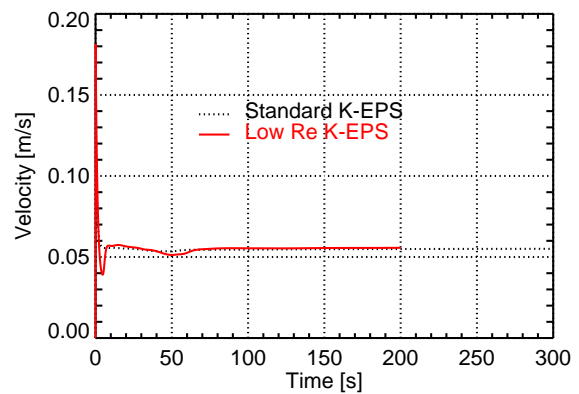


Fig. 9: Local inlet velocity at (0.049; 0.0); Test 4

The Standard K- $\epsilon$  model, which was applied using the default turbulence coefficients, assumes a laminar sublayer with a logarithmic flow profile according to a constant shear stress near the wall. Launder [4] (1988) showed, that a fine-grid low Reynolds-number treatment may mitigate the weaknesses of the standard K- $\epsilon$  model describing natural convection. The code CFX offers the application of a Low Reynolds Number K- $\epsilon$  Model according to Launder and Sharma [5] (1974), which allows to resolve the laminar sublayer. The disadvantage is the higher necessary computation effort because of the finer meshes. During all CFX calculations a modified upwind differencing scheme for the determination of the advection term and a fully implicit backward time stepping procedure was applied.

In the Figures 3 to 6 the results for the Low Reynolds Number K- $\epsilon$  Model and the Standard K- $\epsilon$  Model are compared. The vertical profiles of the horizontal velocity  $v_x$  and of the temperatures show a good agreement for both turbulence models. Figure 6 shows the inlet velocity at the right side of the entry plane into the tank. A negative velocity indicates the cold penetration phenomenon, which has a time period of about 50 seconds for the Low Reynolds Number K- $\epsilon$  turbulence model. Using the Standard K- $\epsilon$  model, no penetration into the inlet channel was found (see Figure 6). One of the reasons might be the better calculated inlet profile for the Low Reynolds Number K- $\epsilon$  turbulence model (see Figure 5). Also the increase of the constant  $C_1$  of the production term in the dissipation rate equation by 15% from the standard value, which was investigated by Kamide et al. [6] (1996) for low Reynolds Numbers, provided no cold penetration. However the temperature stratification was modelled in better accordance to the experiment (see Figure 4b). For test 2 the Low Reynolds Number K- $\epsilon$  model gave a cold penetration having a time period of about 200 seconds (see. Figure 8). For the tests 3 and 4 with the higher inlet velocity, the cold penetration was not found (see. Figure 8 and 9). The temperature con-

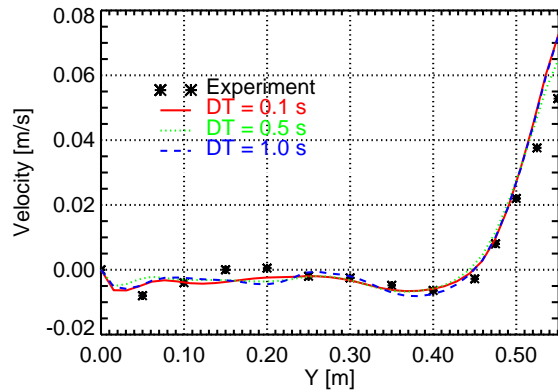


Fig. 10: Vertical  $v_x$  profiles for test 1 P1 ( $x = 0.1875$  m) with different constant time steps

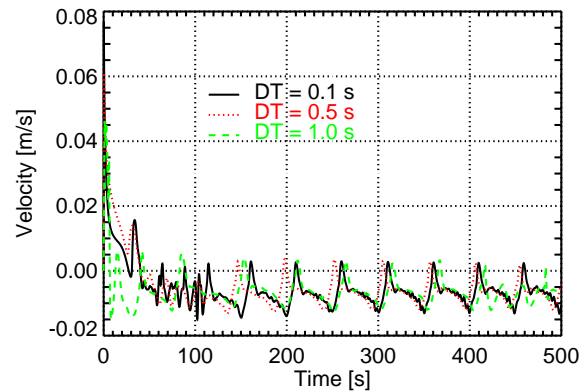


Fig. 11: Local inlet velocity at (0.049; 0.0) for different time steps

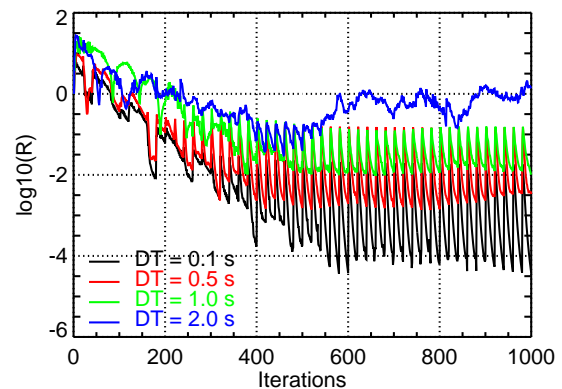


Fig. 12: Logarithmically scaled mass residuals

four plots in Figure 7 show, that for test 1 the temperature stratification and for test 4 with the higher inlet velocity the vortex in the test section is predominating. This was observed in the experiments, too.

## 5.2. Influence of the time step

The CFX-calculations using the Low Reynolds Number K- $\epsilon$  model were performed as transients with a constant time step. Different constant time steps were investigated for test 1. Figure 10 shows, that the constant time step in the range from 0.1 up to 1.0 seconds has almost no influence on the solution. In all these calculations the cold penetration phenomenon could be found (see Figure 11). A time step of 2.0 seconds however, does not result in a converged solution (see Figure 12).

## 6. Results of ANSYS/FLOTRAN calculations

The FE-model consisted of 4,400 quadrilateral elements with 4 nodes. In the ANSYS/FLOTRAN (Version 5.4) code the monotone streamline upwind spatial discretisation and the fully implicit backward difference time stepping were used.

Unfortunately in the finite element based code no Low Reynolds Number K- $\epsilon$  turbulence model is implemented. The applicability of the laminar approach was investigated, but no reasonable converged solutions were achieved. The cold penetration phenomenon was observed, but its depth was overestimated like it has been reported for laminar models by Kamide et al. [6] (1996).

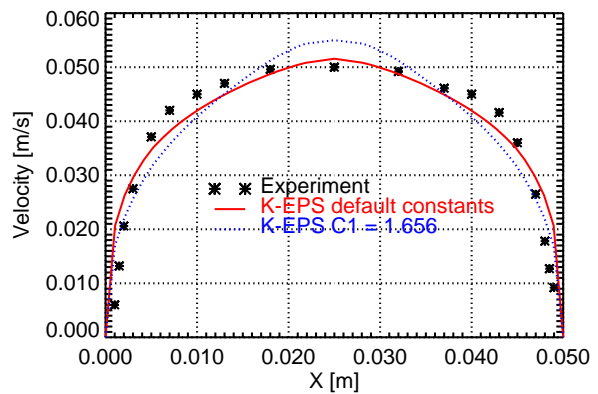
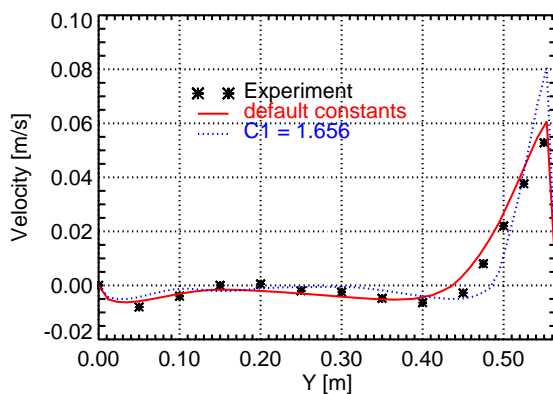
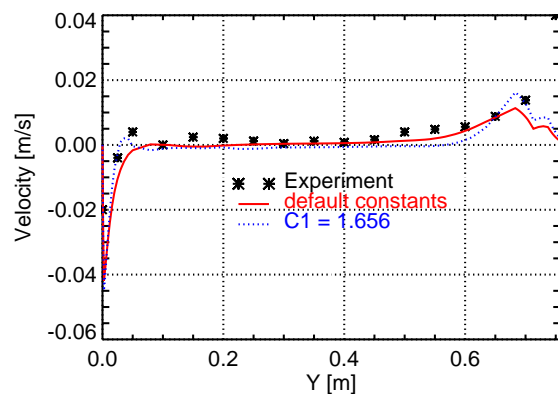


Fig. 13: Inlet velocity profiles (ANSYS/FLOTRAN)

### ANSYS/FLOTRAN-results for test 1



a) P1 (x = 0.1875 m)



b) P4 (x = 0.725 m)

Fig. 14: Vertical profiles for vx

## ANSYS/FLOTRAN-results for test 1

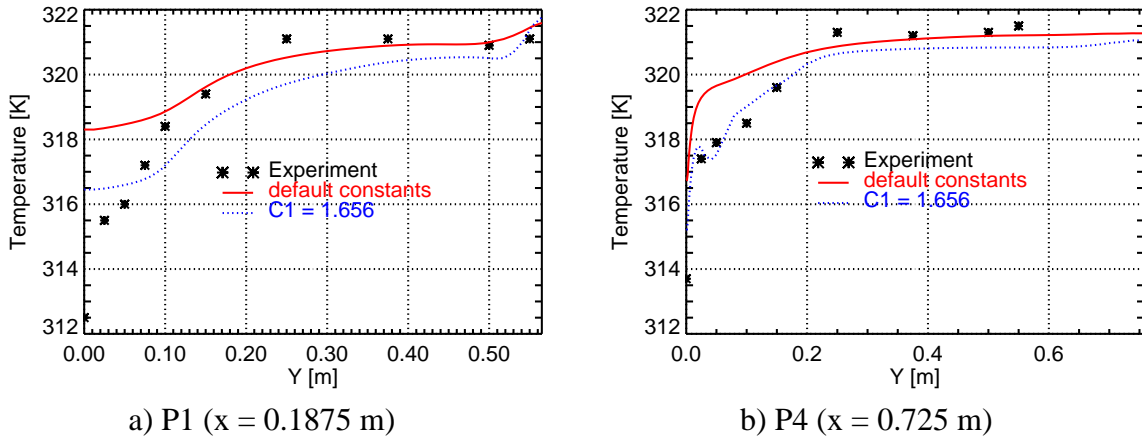


Fig. 15: Vertical profiles for the temperatures

The application of the Standard K- $\epsilon$  turbulence model using the default turbulence constants yielded results for the temperature and the velocity field with good agreement to the experimental data (see Figures 14 to 16). But no calculations provided the cold penetration phenomenon. The increasing of the turbulence constant for C1 by 15% to 1.656 improved the modelling of the temperature stratification (see Figure 15a and b), but also did not show the penetration. For test 4 the Standard-K- $\epsilon$  results are almost identical with the CFX-results.

## 7. Summary and conclusions

The flow field in the test section results from the interaction of the forced flow with heat transfer phenomena. Depending on the inlet velocity, a temperature stratification caused by the cooled wall (for Test 1) or a large vortex caused by the inlet flow (for Test 4) is predominating (see e.g. Figure 7a and b). For low inlet velocities a periodic cold fluid penetration back into the inlet channel was found in the tests.

The differences between the results of both codes are more dependent on the choice of the turbulence model than on the FEM or FVM numerical scheme. The laminar approach did not yield a reasonable converged solution. In both codes the Standard K- $\epsilon$  turbulence model is capable to model the flow and the temperature field in good agreement to the experimental data. But only the Low Reynolds Number K- $\epsilon$  turbulence model, which is available in the FVM-code CFX,

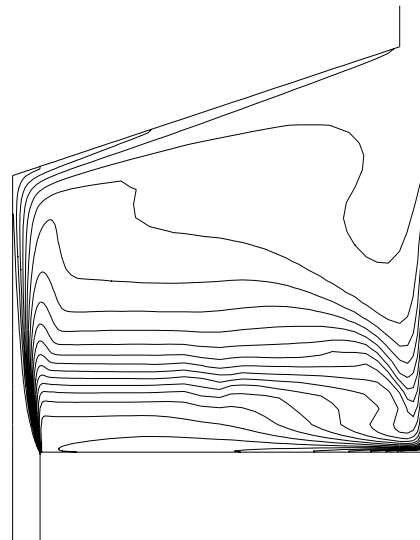


Fig. 16: ANSYS/FLOTRAN  
K-Epsilon, default constants  
contour distance 0.2 K

has been proven, to be capable of describing the cold penetration back into the inlet channel.

A precondition for the simulation of the observed phenomena is the exact description of the inlet profile of the flow into the test section. A fine meshing of the cross section in the inlet channel is required. Other CFX calculations showed, that a fine meshing at the wall with heat transfer is a sensitive characteristic of the grid.

The considered experiment was performed with steady state boundary conditions. But only the tests with higher inlet velocity finally resulted in a steady state flow. The tests with lower inlet velocity show flow oscillations with a constant period. The calculations using the Low Reynolds Number  $k-\epsilon$  turbulence model were capable of modelling this phenomenon.

## References

- [1] T. G. Theofanus, C. Liu, S. Additon, S. Angelini, O. Kymäläinen, T. Salmassi (1997), In-vessel coolability and retention of a core melt, Nuclear Engineering and Design 189, 1-48
- [2] T. N. Dinh, R. R. Nourgaliev (1997), Turbulence modelling for large volumetrically heated liquid pools, Nuclear Engineering and Design 169, 131-150
- [3] H. Kamide, Y. Ieda, and H. Ninokatá (1991), Benchmark Problem Description, prepared for the 7<sup>th</sup> Meeting of the IAHR Working Group on Advanced Nuclear Reactors Thermal Hydraulics, Kernforschungszentrum Karlsruhe GmbH, August 1991.
- [4] B. E. Launder (1988), On the computation of convective heat transfer in complex turbulent flows, Transactions of the ASME Vol. 110 No. 11, pp. 1112-1128
- [5] B. E. Launder, B. I. Sharma (1974), Application of the energy dissipation model of turbulence to the calculation of flow near a spinning disc, Lett. Heat and Mass Transfer 1, 131-138
- [6] H. Kamide, J. Kobayashi, Y. Ieda, H. Ninokata (1996), Benchmark exercise for multi-dimensional thermohydraulic analysis codes, Journal of Hydraulic Research 34 No. 3, pp. 317-344

## Acknowledgements

The authors would like to thank E. Altstadt and U. Rohde for fruitful discussions and particularly E. Altstadt for support preparing the ANSYS/FLOTRAN input data deck.

# INVESTIGATION OF HEATING UP AND EVAPORATION OF FLUIDS IN STORAGE TANK-EXPERIMENTS AND NUMERICAL SIMULATION

Attila Aszódi<sup>1</sup>, Eckhard Krepper and Horst-Michael Prasser

## 1. Introduction

Storage tanks for fluids are widely used industrial facilities. As a consequence of an external fire, the heat-up of the inventory may lead to the evaporation of the liquid and to release of significant quantities of dangerous gases into the environment. Comprehensive experiments were performed, to investigate the heating up processes. The experiments have shown that the liquid inventory behaves very differently depending on the mode of heating. Bottom heating leads to an irregular thermoconvective motion of the liquid, which causes good mixing, so that saturation is reached at all points inside the tank approximately at the same time. The maximum enthalpy of the liquid always remains close to the average value. If the vessel is heated from the side, stable temperature stratification is observed leading to large temperature gradients. Evaporation can start much earlier than the average temperature reaches saturation. The scenario is very realistic for cylindrical barrels, which are exposed to an external fire. In the paper, the experimental results of the tests with side wall heating are presented and the observed phenomena are described.

The first experiments were performed with temperature measurements only [3-5]. In order to clarify the physical nature of the details of the heating up process in simple geometrical boundary conditions,

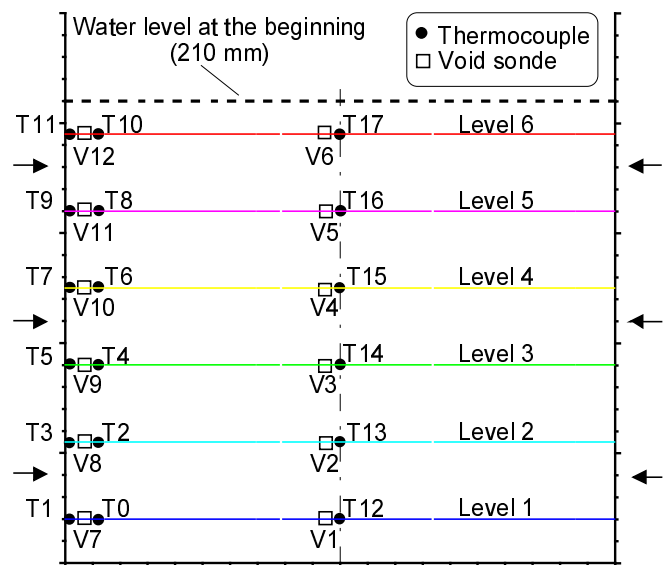


Fig. 1: Test arrangement and localisation of the measuring probes

Table 1: Localisation of the measurements

Level	H [mm]	Near the Wall		Centre of the tank		
		(1mm)		(10mm)		
		Temp.	Void	Temp.	Temp.	Void
6	195	T11	V12	T10	T17	V6
5	160	T9	V11	T8	T16	V5
4	125	T7	V10	T6	T15	V4
3	90	T5	V9	T4	T14	V3
2	55	T3	V8	T2	T13	V2
1	20	T1	V7	T0	T12	V1

<sup>1</sup> Technical University Budapest, Institute of Nuclear Techniques, Hungary

a two-dimensional mathematical model was developed, which also includes evaporation and two-phase flow. The calculated results of the model essentially contributed to the understanding of the phenomena observed during the tests. It was found that two-phase processes play an important role. Therefore, the tests were repeated, in which the local void fractions were measured too (see Figure 1).

**2. The experimental test arrangement**

The experimental test arrangement consisted of a cylindrical tank with a diameter of 0.25 m and a height of 0.25 m (see Figure 1). On the side walls, heating elements with an overall power of 4 kW are arranged, so that the heating power was equally distributed over the wall. During the tests, the tank was equipped with thermocouples and with conductivity probes for measuring the local void fractions at different locations. The measuring devices were arranged in certain heights over the bottom in the centre of the tank and near the walls (see Figure 1 and Table 1).

**3. The experimental results**

Different experiments were performed with different distances of the needle shaped void fraction measurements from the side wall between 1 mm and 5 mm. The experiments showed qualitatively the same behaviour of the fluid during the heating up process. The time dependence of the temperatures measured in different heights from the tank bottom is shown in Figure 2 for the thermocouples in the centre. Temperature and void fraction signals for the

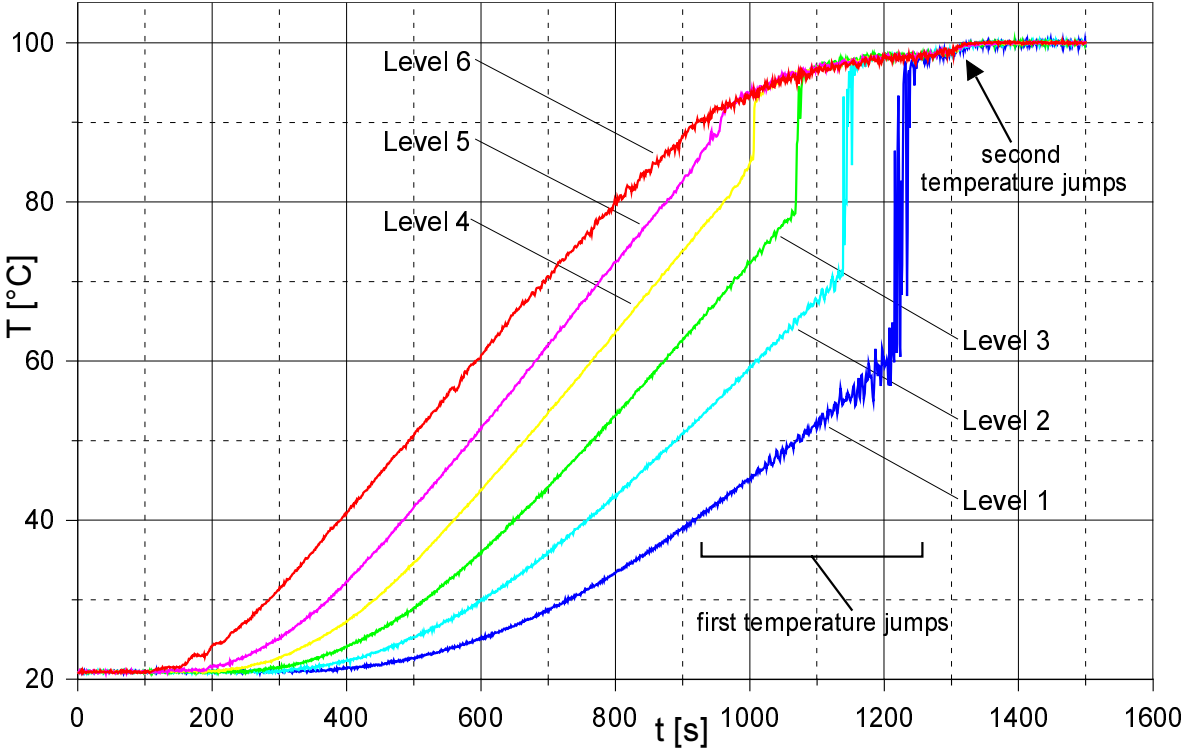


Fig. 2: Experimental results of the temperature measurements in the centre of the tank (T12 through T17)

different levels are shown in Figure 3a to 3f. During the experiment the void fraction probes V7 through V12 had a distance of 1 mm from the wall.

Already some hundreds of seconds after the beginning of the heating a strong temperature stratification occurs. Temperature differences up to 50 degrees between the 1<sup>st</sup> and the 6<sup>th</sup> height level are observed (see Figure 2 after about 1000 seconds). The different temperatures of the thermocouples at 1 mm and at 10 mm distance from the wall show, that already shortly after starting the test a small boundary layer of only a few millimetres is established with up to 7 °C higher fluid temperature (see Figure 2 and 3a to 3f).

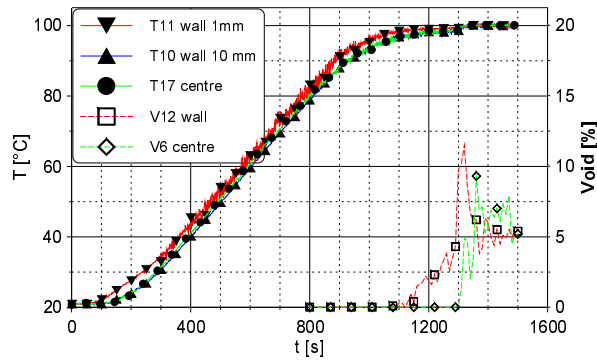


Fig. 3a: Level 6, H = 195 mm

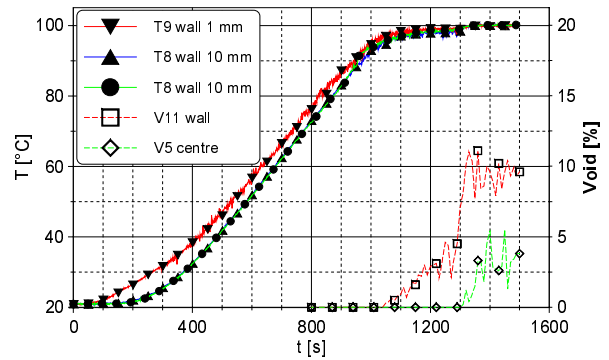


Fig. 3b: Level 5, H = 160 mm

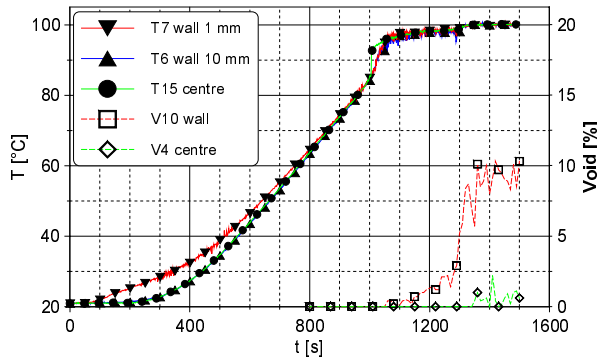


Fig. 3c: Level 4, H = 125 mm

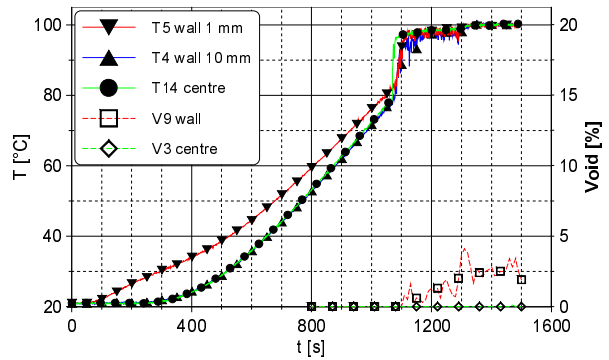


Fig. 3d: Level 3, H = 90 mm

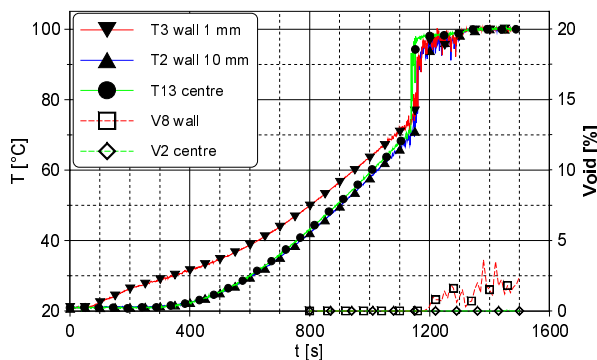


Fig. 3e: Level 2, H = 55 mm

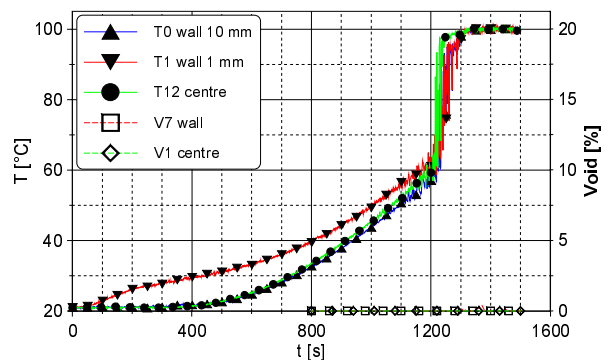


Fig. 3f: Level 1, H = 20 mm

Fig. 3: Fluid temperature and void fraction courses at different height levels in the tank

After about 1100 seconds first boiling is detected by the void probes near the wall at the levels 6 to 3 (see Figure 3a to 3e). During the time period from 900 to 1200 seconds temperature jumps to about 98 °C are observed. The jump is only small in the level 5. The jumps for the levels 4 to 1 are clearly to be seen in Figures 2 and 3c to 3f: in level 4 at 1000 seconds, level 3 at 1080 seconds, level 2 at 1130 seconds and finally in the lowest level 1 the largest jump (approximately 40 °C) at 1220 seconds. In the lower levels temperature oscillations are observed shortly before the jump. During this period no steam is detected in the centre of the tank (see Figure 3). Shortly after the last jump at level 1 a second temperature jump from 98 °C to 100 °C is observed for all thermocouples at about 1300 seconds (see Figure 2).

Simultaneously with the second temperature jump the needle probes V9 to V12 near the wall indicate a clear increase of the void fraction. Only after that steam was detected in the levels 6 to 3 in the centre of the tank (see Figure 3a to d). As an additional effect the void fraction detected by the wall probe at the highest level 6 decreases (see Figure 3a).

The needle shaped probes during the experiments yielded reliable signals, but problems occurred because of the probe size. The probes had a diameter of 1 millimetre. Therefore, they are not capable of detecting bubbles with a diameter smaller than about 1.5 mm. During the tests small bubbles were seen at the wall already after about 950 seconds. Also the typical noise at subcooled boiling was heard. The probes detect first boiling only after about 1100 seconds.

#### **4. A numerical model**

In order to clarify the physical nature of the details of the heating-up and the evaporation process in simple geometrical boundary conditions, a two-dimensional mathematical model was developed. The flow in the vessel was approximated by a two-dimensional flow in a rectangular area in Cartesian co-ordinates. It was assumed that neither temperature nor gas fraction influences the density of the liquid in the mass conservation equation and in the inertial term of the momentum equation. The changing density was taken into account only at the volume force term in the momentum equation (Boussinesq-approximation). This simplification leads to simpler calculation of the velocity field of liquid phase: when actual temperature and gas fraction distributions are given over the time, the volume force term can be determined explicitly and the motion of the liquid can be further calculated independently from the gaseous phase. For the gaseous phase, a constant bubble rise velocity was assumed. The vector of the gas velocity results from the liquid velocity by adding a constant value to the vertical velocity component.

Caused by these simplifications, the momentum of the gaseous phase is neglected and there is no need to solve a second momentum equation. The model is therefore restricted to low gas densities. This condition holds in the majority of practical applications.

So the model consists of four main equations [7]: the energy conservation equation, the momentum and mass conservation equation for the fluid and the mass conservation equation for the gaseous phase. The continuity equation was considered for each phase. The transport of the gaseous phase was described by a mass conservation equation that contains an empirical bubble diffusion coefficient. The energy conservation equation was simplified to the heat transport equation, which includes an effective thermal conductivity coefficient. The

momentum equation was considered only for the fluid phase. A constant turbulent viscosity represented turbulence.

The phase transition due to evaporation and condensation was modelled assuming thermodynamic equilibrium. The mass source of steam was computed from the superheating or subcooling of water. The heating power was considered by the source term in the heat transport equation. The heat is added to the cells near to the heated wall. The time dependent power derived from the measured heater sheet temperatures is shown in Figure 4.

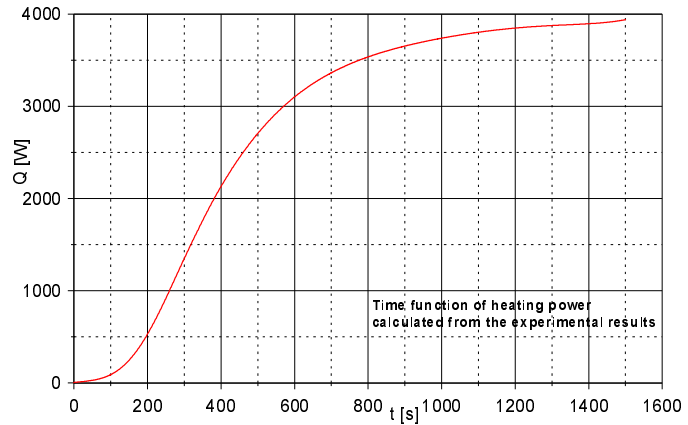


Fig. 4: Calculated time function of heating power

## 5. Numerical results and physical interpretation of the heating up process

The 2D model described in chapter 4 reproduces the experimental results and all phenomena in good agreement to the experiment (see Figure 5). The simulations enabled to clarify the physical reasons for the occurrence of the temperature jumps, which are explained in the following.

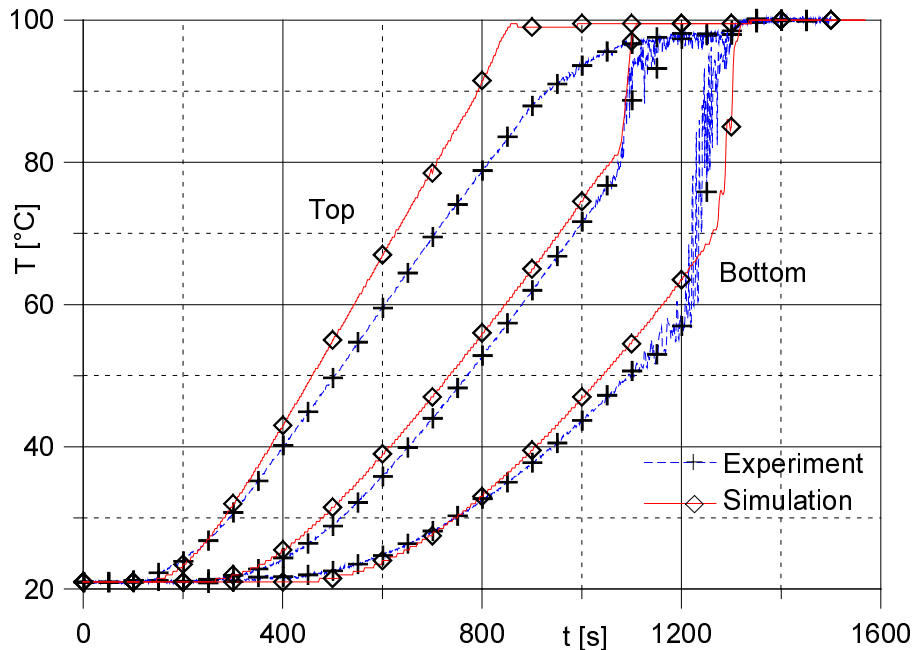


Fig. 5: Calculated and measured time dependence of temperatures. The bottom temperature corresponds to the probe T13, the middle to T14 and the top to T17 (compare Fig. 1)

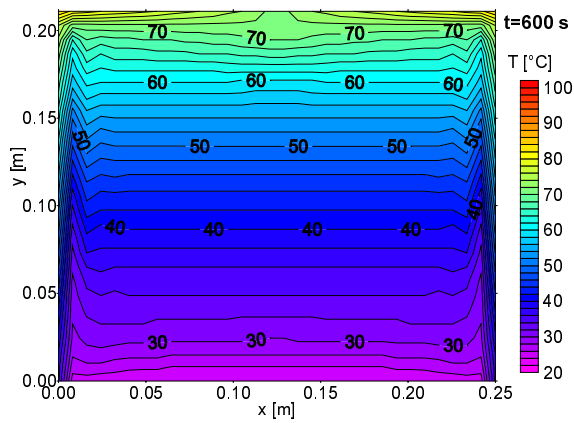


Fig. 6: Calculated temperature field at 600 seconds

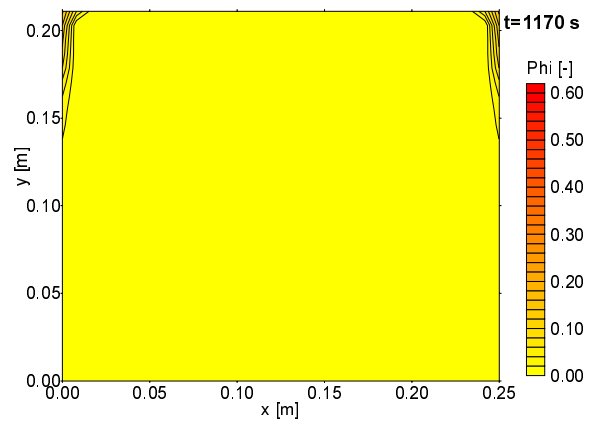


Fig. 7: Calculated void fraction field at 1170 seconds

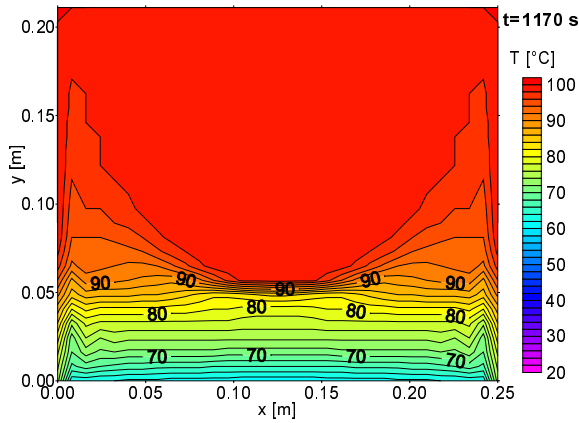


Fig. 8: Calculated temperature field at 1170 seconds

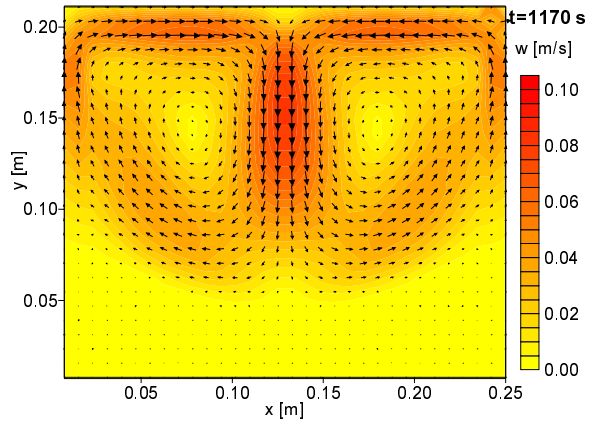


Fig. 9: Calculated velocities at 1170 seconds

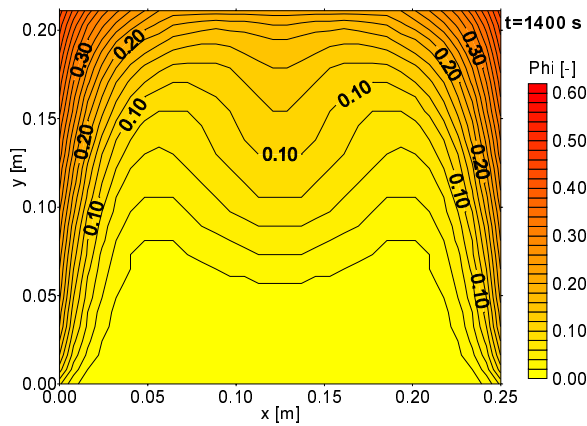


Fig. 10: Calculated void fraction at 1400 seconds

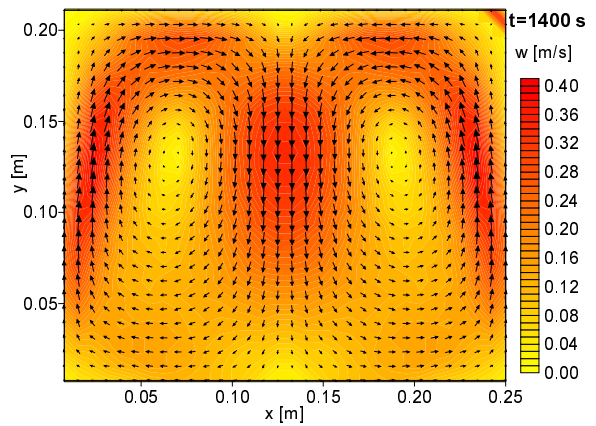


Fig. 11: Calculated velocities at 1400 seconds

Figure 6 shows the temperature distribution after 600 seconds. Heating of the side walls leads to significant horizontal temperature and density gradients in the vertical boundary layer. The resulting volume forces impose a strong preference direction of circulation. The result is a

stable vortex that transports the warm liquid from the heated wall to the surface. In the bulk, stable temperature stratification develops. As the temperature in the boundary layer increases in time, the liquid arriving at the surface is always piled up at the top. In the bulk a large vertical temperature gradient arises. In the consequence, evaporation starts much earlier than predicted by the average enthalpy. The steam generated in the boundary layer and at the top of the liquid discharges from the vessel. That leads to early mass losses.

The system responds very sensitively to the appearance of steam in the boundary layer. As it is seen also in the experiments, evaporation is first observed in the upper region of the side wall (see Figure 7). There, the buoyancy force caused by the bubbles is much higher than in the region below, where only density differences of the liquid phase drive the circulation. In the result, the upper region is well mixed, while the fluid in the region below remains stratified (see Figure 8 for the temperatures, Figure 9 for the velocities and Figure 7 for void fraction distribution).

The region of good mixing is extending downwards, because the onset of boiling moves down in the boundary layer. When the mixing front reaches the position of a thermocouple, its reading rapidly increases to a value close to saturation temperature. This explains the first successive temperature jumps found in the experiment.

Approaching saturation, the steam generation in the boundary layer gets more and more intensive causing significant mass and energy losses, but also accelerates natural circulation. When the sink velocity at the centre of the vessel becomes greater than the bubble rise velocity, suddenly a part of the produced steam is entrained into the bulk of the liquid. This causes a rapid approach to the saturation temperature in the entire fluid volume. In the temperature measurements this event is seen as the second temperature jump after 1300 seconds (see Figure 2). Figure 10 and Figure 11 show the calculated void distribution and velocities during the period of pool boiling. The described scenario yields the explanation, that during the heating up process before the second temperature jump no steam is found in the centre of the tank. The increased mixture velocity after the second jump causes a

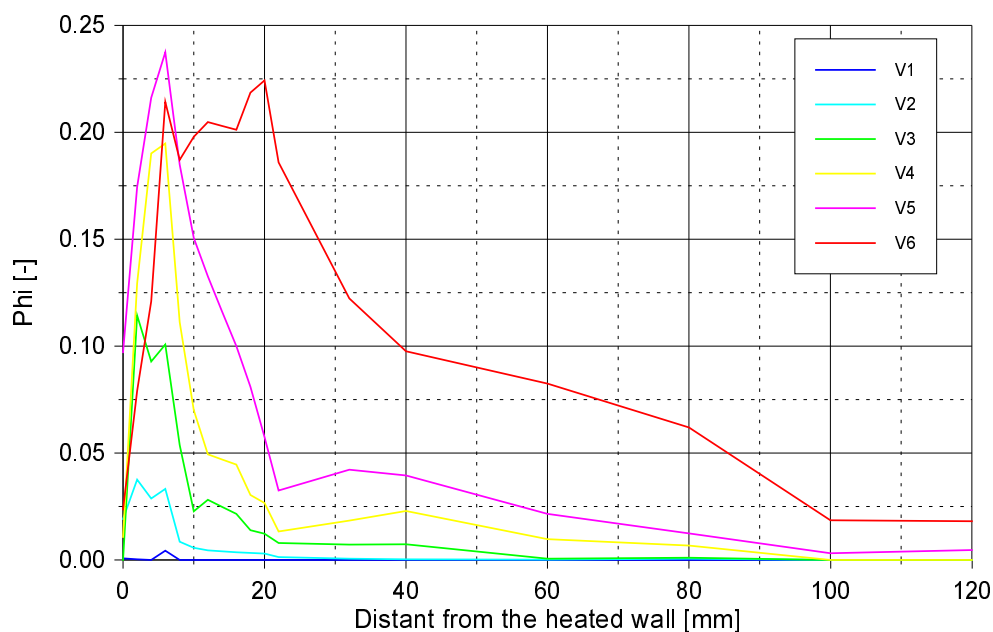


Fig. 12: Measured void fraction profiles after the second temperature jump

decreased void fraction at the upper probe on the wall (V12, see Figure 3a). This effect could be confirmed during several tests.

Additional measurements during further tests were performed, which aimed at the determination of the void fraction profiles during the period of pool boiling after 1300 seconds. For this purpose, the void fraction measurement arrangement V1 to V6 was moved through the tank in radial direction. The result is shown in Figure 12 and Figure 13. Figure 12 shows the measured void fractions depending on the distance from the heated wall. The figure shows clearly that steam is measured not only near the wall, but also in the bulk. Steam bubbles are carried down in the centre of the tank. The void fraction field in Figure 13

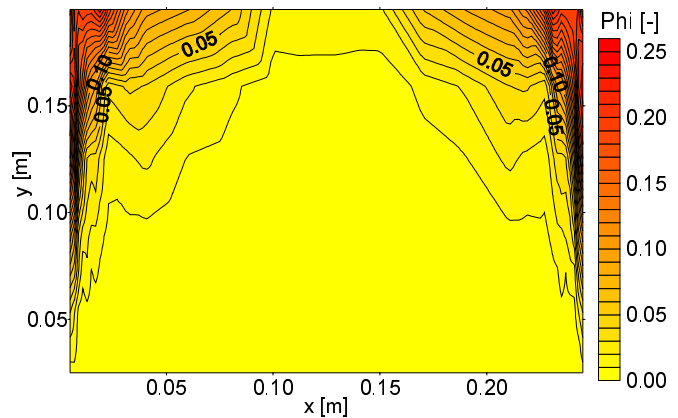


Fig. 13: Measured void fraction field after the second temperature jump

was derived by interpolation of the data of Figure 12. Figure 13 can be compared with Figure 10. The computed void fraction field shows a qualitatively good correspondence to the measured data. During the pool boiling period of the test the void distribution in the tank is very sensitively influenced by the relation of steam degassing from the tank surface and steam entrainment by the downward moving fluid into the centre of the tank.

## 6. Conclusions

The paper presents experimental and numerical investigations of single and two phase heating up processes of tanks with side wall heating. The measurement of the temperature and of the void fraction at different locations in the tank provides deeper insight into the mechanisms of two-phase natural convection in a tank. Despite some simplifications, the numerical 2D-model served as a tool, to understand and explain the observed events.

It was found, that side wall heating yields a considerably non-uniform temperature distribution in the tank. Assessing the numerical and experimental results, it is possible to identify the temperature stratification and the subcooled boiling near the wall as the cause of the first temperature jumps observed in the experiments. The quick transition from slight subcooled to volumetric boiling causes the second temperature jumps and a rapid approach to the saturation temperature in the entire fluid volume. This event was reproduced correctly by the two dimensional model.

## References

- [1] Aszódi A., E. Krepper and H.-M. Prasser, 1999, Investigation of heating up processes of fluids in storage tanks by experiments and by numerical simulation, 2<sup>nd</sup> International Symposium on Two-Phase Flow Modelling and Experimentation, Pisa Italy, 23-26.May 1999, Proc. Vol III, pp. 1667-1674
- [2] Aszódi A., E. Krepper and H.-M. Prasser, 1999, Experimental and numerical investigation of one and two phase natural convection in storage tanks, EURO THERM Seminar No. 63, Genua, Sept. 1999
- [3] A. Aszódi, P. Liewers, E. Krepper and H.-M. Prasser, 1997, Erwärmungsprozesse in Lagertanks mit gefährdenden Flüssigkeiten bei äußerer Brandeinwirkung, VDI Technische Überwachung, Springer Verlag Düsseldorf, Vol. 4/97, pp. 22-25
- [4] A. Aszódi, E. Krepper and H.-M. Prasser, 1997, Investigation of heating up processes in storage tanks with dangerous fluids influenced by an external fire, Achema '97, Frankfurt/Main, Germany, Session Safety Technology
- [5] A. Aszódi, 1996, Simulation der transienten Naturkonvektion in einem seitlich beheizten Behälter, Proc. of Annular Meeting on Nuclear Technology '96, Mannheim, Germany, pp. 106-109
- [6] M. A. Grolmes, M. Epstein, 1985, Vapor-Liquid Disengagement in Atmospheric Liquid Storage Vessels Subjected to External Heat Source, Plant/Operations Progress 4, pp. 200-205
- [7] A. Aszódi, 1996, Modelling of transient natural convection – Thermal-hydraulic analysis for an accident of dangerous fluid storage tanks, PhD. Thesis, Technical University Budapest, p. 95
- [8] A. Aszódi , P. Liewers , H.-M. Prasser, 1995, Simulation of transient natural convection in side wall heated storage tanks in F.-P. Weiß, U. Rindelhardt (Ed.) Institute of Safety Research, Annual Report 1995, pp. 20-26.
- [9] A. Aszódi, E. Krepper, 1995, Investigation of an external heated storage vessel by means of CFX-4 calculations in F.-P. Weiß, U. Rindelhardt (Ed.) Institute of Safety Research, Annual Report 1995, pp. 27-29.

## Acknowledgements

The work was initiated by safety investigations concerning a storage tank of liquid nuclear waste owned by the Verein für Kernverfahrenstechnik und Analytik Rossendorf e.V.. The authors wish to thank Prof. P. Liewers and his co-workers for the fruitful co-operation and making available the experimental facility. The authors wish to thank also for the support of the void fraction measurements by D. Baldauf (Research Center Rossendorf).

The work of Dr. Attila Aszódi was sponsored by the Hungarian Scientific Research Fund under the number D 25134.

# BRICK - A ONE-DIMENSIONAL MODEL FOR TRANSIENT SIMULATION OF PRESSURE RELIEF FROM BATCH REACTORS

Dirk Lucas

## 1. Introduction

Usually batch or semi-batch reactors are used for exothermic reactions. Often the reaction systems and the process control change. For this reason they imply a high risk potential. The reliable design of the emergency pressure relief system is very important to guarantee the safe operation of such reactors.

A new one-dimensional model for the transient simulation of pressure relief from batch reactors based on a particle method was developed. It belongs to the class of Particle-In-Cell (PIC) methods [1]. The main emphasis was given to a stable solution of the transient mass conservation equations, which is free of numerical diffusion and insensitive against user defined completions to describe chemical reactions, phase transfer, bubble generation, bubble coalescence, physical properties in multi-component systems, foam effects a.s.o. A particular goal was the accurate simulation of the behaviour of the top level of the mixture in the presence of foaming fluids. Flexible interfaces allow a convenient coupling of the model model for multiphase transport with constitutive laws and models as mentioned above.

## 2. The BRICK model

The basic equations solved by the BRICK model are the one-dimensional balances for the phase fraction  $\varepsilon^i$  for each phase  $i$ , which may be easily derived from the conservation of mass:

$$\frac{\partial \varepsilon^i}{\partial t} + \frac{\partial}{\partial z}(w^i \varepsilon^i) = \frac{\dot{m}^i}{\rho^i} - \frac{\varepsilon^i \partial \rho^i}{\rho^i \partial t} - \frac{w^i \varepsilon^i \partial \rho^i}{\rho^i \partial z}$$

These equations correspond to a balance of volumes if multiplied with a reference volume ( $w$  is the velocity,  $\rho$  the density and  $\dot{m}$  is the mass transfer rate).

In the three-dimensional reality there is only one phase at any point in space and time. Usually the numerical representation of the phase distributions is given by averaged volume fractions for discrete subvolumes called nodes in the following. Figure 1 gives a comparison of the one-dimensional representation of the phase volume fraction in case of common nodal models and in case of the new BRICK method. Using the BRICK method the whole volume of the vessel is subdivided into nodes of equal volumes. Every node is again divided into a large number ( $\sim 1000$ ) of equal volume elements. These volume elements always represent a defined phase, but they may additionally carry other properties like enthalpy, density of particles or concentration of components. The state of the system is characterised by the arrangement of these volumes and the properties assigned to them. Due to the model limitation to one dimension the system can be regarded as a tower of volume elements stacked on top of each other. Therefore, the volume elements are later on called bricks. Node values are calculated as average values

over all the bricks within a node. This causes discrete steps for the node volume fractions in units of  $1/N_{\text{Bricks}}$ , where  $N_{\text{Bricks}}$  is the number of bricks per node. Residual volumes (less than the volume of one brick) are stored and may be considered in the next time step to guarantee the exact conservation of mass.

The model allows the introduction of discontinuities (levels). At these discontinuities e.g. the continuous phase changes. The sections between two levels are called regions. A special region is the foam layer. At the lower end of this region the continuous phase does not change (liquid), but an additional level marks the change of the drift velocities (drain of liquid within the foam structure has to be supplied by a foam model). Levels may be generated or vanish during the transient calculation.

The transport problem is solved by the displacement of the bricks, i.e. the exchange of the brick positions. In a one-dimensional model motion has two reasons. One reason is the displacement caused by volume sources (e.g. external feed, steam generation by evaporation, compression). This is realized by inserting or removing (case of a sink) bricks at the location of the source. All bricks above this location are lifted up or descent according to the number of inserted or removed bricks, like in a tower of bricks. In the result all bricks move with total superficial velocity of the mixture. Discontinuities like the mixture level remain sharp. The other reason for the displacement are the relative velocities of the phases compared with this superficial velocity. This motion is realized by the exchange of brick positions within the single regions. The drift velocities are calculated by drift models for the dispersed phases (except the foam region). The bricks of these phases are shifted over a distance according to the time step. The bricks of the continuous phase are moved to the remaining free places beginning at the bottom of the considered region. With the displacement of the bricks all properties of the bricks are transferred, too. After completion of a transport step the properties of the bricks are translated into node values. These node values are the basis for the calculation of new volume sources and new drift velocities by models for particular effects, like e.g. models for phase transfer or drift models.

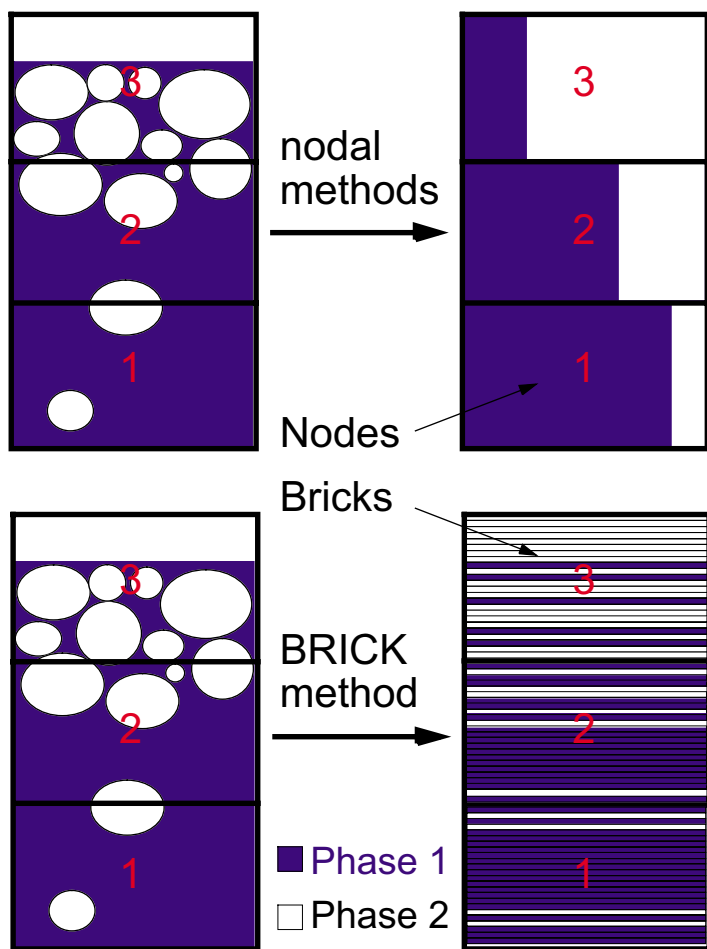


Fig. 1: Methods of representation of phase volume fractions

This motion is realized by the exchange of brick positions within the single regions. The drift velocities are calculated by drift models for the dispersed phases (except the foam region). The bricks of these phases are shifted over a distance according to the time step. The bricks of the continuous phase are moved to the remaining free places beginning at the bottom of the considered region. With the displacement of the bricks all properties of the bricks are transferred, too. After completion of a transport step the properties of the bricks are translated into node values. These node values are the basis for the calculation of new volume sources and new drift velocities by models for particular effects, like e.g. models for phase transfer or drift models.

This method enables the separation of the transport problem from other phenomena. The transport model as the core of the whole tool only needs the input of volume sources for each phase and node and the

drift velocities of the dispersed phases for each node and phase. The method is completely free of numerical diffusion. The levels always stay sharp and are an implicit result of the transport. It is not necessary to implement an explicit level tracking method.

### 3. Complementary models

Models for particular effects are included for the relevant processes in case of pressure relief. Most of them are coupled by flexible interfaces, which allow to add or substitute models and constitutive laws. There is a very close coupling between the transport model described above and the pressure iteration procedure. This procedure has to guarantee, that the sum of source bricks within the whole vessel is zero. Internal volume sources caused by the compressibility of the fluid and phase transfer depend on the pressure in the vessel. The pressure is changed until the above mentioned requirement is fulfilled.

Phase transfer equilibrium models are included for one-component evaporation, dissolving gas without evaporation and multi-component mixtures with evaporating and/or dissolving components based on ideal mixture theories. Additionally a non-equilibrium model for one-component evaporation is available. The specific enthalpy is assigned to the bricks as a special property. In case of a multi-component system the temperature is defined as brick property instead of the enthalpy. According to the different models for phase transfer different Lagrangian formulations of the energy conservation equation are used.

The BRICK code includes a balance of particle densities. The particle density is also treated as a property of the bricks. Bricks, which belong to the continuous phase are marked by a negative value for the particle density. This enables the division of the vessel volume into regions as mentioned above. Particle densities may change by particle sources (external sources or phase

transfer), by coalescence or decay of particles. Up to now a model for coalescence or decay of particles has not yet been included.

A flexible interface allows to couple the vessel model with models for discharge via a ventline or without a ventline. The interface includes the possibility of countercurrent flow, that means e.g. gas may be vented, but condensed liquid flows back from the ventline into the

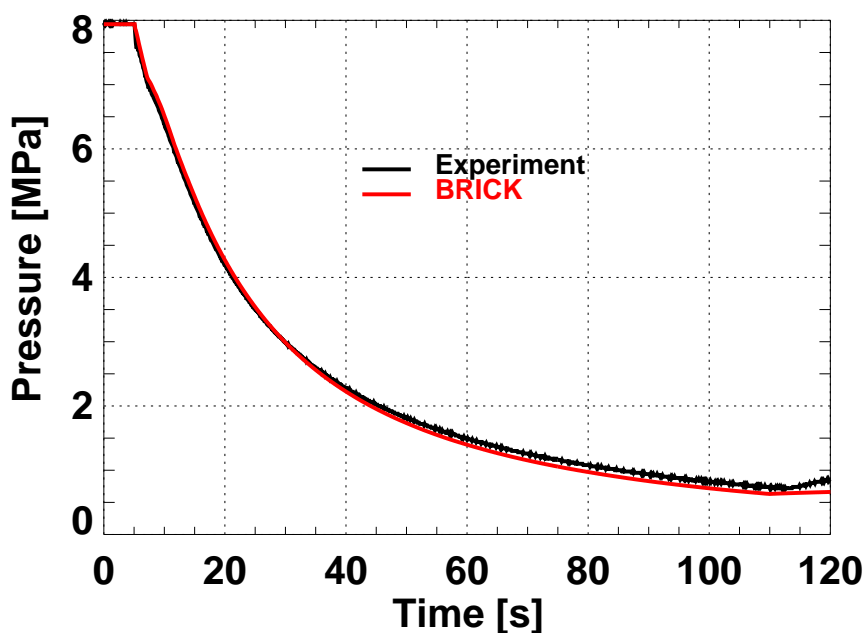


Fig. 2: Measured and calculated vessel pressure. Vessel volume: 175 litre. Initial filling 72%. Diameter of the orifice: 15 mm.

vessel. For critical flow a frozen flow model, valid for a small orifice, is implemented. Several ventline models are available.

For the simulation of the heat release from the vessel wall a model from the BLDN code [2] was used. It includes the heat release from the vessel jacket as well as from the bottom and the top

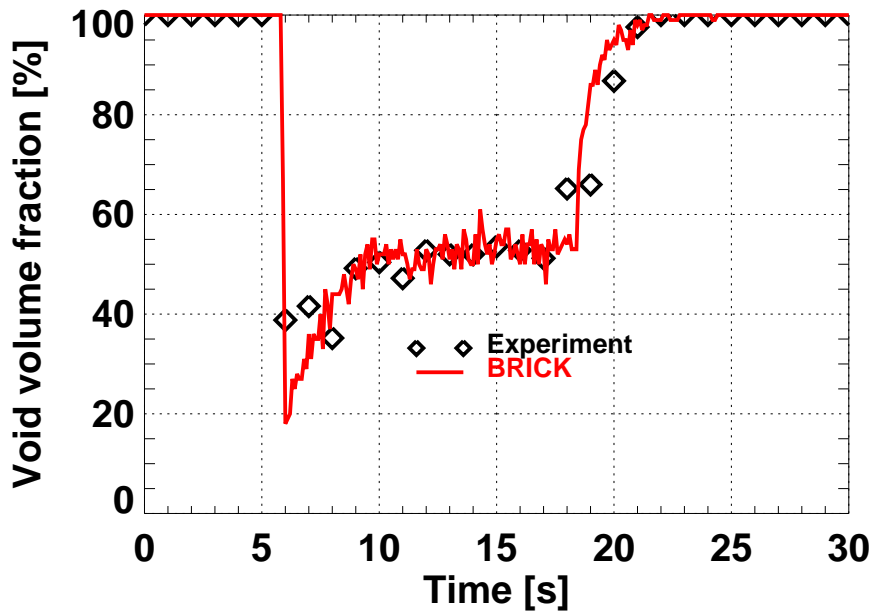


Fig. 3: Measured and calculated local void volume fraction at 85% of the vessel height. (same experiment as Fig. 2)

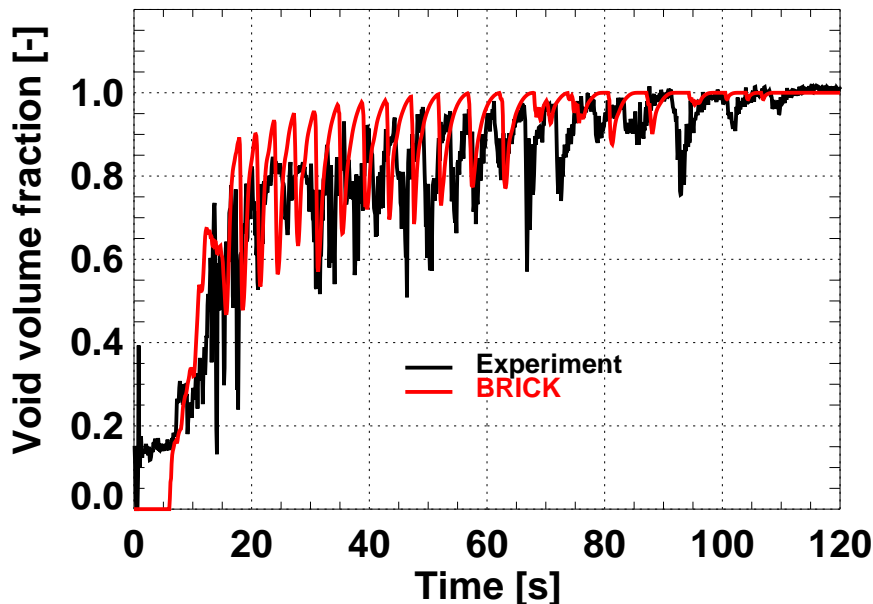


Fig. 4: Oscillations of the average void volume fraction within the ventline (top venting). vessel volume: 175 litre, diameter of orifice: 6 mm, length of ventline: 1.8 m, diameter of the ventline: 25 mm.

of the vessel. The wall of the vessel is subdivided into axial nodes. In nodes, where a level is present, the calculation of the heat flux between wall and fluid is done separately for the volume below and above the level. For different regions different correlations for the heat transfer coefficient can be defined. At the outer boundary of the vessel wall a heat flux may be defined to simulate heating or cooling.

The model for homogeneous chemical reactions, based on the Arrhenius law, allows the simulation of any number of simultaneously running reactions between the single components.

Drift models have to be chosen for each combination of dispersed and continuous phases. They are valid always for a dispersed phase within a continuous phase. That means for a rising gas bubble in a liquid another drift correlation may be used as for a falling liquid drop in the gas volume above. There several options for the

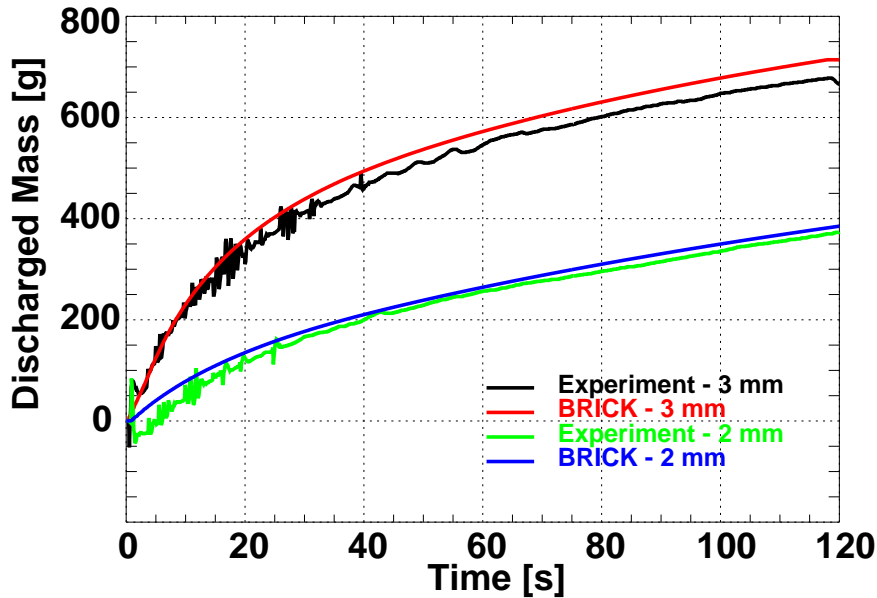


Fig. 5: Measured and calculated discharged mass for different diameters of the orifice. Vessel volume 1.96 litre.

lower boundary of the foam layer as a fictitious level. A special procedure makes the transient generation of foam possible. A foam model has to supply the drainage velocity of liquid within the foam structure. To test the interface up to now only simple equations have been used instead of a real foam model.

#### 4. Validation

The whole model as well as partial models were verified by many test cases including comparisons with analytical solutions for special cases. For the validation of the code numerous depressurization experiments with water/steam were analysed. Fig. 2 shows the experimental and calculated pressure curves for a blowdown experiment from a 175 l vessel. Fig. 3 shows the local void volume fraction at a position in the upper part of the vessel for the same experiment. The level swell causes a two-phase flow at this position for a period of about 15 seconds.

Theoretically predicted and experimentally confirmed oscillations of the discharge mass flow rate, which may occur at defined parameters [3,4], were also well calculated with the BRICK-model. Fig. 4 shows the corresponding oscillations of the average void volume fraction within the ventline. The experimental data were obtained by measuring the pressure drop over the ventline. The frequency of the oscillations as well as the sawtooth shape and the decrease of the frequency agree in experiment and calculation. The discharged mass from a small (1.9 l) vessel with 2 different diameters of the orifice is shown in Fig. 5.

#### References

- [1] M.W. Evans, F.H. Harlow (1957), The Particle-In-Cell Method for Hydrodynamic Calculations, LA-2139, Los Alamos

calculation of the properties of the continuous phase ( $\rho, \eta$ ) used by the drift correlation. They may be calculated as pure properties of the continuous phase, as mixed properties of all phases excluding the considered dispersed phase and as mixed properties for all phases. A flexible interface allows easily to add further drift correlations.

An interface is implemented, which enables to include a foam model. It introduces the

- [2] H.-M. Prasser, H. Steinkamp, U. Rohde (1995), Aufwallen und Austragen von zweiphasigen Gemischen. DECHEMA-Jahrestagung 95, Wiesbaden, 30.5.-1.6. 1995
- [3] D. Lucas, H.-M. Prasser (1996), Schwankungen des Massenstroms bei Druckentlastungsvorgängen, 3. Fachtagung Anlagen-, Arbeits- und Umweltsicherheit, Köthen, 7./8. November 1996, Preprints, pp. 233–240
- [4] D. Lucas, H.-M. Prasser (1997), Pulsationen bei der Druckentlastung von Reaktoren, AICHEM'A'97, Frankfurt am Main, 9.–14. Juni 1997

This work was supported by the Volkswagen-Stiftung.

# CHARACTERIZING THE KINETICS OF HETEROGENEOUS EXOTHERMIC REACTIONS

**Kathrin Biskup<sup>1</sup>, Heiko Bothe<sup>1</sup>, Günther Hessel, Günther Hulzer<sup>1</sup>, Holger Kryk, Wilfried Schmitt, Nurelegne Tefera**

## 1. Introduction

In the pharmaceutical and fine chemical industry the knowledge of thermo-kinetic reaction parameters is of practical interest to the process optimization for economic and environmental reasons as well as to the risk management of exothermic reactions with a high hazardous potential. Since the thermo-kinetic data are mainly determined at the laboratory scale, the scale-up problem plays a crucial role when the results have to be adapted to the production plant. For this purpose, reaction calorimeters are a well-suited tool because they allow to work under conditions of stirred industrial tank reactors. In recent years the performance of calorimetric methods has been proven for homogeneous reactions. The aim of this paper is to present a set of experiments which allow to characterize exothermic reactions in heterogeneous systems. Results are described for the catalytic hydrogenation of a nitro aromatic compound.

## 2. Fundamentals of the heterogeneous process

The kinetics of homogeneous exothermic reactions can be characterized by the reaction enthalpy and the thermo-kinetic parameters such as the rate of reaction, the activation energy and the order of reaction. Due to multiphase reactions in heterogeneous systems, the reaction kinetics is additionally affected by the phase equilibrium and the mass transfer. Therefore, the gas solubility and the mass transfer coefficients have to be determined if they significantly affect on the reaction rate. As an example for complex heterogeneous reactions, the process kinetics of the catalytic hydrogenation of a substituted nitrobenzoate (SNBE) to a substituted aminobenzoate (SABE) is described in the following.

The three-phase process (gas-liquid-solid) of the catalytic hydrogenation is not only influenced by the reaction kinetics, but also by the hydrodynamics and the mass transfer. During the hydrogenation reactions which are catalysed by solids, the reactants must be transferred to the reaction site. The chemisorption onto the catalyst surface could be a rate determining step. Depending on the process conditions and the effects of the mass transfer, two pathways for the reduction of nitro compounds to amines are possible (Fig. 1). The first path a) proceeds from the sequential reduction of nitro compounds to nitroso compounds, next to hydroxylamine, and finally, to amine. This path a) is favoured when the reduction of nitro compounds is conducted with metals and mineral acids. The second path b) is possible under process conditions that lead to an increase of concentration of the intermediates nitroso and hydroxylamine. Both intermediates can combine to the azoxy compound followed by reduction to the azo compound, hydrazo compound, and finally, to the amine (SABE). The kinetics of this pathway of the SABE formation is much slower. Due to the accumulation of intermediates, the

---

<sup>1</sup> Arzneimittelwerk Dresden GmbH (AWD)



The integration of the mass balance between gas and liquid phase gives the following equation:

$$\ln \left[ \frac{P_m - P_\infty}{P - P_\infty} \right] = k_L a \frac{P_m - P_0}{P_\infty - P_0} \cdot t \quad (2)$$

where P is the pressure at the time t.

Equation (2) shows that the value of the volumetric mass transfer coefficient  $k_L a$  as the product of the mass transfer coefficient and the specific boundary surface can be determined from the slope of the pressure drop (Fig. 2).

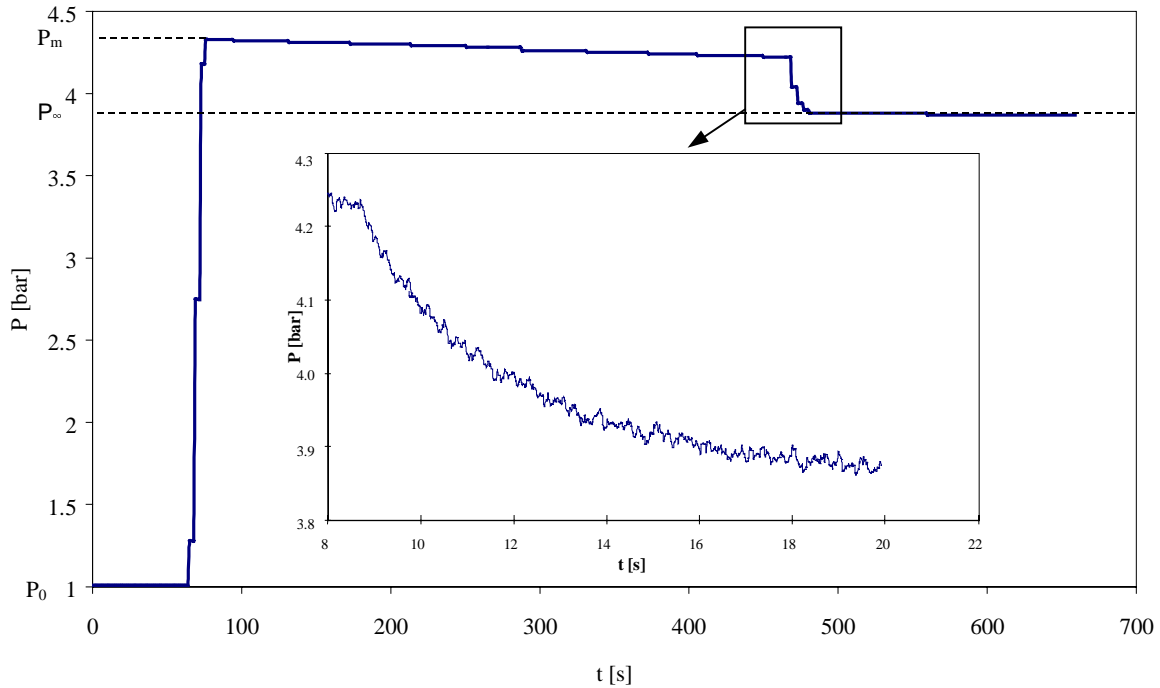


Fig. 2: Pressure profile during the batch absorption of  $H_2$

### 3.2 Reaction enthalpy and thermo-kinetic parameters

Since the heat release rate  $\dot{Q}_r$  of exothermic reactions is proportional to the rate of reaction  $r$ , to the volume of the reaction mixture  $V$ , and to the enthalpy ( $-\Delta H_r$ ), calorimetric methods can be used to determine the reaction enthalpy and the overall rate of reaction:

$$\dot{Q}_r = rV(-\Delta H_r) \quad (3)$$

According to Arrhenius' law, the rate of reaction  $r$  is an exponential function of temperature:

$$r = k_0 \exp(-E_a / RT) C_{A0}^n (1 - x)^n \quad (4)$$

where

$k_0$	pre-exponential factor (unit depends on reaction order)
$E_a$	activation energy [kJ/kmol]
$C_{A0}$	initial concentration of reactant [kmol/m <sup>3</sup> ]
$n$	reaction order.
$x$	conversion of reactant during the reaction
$r$	rate of reaction [kmol/(m <sup>3</sup> · s)]

To determine the activation energy and the pre-exponential factor, a set of isothermal experiments at different temperatures have to be carried out in the reaction calorimeter.

#### 4. Experimental equipment

The experiments were carried out in the METTLER high pressure reaction calorimeter RC1e/HP60 that was equipped with a high speed gassing-stirrer. To insure a good gas dispersion, the stirrer operated at 1000 rpm. This reaction calorimeter was mainly used to determine the reaction enthalpy with in situ high accuracy and to investigate the reaction kinetics. An FTIR spectrometer was applied to monitor the concentration profiles of reactants, products, and, if possible, of intermediates. The hydrogen uptake was monitored by gas flow measurements. The studies of mass transfer processes were carried out in the automatic laboratory reactor (ALR) that was additionally equipped with a fast-response pressure sensor.

#### 5. Results

##### 5.1 Gas solubility and mass transfer

According to equation (1), the H<sub>2</sub> solubility  $\alpha_{H_2}$  was determined from the pressure values  $P_m$ ,  $P_\infty$  and  $P_0$ . The solubility measurements in the reaction mixture, consisting of isopropanol and SNBE without the catalyst, provided a mean solubility coefficient  $\bar{\alpha}_{H_2}$  at 30 °C

$$\bar{\alpha}_{H_2, mix} = 4 \cdot 10^{-5} \frac{kmol}{m^3 kPa}$$

In isopropanol (tech), a little lower H<sub>2</sub> solubility at 30 °C was obtained

$$\bar{\alpha}_{H_2, isop} = 2,9 \cdot 10^{-5} \frac{kmol}{m^3 kPa}$$

As presented by the Arrhenius plot (Fig. 3) of the H<sub>2</sub> solubility in isopropanol (tech), there is an exponential dependence on the temperature of the liquid.

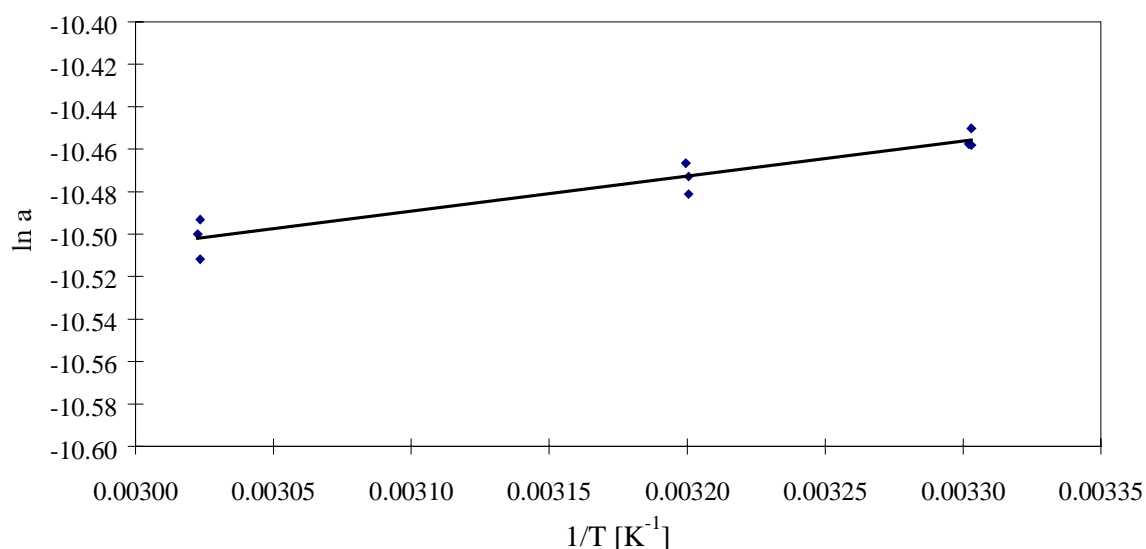


Fig. 3: Arrhenius plot of the H<sub>2</sub> solubility in isopropanol (tech.) using a gassing stirrer.

From the Arrhenius plot (Fig. 3), the following dependence of the H<sub>2</sub> solubility on the temperature was determined

$$\alpha_{H_2, isop}(T) = 1.67 \cdot 10^{-5} \exp\left(\frac{1373}{RT}\right) \frac{kmol}{m^3 kPa} \quad (5)$$

Obviously, the low content of water in technical isopropanol seems to be responsible for the opposite dependence on the temperature [2].

The results of the k<sub>L</sub>a-determination, represented in Tab. 2, show that the H<sub>2</sub> transfer to the liquid phase of the isopropanol depends on the stirrer speed and on the temperature of the liquid. For comparison, the mass transfer coefficients for a three-blade stirrer are also given. The gassing stirrer provides higher k<sub>L</sub>a-values because the H<sub>2</sub> gas is well-dispersed into the liquid volume in small bubbles as observed in a glass reactor.

Table 2: Experimental k<sub>L</sub>a-values for the H<sub>2</sub> transfer into isopropanol (tech.) at different temperatures and two stirrer speeds of the gassing stirrer.

T <sub>r</sub> [°C]	n [1/min]	k <sub>L</sub> a [1/s]
30	1000	0,26
40	1000	0,31
60	1000	0,57
30	600	0,021
60	600	0,036
30,0*	600	0,013
30,0*	1000	0,175

\* 3-blades impeller stirrer

## 5.2 Reaction enthalpy

The overall heat Q<sub>r</sub> of the reaction was determined from isothermal experiments in the RC1 reaction calorimeter. The molar reaction enthalpy ΔH<sub>r</sub> is defined by

$$\Delta H_r = \frac{Q_r}{n_{SNBE}} \quad (6)$$

where n<sub>SNBE</sub> is the amount of moles of SNBE. The experimental results for different reaction conditions and SNBE charges are listed in Tab. 3. Assuming a complete conversion of SNBE, an average value of the molar reaction enthalpy ΔH̄<sub>r</sub> can be calculated:

$$\Delta \bar{H}_r = -558 \text{ kJ/mol}_{SNBE}$$

This mean value is in good agreement with the known molar reaction enthalpy for nitrobenzene [3]:

$$\Delta H_r = -560 \text{ kJ/mol}$$

A significant dependence of the reaction enthalpy on the temperature was not found.

Table 3: Heat of reaction and molar reaction enthalpy for the hydrogenation of SNBE to SABE

Experiment	$T_r$ [°C]	$n_{\text{SNBE}}$ [mol]	$m_{\text{cat}}^c$ [g]	$Q_r$ [kJ]	$\Delta H_r$ [kJ/mol]
SNBE02** <sup>b</sup>	30	1,5	0,75	-879,6	-586
SNBE18** <sup>a</sup>	30	0,25	0,75	-129,7	-519
SNBE20 <sup>a</sup>	30	0,25	0,75	-136,0	-544
SNBE24**	60	0,25	0,75	-149,4	-597
SNBE25**	30	0,25	2,25	-135,6	-542
Average					-557,8

\* SNBE(new charge), \*\* SNBE(old charge)

<sup>a</sup> with after more than 15h hydrogenation, <sup>b</sup> concentrated SNBE, <sup>c</sup> catalyst 5% Pt in Carbon

### 5.3 Reaction rate

Experimental results show that the overall reaction rate  $r$  and therefore the heat release rate  $\dot{Q}_r$  is directly proportional to the amount of the added catalyst. This is illustrated in Fig. 4 for 0,54 and 1,08 wt% Pt.

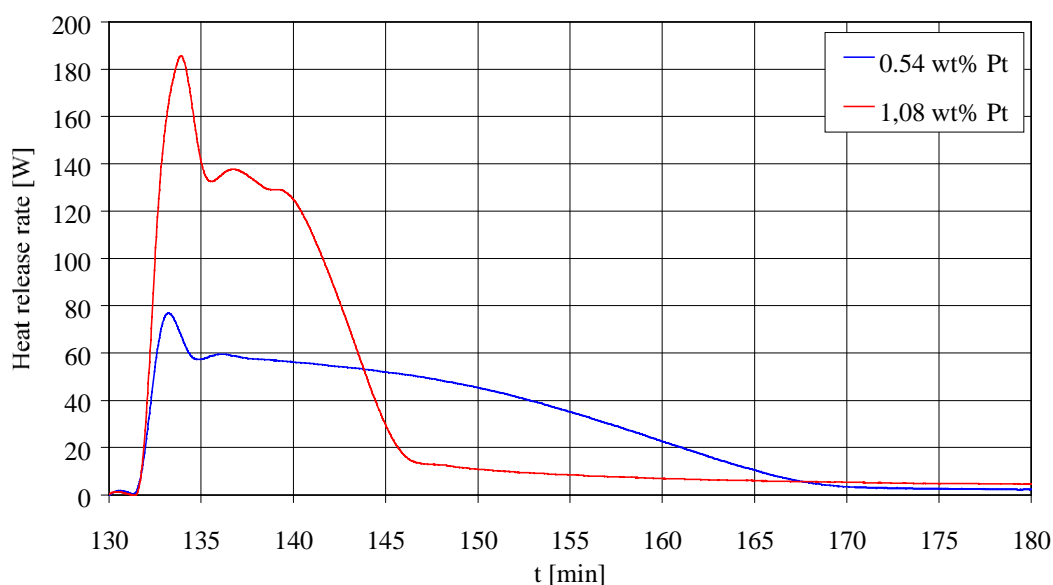


Fig. 4: Influence of the catalyst concentration on the heat release rate.

The influence of pH on the reaction rate was also studied. In the acidic solution (with HCl), the reaction rate is very slow, whereas in the basic solution (pH = 8) the reaction rate is very high. This result is in agreement with the investigation of Turek and Co-workers [4] for the hydrogenation of glucose.

Experimental investigation of another charge of SNBE (new charge) shows a higher reaction rate compared to the old charge at the same reaction conditions (see Fig. 5). FTIR spectroscopy of both SNBE charges gives the same result. There is only a slight difference in colour of the SNBE.

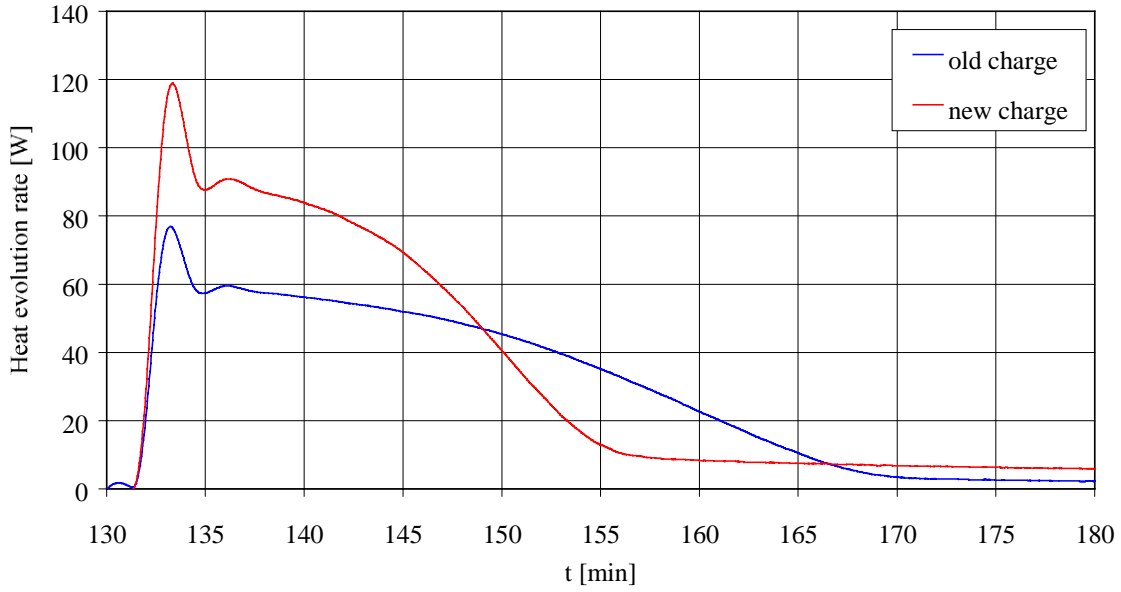


Fig. 5: Influence of the SNBE quality on the heat release rate.

It is advisable to investigate whether path a) or path b) is favoured under the above experimental conditions. In a basic solution of an alcohol, the rate of the reaction between nitroso and hydroxylamine, forming the azoxy compound, is much higher than the reduction step. If this is true, the rate of formation of amine through path b) seems to be the probable mechanism. According to the information of the industrial partner (AWD), the reason for the azoxy formation lies in the type of SNBE that was used.

## 5.4 Reaction kinetics

To investigate the kinetics of the hydrogenation of SNBE to SABE, the following process model is assumed. The solubility of  $H_2$  in the reaction mixture is modelled as follows



$$r_1 = k_1 P_{H_2} \quad \text{and} \quad r_2 = k_2 [H_2 (l)] \quad (8)$$

The equilibrium condition is given by

$$[H_2 (l)] = \frac{k_1}{k_2} P_{H_2} = \alpha_{H_2} P_{H_2} \quad (9)$$

Assuming that only Hydrogen is adsorbed onto the catalyst surface and that the adsorption/desorption of  $H_2(l)$  onto the catalyst is the rate determining step, the following mechanism can be formulated:

- Adsorption/desorption of hydrogen onto the catalyst (E)



$$r_3 = k_3 [H_2 (l)][E] \quad \text{and} \quad r_4 = k_4 [H_2 - E] \quad (11)$$

- Intermediate formation (hydroxylamine) and desorption of the hydroxylamine



$$r_5 = k_5 [R-NO_2][H_2-E], \quad \Delta H_{r,5} \quad (13)$$

- Product formation (amine): reaction between the adsorbed hydrogen and hydroxylamine from the liquid phase to amine and desorption



$$r_6 = k_6 [R-NHOH][H_2-E], \quad \Delta H_{r,6} \quad (15)$$

The above equations are used to fit the experimental data of the heat release rate  $\dot{Q}_r$  by means of the program RATE (BATCHCAD). To determine the model parameters, the molar reaction enthalpy should be known for each reaction step. In [3] the following molar reaction enthalpies were experimentally determined for the hydrogenation of nitrobenzene to aniline for path a):

$$\Delta H_{r,5} = -320 \text{ kJ/mol} \quad \text{and} \quad \Delta H_{r,6} = -225 \text{ kJ/mol}$$

Using these molar reaction enthalpies, the model parameters  $k_3$ ,  $k_4$ ,  $k_5$  and  $k_6$  were adjusted with isothermal experiments. Fig. 6 shows experimental data  $\dot{Q}_{\text{exp}}$  and model predictions  $\dot{Q}_{\text{model1}}$  for the best fit using these enthalpies. There is a big discrepancy between the predicted and experimental values of  $\dot{Q}_r$ .

Next, the molar reaction enthalpies  $\Delta H_{r,5}$  and  $\Delta H_{r,6}$  were assumed to be proportional to the hydrogen uptake for each step and were set to be 2/3 of the overall reaction enthalpy for the formation of hydroxylamine and 1/3 for the formation of amine, respectively. The overall molar reaction enthalpy is  $-560 \text{ kJ/mol}$  SNBE. Using these molar reaction enthalpies  $\Delta H_{r,5} = -373 \text{ kJ/mol}$  and  $\Delta H_{r,6} = -187 \text{ kJ/mol}$ , the isothermal model parameters were estimated. The results are also plotted in Fig. 6 ( $\dot{Q}_{\text{model2}}$ ). This model provides a better approximation of the experimental data. Therefore, in this study  $\Delta H_{r,5} = -373 \text{ kJ/mol}$  and  $\Delta H_{r,6} = -187 \text{ kJ/mol}$  were adopted.

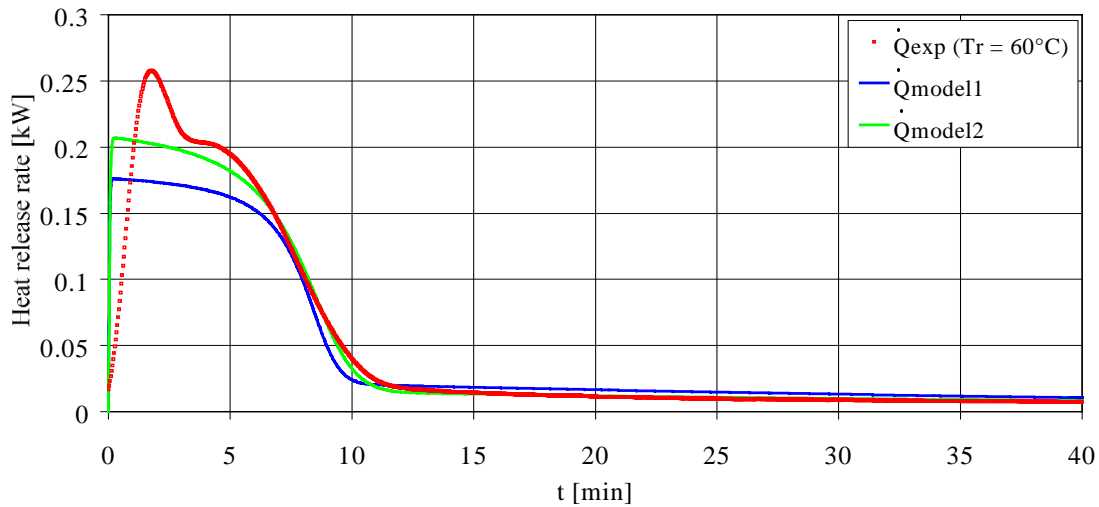


Fig. 6: Comparison between experimental data ( $\dot{Q}_{\text{exp}}$ ) and model ( $\dot{Q}_{\text{model1/2}}$ ) heat release rate.

Using the above molar enthalpies, the model parameters  $k_3$ ,  $k_4$ ,  $k_5$  and  $k_6$  were estimated for the isothermal hydrogenation of SNBE to SABE in the temperature range of 30°C to 60°C. The numerical values of the adjusted parameters are given in Table 4.

Table 4: Estimated parameters for the isothermal hydrogenation of SNBE to SABE

Parameter	30°C	40°C	50°C	60°C
$k_3$ [ $\text{m}^3 / (\text{kg} \cdot \text{s})$ ]	0,501343	0,741837	1,061190	1,279040
$k_4$ [1/s]	$4,47 \cdot 10^{-5}$	$4,47 \cdot 10^{-5}$	$4,47 \cdot 10^{-5}$	$4,47 \cdot 10^{-5}$
$k_5$ [ $\text{m}^3/(\text{kmol} \cdot \text{s})$ ]	0,101043	0,202933	0,311271	0,769326
$k_6$ [ $\text{m}^3/(\text{kmol} \cdot \text{s})$ ]	$5,4288 \cdot 10^{-4}$	$1,3739 \cdot 10^{-3}$	$3,8408 \cdot 10^{-3}$	$9,2715 \cdot 10^{-3}$

The parameters  $k_3$  and  $k_4$  are the adsorption and desorption rate constants for hydrogen onto the catalyst.  $k_4$  appears to be independent of the temperature and constant, where as  $k_3$ ,  $k_5$  and  $k_6$  increase with the reaction temperature. The Arrhenius plot is illustrated in Fig. 7.

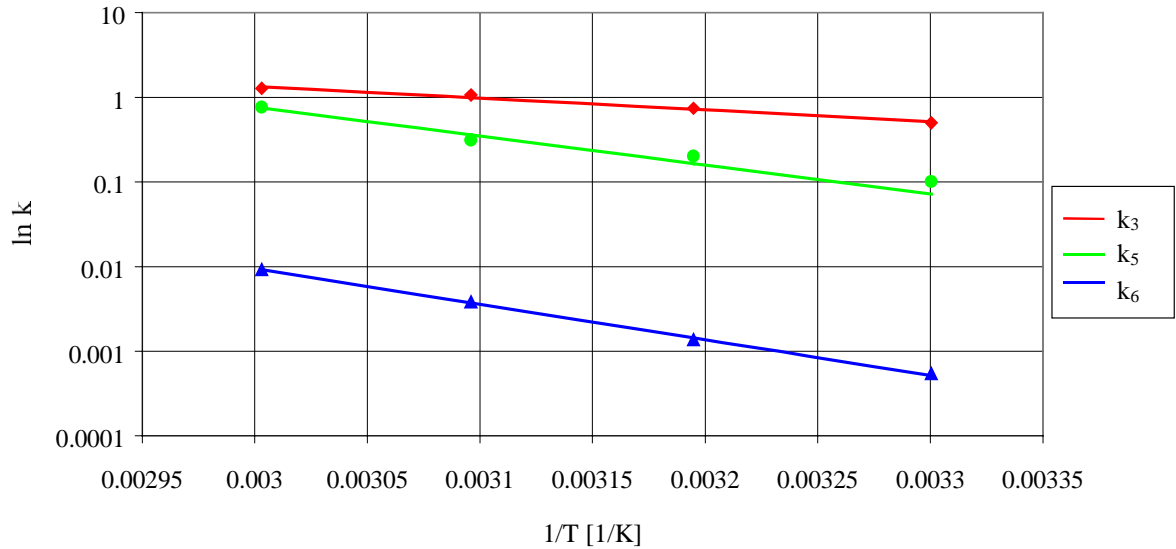


Fig. 7: Arrhenius plot of the reaction rate constants.

The following dependencies on the temperature were found:

$$k_3 = 2.058 \cdot 10^4 \exp\left(\frac{-26690}{RT}\right) \frac{\text{m}^3}{\text{kg} \cdot \text{s}} \quad k_4 = 4.47 \cdot 10^{-5} \text{ s}^{-1} \quad (16)$$

$$k_5 = 1.3708 \cdot 10^{10} \exp\left(\frac{-65430}{RT}\right) \frac{\text{m}^3}{\text{kmol} \cdot \text{s}} \quad k_6 = 3.6747 \cdot 10^{10} \exp\left(\frac{-80344}{RT}\right) \frac{\text{m}^3}{\text{kmol} \cdot \text{s}}$$

Figure 8 compares simulation and experimental results of the heat release rate at different temperatures. Now there is a good agreement between the model and experimental results. Qualitative analyses of the reaction product show that an intermediate product which seems to be the azoxy compound was produced. Therefore, the reaction mechanism given in path b)

(Fig. 1) should also be considered to model the hydrogenation of SNBE to SABE, especially if the overall reaction rate is low.

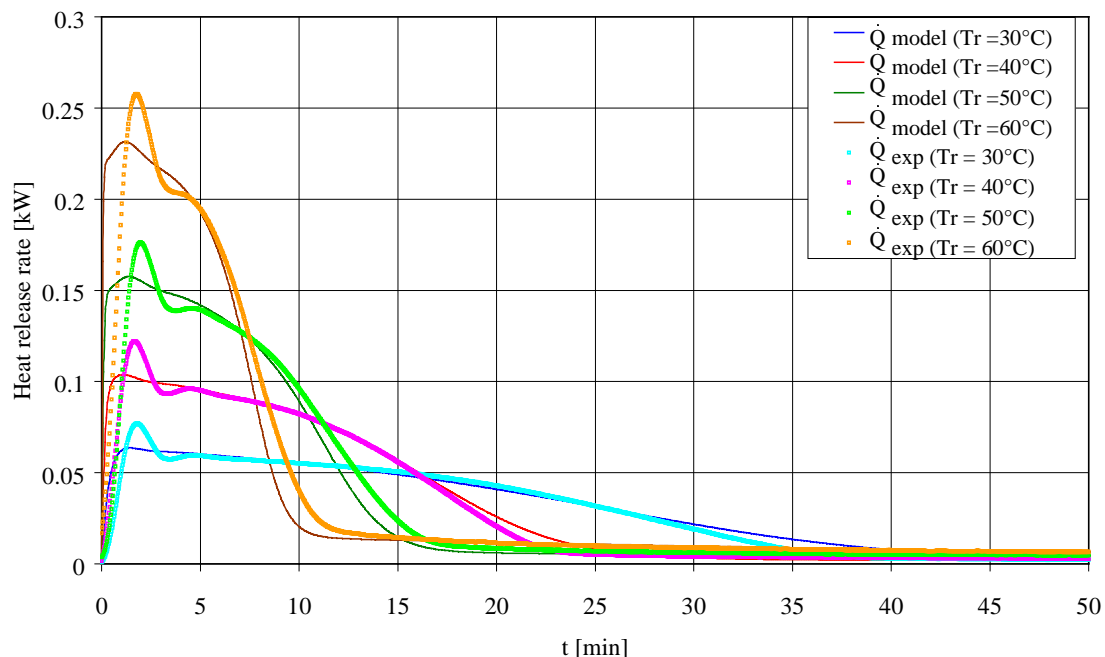


Fig. 8: Comparison of the heat release rate between simulation and experimental results.

## 6. Conclusions

The catalytic hydrogenation of SNBE to SABE is a complex exothermic process influenced by the competing effects of mass transfer and kinetics. In reaction calorimeters, several methods were applied to determine the parameters of kinetics and mass transfer under different process conditions. The reaction pathway is determined by the reactant quality and the process conditions. It was found that a bad quality of SNBE and disadvantageous process conditions can cause an accumulation of intermediates which probably deactivate the catalyst and lead to low process rates. Further work is necessary to investigate the gas solubility and mass transfer in the production plant as well as to simulate and to study the industrial conditions in the laboratory reactor.

## References

- [1] E. Dietrich, C. Mathieu, H. Delmas, J. Jenck, Raney-Nickel Catalyzed Hydrogenations: Gas-Liquid Mass Transfer in Gas-Induced Stirred Slurry Reactors, *Chemical Engineering Science*, 1992, Vol. 47, No. 13/14, 3597-3604
- [2] Landolt-Börnstein, 6. Aufl., Bd. II/2 b, pp 1-184
- [3] F. Stoessel, Experimental study of thermal hazards during the hydrogenation of aromatic nitro compounds, *J. Loss Prev. Process Inc.*, 1993, Vol. 6, No. 2, 79-85
- [4] Turek, Dissertation, Technische Hochschule Merseburg, 1980

# PLUME AND FINGER REGIMES DRIVEN BY AN EXOTHERMIC INTERFACIAL REACTION

Alexander Grahn and Kerstin Eckert<sup>1</sup>

## 1. Introduction

Studies of convection in fluids, like Rayleigh-Bénard- [1] or Bénard-Marangoni convection [2] have strongly influenced our understanding of pattern formation and turbulence. In these systems energy is supplied by an external temperature difference applied across a given vertical length scale. However, this situation is not representative for a variety of systems occurring in nature. Here, the dynamics is driven by internal sources of energy and the selected length scale is a part of the solution of the problem. The study of such systems is interesting from both a fundamental point of view and with respect to potential applications of basic research. Promising candidates for such studies are systems involving chemical reactions. Consumption of educts and the release of reaction enthalpy are sources of solutal and thermal gradients. Hydrodynamic instabilities, driven by these gradients, can drastically alter the chemical reaction rate [3]. We demonstrate that a rather simple interfacial neutralization reaction can develop an unexpected coupling of different hydrodynamic instabilities (for details we refer to [4]).

## 2. Experimental set-up and chemistry

The experiments were performed in a two-layer system, placed in a Hele-Shaw-cell (Fig. 1). The gap width was  $d = 0.1$  cm. Visualization of the patterns was done by means of a shadowgraph technique. The two-layer-system inside the cell consisted of a lower aqueous layer (water and base) and an upper organic layer (isobutyl-alcohol and carboxylic acid). The viscosity of the organic solvent is four times higher than that of water. Since water and isobutyl-alcohol have a certain solubility (12 % at  $T = 25$  °C) saturated solutions were prepared before filling. Saturation was to prevent interfacial turbulence arising from counterdiffusion of the solvents into each other. The respective densities are  $0.987$  g/cm<sup>3</sup> (upper layer) and  $1.016$  g/cm<sup>3</sup> (lower layer, including the base concentration). The density of both phases increases with increasing acid concentration. While the concentration of the base B in the water was fixed to  $c_B = 1$  mol/l, different concentrations  $c_{HA}$  of the acids have been used ( $c_{HA} = 0.04$  to  $0.08$  g/l or equivalently  $0.5$  to  $2$  mol/l).

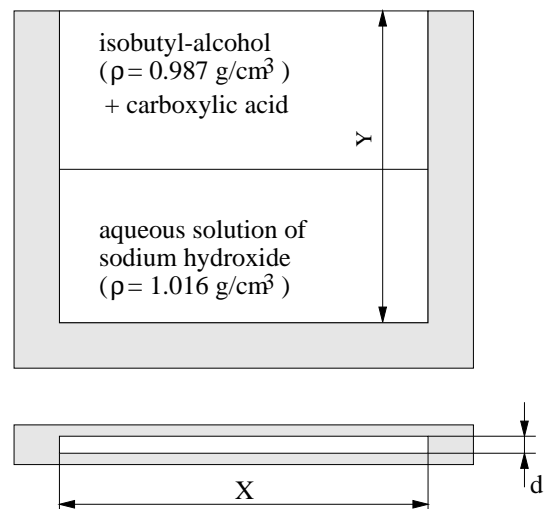
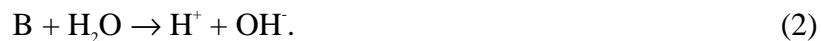


Fig. 1: The two-layer system in the Hele-Shaw cell. The given densities refer to the saturated phases.

<sup>1</sup> Institute for Thermofluid Dynamics, TU Dresden, Germany

The basic reaction is the neutralization of carboxylic acid by a base, sodium hydroxide, close to the interface. Precondition of this reaction is the dissociation of both species, i.e.,



sodium hydroxide as a strong base is completely dissociated, the dissociation degree of the weak organic acids is smaller than 1 %. If a hydronium ion  $\text{H}_3\text{O}^+$ , formed by dissociation, encounters a  $\text{OH}^-$  ion, neutralization takes place, i.e.,



The enthalpy released by this reaction amounts to -57 kJ/mol.

### 3. Observations

The system displays three basic regimes (Fig. 2). The initial one (Fig. 2a) is dominated by rising *plumes* in the upper organic layer. The plumes are emitted from an unstable boundary layer (b.l.) above the interface. We assume that they consist of warmer fluid with lower acid concentration. The intensity of the plume regime is most distinct in the formic-acid system and decreases with increasing chain length. The duration is of the order of minutes.

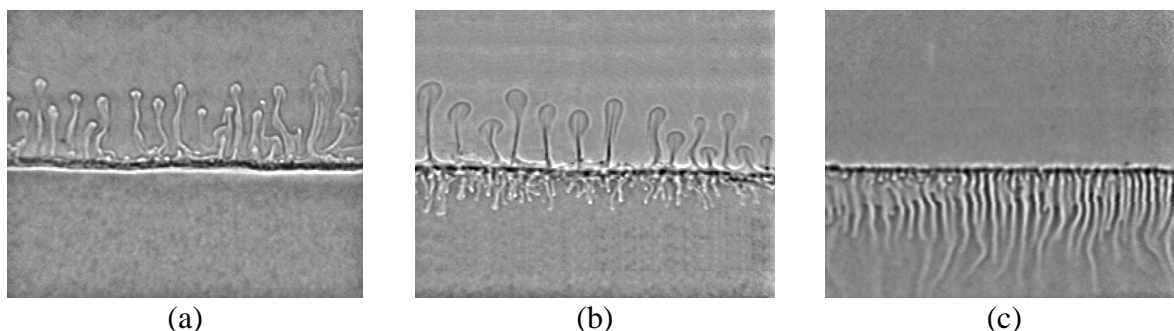


Fig. 2: The three basic regimes. (a) Rising plumes, (b) plumes and irregular fingers, (c): nearly regular fingers in the lower.

The intermediate regime (Fig. 2b) is characterized by plumes in the upper layer and by an irregular formation of fingers in the lower layer. The onset of the fingers starts the earlier the longer the acid chain length is. The duration of this second regime is of the order of 1 hour. In its course the upper layer plume regime becomes increasingly disorderd till it fades away.

In the final regime (Fig. 2c) the system displays an array of regularly spaced *fingers*. In the fingers warmer fluid, rich in acid/acetate ions, moves downwards. In between the fingers colder fluid, which should have a higher hydroxide concentration, moves in the opposite direction towards the interface. This is a double diffusive instability arising from the different diffusivities of heat and mass. Since heat diffuses 100 times faster than mass, the convective motion is driven by the horizontal concentration difference between the rising and falling fluid columns. Next we analyse the upper-layer motions by studying the advancing of the Plumes with time (Fig. 3). This is done by tracing the head positions of the plumes in the

digitized shadowgraph images and averaging over the plume ensemble. Usually approx. 10 plumes are taken into account. We find that the velocity of the upper layer plume ensemble decreases with increasing chain length of the carboxylic acid.

To determine the wavenumber as the characteristic horizontal length scale of the finger structure we apply the one-dimensional Fourier transformation to lines parallel to the interface. The corresponding power spectra are shown in Fig. 4. At equal molar concentrations all three systems display nearly the same wave numbers  $k$ . After 90 min we find  $k = (3.9 \pm 0.3) \text{ mm}^{-1}$ . We could not detect a significant dependence on the gap width (0.5, 1.0 and 2.0 mm).

#### 4. Discussion

The engine of the dynamics is the diffusion of acid from the upper into the lower layer. The acid diffusion leads to an unstable density stratification at both sides of the interface since heavier fluid lies above lighter fluid. Convection in the form of plumes, emitted from the concentration boundary layer, sets in (Fig. 1a). The neutralization reaction provides a local heating and an additional decrease of the density of regions close to the interface. Consequently, the effective Rayleigh number, governing the stability of the boundary layer of the upper phase, is higher. Solutal plumes move faster due to additional thermal buoyancy in the systems with reactive mass transfer.

However, the temperature gradient has a stabilizing effect on the boundary layer below the interface. The destabilizing concentration gradient is superimposed by the stabilizing temperature gradient. This configuration leads to double-diffusive instability which is known from thermohaline convection in oceans, responsible for the exchange of salt and heat between surface and deeper water layers. The nature manages both effects by switching to the finger instability to provide a very efficient mixing. Both plume and finger instability are responsible for the self-sustained dynamics observed in the experiment for more than 2 hours. We expect that numerous interfacial reactions are accompanied by the formation of fingers and plumes. Since both instabilities lead to an efficient mixing they can strongly accelerate diffusion-controlled interfacial reactions. Thus, the understanding of the hydrodynamics offers a possibility to control this reaction type.

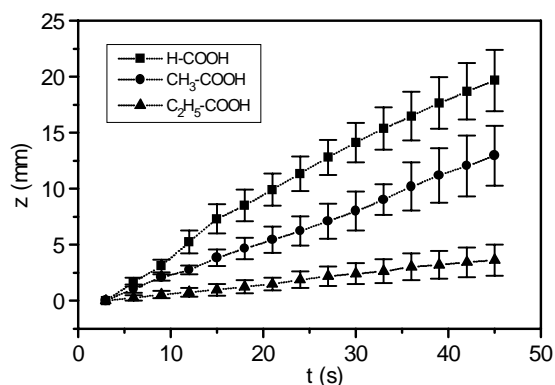


Fig. 3: Advancing of the plume ensemble with time for three diffusing acids.

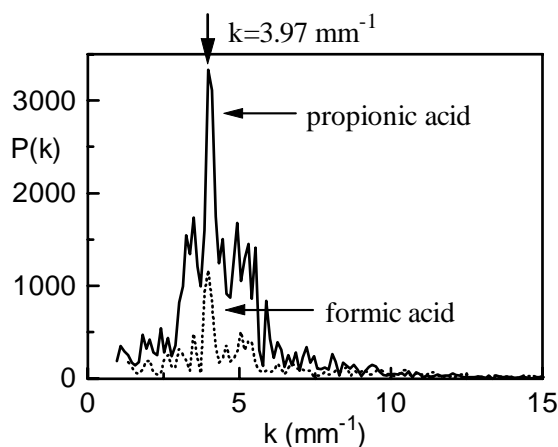


Fig. 4: One-dimensional power spectra of the fingers,  $C_{\text{HA}}=1 \text{ mol/l}$ . For the sake of clarity the acetic-acid system has been omitted.

## 5. References

- [1] M. C. Cross and P. C. Hohenberg (1993), Pattern formation outside equilibrium, *Rev. Mod. Phys.* 65, 851-1112
- [2] K. Eckert, M. Bestehorn and A. Thess (1998), Square cells in surface tension driven Bénard convection: experiment and theory, *J. Fluid Mech.* 356, 155-197
- [3] T. S. Sherwood and J. C. Wei (1957), Interfacial Phenomena in Liquid Extraction, *Ind. Eng. Chem.* 49, 1030-1034
- [4] K. Eckert and A. Grahn (1999), Plume and Finger Regimes Driven by an Exothermic Interfacial Reaction, *Phys. Rev. Lett.* 82, 4436-4439

# FINITE ELEMENT BASED VIBRATION MODELING OF VVER-1000 TYPE REACTORS

Matthias Werner, Eberhard Altstadt, Sergey Perov <sup>1</sup>

## 1. Introduction

The aim of this work is to contribute to the improved evaluation of the mechanical integrity of VVER type reactors. The contribution to a sensitive early failure detection and to the localization of mechanical damages of reactor components by means of vibration monitoring is especially important. For that purpose the finite element model for the simulation of mechanical vibrations of all primary circuit components of a VVER-1000 was established.

With an adjusted calculation model it is possible to clarify how hypothetical damages of reactor internals influence the vibration signature of the primary circuit. For a better recognition and analysis of damages at VVER-1000 reactors it is intended to integrate the simulation results in a catalogue of spectral signatures. Such kind of damage simulation is an appropriate means to find sensitive measuring positions for on-line monitoring and to define physically based threshold values for frequency shifts and amplitude changes. With that a contribution to the increase of the systems safety will be provided. According to the state of the art such models are based on the finite elemente (FE) method [1]. The modeling in our case is based on the finite elemente code ANSYS®.

## 2. FE-modelling of the primary curcuit

### 2.1. Creation of a global vibrational model

The global model of the VVER-1000 can be divided into two parts. The first is the model of the reactor pressure vessel (RPV) including its internals and the upper structures, the second part of the model consists of the 4 identical coolant loops. The internals of the RPV which are considered in the model are

- core barrel (CB) and thermal shield (TS)
- core with the fuel assemblies
- upper core structure with control element guide tubes.

Also the reactor components outside the vessel are modeled:

- upper block (UB)
- and the structure of the control element standpipes (CES) above the RPV-head.

The following elements are used for the idealization of the reactor structure: pipe elements PIPE16, beam elements BEAM4, mass elements MASS21 and stiffness matrices MATRIX27.

---

<sup>1)</sup> Baumann Moscow State Technical University, Moscow

The connection and the support of the components are realized by constraints (fixed coupling) and by stiffness matrices (elastic coupling). These stiffness matrices were determined by separate calculations with higher dimensional FE-models (chpt. 2.2.). Figure 1 shows the topology of the global reactor model.

The second part of the global model represents the coolant loops. Each loop of the VVER-1000 consists of the steam generator (SG), main coolant pump (MCP), hot leg (HL), cold leg (CL) and a U-shaped leg (UL). These components are idealized mainly by straight and elbow pipe elements (PIPE16, PIPE18). The topology of this part is shown in figure. 2.

The coolant in the RPV and also in the loops is considered as frozen liquid. To build the whole model of the primary circuit both parts must be connected (that means 4 identical loop models have to be connected to the nodes 7 and 10 of RPV-model).

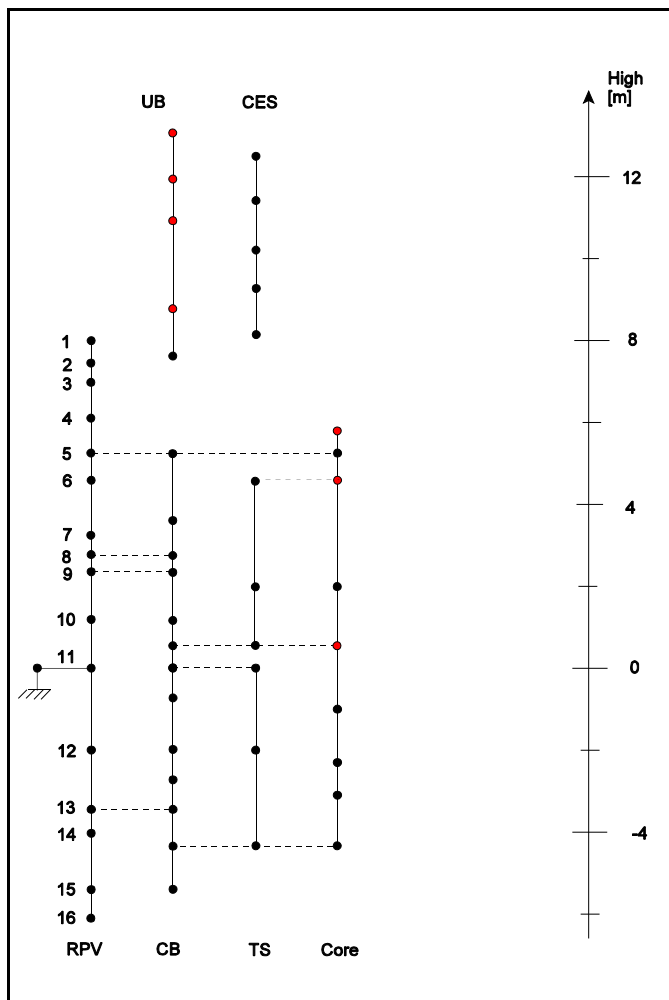


Fig. 1: Topology of the global model of the VVER-1000 reactor

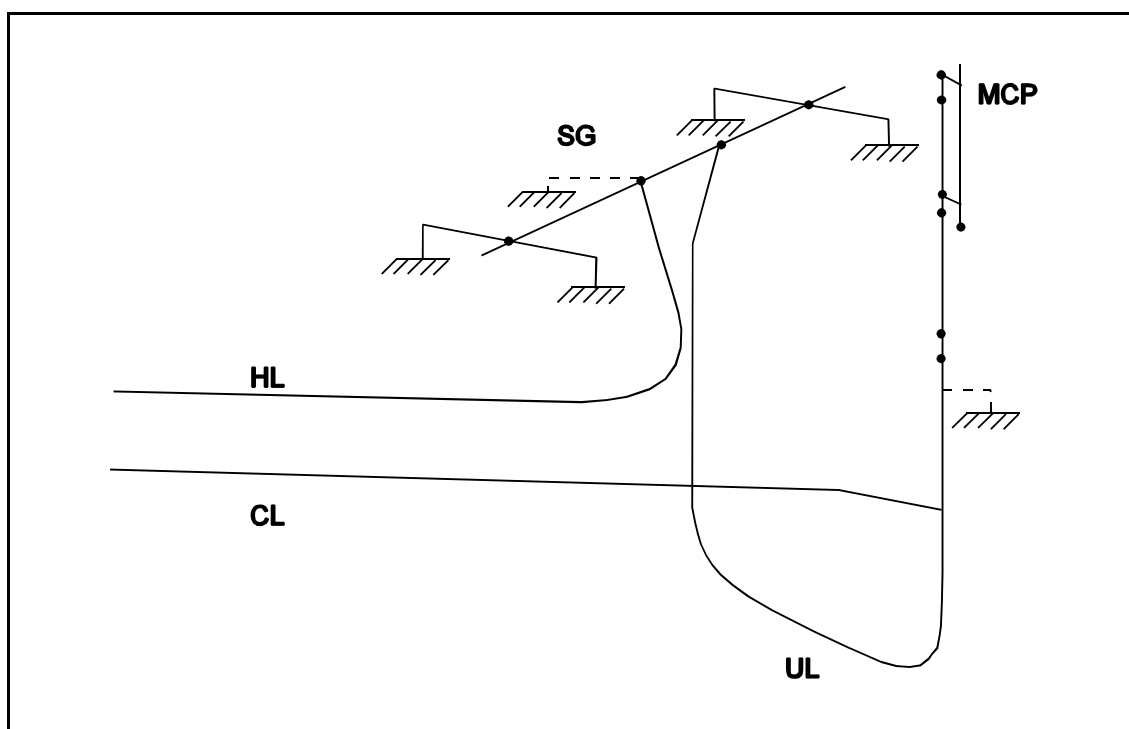


Fig. 2: Topology of the coolant loop FE-model

## 2.2. Separate calculations with local models

The main object of this part is to develop detailed models of single components of the VVER-1000 reactor. More complicated components that cannot be idealized by beam or pipe elements have to be modeled by higher dimensional FE (shell elements SHELL63, 3-D elements SOLID73). These local models are necessary to

- identify the shell mode vibration of RPV, CB and TS,
- determine the stiffness of bearing and clamping elements,
- evaluate the quality of parts of the global model.

This approach makes it possible both to analyse the separate units in all details and to build a global model of the VVER-1000 primary circuit as a whole. The results of such calculations are used for the initial determination of certain parameters of the global FE-model (especially the parameters of the stiffness matrices). The local models of core barrel guide lugs, the reactor pressure vessel, the fuel assemblies, the RPV supporting ring, the upper block (exemplarily seen in figure 3), the main coolant pump supporting structure and the steamline (secondary circuit) are used for such separate calculations.

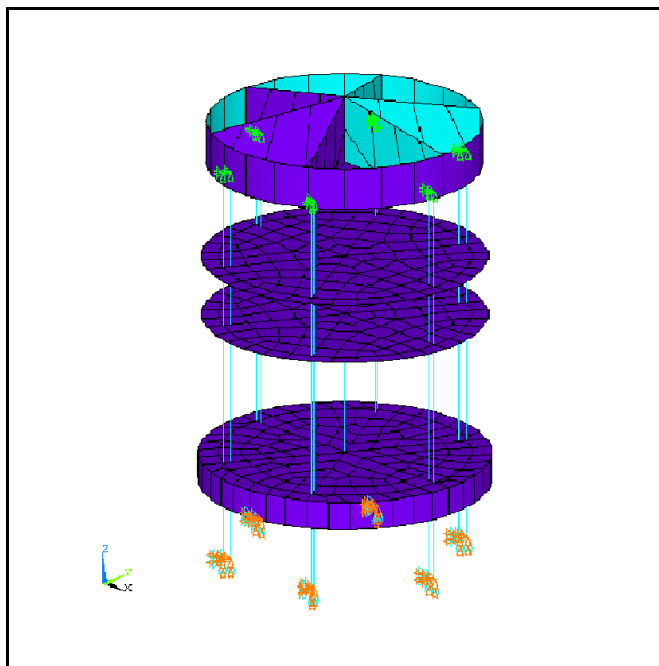


Fig. 3: The local model of the upper block

Table 1: Eigenfrequencies and mode shapes of the global vibrational model of the reactor pressure vessel and its internals, nonadjusted

Mode-No.	Frequency [Hz]	Vibration mode
R1	2.3	Bending of core (1st shape)
R2	3.9	Bending of UB (1st shape) + RPV (in phase)
R3	5.9	RPV (pendular) + UB (in antiphase)
R4	9.3	Bending of core (2nd shape)
R5	20.6	Bending of UB (2nd shape)
R6	21.5	Bending of core (3rd shape) + UB (2nd shape)
R7	25.3	Bending of UB (3rd shape)
R8	32.2	Axial CB, core
R9	34.4	Bending CPS (1st shape)

### 3. Modal analysis with the global FE-model

In the first step the modal analysis for both model parts was carried out separately. Table 1 contains the eigenfrequencies and mode shapes of the nonadjusted global FE-model of the reactor part up to 35 Hz. The model does not take into account the fluid-structure interaction. All eigenfrequencies associated with relative displacements between RPV and CB will be shifted down after the integration of fluid-structure elements. The model of the core is tuned on the first mode only. Figure 4. shows the vibration mode R3 at 5.9 Hz as an example.

The results of the modal analysis for a single loop model is shown in table 2 and for one selected mode in figure 5. The model for the whole VVER-1000 primary circuit includes the RPV with internals and upper structure and 4 identical loops. The modal analysis of the coupled systems reveals the following effects:

- Most of the modes does not change after coupling the models. Especially the modes of the internals and upper structure are undependend from the coupling.
- Because of the 4 identical sub-models (4 loops) multiple eigenfrequencies are obtained (eigenfrequencies identical or close together). The corresponding modes differ only by the phase relations between the loops.
- The pendular mode R3 of the RPV has two different eigenfrequencies in x- and y-direction (5.2 Hz and 5.7 Hz) because the loop arrangement is not axi-symmetric.
- Some few new modes originate from the coupling of hot and cold legs with the RPV, for example 8.5 Hz and 10.5 Hz. These modes are associated with bending modes on CL and HL interacting with the pendular motion of RPV in x- and y-direction.
- New modes emerge at 32.1 Hz because of a rotational motion of the whole loop arrangement around the z-axis of the RPV.

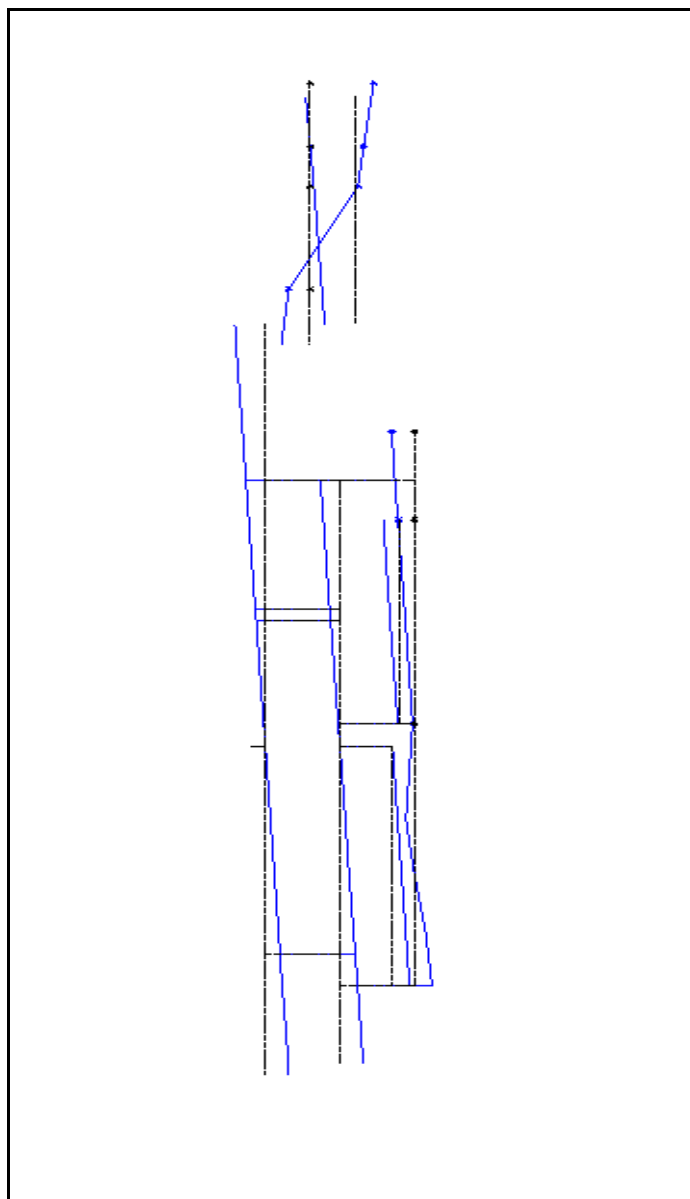


Fig. 4: Mode R3 of the reactor vibration model

Table 2: Eigenfrequencies and mode shapes of the global vibrational model for a separate coolant loop

Mode-No.	Frequency [Hz]	Vibration mode
S1	0.74	Rotation SG around z-axis, movement of UL, MCP
S2	1.75	Rotation SG around z-axis
S3	2.5	Rotation SG around z-axis, movement of UL, MCP
S4	7.4	Horizontal movement of SG, pendular movement of MCP
S5	8.0	Pendular movement of MCP, movement of UL, CL
S6	11.2	Pendular movement of MCP
S7	12.7	Pendular movement of MCP, bending of CL
S8	17.2	Movement of UL
S9	26.1	Bending of CL
S10	27.8	Bending of CL, pendular movement of MCP, bending of MCP shaft
S11	33.2	Bending of MCP shaft, y-direction
S12	33.7	Bending of MCP shaft, x-direction
S13	34.5	Bending of CL, vertical movement of MCP, bending of MCP shaft

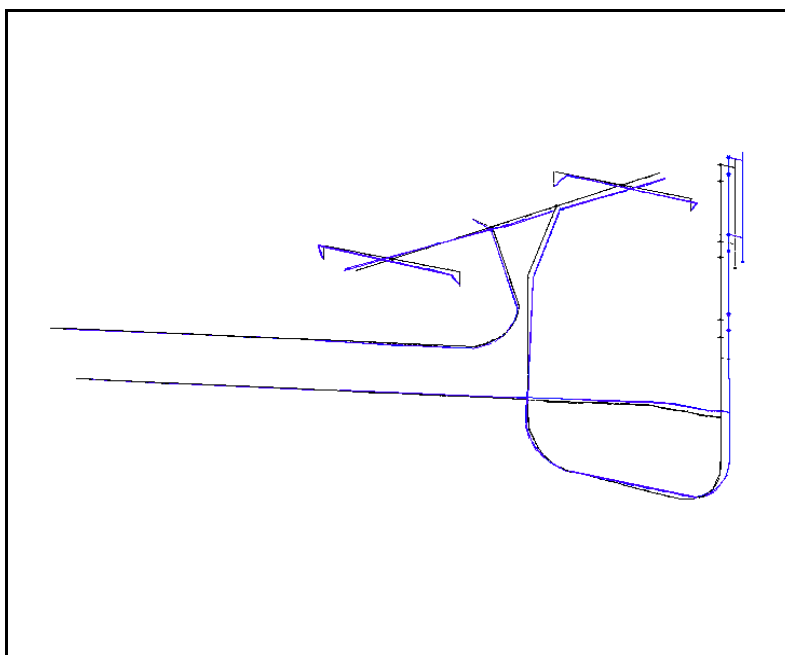


Fig. 5: Mode S3 of the loop vibration model

#### 4. Outlook

For the accomplishment of the global model it is necessary to consider the interaction between the coolant flowing in the downcomer and the vibrating components by fluid-structure elements.

After this the next step has to be the adjustment of the calculation model using data from vibrational measurements. The modelling of exciting forces is another important task,

which affects the vibrational behaviour of the system. For example, such forces arise from pressure fluctuations caused by coolant turbulencies (downcomer) or they are caused by acoustic standing waves. Even the exciting forces from unbalancies of the main coolant pump must be considered.

## References

- [1] E. Altstadt, G. Grunwald, M. Scheffler, F.-P. Weiß (1996), Analytische Modellierung mechanischer Schwingungen von Primärkreislaufkomponenten des Druckwasserreaktors WWER-440 mit finiten Elementen, Abschlußbericht zum BMBF-Förderprojekt Nr. 1500916, Rossendorf, Report FZR-172

# FINITE ELEMENT ANALYSIS OF A BWR FEED WATER DISTRIBUTOR UNDER EXTREME TRANSIENT PRESSURE LOAD

Eberhard Altstadt, Hermann Ohlmeyer<sup>1</sup>, Frank Otremba<sup>1</sup>, Frank-Peter Weiss

## 1. Introduction

The break of a feed water line outside of the containment is a hypothetical accident scenario for German boiling water reactors (BWR). Fig. 1 shows a simplified scheme of this scenario. It is assumed that the pressure in the feed water system drops to ambient pressure within a few milliseconds. The feed water distributor (FWD) consists of four hydraulically separated ring lines supported at the feed water nozzles of the RPV. The cross section of the FWD ring lines is rectangular (inner height 210 mm, inner width 155 mm, wall thickness 10 mm). Figure 2 shows a 3D-view of the FWD in the region of RPV inlet nozzle. The feed water is normally sprayed into the reactor pressure vessel (RPV) through a number of small nozzles with a rather high flow resistance, located at the top wall of the FWD. Therefore in the case of a feed water line break the pressure within the RPV drops not as fast as the pressure of the feed water system. Thus for a short time the FWD is exposed to high difference pressure between its outer and its inner surface. The maximum pressure peak is 62 bar. The linear stress analysis shows that the ring line is one of the locations where large deflection and large strain is to be expected (Fig. 3). Within this paper the non-linear behaviour of the FWD ring line is investigated.

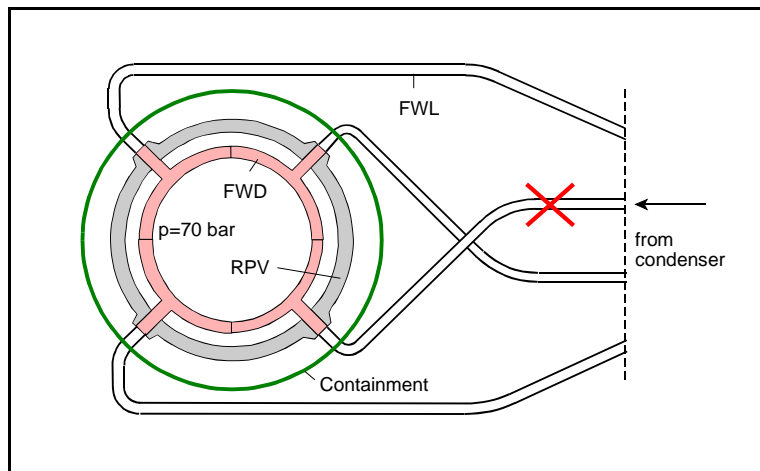


Fig. 1: Scheme of reactor pressure vessel, feed water distributor (horizontal section) and feed water lines

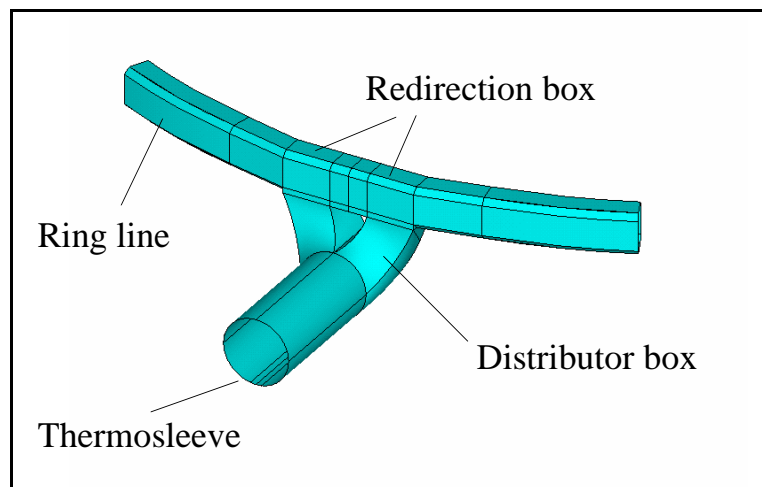


Fig. 2: Feed water distributor (region of RPV nozzle)

<sup>1</sup> Hamburgische Elektrizitätswerke AG

**2. Mechanical phenomena and solution method**

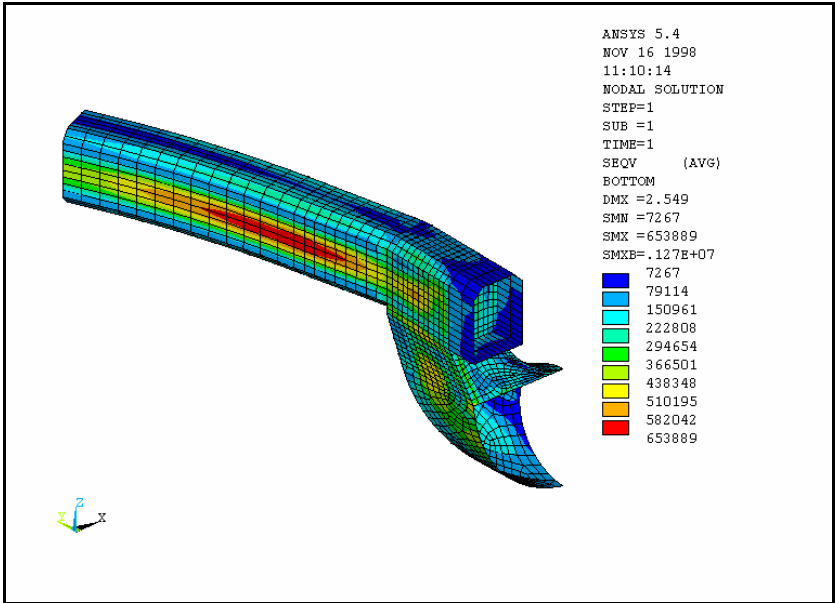


Fig. 3: Equivalent stress (kPa) in the FWD at maximum pressure load. Linear analysis.

Figure 3 shows the distribution of the equivalent stress at maximum pressure calculated with a linear shell model. Due to the high pressure load the elasticity limit of the FWD (austenitic steel) is clearly exceeded. Hence the mechanical stress analysis must consider the on non-linear material behaviour. An elastic-plastic material law with an isotropic hardening rule is adopted (section 3).

Furthermore the problem is geometrically non-linear because large strain and large deflection have to be expected. Due to the fact that the load is imposed by external pressure the deflection process is connected with instabilities (buckling). The buckling process of the FWD ring pipe is illustrated in Figure 4. The height of the cross section of the ring line is larger than the width, so the vertical walls are bended to the inside and the horizontal walls to the outside. The pressure upon the horizontal walls leads to additional negative membrane stress in the vertical walls and thus causes a stress weakening. As a consequence, the ring line tends to buckling. This process is unstable until the opposite horizontal walls get in contact. This phenomenology can be characterized by the load-displacement curve shown in Fig. 5 (p is the external pressure and u the deflection of the vertical wall).

Furthermore the problem is geometrically non-linear

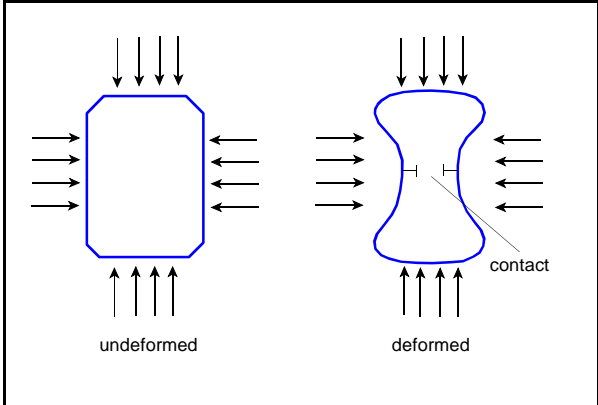


Fig. 4: Buckling of the FWD ring line

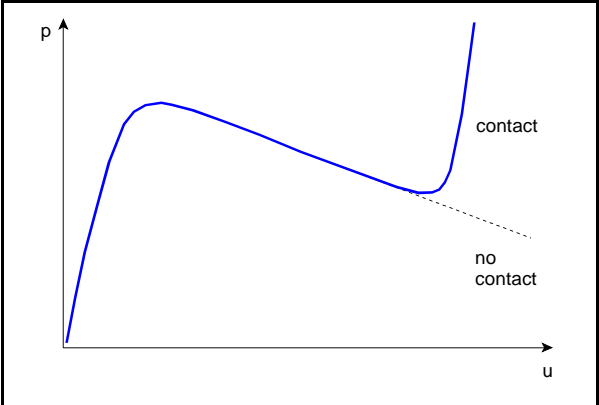


Fig. 5: Load-deflection curve for buckling

Due to these instabilities special mathematical tools are required to get a converging solution. Like for all non-linear problems the load must be applied in small steps even in a static analysis. Equilibrium iterations are performed at every load step to solve the equations. For stable load-

deflection behaviour the classical Newton-Raphson procedure is an adequate algorithm (Zienkiewicz,1977):

$$\underline{\phi} = \underline{K}(\underline{u}) \cdot \underline{u} - \underline{f}_a = \underline{0} \quad (1)$$

$$\underline{f}_r^{(i)} = \underline{K}^{(i)}(\underline{u}^{(i)}) \cdot \underline{u}^{(i)} - \underline{f}_a \quad (2)$$

$$\underline{f}_r(\underline{u}^{(i)} + \Delta \underline{u}^{(i)}) = \left[ \frac{\partial \underline{\phi}}{\partial \underline{u}} \right]_i \Delta \underline{u}^{(i)} + \underline{f}_r(\underline{u}^{(i)}) = \underline{0} \quad (3)$$

$$\Delta \underline{u}^{(i)} = \left[ \underline{K}_T^{(i)} \right]^{-1} \underline{f}_r^{(i)} \quad (4)$$

$$\underline{u}^{(i+1)} = \underline{u}^{(i)} + \Delta \underline{u}^{(i)} \quad (5)$$

$$\underline{f}_r^{(i+1)} = \underline{K}^{(i+1)} \underline{u}^{(i+1)} - \underline{f}_a \quad (6)$$

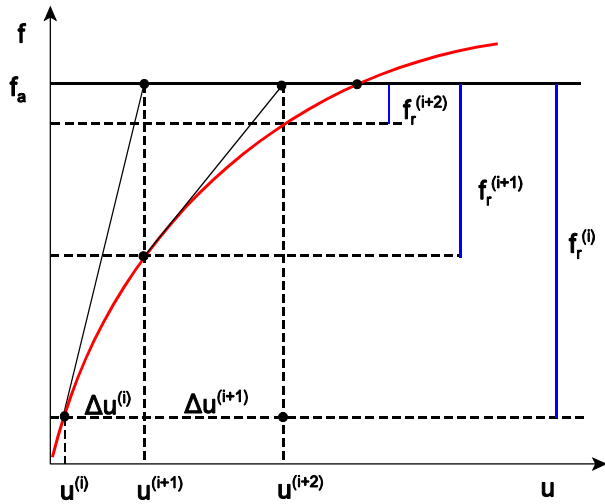


Fig. 6: Newton-Raphson procedure

The Newton-Raphson procedure (equations 1-6) iterates the equilibrium at each load step.  $\underline{K}$  is the stiffness matrix of the FE-model,  $\underline{K}_T$  the tangent stiffness matrix,  $\underline{u}$  the vector of the nodal degrees of freedom (deflection),  $\underline{f}_a$  is the vector of the applied loads at the current load step and  $i$  the iteration index. Figure 6 shows a simplified scheme of that procedure for a one degree of freedom model. The solution is converged if the vector of residual forces  $\underline{f}_r$  is sufficiently small (equilibrium between applied loads and internal forces).

However, if the load-deflection curve exhibits instability points (negative slope) the classical Newton-Raphson algorithm does not

work. This is illustrated in Fig. 7. A numerical algorithm to solve problems with instabilities is the arc-length method (Kolar and Kamel, 1986). The basic idea of this method is to control the gradual application of the load by a relative load factor  $\lambda$  in such a way that the distance between two iterations points in the load-deflection space is limited by an arc length radius. Thus the load can be increased and decreased during the progress of the equilibrium iterations. Figure 8 illustrates this strategy. The second equation of the classical Newton-Raphson procedure (eq. 2) is modified as follows:

$$\underline{f}_r^{(i)} = \underline{K}^{(i)}(\underline{u}^{(i)}) \cdot \underline{u}^{(i)} - \lambda \underline{f}_a \quad (7)$$

The load factor  $\lambda$  is determined from the additional condition:

$$l_i^2 = \Delta \lambda_i^2 + \beta^2 (\Delta \underline{u}_n^i)^T (\Delta \underline{u}_n^i) \quad (8)$$

where  $l_i$  is the arc-length radius and  $\beta$  a scaling factor to consider the different units of load and deflection,  $n$  is the load step index and  $i$  the iteration index.

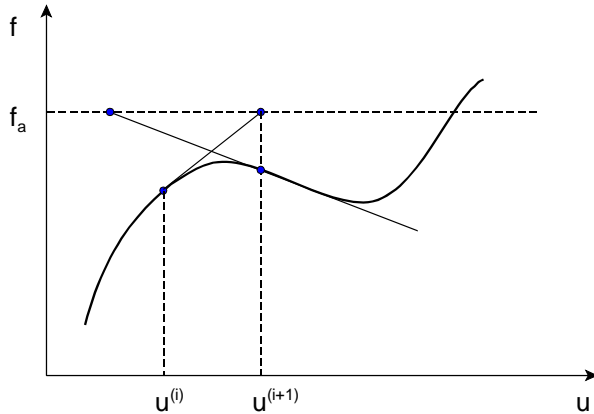


Fig. 7: Divergence of the classical Newton-Raphson procedure at instability points

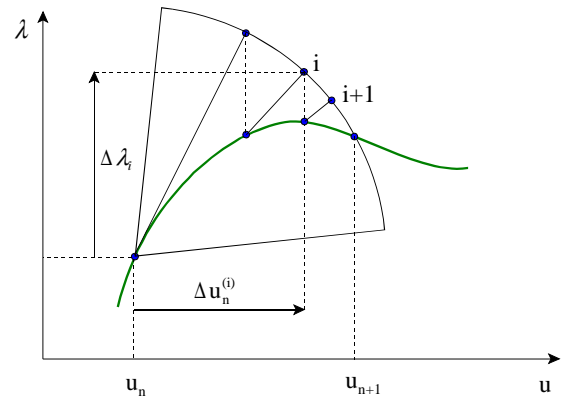


Fig. 8: Arc-length procedure

The arc-length method is only applicable to static analyses. If the load is time dependent in such a way that the dynamic forces of the structure cannot be neglected, a non-linear transient analysis is to be performed. In this case the inertia and damping forces have to be included into the equilibrium iterations of the classical Newton-Raphson procedure. The residual force vector then reads:

$$\underline{f}_{r,n}^{(i)} = \underline{M} \ddot{\underline{u}}_n + \underline{B} \dot{\underline{u}}_n + \underline{K}^{(i)}(\underline{u}_n^{(i)}) \cdot \underline{u}_n^{(i)} - \underline{f}_{a,n} \quad (9)$$

with  $\underline{M}$  being the mass matrix,  $\underline{B}$  the damping matrix and  $n$  the time index. Equilibrium iterations are performed for each time step of the analysis. For the time integration the Newmark method is adopted (Bathe, 1982).

### 3. Finite element model and loading

#### 3.1 Elements

The FWD is modelled using the FE code ANSYS<sup>®</sup>. Various models are available. The first analyses were done using a shell model of the complete 90° segment of the FWD (curvator, redirection box and ring line, Fig. 1). This model is only useful for linear static and dynamic calculations. In the non-linear large strain analyses no convergent solutions could be obtained. Therefore the model was separated into one model for the curvator and one model for the ring line. For the ring line a shell model and a volume model can be used. The volume model was used because of the missing convergence with shell elements (see section 4). All element types have plasticity, large strain, large deflection and stress stiffening capabilities. To cope with the dependence of the stiffness of the structure on the deflection an updated Lagrangian formulation is used (Mattiasson, et. al. 1986). Contact elements are used to model the touching of the two opposite vertical walls of the ring line.



where  $p(\bar{x})$  is the distribution of the pressure according to Fig. 9 and  $\lambda(t)$  a relative load factor which corresponds to the pressure curve of Fig. 10 between  $t = 0.04$  s and  $t = 0.056$  s.

#### 4. Results

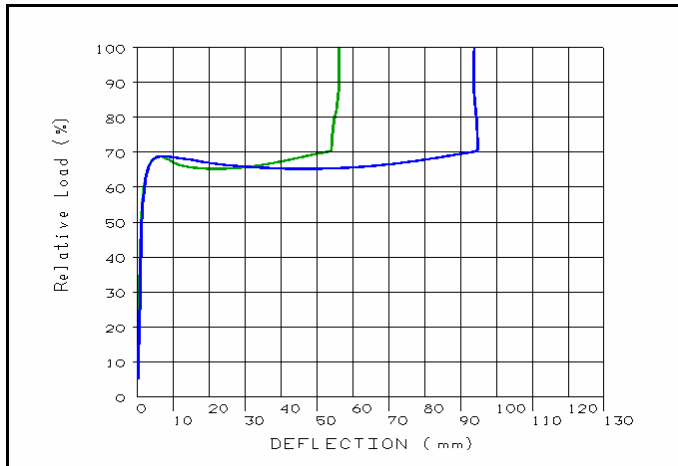


Fig. 11: Static analysis of the ring line. Load deflection curve for nodes at the inner wall (green) and the outer wall (blue) at azimuthal position  $15^\circ$ .

at the same axial and azimuthal position. Up to about 50% load the curves are linear with a rather steep slope. This is the range of elastic deformation (high stiffness). If the relative load factor gets higher than 50% the plastic deformation starts to develop. The point of instability is around 68% of load. The instability is a result of the stress weakening of the vertical walls (Fig. 4). At about 50 mm deflection of the outer node (blue curve Fig. 11) and 20 mm deflection of the inner node (green) the structure

As stated in section 3.1 the non-linear mechanical analysis for the FWD has to be carried out with separate models for the curvator and for the ring line, because a convergent solution could not be obtained with the shell model for the complete structure. For the ring line the best results were achieved with volume elements. First the static analysis is discussed. Figure 11 shows two load deflection curves. The relative load factor (eq. 12) is drawn vs. two nodal displacements. The green curve is for the node at the inner vertical wall of the FWD ring line, half height at an azimuthal position  $15^\circ$  from the nozzle. The blue curve is for the node displacement of the outer vertical wall

becomes stable again. This is a consequence of the hardening of the material (increasing yield stress due to plastic strain). At about 95 mm deflection of the outer node and 54 mm of the inner node the first contact between the opposite wall takes place. This leads to a high stiffness of the structure again (extremely steep slope). The slope of the blue curve is even higher than  $90^\circ$ , because of the increasing contact region between the walls.

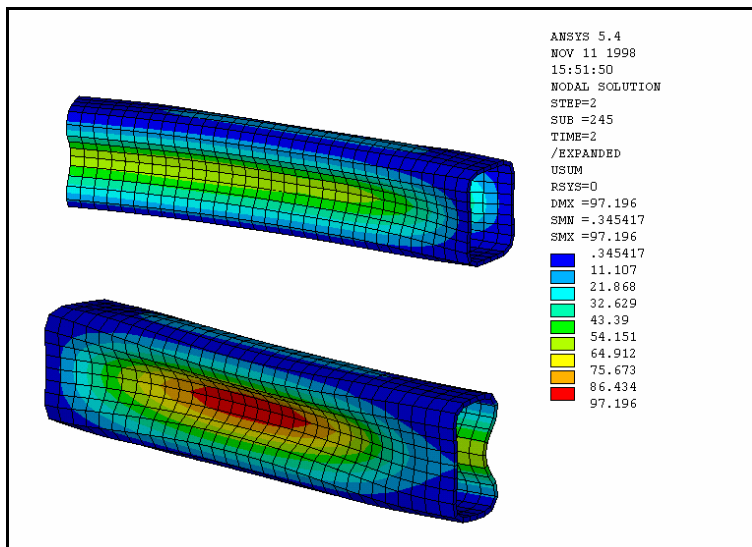


Fig. 12: Deflection (mm) of the ring line at 100% load. Static calculation, volume model. View to the inner wall (upper figure) and to the outer wall (lower figure).

Fig. 12 shows the deflection of the structure at 100% load and Figure 13 the plastic equivalent

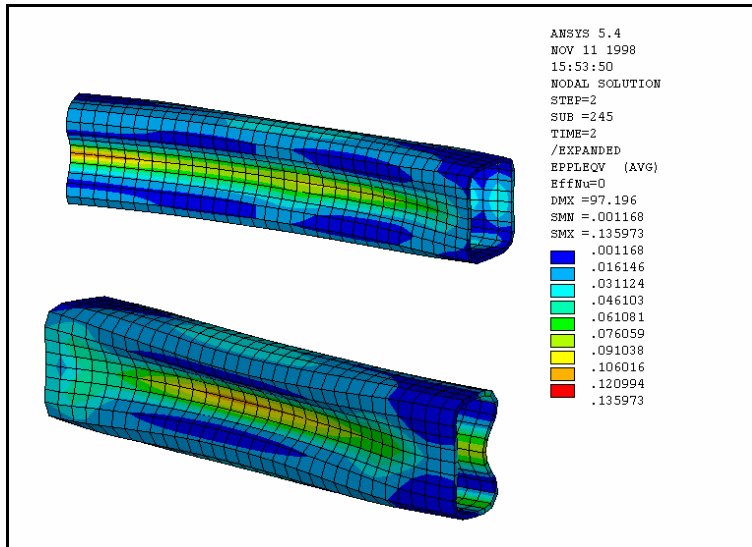


Fig. 13: Plastic equivalent strain of the ring line at 100% load. Static calculation, volume model. View to the inner wall (upper figure) and to the outer wall (lower figure).

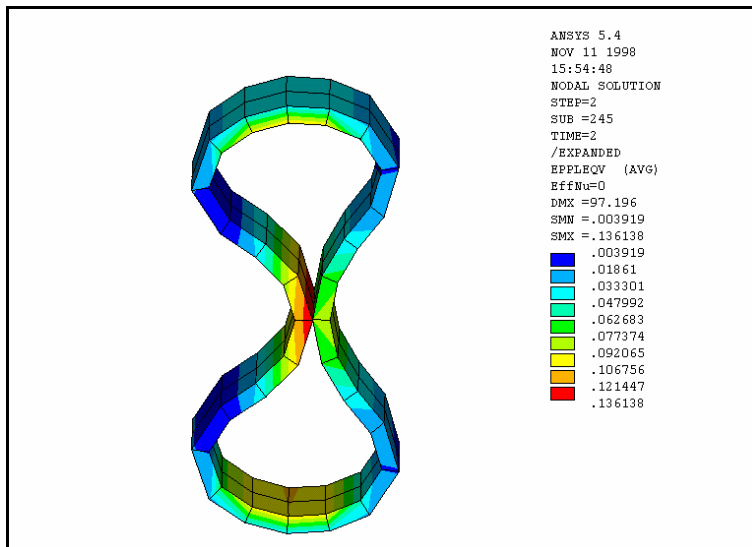


Fig. 14: Plastic equivalent strain of the ring line at 100% load. Static calculation, volume model. View to the ring line cross section at 15 °. Left side is outer wall.

strain. In spite of the large deflection the maximum strain (0.14) is clearly below the fracture strain (0.44). Figure 14 shows a detail of the strain distribution to demonstrate that there is contact between the opposite walls. The maximum deflection of the outer wall is larger than that of the inner wall. The maximum equivalent stress is about 320 MPa. This agrees to the  $\sigma$ - $\epsilon$  curve of the FWD steel (Fig. 9). The static calculation with the shell model exhibits a worse convergence in comparison with the volume model. At a relative load factor greater than 58% the solution is not convergent.

For the transient calculation the deflection and the relative load factor are displayed versus time (Fig. 15). The relative load factor (blue) corresponds to the part of the pressure curve in Fig. 12 between 0.04 s and 0.056 s. It is to be seen that there is a remarkable time delay between the maximum pressure peak and the response of the structure. At 100% load there is only a deflection of 15 mm at both vertical walls. This is a consequence of the inertia of the material which acts as an additional resistance in the beginning of the deformation. But at the time of the maximum pressure peak there is a high

velocity of deformation, and the kinetic energy promotes a further deflection even when the load is already decreasing again. The motion is only stopped when contact between the walls takes place. The maximum deflection and the maximum strain are very similar to those of the static calculation. The maximum strain is 0.13. The maximum deflection of the outer wall is 85 mm and that of the inner wall is 70 mm. The corresponding values from the static calculation are 97 mm and 58 mm. This means that the deformation of the ring line cross section calculated in the transient analysis is not as skew than that calculated in the static analysis. According to the maximum stresses and strains the static solution is sufficiently precise.

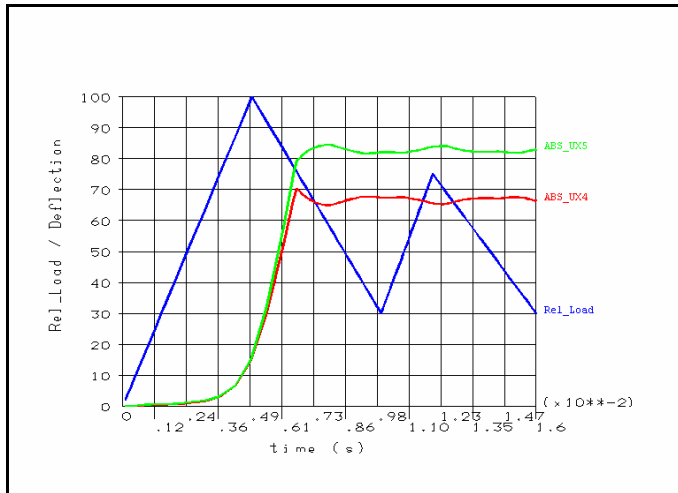


Fig. 15: Transient analysis of the ring line. Deflection curves vs. time for nodes at the inner wall (red) and the outer wall (green) at azimuthal position 15°. Relative load vs. time (blue).

## 5. Conclusions

Within the considered scenario - break of a BWR feed water line - the elasticity limit of the feed water distributor is exceeded. Hence the stress analysis has to be done with consideration of material and geometrical non-linearity. Within a static analysis the arc-length procedure is an adequate numerical tool to handle instabilities occurring with the buckling of the FWD ring line. However, a convergent solution up to 100% load could only be obtained with volume elements. The shell elements which were also used proved not to be sufficiently stable. The results of the transient analysis show that there is a

time delay between maximum load and maximum deflection. The maximum stresses and strain do not differ significantly between static and transient solution. In spite of the large deformation the FWD ring line the maximum strain remains clearly below the break limit.

## References

Hughes, T.J.R. (1987), *The Finite Element Method - Linear Static and Dynamic Finite Element Analysis*. Prentice-Hall International Editions.

Zienkiewicz, O.C. (1977), *The Finite Element Method*, Maidenhead, McGraw-Hill Book Company.

Kolar, R. and H.A. Kamel (1986), On some efficient solution algorithms for nonlinear finite element analysis. In: *Finite Element Methods for Nonlinear Problems*, Heidelberg, Springer-Verlag Berlin, Editors P. Bergan, K.J. Bathe and W. Wunderlich.

Bathe, K.J.(1982), *Finite Element Procedures in Engineering Analysis*, Prentice-Hall, Englewood Cliffs.

Mattiasson, K., A. Bengtsson, A. Samuelson (1986), On the accuracy and efficiency of numerical algorithms for geometrically nonlinear structural analysis. In: *Finite Element Methods for Nonlinear Problems*, Heidelberg, Springer-Verlag Berlin, Editors P. Bergan, K.J. Bathe and W. Wunderlich.

# CALCULATIONS WITH ANSYS/FLOTRAN TO A CORE CATCHER BENCHMARK

Hans-Georg Willschütz

## 1. Introduction

There are numerous experiments for the exploration of the corium spreading behaviour, but comparable data have not been available up to now in the field of the long term behaviour of a corium expanded in a core catcher. The difficulty consists in the experimental simulation of the decay heat that can be neglected for the short-run course of events like relocation and spreading, but must, however, be considered during investigation of the long time behaviour. Therefore, the German Gesellschaft für Reaktorsicherheit (GRS) defined together with Battelle Ingenieurtechnik a benchmark problem, in order to determine particular problems and differences of computational fluid dynamics codes (CFD codes) during simulation of ex-vessel-corium. In this case, the codes CFX-TASCflow, CFX 4.2 and Comet 1.023 based on the finite-volume-method (FVM) were firstly used. To be able to compare the results with those from a finite-element code (FE), later on also ANSYS/FLOTRAN calculations were carried out at the Institute of Safety Research of Forschungszentrum Rossendorf.

For the calculations a pure liquid oxidic melt with a homogenous internal heat source was assumed. The melt was distributed uniformly over the spreading area of the EPR core catcher. All codes applied the well known  $k$ - $\epsilon$ -turbulence-model [1] to simulate the turbulent flow regime of this melt configuration.

While the FVM-code calculations were performed with three dimensional models using a simple symmetry, the problem was modelled two-dimensionally with ANSYS due to limited CPU performance. In addition, the 2D results of ANSYS should allow a comparison for the planned second stage of the calculations. In this second stage, the behaviour of a segregated metal oxide melt should be examined. However, first estimates and pre-calculations showed that a 3D simulation of the problem is not possible with any of the codes due to lacking computer performance.

## 2. Description of the model

For the modelling of a fluid dynamic problem with the FE program ANSYS the module FLOTRAN is required [2]. The procedure for the fluid dynamic modelling is similar to the procedure in case of mechanical or thermodynamic FE problems in solids. The material properties are first determined in the preprocessor. After this, the geometry of the model is defined and the model is meshed with the selected element type. In the last step the initial and boundary conditions for the corresponding nodes of the model are fixed. All quantities in the model are SI units (m, kg, s); temperatures are given in K.

The material properties are determined within a macro. They can be independent on temperature, can be calculated according to a temperature dependent function or can depend on the temperature and be interpolated between the values of a table defined by the user.

At the considered temperature range, the dynamic viscosity is assumed to be constant at  $\mu=2.5$  mPa·s. The thermal conductivity is set on  $\lambda=2.2$  W/mK, independent on the temperature, too. The Boussinesq-approximation cannot be chosen for the temperature dependency of the density in ANSYS as it is possible in case of the FVM codes. With the usual Boussinesq-approximation the density becomes constant in all equations except for the buoyancy term of the equation of motion. Contrary to this, the temperature tracking of density is considered in all equations in the ANSYS-model.

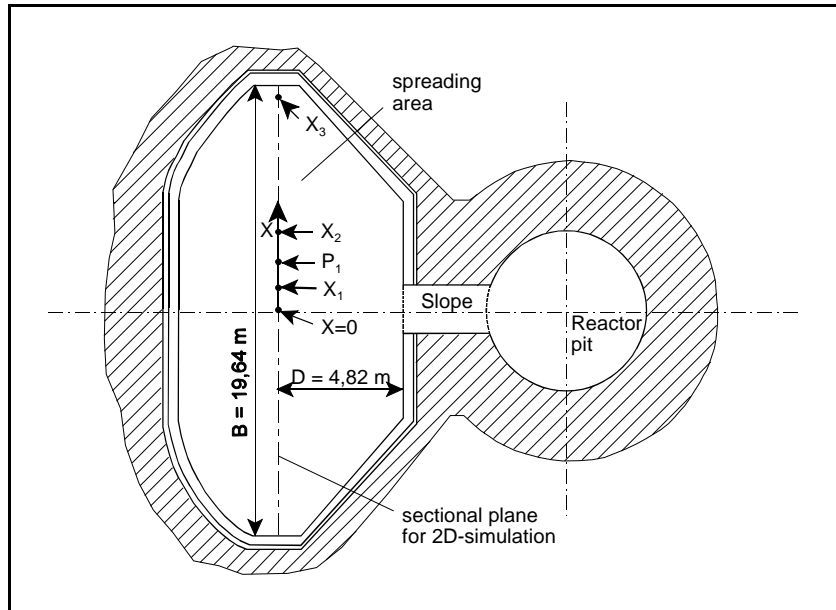


Fig. 1: Top view of the EPR core catcher configuration.

Two temperatures are defined for a linear interpolation:  $\rho(T=1600\text{ K})=6730$  kg/m<sup>3</sup> and  $\rho(T=2400\text{ K})=6469$  kg/m<sup>3</sup>. These values correspond to a volumetric coefficient of expansion of  $\beta=5 \cdot 10^{-5}$  1/K, at a reference density of  $\rho_0(T_0=2275\text{ K})=6510$  kg/m<sup>3</sup>, as it was determined for the benchmark calculations. The specific heat capacity is defined according to the same procedure:  $c_p(T=1600\text{ K})=590$  J/kgK and  $c_p(T=2400\text{ K})=618$  J/kgK.

As mentioned in the introduction 2D simulations of the problem are performed with ANSYS. The problem domain is meshed with the element type *fluid141*. These are quadrilateral elements with four nodes, one in each corner. For the considered problem each node has 6 degrees of freedom (DOF): temperature  $T$ , pressure  $p$ , horizontal velocity  $v_x$ , vertical velocity  $v_y$ , turbulent kinetic energy  $k$ , and turbulent kinetic energy dissipation rate  $\epsilon$ .

The considered vertical plane represents a cut through the core catcher on the position  $D=4.82$  m (s. fig. 1). The height of the melt layer is  $H=0.3$  m, the width is  $B=9.64$  m if symmetry is used and it is  $B=19.28$  m in the case of modelling the full width of the core catcher. In the following  $y$  is oriented along the vertical axis,  $x$  along the horizontal axis with  $x=0$  m at the symmetry axis of the core catcher (see figs. 1 and 2).

In vertical direction the problem domain is meshed with 14 elements, this corresponds to an upright arrangement of 15 equidistant nodes.

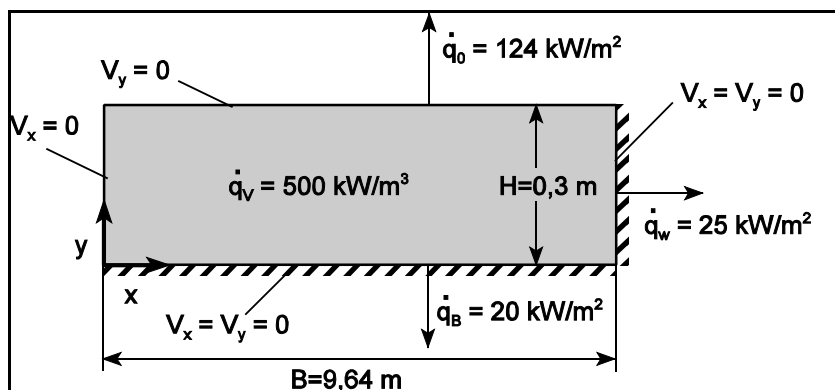


Fig. 2: Thermo- and fluiddynamic boundary conditions of the 2D-simulation.

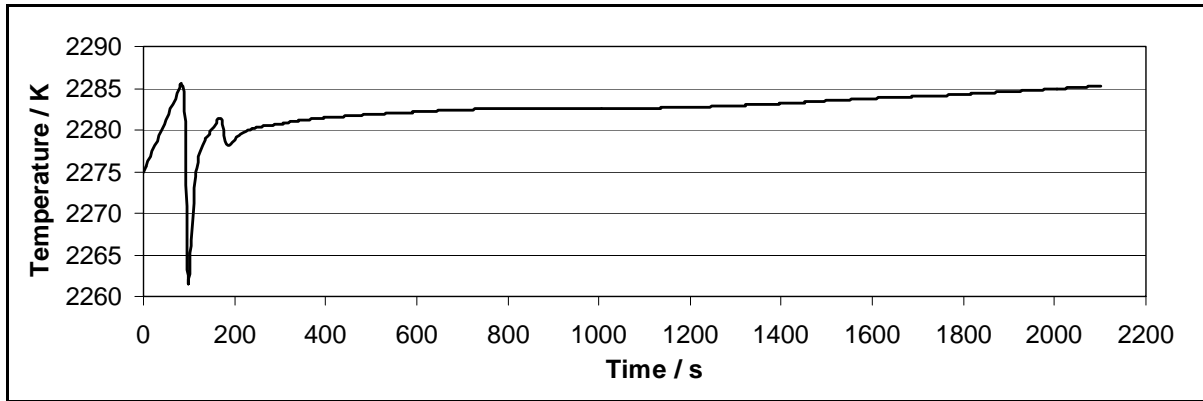


Fig. 3: Temperature vs. time at P1 ( $x=2.4$  m;  $y=0.15$  m).

A division of 80 equidistant elements over a length of 9.60 m was chosen for the horizontal direction. At the vertical boundary wall of the core catcher, a column with narrower elements (width  $b=0.04$  m) was used for a better modelling of the boundary conditions, so that in the half symmetrical case 81 elements are arranged over the horizontal direction. For the half symmetrical 2D model there are in total 1134 *fluid141* elements with 1230 nodes.

For the benchmark calculations, the essential thermodynamic initial and boundary conditions were prescribed. Additional fluid dynamic limiting conditions result from the problem to be modelled. The inner heat sources were modelled with  $q_v=500$  kW/m<sup>3</sup> according to the benchmark requirements.

The heat flux into the sidewalls is  $q_w=20$  kW/m<sup>2</sup>, that into the ground  $q_B=25$  kW/m<sup>2</sup>. The heat flow at the free surface has been chosen in such a way, that the total heat balance is in equilibrium. In this way, a heat flow of  $q_o=123.146$  kW/m<sup>2</sup> at the free surface resulted for the 2D model.

At the starting time  $t=0$  s the melt is not in motion. For modelling the volume force of gravity, an acceleration of  $g=9.81$  m/s<sup>2</sup> is set in  $y$ -axis direction. For all nodes at a wall, the wall boundary condition is no slip. The free slip condition is applied to the nodes at the free surface and on the symmetry line.

### 3. Results of the 2D calculations

In the following the essential parameters, courses of events and results of the transient 2D simulation of the one component-melt are explained and discussed. At the beginning of the calculation the melt has a uniform temperature of  $T_0=2275$  K and is in rest. After this, the temperatures within the boundary layers to the ground, to the sidewall and the free surface decrease due to the small thermal conductivity of the oxidic melt ( $\lambda=2.2$  W/mK). The temperature drop is proportional to the heat flow. Therefore, the temperature minima are at the free surface.

At the beginning the temperatures in the interior of the pool increase linearly, as can be seen from Fig. 3. It shows the time dependent temperature at point P1 (cf. Fig. 1) which is in the vertical centre of the melt pool. After some 80 s, the melt stratification becomes unstable at the surface on account of the increase of the density of the colder melt. Irregularly distributed plumes are found (s. fig. 4). The node represented in Fig. 3 is near to the right side of such a

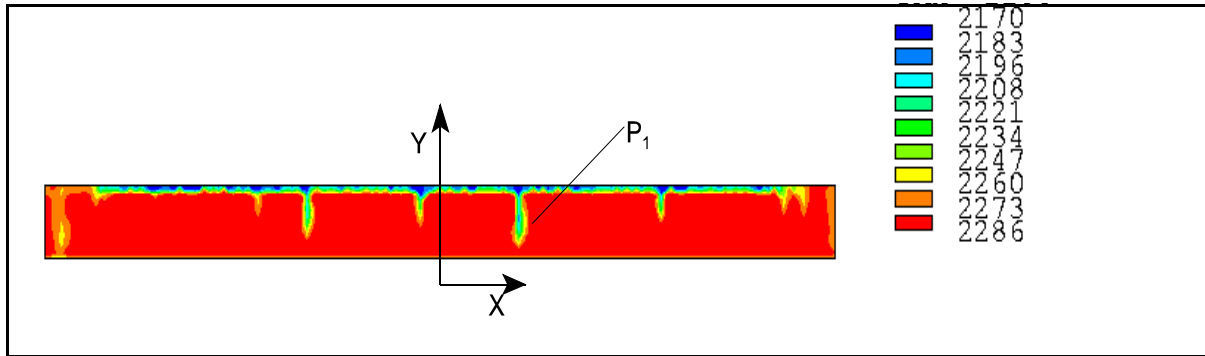


Fig. 4: Temperature field in K for the whole section after 85 s.

plume. That explains the strong temperature drop of almost 25 K after 85 s within 15 s.

After the plume has achieved the ground of the pool, it tears off because the denser fluid is relocated from the melt surface. Strictly speaking this only applies to the temperature field because the plume initializes a Rayleigh-Bénard-convection velocity field through the interaction of neighbouring plumes. Between two plumes two rotating convection rolls are established.

The initial number of rolls and their structure appears chaotic after some 120 s. Through coalescence of side-by-side rolls, the number decreases and a regular structure develops. Two kinds of coalescences are to be distinguished: neighbouring rolls with equidirectionally rotation tend to merge, while rolls with opposite rotational sense can disturb each other and the bigger and/or faster rotating one can remove the smaller one. This course of events is finished after about 300 s. At this time 18 rolls with alternating rotational sense can be observed over the entire width of the EPR core catcher of 19.64 m, this means the average width of a roll is 1 m (s. Fig. 5).

One can recognize in the time dependent diagram (cf. Fig.3) that the temperature field is in a quasi-stationary state after those 300 s. Then two new rolls form slowly at the two outsides of the melt configuration. They are additionally driven by the heat losses at the sidewalls. As a result, they receive a greater spin than the other rolls. The two exterior rolls increase slowly to the middle of the corium pool. Each of them removes two of the rolls formerly located next to the walls until the end of the calculation after 2100 s, so that 16 rolls are observed then. This evolution seems not to be finished at the end of the considered calculation time. However, it is probable that the large rolls near the vertical walls are not stable in the three dimensional case.

For the benchmark calculation, temperature and velocity field should be calculated up to 2100s.

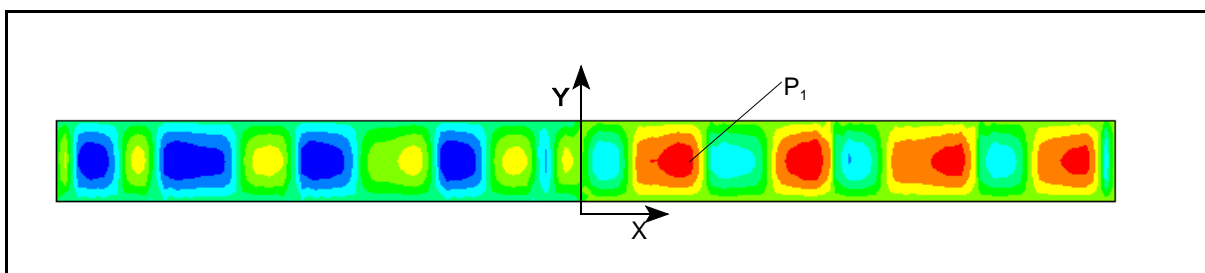


Fig. 5: Streamlines for the whole section after 300 s (clockwise rotating cells are blue; counter-clockwise rotating cells are red or yellow; the colour scale corresponds to the velocity).

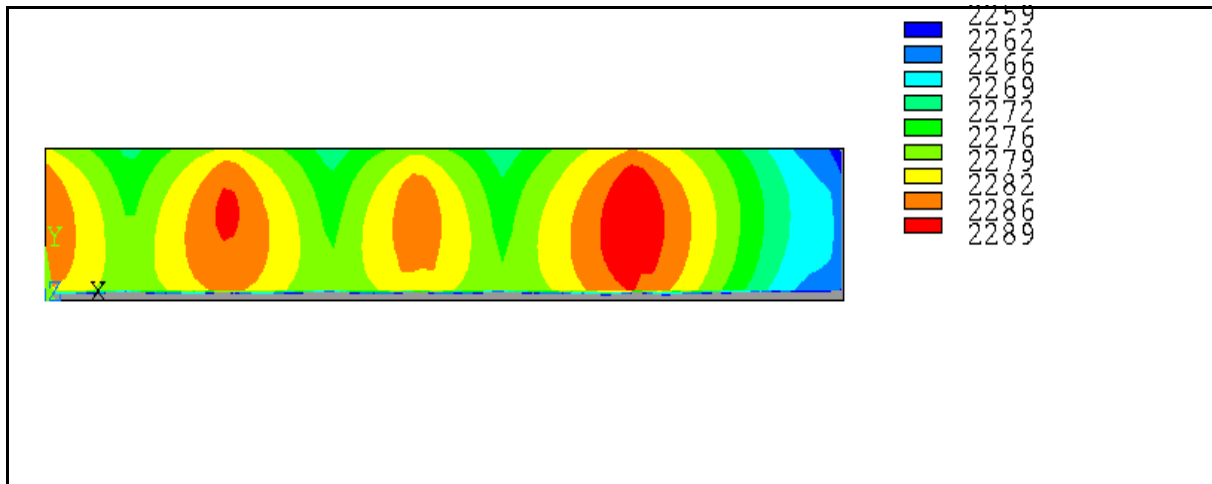


Fig. 6: Temperature field in K for the half section after 2100 s. (Temperatures below 2259 K are grey).

The number of the rolls in the considered sectional plane (cf. Fig. 1;  $D=4.82\text{m}$ ) is of particular interest. The temperature field after 2100 s is shown in Fig. 6. The maximum temperature is  $T_{\max}=2289\text{ K}$ . The temperature scale ends at a lower bound of  $T=2259\text{ K}$  for a better representation of the temperature field. All temperatures below 2259 K are represented grey.

In Fig. 6, one recognizes 4 zones with higher temperatures, these are the ascending zones of two neighbouring convection rolls with counter rotating senses. The biggest roll is at the right end of the section, it turns to the right (mathematically negative) and extends from the wall to the centre of the first high temperature region. Due to the size of the roll and the additional heat losses at the right wall, it exhibits the greatest temperature difference of all convection rolls between the hot buoyancy zone and the cold sinking zone. With an assumed solidification temperature of 2175 K for the oxidic melt it can be stated that there is no crust formation at the surface due to the high convection heat transfer.

Considering the vertical temperature profiles over the height at position  $X_3$  (s. Fig. 7) it can be stated that the codes CFX 4.2 and Comet 1.023 calculate steeper temperature gradients at the free surface than at the ground [3]. But CFX 4.2 calculates a several times higher temperature difference within the boundary layers. CFX-TASCflow calculates a steeper gradient at the ground than at the surface. In fact the temperature gradient at the surface is relatively flat. Looking at the temperature profiles calculated by ANSYS/FLOTRAN the following comparisons can be made:

- The steep gradients on the ground are comparable with that ones calculated by CFX 4.2 and CFX-TASCflow. But the boundary layer calculated by ANSYS has a greater vertical extension.
- At the free surface the ANSYS temperature curves are comparable with those from CFX-TASCflow.

For the ANSYS results the explanation is: As a result of the free slip condition, the turbulence model provides high effective thermal conductivities at the free surface, those are up to 3 orders higher than the laminar conductivity, that is the reason for the small temperature gradients despite of the five times higher heat flow to the surface compared to that to the ground. The large temperature gradients on the ground result from the no-slip-condition because a small kinetic turbulent energy is calculated by the turbulence model in the wall region.

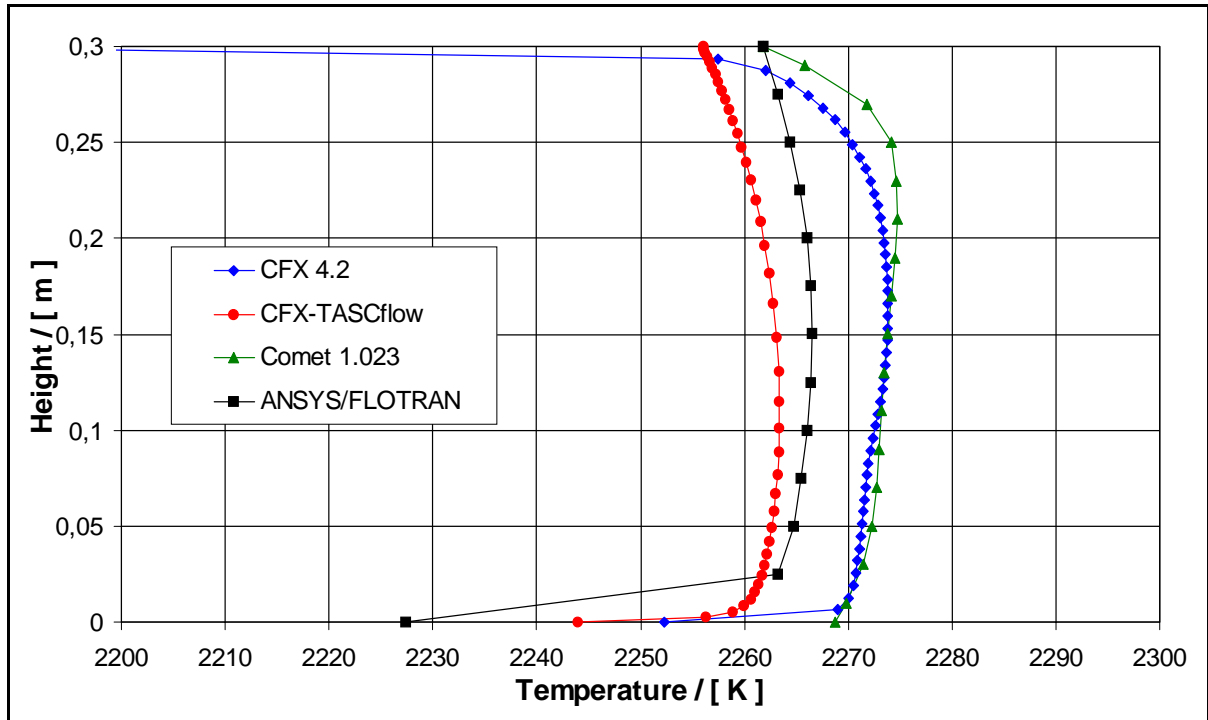


Fig. 7: Vertical temperature profiles of all codes at position  $X_3$  after 2100 s.

This leads to a small effective thermal conductivity and therefore to a large temperature difference corresponding to the heat flux into the ground.

#### 4. Outlook

For the first stage of the benchmark calculations for an EPR-core catcher the 2D-ANSYS/FLOTRAN-calculations show a good agreement to the 3D-FVM-code calculations. This gives a basis for comparisons with the next calculations considering a separated melt of an oxidic layer and a metallic layer. These calculations have to be modelled with all codes as 2D-models because of limited computer resources. With the assumed physical boundary conditions and material properties the selected numerical models do not predict a crust formation for the oxidic melt. The behaviour of the melt temperature within the boundary layers has to be investigated and discussed in more detail, because it has not only consequences at the free surface of the melt pool but it also affects the fluid-fluid-boundary in the calculations to be performed in the future.

#### References

- [1] B. E. Launder, D. B. Spalding (1974), The Numerical Computation of Turbulent Flows, Computer Methods in Applied Mechanics and Engineering 3, pp. 269-289
- [2] ANSYS Code Manual, Release 5.4 (1997), ANSYS Inc. Houston, USA
- [3] H.-J. Allelein, A. Breest, W. Erdmann, M. Heitsch, A. K. Rastogi, A. Scheuer, H.-G. Willschütz, Specification of the Benchmark Conditions - First Comparison of Results, Internal Communications, Meeting of the 14<sup>th</sup> of September 1998.

# MATERIALS TESTING AT THE HOT CELL LABORATORY OF THE INSTITUTE FOR SAFETY RESEARCH

Hans-Werner Viehrig

## 1. Introduction

The hot cell laboratories for handling and testing of irradiated specimens were firstly introduced in the annual report 1997 [1]. The following equipments are installed in the "Shielded Containment" of the materials testing laboratory:

- an instrumented pendulum impact testing machine,
- a servo-hydraulic testing system MTS 810-Test Star (load capacity 50 kN) and
- a video-measuring microscope.

Different test methods can be applied, like:

- instrumented Charpy impact testing,
- static fracture toughness testing and
- tensile testing with sub-size tensile specimens.

Irradiated specimens must be tested and handled remotely, i.e. automatically by manipulators. Any direct action by hand is impossible as routine and only very restricted in case of uncommon events. Therefore, the handling, testing and measuring systems must work practicably, correctly and reliably. To prove this, a comprehensive test programme was accomplished before starting testing of irradiated specimens. In detail, the programme had to show that:

- all systems work satisfactorily under the hot cell conditions,
- the testing procedures fulfill the recommendations of the test specifications according to the standards, and
- the results measured are accurate.

Additionally, the techniques of handling and testing should be trained.

## 2. Material and Specimens

The material tested was a forged plate of DIN 10 CrMo 9 10 heat resistant structural steel. After forging to a cross-section of 70 mm · 120 mm the steel block was austenitizing heat treated at 950°C, oil quenched and annealed at 600°C (code D), 640°C (code E), 720°C (code F) and 760°C (code G) for 2 hours. The microstructure is bainitic. Table 1 contains the chemical composition and Table 2 provides the mechanical properties of the different tempering states. The heat treated blocks were cut into specimens. The specimens were taken from five thickness layers indicated with the numbers:

- 1 and 5 for the surfaces and
- 2, 3 and 4 for the middle section.

The following specimen types were tested:

- standard Charpy V-notched specimen (L-T orientation),
- precracked and side grooved (20%) Charpy size SENB specimens (L-T orientation) and
- sub-size tensile specimens (diameter: 3 mm, gage length: 15 mm, overall length: 25 mm).

Table 1: Chemical composition (wt. %) of the DIN 10 CrMo 9 10 structural steel (Fe balance)

C	Si	Mn	Mo	Cr	Ni	Al
0.095	0.31	0.55	2.28	0.97	0.10	0.013

Table 2: Mechanical properties of the different tempering states

material code	$R_{p0.2}$	$R_m$	$A_g$	$A_5$	$A_5^d$	$A_5^m$	Z
	MPa	MPa	%		%	%	%
D: standard	739	846	7	18			73
D: sub-size	752	851	7		16	18	63
E	630	723	8	21			76
F: standard	457	569	10	26			80
F: sub-size	465	588	10		22		70
G	393	513	17	35			81

$R_{p0.2}$  tensile yield strength

$R_m$  ultimate tensile strength

$A_g$  elongation without necking

$A_5$  elongation at break

d: sub-size tensile specimen measured with the displacement gage

m: sub-size tensile specimen measured with the microscope after testing

Z reduction of area

### 3. Measuring of Geometrical Dimensions

The video-measuring microscope is used to measure both the geometrical dimensions of the specimens and characteristic parameters on the fractured surface. The measuring resolution of the microscope is 0.001 mm and fulfills the recommendations of the test specifications. The following dimensions and parameters were measured:

- initial geometrical dimensions: width (W), thickness (B) and notch depth ( $a_0$ ) of the specimens,
- lateral expansion (LE) and the percentage of shear fracture (PSF) according to DIN 50115 [2] ASTM E 23 [3] and
- initial crack length and the ductile crack extension (fracture mechanical tests).

Parameters, which are needed for the evaluation of the tests, were measured from 15 Charpy V and Charpy size SENB specimens by five operators. To assess the accuracy of the video-measuring system all measurements were checked with a well-tried, conventional measuring light microscope (Großes Werkzeug mikroskop, Carl Zeiss Jena).

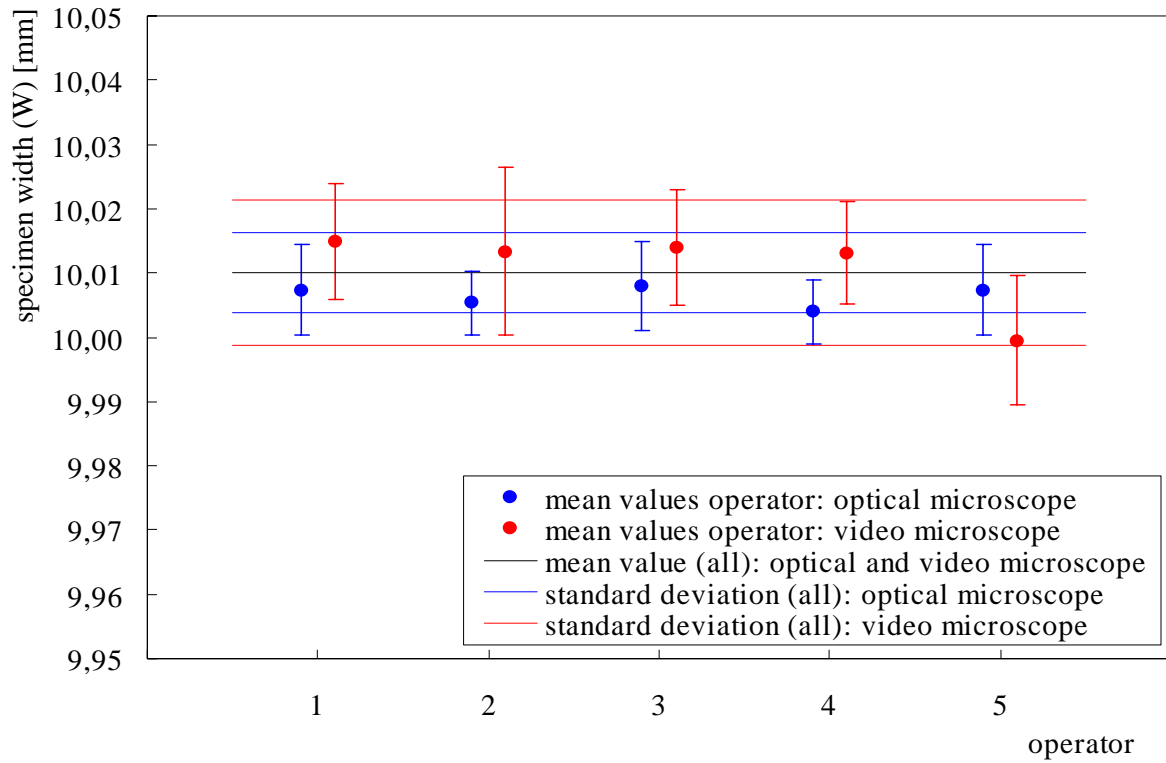


Fig. 1: Results of geometrical dimension (W) measurements

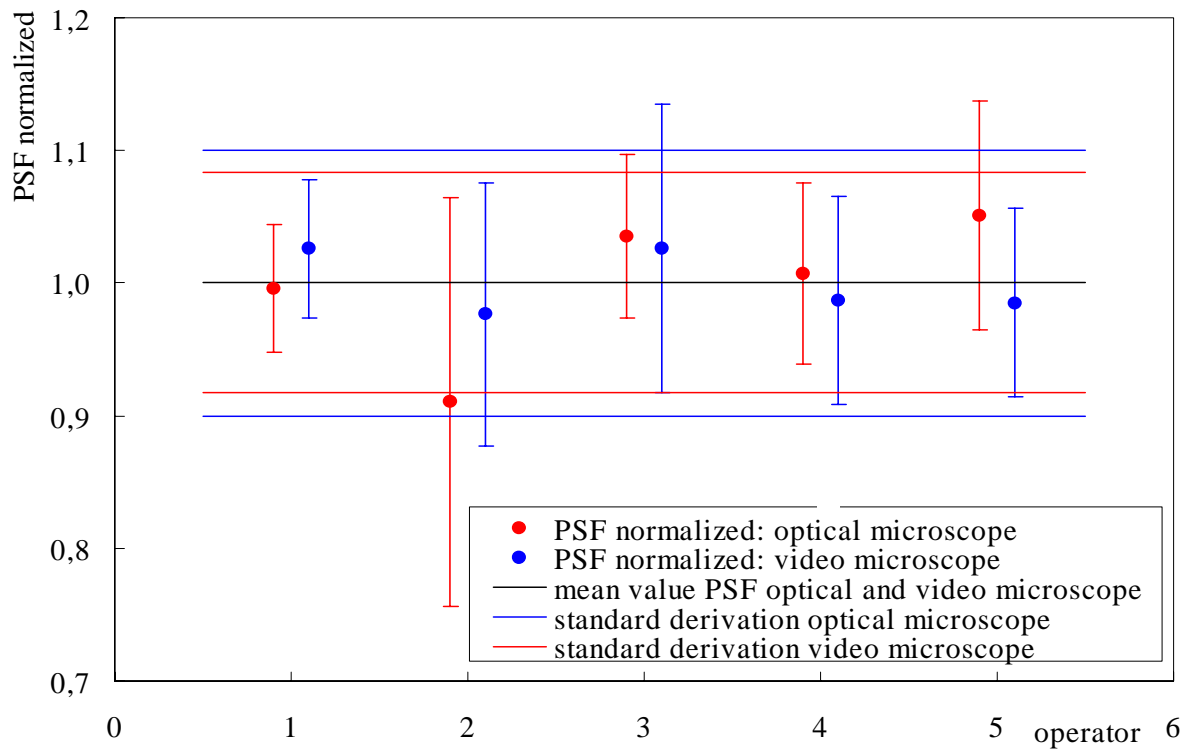


Fig. 2: Results of PSF measurements

Fig. 1 shows the results of the specimen width ( $W$ ) measured with both microscopes by five different operators. There are no significant differences in the mean values between the different operators and both measuring microscopes. This result is significant for the geometrical dimensions measured on the specimens before testing. The mean LE values measured by the video-measuring system are lower than 0.03 mm. This difference can be neglected. The PSF measured on the fractured surfaces by both microscopes are shown in Fig. 2. The PSF values are normalized to the mean value of each specimen measured by all five operators. There is no significant difference between the PSF values measured with both microscopes. The scattering of the normalized PSF values must be considered as the subjective factor of the different operators during the evaluation of the fractured surface. Round-robin results of PSF measurements reported on in [4] show comparable deviations. To evaluate the fracture mechanical tests the initial crack length and the ductile crack extension have to be measured on the fractured surface of the specimen after loading. These values were measured with both microscopes. The differences between both measurements are lower than  $\pm 0.05$  mm. Such small deviations are tolerable.

#### 4. Instrumented Charpy V Impact Testing

The pendulum impact testing machine PSd300 (WPM Leipzig) [1] is equipped with an automatic temperature conditioning and specimen manipulation (ATCM) system. The compliance with the recommendations of DIN 51 222 [5] was checked before testing. For measuring the impact force the hammer tup is instrumented and statically calibrated according to the ISO/DIS 14556 standard [6]. The used calibration load cell is described in [7]. The Charpy V impact tests are performed according to the DIN EN 10045 standard [8] under the following test conditions:

- impact energy: 300 J
- impact velocity: 5.5 m/s
- temperature range: -150 to +300°C.

In Charpy V impact testing, the energy to break a V-notched bend specimen is determined from the difference of the pendulum heights before and after the impact. This energy is directly obtained from the dial or a rotation angle measuring system. In instrumented impact testing the load is measured that the specimen is exposed to during the loading and the subsequent failure process. The impact energy is determined from the load-time record by integration procedures. These two energy quantities, in the following denoted as KV (dial) and  $W_t$  (calculated), are generally identical. Friction effects are included in KV but cannot influence  $W_t$ . The recommendations on the accuracy of the test specifications are ensured by applying the ATCM system. Before testing the ATCM system was optimized and calibrated. Tab. 3 shows the recommendations of the DIN EN 10045 and the results which were achieved.

Table 3: Positioning accuracy of the specimen on the anvil

condition	DIN EN 10045	measured
centring of the specimen (alignment of notch and impact point)	$\pm 0.5$ mm	$\pm 0.1$ mm
test temperature	$\pm 2$ K	$\pm 1$ K
interval time between removal from the furnace to the impact	$\leq 5$ s	$\leq 3$ s

Fig. 3 shows the load-displacement curve of a specimen tested in the ductile to brittle transition region showing ductile and brittle fracture as an example. In Fig. 4, the absorbed energy-temperature hyperbolic tangent fit curves are presented for the tempering state F. The quality of the instrumentation can be assessed by comparing the KV and  $W_t$  values.

Experience indicates that deviations within  $\pm 5$  J can be accepted. As indicated by Fig. 5 the values are within the  $\pm 5$  J scatter band. The main benefit of the instrumentation is the determination of characteristic loads: yield, maximum, brittle initiation and arrest load. The dynamic yield ( $R_{ed}$ ) and ultimate tensile strength ( $R_{md}$ ) can be calculated from the bending yield and the maximum load in the course of the load-displacement curve [9].

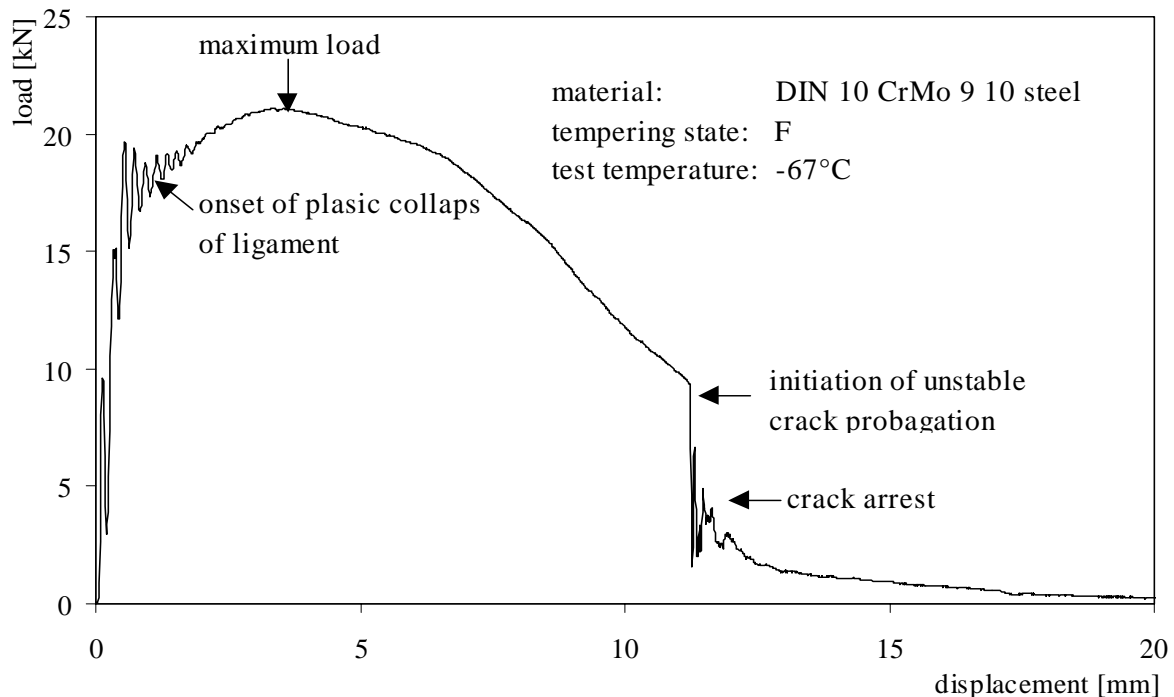


Fig. 3: Load-displacement curve of a Charpy V specimen tested in the ductile to brittle transition region

The estimated strength values  $R_{ed}$  and  $R_{md}$  are presented in Fig. 6 versus test temperature. The steel block under investigation shows an increase of the Charpy transition temperatures of about 30 K in thickness direction (Fig. 2) and almost the same upper shelf energies. The different thickness layers have no significant differences in the strength properties and the scatterband is very small (Fig. 6). The differences in the transition temperatures must be caused by the modification of the structure between the surface and the middle of the block.

The obtained results are comparable with those of specimens, which were measured with the same type of impact pendulum outside the hot cell (material code F in Fig. 4). These specimens were machined from a thickness layer comparable with F2. In contrast to the other specimens these specimens were machined from the material after quenching. The final heat treatment was performed with the finished specimens.

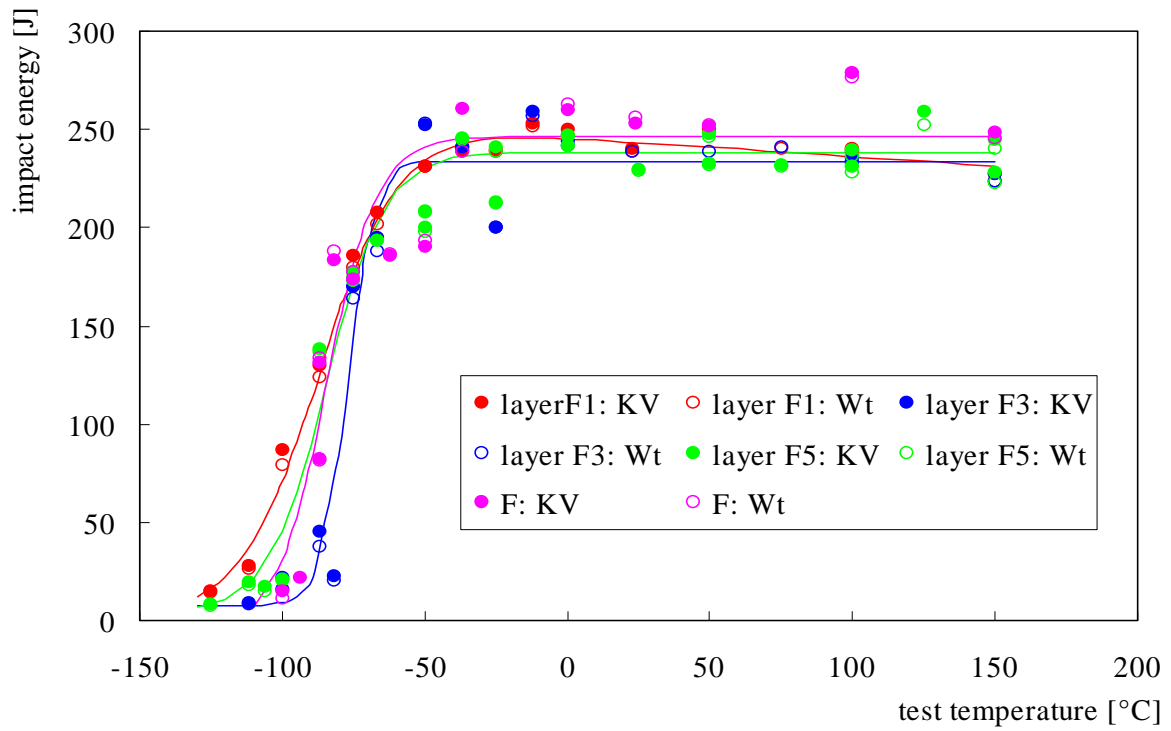


Fig. 4: Absorbed energy-temperature hyperbolic tangent fit curves

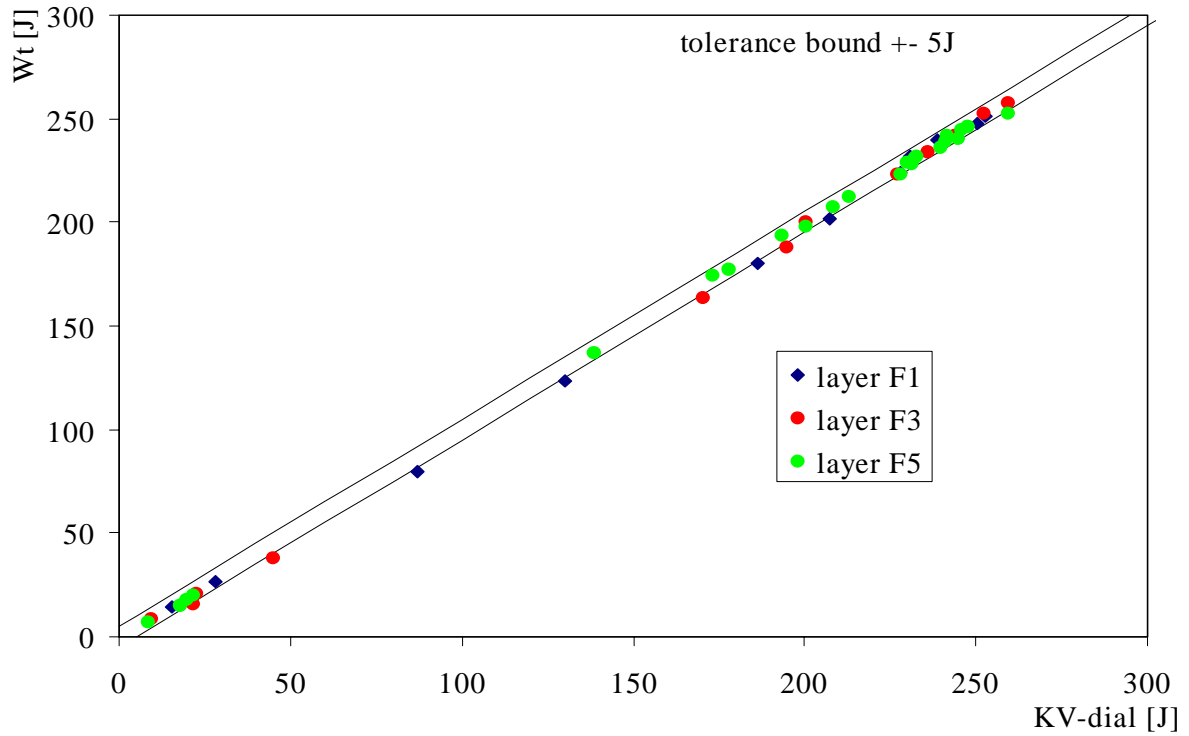


Fig. 5: Calculated impact energy (Wt) vs. Impact energy dial (KV)

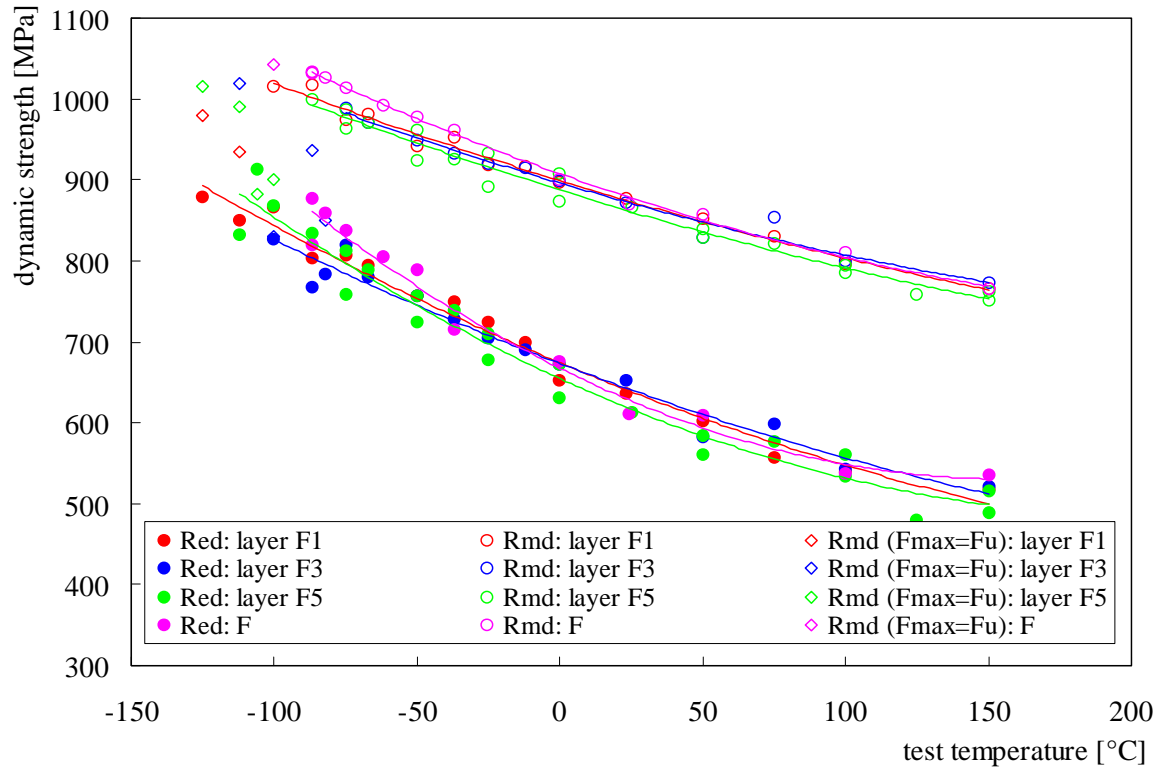


Fig. 6: Estimated strength values Red and Rmd versus test temperature

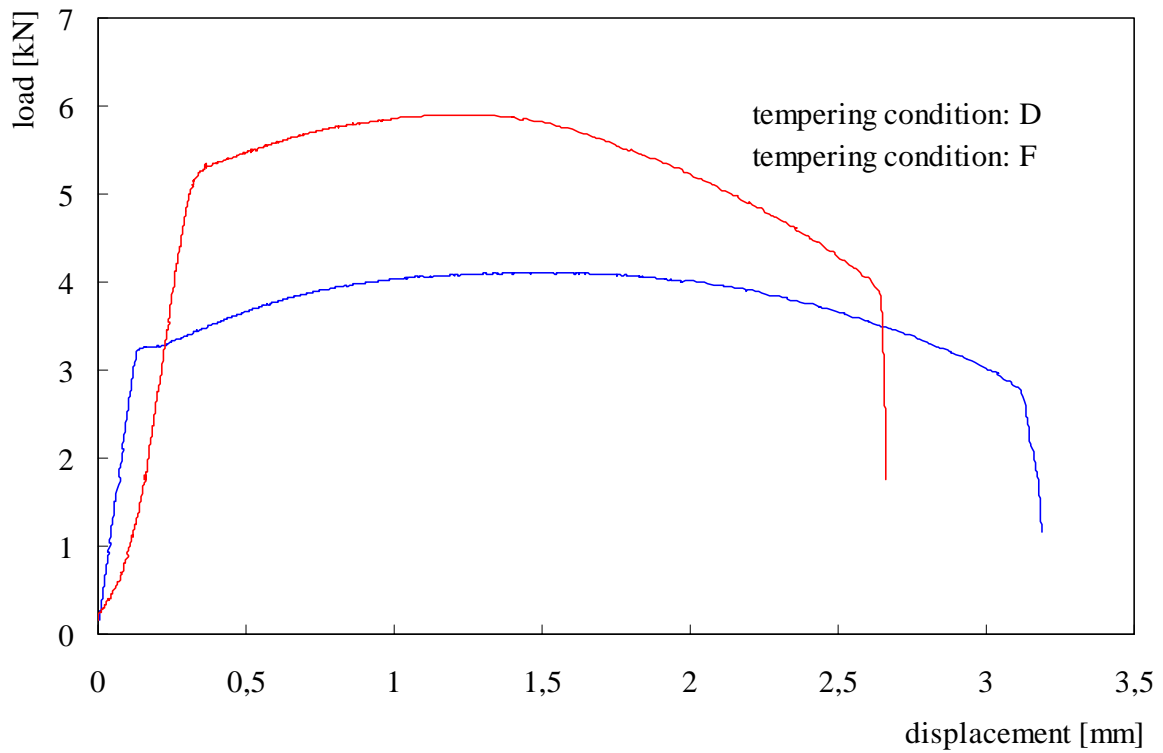


Fig. 7: Load-displacement curves for sub-size tensile specimens

## 5. Tensile Testing

The sub-size tensile specimens are handled with the manipulators and loaded at a special loading equipment. To measure the displacement an additional extensometer positioned outside the tempering chamber below the load cell has been used. Fig. 7 shows load-displacement curves of tested specimens for the tempering conditions D and F. The evaluated test results presented in Tab. 2 are comparable with the results of standard specimens tested outside the hot cell. The significant differences of the elongation and reduction of area are expected and result from the shorter gage length and the lower diameter of the sub-size tensile specimens.

## 6. Static Fracture Toughness Testing

Static fracture resistance ( $J_R$ ) curves, have been obtained following the standards ASTM E813-89 [10], EGF P2-91D [11], and EFAM GTP 94 [12]. Side grooved and precracked Charpy size SENB and CT specimens can be loaded with the servohydraulic test systems "MTS 810 - Test Star" using the unloading compliance technique. The servohydraulic test system with a load capacity of 50 kN is equipped with a tempering chamber and special devices for manipulating the specimens. The fixture of the gage for measuring the crack mouth opening displacement (CMOD) at the internal seats (knife edges) of the SENB specimens and the alignment of the specimen on the anvil under hot cell conditions are the main problems which have to be solved.

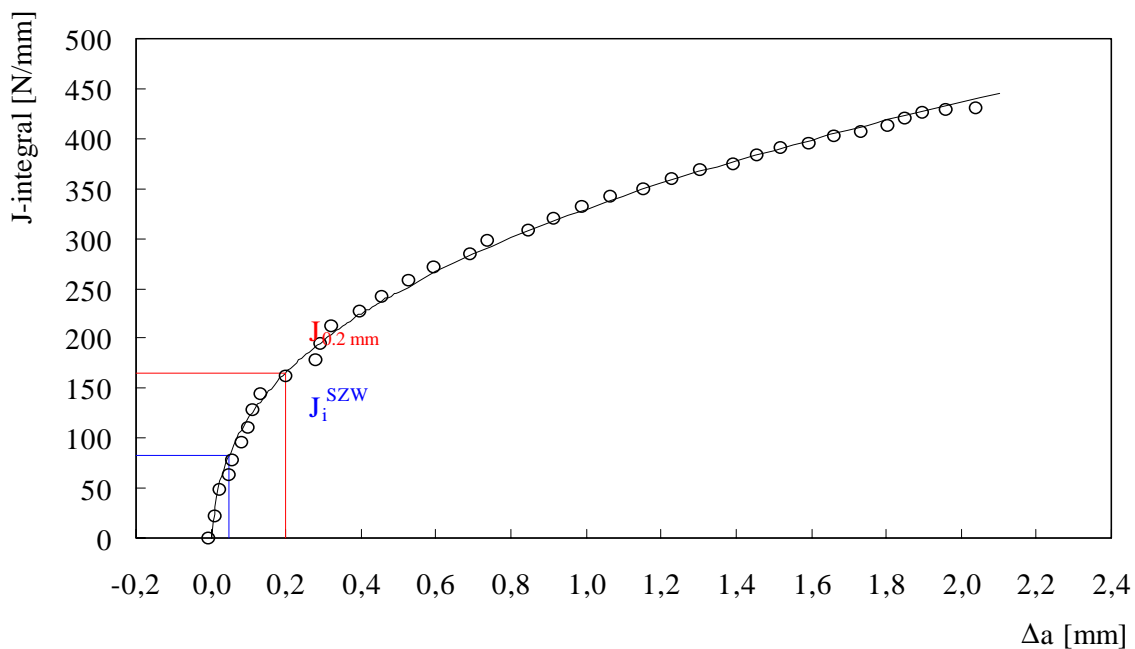


Fig. 8:  $J_R$  curve of a side-grooved and precracked Charpy size SENB specimen of tempering condition D loaded at 200 °C

A special CMOD gage and pertinent handling device have been designed. After fixing the CMOD gage in the knife edges the specimen is put on the anvil with manipulators. A special alignment device has been designed and installed at the anvil. After alignment the Charpy size SENB specimen is fixed by pre-loading with about 100 N and then ready for temperature conditioning and testing. For comparison, specimens of each tempering condition were addi-

tionally tested with a servohydraulic test system MTS 810 - Test Star outside the hot cell. The test temperature for these specimens was 200°C.

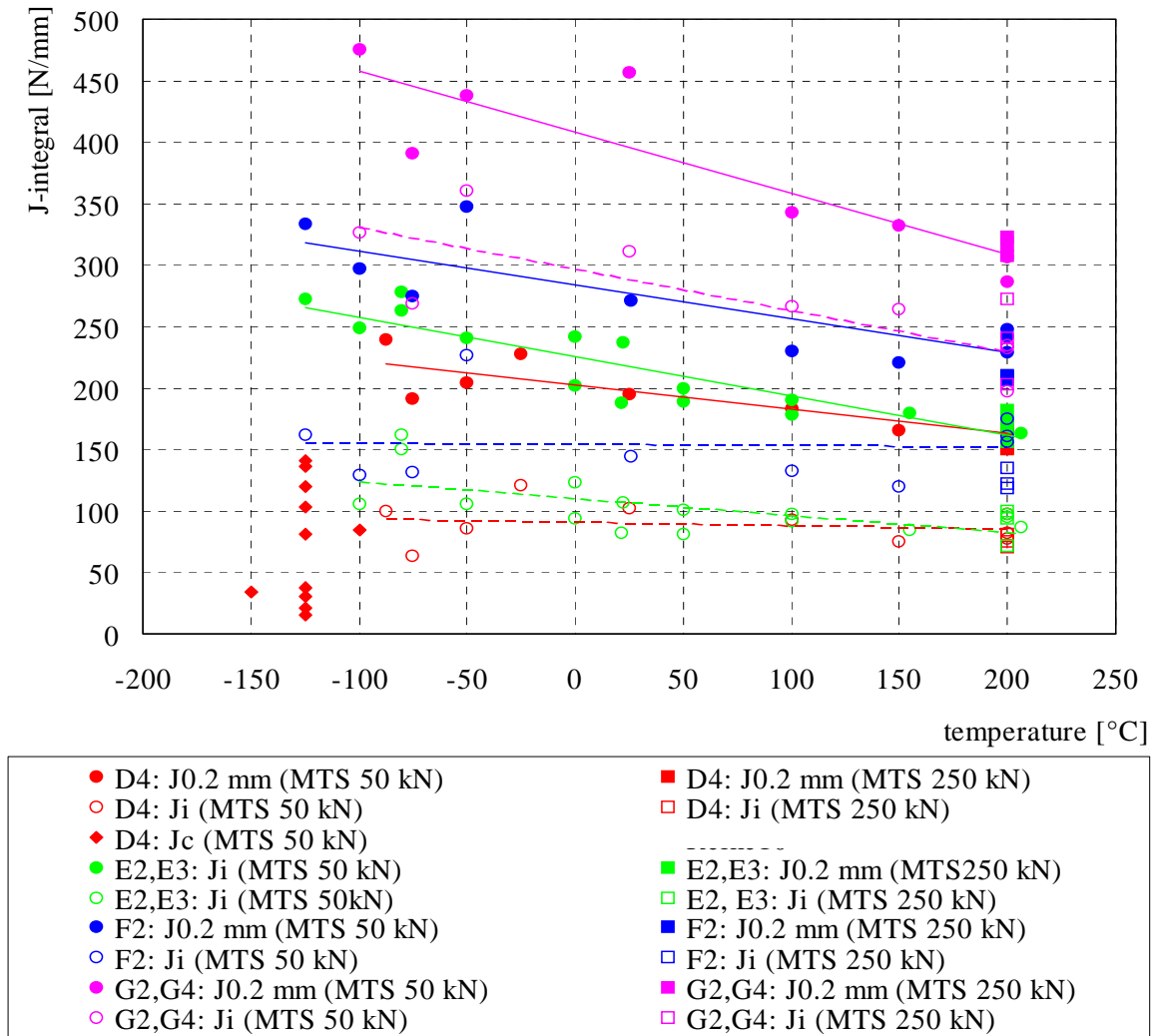


Fig. 9: Initiation and fracture toughness values in dependence on the temperature for the different tempering conditions

Fracture resistance ( $J_R$ ) curves were determined from measured crack lengths using the unloading compliance technique [10,11,12]. As an example, Fig. 8 shows the  $J_R$  curve of a specimen from tempering state D. This  $J_R$  curve proves that the crack extension can be determined using the unloading compliance technique. Scattering of the values is negligible. From these  $J_R$  curves J-integral values were determined at brittle fracture initiation ( $J_C$ ), at a crack extension of 0.2 mm ( $J_{0.2}$ ) and at crack blunting ( $J_i^{SZW}$ ) as measured from the width of the stretch zone (SZW). The  $J_C$  value characterizes the fracture toughness, whereas the  $J_{0.2}$  and  $J_i^{SZW}$  values are parameters of the initiation toughness for stable crack growth. Fig. 9 shows the initiation and fracture toughness values in dependence on the temperature for the different tempering conditions. The toughness is increasing with the tempering temperature.

The material tempered above 600°C has such a high toughness that test temperatures below -125°C are necessary for measuring valid  $J_c$  values.

## 7. Summary and Conclusions

The handling, measuring and testing systems installed in the new hot cell laboratory of the Institute for Safety Research were tested in a dedicated testing programme. This programme demonstrates that the systems work satisfactorily and reliably. It is possible to perform instrumented Charpy V tests, 3 point bending tests and tensile tests according to current testing standards under remote handling conditions. The results are comparable with those obtained in conventional testing laboratories.

## References

- [1] H.-W. Viehrig (1997), The hot cell laboratories for material investigations of the Institute for Safety Research, in F.-P. Weiß and U. Rindelhardt (Ed.), Annual Report 1997 of the Institute for Safety Research (pp. 80-85)
- [2] DIN 50 115, Kerbschlagbiegeversuch, besondere Probenformen und Auswerteverfahren, April 1991
- [3] ASTM E 23-82, Standard methods for notched bar impact testing of metallic materials, Philadelphia
- [4] W. Boehme (1996), Experience with instrumented Charpy tests obtained by a DVM round-robin and further developments, in E. van Walle (Ed.), Evaluating material properties by dynamic testing, ESIS 20 (pp. 1-23), Mechanical Engineering Publications, London
- [5] DIN 51 222, Werkstoffprüfmaschinen, Pendelschlagwerke, Januar 1985
- [6] ISO/DIS 14556, Standard Draft "Steel - Charpy V Pendulum Impact Test-Instrumented Test Method
- [7] S. Winkler and B. Voß (1996), Static force calibration of charpy impactors" evaluating material properties by dynamic testing, in E. van Walle (Ed.), Evaluating material properties by dynamic testing (pp. 37-44), Mechanical Engineering Publications, London
- [8] DIN EN 10045, Kerbschlagbiegeversuch nach Charpy, Teil 1: Prüfverfahren, April 1991, Teil 2: Prüfung der Prüfmaschine (Pendelschlagwerk), Januar 1993
- [9] W. L. Server (1980), Linear Elastic and Elastic-Plastic Fracture Toughness Using Instrumented Impact Testing, in R. A. Wullaert (Ed.), C.S.N.I. Specialists Meeting on Instrumented Precracked Charpy Testing, Proc. EPRI NP-2102-LD Prepared by Electric Power Research Institute (pp. 1-133 to 1-150), Palo Alto, USA
- [10] ASTM E 813-89 (1989), Standard Test Method for JIC, A Measure of Fracture Toughness, Philadelphia, USA
- [11] EGF P2-91D (1991), EGF Recommendations for Determining the Fracture Resistance of Ductile Materials, European Group on Fracture
- [12] K.-H. Schwalbe, B.K. Neale, and J. Heerens (1994), The GKSS Test Procedure for Determining the Fracture Behaviour of Materials: EFAM GTP 94, GKSS Report GKSS/E/60, Geesthacht

# SMALL ANGLE SCATTERING EXPERIMENTS AT VVER 440-TYPE WELD METAL Sv-10KhMFT

Mirco Grosse, Jürgen Böhmert, Valerie Denner

## 1. Introduction

The weld joint of a reactor pressure vessel near the core is the most critical point if one considers the phenomenon of neutron embrittlement. This does not only result from an often higher content of elements enhancing the sensitivity against neutron embrittlement but also from the special metallurgical state of the weld metal. The reason for this special, metallurgically induced sensitivity has not yet been clarified. Only sophisticated microstructural investigations can help to improve the understanding of the effects.

The microstructure of surveillance weld material of VVER 440 reactors was investigated by small angle scattering experiments with both neutrons (SANS) and X-rays (SAXS). Using methods of contrast variation, the experiments should give a deeper insight into the nature of the irradiation-induced microstructure defects.

## 2. The methods of contrast variation in SANS and SAXS experiments

The differential scattering cross section  $d\Sigma(Q)/d\Omega$ , which is calculated from the measured small angle scattering intensity, is

$$\frac{d\Sigma(Q)}{d\Omega} = K \int_0^{\infty} D_v(R) \cdot R^3 \cdot \Delta\eta^2 \cdot \phi(Q,R) dR \quad (1)$$

according to Glatter [1].  $Q$  is the scattering vector,  $K$  is a constant depending on the shape of the scattering defects and  $R$  is their characteristic dimension.  $D$  is the size distribution function of the defects.  $\phi(Q,R)$  is the so-called shape factor meaning the Fourier transform of the shape.  $\Delta\eta^2$  characterizes the scattering contrast and is calculated from the scattering density  $\eta$

$$\eta = n \cdot b \quad (2)$$

$n$  is the mean number density of the atoms or isotopes and  $b$  their mean scattering length (instead of  $b$ , for X-rays the atomic form factor  $f$  is used).  $\Delta\eta$  is the difference between the scattering

$$A = \frac{I(Q)_{\perp}}{I(Q)_{\parallel}} = \frac{\left(\frac{d\Sigma(Q)}{d\Omega}\right)_{nucl} + \left(\frac{d\Sigma(Q)}{d\omega}\right)_{mag}}{\left(\frac{d\Sigma(Q)}{d\Omega}\right)_{nucl}} \quad (3)$$

densities of the matrix and the scattering defects. It depends on the composition and the structure of the matrix and the defects (precipitation, voids, cluster etc.) Thus, by changing the scattering contrast information about the type and the composition of the scattering defects can be obtained. There are two simple ways to vary the scattering contrast. For materials with at least one ferromagnetic component, SANS experiments can be performed in a strong magnetic field and the difference between the magnetic and nuclear contrast can be determined. Defining a parameter 'A-ratio' as the ratio between the scattering intensities  $I(Q)$  measured perpendicular and parallel to the magnetic field the contrast variation can be quantified. SAXS experiments allow to use the resonant scattering effects at energies near the X-ray absorption edge of the elements being contained in the alloy system. For small  $Q$  the dependence of  $f$  on the energy can be calculated by

$$\lim_{Q \rightarrow 0} (f) = Z + f' + f'' \quad (4)$$

$Z$  is the atomic number,  $f'$  and  $f''$  are real and imaginary part of the resonant scattering contribution. The values of  $f'$  and  $f''$  are significantly different from zero only near the X-ray absorption edge of the concerned element. They can be calculated by the well-known Kramers-Kronig [2,3] and Cromer-Lieberman[4] relations.

### 3. Experimentals

The materials investigated originate from surveillance weld metal of the VVER 440 reactors Rovno 1 and Armenia 2. Rovno 1 is operated with a modified low-leakage core. Thus, the neutron flux is only  $0.36 \times 10^{12} \text{ n/cm}^2 \cdot \text{s}$  ( $E > 0.5 \text{ MeV}$ ). For Armenia 2 a standard core is used with a nearly 10-times higher neutron flux. The irradiation was carried out over several reactor cycles at  $270^\circ \text{ C}$ . The fluence after irradiation reached  $0.62 \cdot 10^{20} \text{ n/cm}^2$  ( $F_1$ ) for Rovno 1 and  $6.3 \cdot 10^{20} \text{ n/cm}^2$  ( $F_2$ ) ( $E > 0.5 \text{ MeV}$ ) for Armenia 2. The chemical composition is the same for both materials and is (in wt-%): 0.05 C, 0.4 Si, 0.014 S, 0.028 P, 0.19 V, 1.3 Cr, 1.24 Mn, 0.18 Cu, 0.12 Ni, 0.43 Mo and balance Fe. It corresponds to the Russian weld metal of the type Sv10KhMVT. The microstructure is the typical as-solidified welding structure (Fig. 1). It is characterized by cellular, columnar-aligned pre-austenite grains. Along the pre-austenite grain boundaries pre-eutectoid ferrite occurs and tempered bainite is formed within the former austenite grains. The SANS experiments were performed on the PAXE facility of the Laboratoire Leon Brillouin (LLB) in Saclay (France). Using neutron wavelengths of 0.5 and 0.6 nm and two

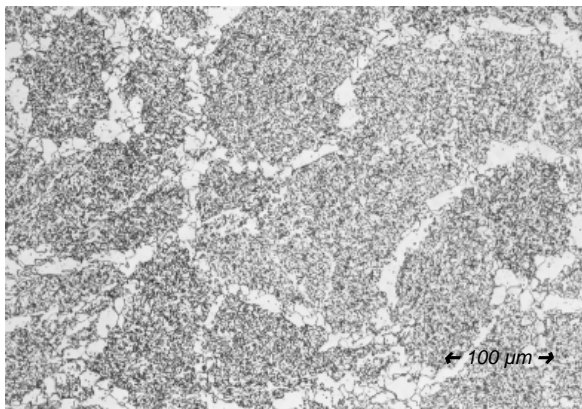


Fig. 1: Metallographic microstructure of the VVER-440-type weld metal

different sample-to-detector distances of 1.5 and 5 m, a  $Q$ -range of  $0.085$  to  $2.42 \text{ nm}^{-1}$  could be measured. For correction and evaluation of the experimental data the LLB software and the Glatter method [1] were applied. The SAXS experiments were performed on the JUSIFA facility at the HASYLAB synchrotron laboratory in Hamburg (Germany). The SAXS intensity was measured in the energy range near the K-absorption edge of vanadium, chromium, manganese and iron, partly in equidistant energy steps for short measuring time, partly with two fixed energies near the absorption edge of vanadium for a long measuring time.

#### 4. Results

Figs. 2 and 3 show the scattering intensity (in terms of the differential neutron scattering cross section) in dependence on the scattering vector for neutrons and X-rays respectively. There are clear differences between both experiments. Whereas the neutron scattering intensities are considerably higher (especially in the range of higher Q-values) for the irradiated states, such differences cannot be observed by the X-ray scattering experiments. This proves:

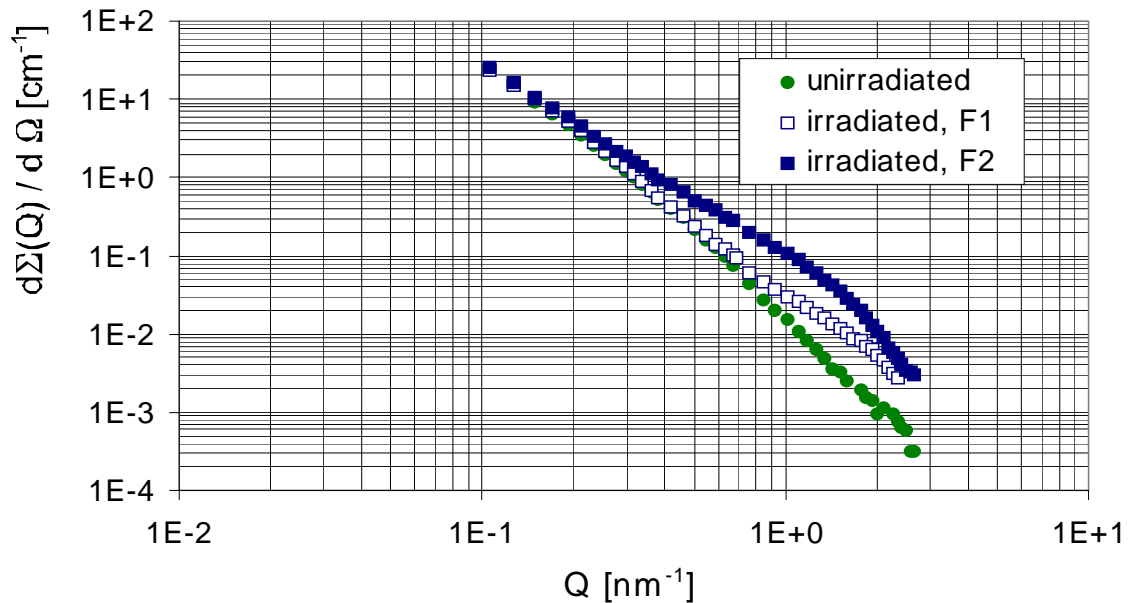


Fig. 2: Differential neutron scattering cross section  $d\Sigma(Q)/d\Omega$  of the unirradiated and two irradiated states of the weld metal Sv-10MFT, perpendicular to the external magnetic field as a function of the scattering vector

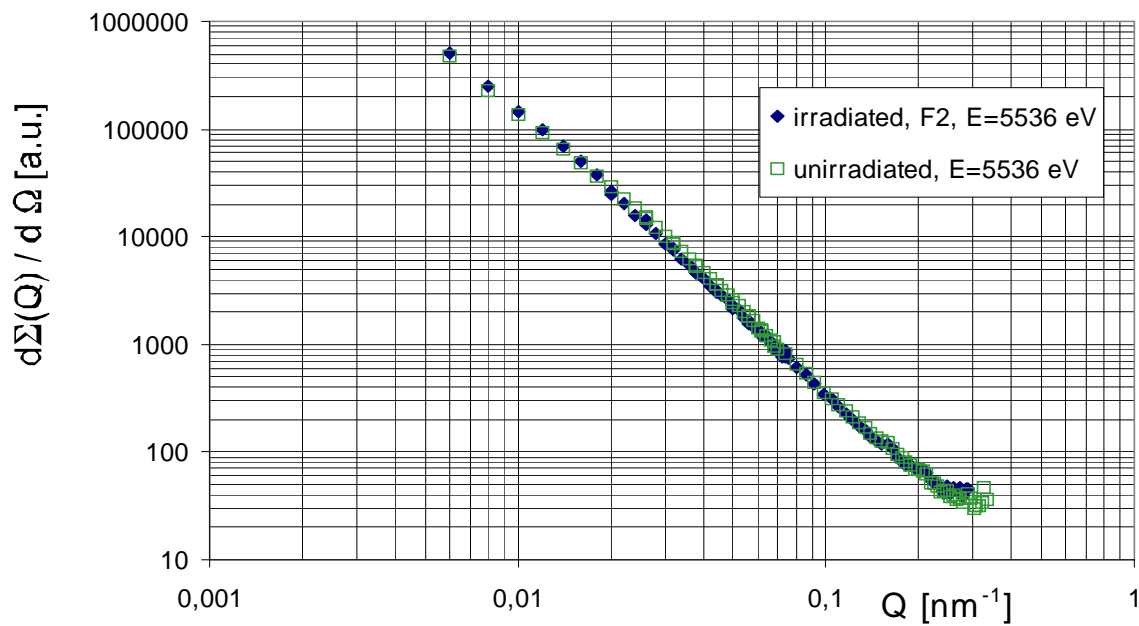


Fig. 3: SAXS intensity of the unirradiated and of the state irradiated to fluence  $F_2$

- There are irradiation-induced scattering defects.
- The irradiation defects cannot be seen by X-rays.

A detailed analysis provides further results. In Fig. 4 the size distribution function obtained from SANS is depicted. Irradiation produces a high volume fraction of nano-scaled particles (or defects) in the size range of 0.5 to 4 nm, especially after irradiation to high fluences. The size distribution of the larger particles is hardly influenced by irradiation. The A-ratio depends on the

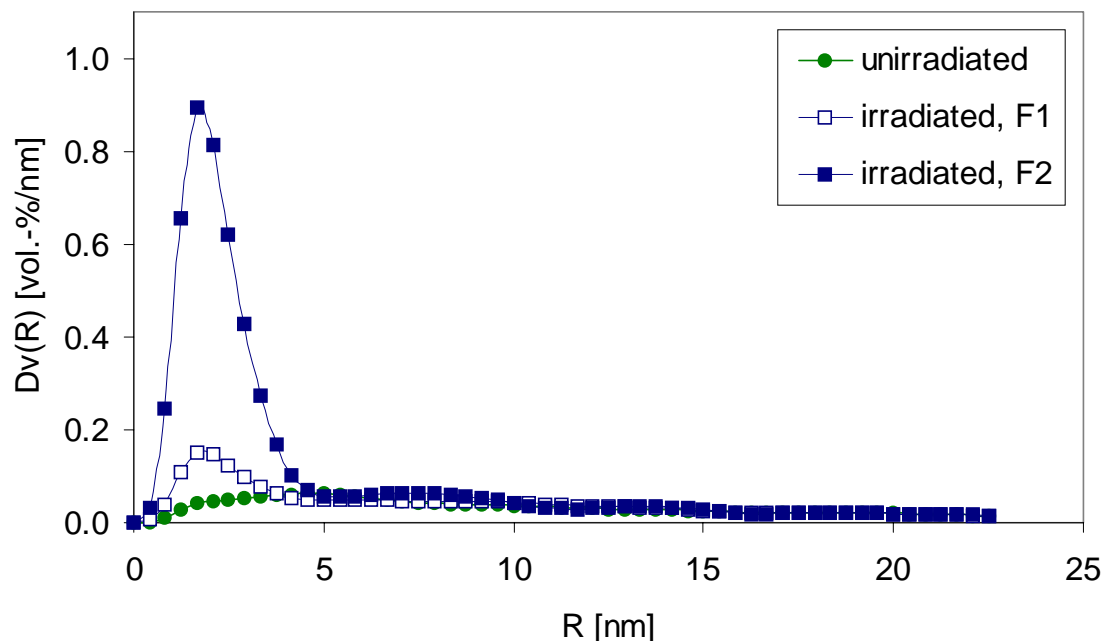


Fig. 4: Particle size distribution of the investigated material states

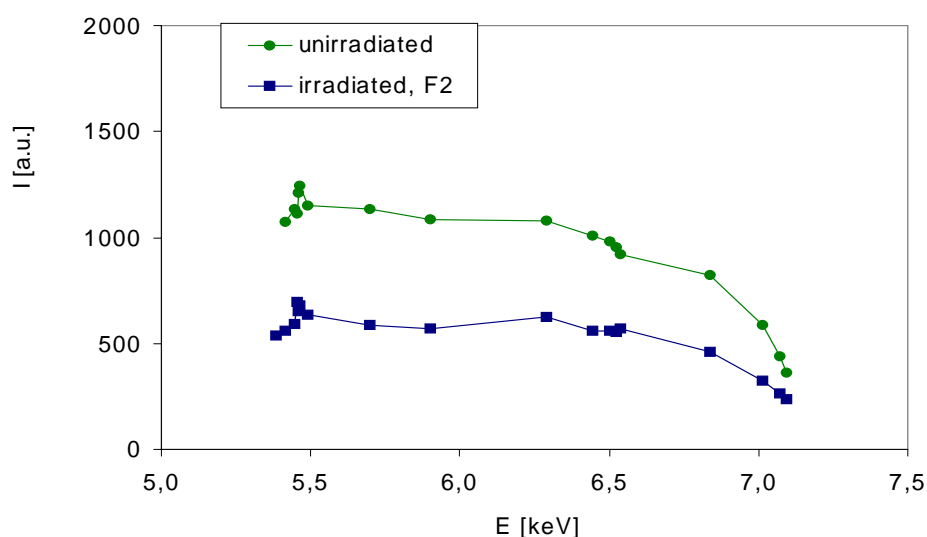


Fig. 5: Dependence of the integral SAXS intensity  $I = \int d\Sigma/d\Omega dQ$  in the range  $0.5 \leq Q \leq 1.0 \text{ nm}^{-1}$  on the X-ray energy

particle size and the fluence and changes from 2.3 for  $F_1$  and 2.0 for  $F_2$  at the size maximum up to 3.0 for the particles with a higher radius. The energy dependence of the SAXS intensity (integrated over the Q-range of  $0.5$  to  $1 \text{ nm}^{-1}$ ) is shown in Fig.5. The intensity is higher for the unirradiated state than for the irradiated one. A clear discontinuity near the absorption edges

cannot be recognized except from the decrease towards the iron absorption edge at  $E=7.112$  keV. In an earlier study [5] at VVER 440-type base metal, it was found that the irradiation-induced defects could be vanadium carbides. Therefore, the proof of the vanadium content in the irradiation defects is specially interesting. As one can show [6] the difference of the scattering cross section for the two energies of 5466 eV and 5536 eV (the K-absorption edge of vanadium lies at 5466 eV) is mainly determined by the atomic form factor  $f$  of vanadium. For the weld metal the experiment does not provide differences between the unirradiated and the irradiated states (Fig.6). Thus, a high vanadium content in the irradiation defects can be excluded for weld metal.

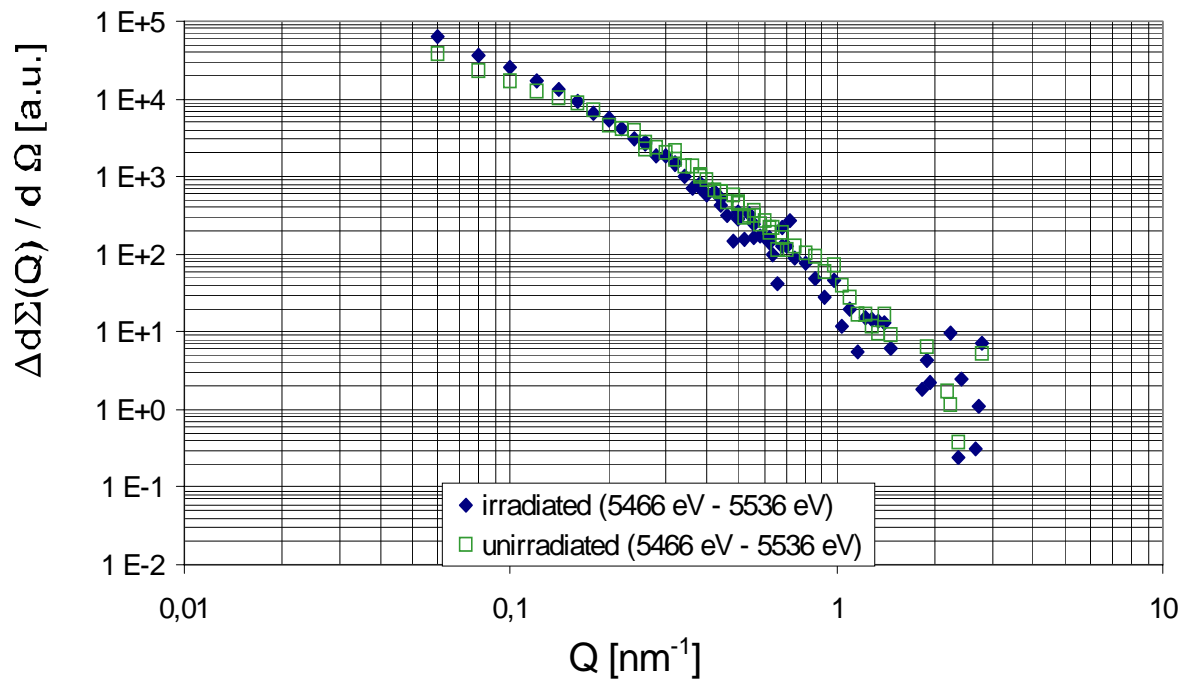


Fig. 6: Difference of the SAXS intensity of vanadium-containing inhomogeneities

It remains an open issue why the irradiation effects can be seen by SANS but not by SAXS. Therefore the scattering contrast of hypothetic structural defects was calculated. The following potential scattering defects were chosen

- vanadium carbides,
- grain boundaries,
- clusters with the same structure but other composition than the matrix.

The composition of the clusters was assumed to correspond to results of atom probe field ion microscopy (APFIM) of VVER-type base metal [7]. Fig. 7 compares the relative scattering contrasts (related to the scattering contrast of grain boundaries) for the different methods and measuring conditions. One can see that

- the vanadium carbides provide the highest scattering contrast in every case
- grain boundaries are better detectable with X-ray than with neutrons
- clusters of the above-mentioned type cannot be seen by SAXS but by SANS.

The results allow the following interpretation:

In the unirradiated state the scattering intensity is mainly caused by vanadium carbides in the

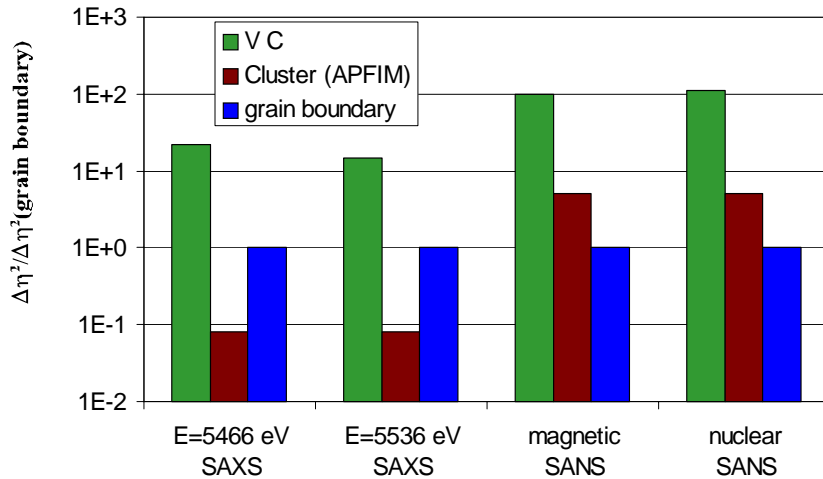


Fig. 7: Comparison of the contrast for magnetic and nuclear neutron scattering and for X-ray scattering at energies of 5466 and 5536 eV of vanadium carbide, grain boundaries and clusters detected by APFIM

ated Sv-10MFT weld metal applied for VVER 440-type reactor pressure vessels offer insights into the irradiation-induced changes of the microstructure if the experiments are analysed using the methods of contrast variation. Irradiation of that type of weld metal creates nano-scaled clusters. These clusters do not appreciably scatter X-rays but provide a strong contribution to the SANS intensity. Increasing fluence mainly changes the volume fraction of the clusters. The size and the composition keeps almost unchanged. Composition and structure of the clusters are unknown. However the assumption that the structure is similar to the matrix and the composition corresponds to those analysed by APFIM can reasonably explain the experimental findings. Prospective SANS and SAXS experiments at specimens after annealing will give additional information about the type of the irradiation defects.

## References

- [1] O. Glatter (1980), *J. Appl. Cryst.*, 13, 7
- [2] H. A. Kramer (1929), *Phys. Z.*, 30, 522
- [3] R. de L. Kronig (1926), *J. Opt. Soc. Amer.*, 12, 547
- [4] D.T. Cromer, D. Liberman (1970), *J. Chem. Phys.*, 53, 1981
- [5] M. Grosse, F. Eichhorn, J. Boehmert, G. Brauer (1996), Characterization of Irradiation-Induced Precipitates by Small Angle X-ray and Neutron Scattering Experiments, in: *Effects of Radiation on Materials 17<sup>th</sup> International Symposium*, ASTM STP 1270, D. S. Gelles, R.K. Nanstad, A. S. Kumar, E. A. Little, Eds., American Society for Testing and Materials, 1996, 1123
- [6] M. Grosse, V. Denner, J. Boehmert, M.H. Mathon (1998), Irradiation-induced Structural Changes in Surveillance Material of the VVER-440-type Welt Metal Sv-10KhMFT, submitted to *J. Nucl. Mat.*
- [7] A. Kryukov (1998), Radiation Embrittlement of WWER-type Reactor Pressure Vessel, paper on the Workshop „Composition Effects on Neutron Embrittlement“, Rossendorf

case of neutron scattering experiments and by vanadium carbides and grain boundaries in the case of X-ray experiments. Irradiation does not considerably affect the vanadium carbides and grain boundaries. But irradiation produces nano-scaled clusters enriched with solute atoms like copper, manganese, silicon, nickel and phosphorus.

## 5. Conclusion

SANS and SAXS experiments at long-time-irradiated

# COMPOSITION EFFECTS ON THE IRRADIATION EMBRITTLEMENT OF VVER REACTOR PRESSURE VESSELS

Jürgen Böhmert, Alexander Kryukov<sup>1</sup>, Yuri Nikolaev<sup>1</sup>, Dimitri Erak<sup>1</sup>

## 1. Introduction

The irradiation embrittlement of the pressure vessels of the VVER Russian type reactors is highly safety-relevant. One of the most important parameters which influences the level of embrittlement is the composition of the steel. Especially copper, phosphorus and nickel are considered as harmful [1]. Whereas the effect of copper is repeatedly proved and is already part of the legal guides for predicting the irradiation embrittlement [2], the influence of phosphorus and nickel is still a matter of investigation. Above all high nickel content of 1.5 to 2 % which is contained in the weld metal of some VVER 1000-type reactors is controversially assessed [3]. Finally the existence of synergistic effects of the several alloy elements is completely obscure. That is why an extensive irradiation programme was started. In the framework of this programme, 19 mock-up alloys with systematically varied content of copper, phosphorus and nickel are irradiated under typical VVER-operating conditions. The mechanical properties of these alloys are tested after irradiation and post-irradiation annealing in order to establish common trends of chemical composition effects on the behaviour under neutron irradiation and after thermal recovery.

For a first step, 8 alloys were selected. The selection of the alloys aimed at maximum variation of these 3 elements. This step is finished. This paper reports on the results obtained from these alloys.

## 2. Experimental

The composition of the 8 investigated mock-up alloys is given in Tab. 1. The alloys were fabricated under the same conditions in an industrial small-scale production. The final thermal treatment complies with the heat treatment of the VVER 1000-type reactor pressure vessel steel. The alloys exhibit a ferritic microstructure. Their grain size is different. Particularly the Ni-rich alloys have a fine grain. From these alloys Charpy-V standard specimens and small tensile specimens were machined. The specimens were irradiated at the surveillance positions of the VVER 440 reactors ROVNO 1 and KOLA 3 over one reactor cycle. Both reactors differ in the core design and, thus, in the neutron flux (ROVNO 1:  $0.4 \times 10^{12} \text{ n/cm}^2\text{s}$ ; KOLA 3:  $3.0 \times 10^{12} \text{ n/cm}^2\text{s}$  [ $E > 0.5 \text{ MeV}$ ]). Fluence of  $10 \times 10^{18} \text{ n/cm}^2$  ( $= F_1$ ) and  $80 \times 10^{18} \text{ n/cm}^2$  ( $= F_2$ ) [ $E > 0.5 \text{ MeV}$ ] were reached respectively. The irradiation temperature was about 270 °C.

---

<sup>1</sup> Russian Research Center „Kurchatov Institute" Moscow

Table 1: Chemical composition of the mock-up alloys (in wt.-%; Fe balance)

Code	C	S	Cu	P	Ni	Si	Mn
A	0.01	0.004	0.015	0.002	0.01	0.15	0.39
B	0.01	0.005	0.42	0.012	0.01	0.24	0.49
C	0.01	0.004	0.12	0.010	1.98	0.09	0.35
D	0.01	0.004	0.12	0.012	1.10	0.12	0.41
E	0.01	0.004	0.12	0.039	1.13	0.20	0.41
F	0.01	0.004	0.42	0.012	1.19	0.21	0.47
G	0.01	0.004	0.11	0.013	0.012	0.37	0.48
H	0.01	0.004	0.11	0.039	0.010	0.24	0.49

The specimens were tested by Charpy-V impact testing and tensile testing in the unirradiated state and the irradiated state. Before testing, a part of the specimens was annealed at 475° C/100 h after the irradiation. The ductile-brittle transition temperature was determined from the impact energy-temperature curves. The transition temperature is related to consumed impact energy of 47 J according to the Russian guide. The Russian guide uses the following relations:

$$\Delta TT_{irr} = TT_o - TT_{irr} = A_{irr} \sqrt[3]{F} \quad (1)$$

$TT_o$  or  $TT_{irr}$  are the transition temperatures in the initial state and after irradiation to the fluence  $F$  ( $F$  in  $10^{18}$  n/cm<sup>2</sup> [ $>0.5$  MeV]).  $A_{irr}$  characterizes the radiation sensitivity and depends on the content  $c$  (in wt-%) of copper and phosphorus

$$A_{irr} = 800 (C_p + 0.07 C_{Cu}) \quad (2)$$

### 3. Results

In every case, irradiation clearly affects the mechanical properties. The strength parameters (ultimate tensile stress, yield stress) increase, the ductility (uniform elongation, total elongation, upper shelf energy) is reduced and, the transition temperature is shifted to higher values. The effect on the transition temperature is the bigger the higher the content of copper (B, F), phosphorus (E, H) and nickel (C-F) and the higher the fluence (Fig. 1).

Comparing the shift  $\Delta TT_{irr}$  of the Ni-poor alloys (A, B, G, H) for the fluence  $F_1$  and  $F_2$ , it does not seem that  $\Delta TT_{irr}$  follows the relation as expected according to (1). This could result from a flux effect. A such effect is described for VVER 440-type weld metal on the base of surveillance results [4]. For comparable differences in the flux and similar level of fluence a constant shift of 40 °C to higher temperature is observed if the flux is lower. The related correction is depicted in Fig. 1 as well (red-marked points corrected).

To evaluate the composition effect the correction was used and all results were related to the fluence level  $F_1$  by means of equation (1).

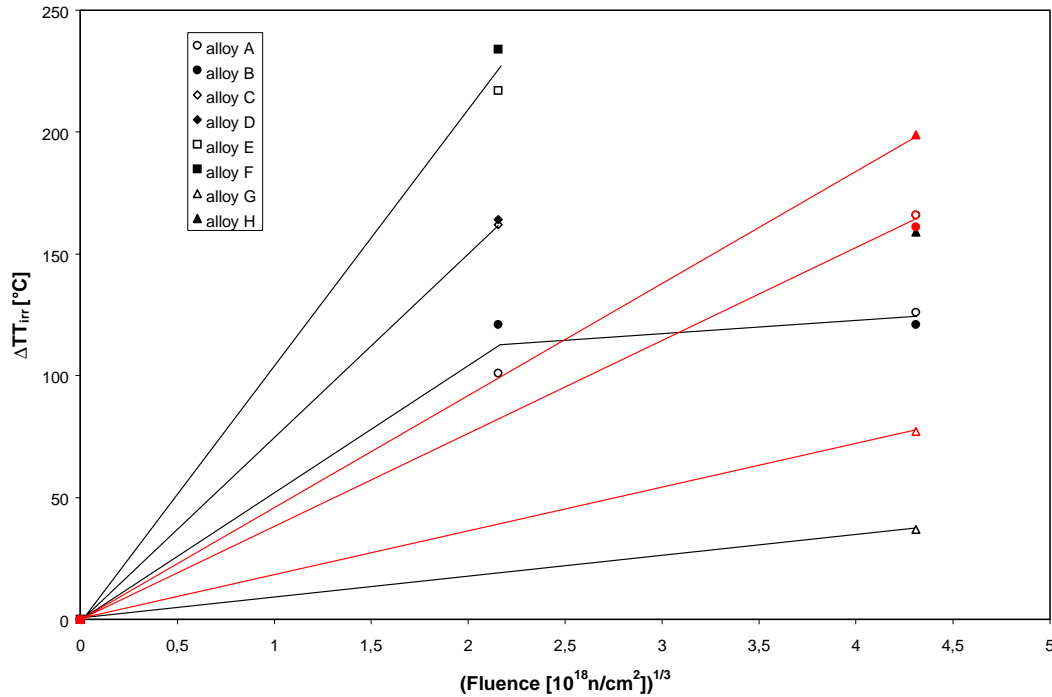


Fig. 1: Irradiation-induced shift  $\Delta T T_{irr}$  of the transition temperature (red-marked points corrected)

Fig. 2 shows the influence of the composition on the transition temperature shift more clearly. Apart from the expected copper effect, phosphorus and nickel affect the transition temperature in the same way. For Ni-poor alloys the shift seems to follow the prediction of the Russian guide for weld metal as the Figs. 3 and 4 show. Nickel produces an additional shift of the transition temperature which hardly depends on the Ni content in the investigated range between 1.1 and 2 %. It amounts to about 120 °C at a fluence of  $10 \times 10^{18} \text{ n/cm}^2$  and at a flux of  $0.4 \times 10^{12} \text{ n/cm}^2 \text{ s}$  [ $E > 0.5 \text{ MeV}$ ].

A surprisingly strong effect occurs at the very pure alloy A (A contains only Mn and Si apart from marginal residues of other elements). This is not understandable from the composition point of view and gives a hint that other irradiation defects with different efficiency as dislocation barriers are formed in a pure  $\alpha$ -iron matrix. Thus, the interaction of the solute atoms, such as copper, phosphorus or nickel, and the primary irradiation defects (vacancies, interstitials) plays an essential role in the mechanism of the irradiation embrittlement.

An influence of the composition on the annealing behaviour can also be proven (Fig. 5). For low copper or phosphorus content, annealing at 475° C/100 h removes the irradiation-induced changes of the mechanical properties completely. If the content of these elements, however, is high, then a residue of 20 to 25 % of the changes survives. Nickel has no influence on that. The pure alloy A again drops out of the trend and exhibits an „overrecovery“.

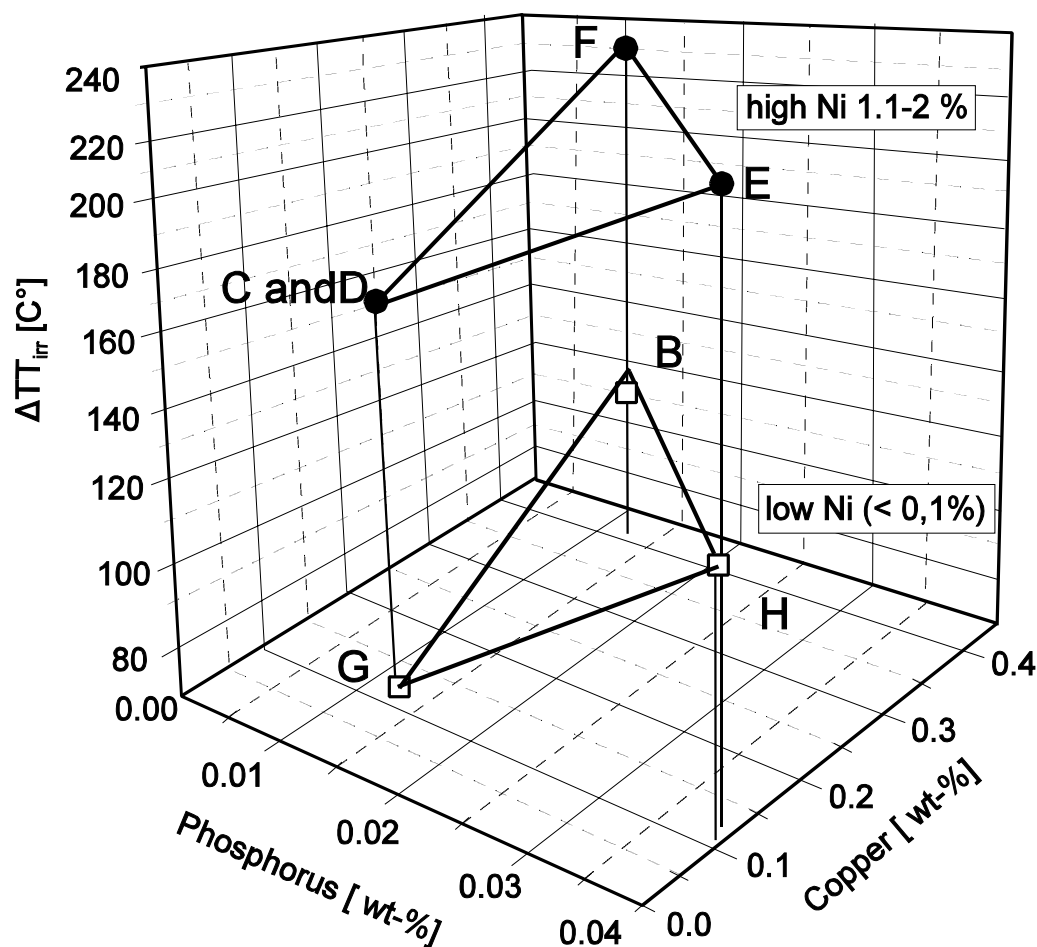


Fig. 2: Chemical composition effect on the irradiation-induced shift  $\Delta T_{ir}$  of the transition temperature

#### 4. Conclusion

The paper presents the first results of an extensive irradiation programme to characterize how the chemical composition affects the irradiation embrittlement. The harmful effect could be proven not only for copper but also for phosphorus and nickel. As the alloys exhibit a ferritic microstructure, the effect can only result from the interaction between the solute atoms and the primary irradiation defects in the iron matrix. The agreement between the results obtained with the Ni-poor alloys of this study and those achieved by the surveillance programmes with weld metal indicates that the irradiation behaviour of VVER 440-type weld metals is not essentially influenced by the metallurgical state but by the chemical composition. The recently valid guide seems to provide a useful assessment of the embrittlement for high flux levels. Ni has a clearly negative effect and must be considered for VVER 1000-type material. However, the results of this study do not suggest an increase of the irradiation sensitivity with the Ni content within the range of 1.1 to 2.0 % as often assumed. In this stage of investigation synergistic effects have not yet been proven. The programme is to be continued and completed by microstructural analysis. This is in preparation.

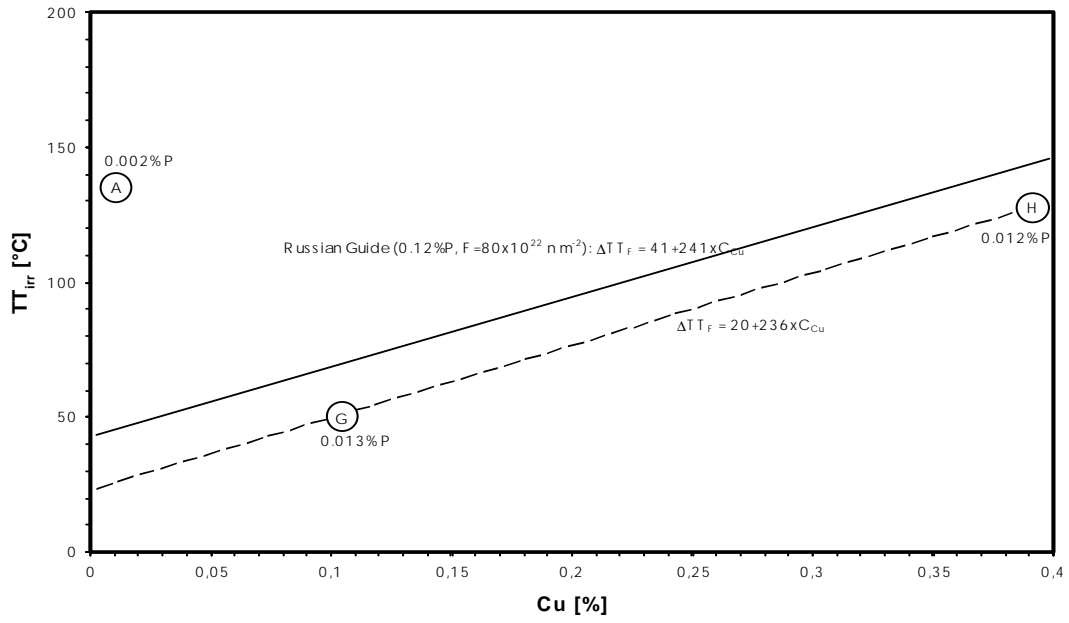


Fig. 3: Phosphorus effect on the irradiation sensitivity for mock-up alloys with low copper

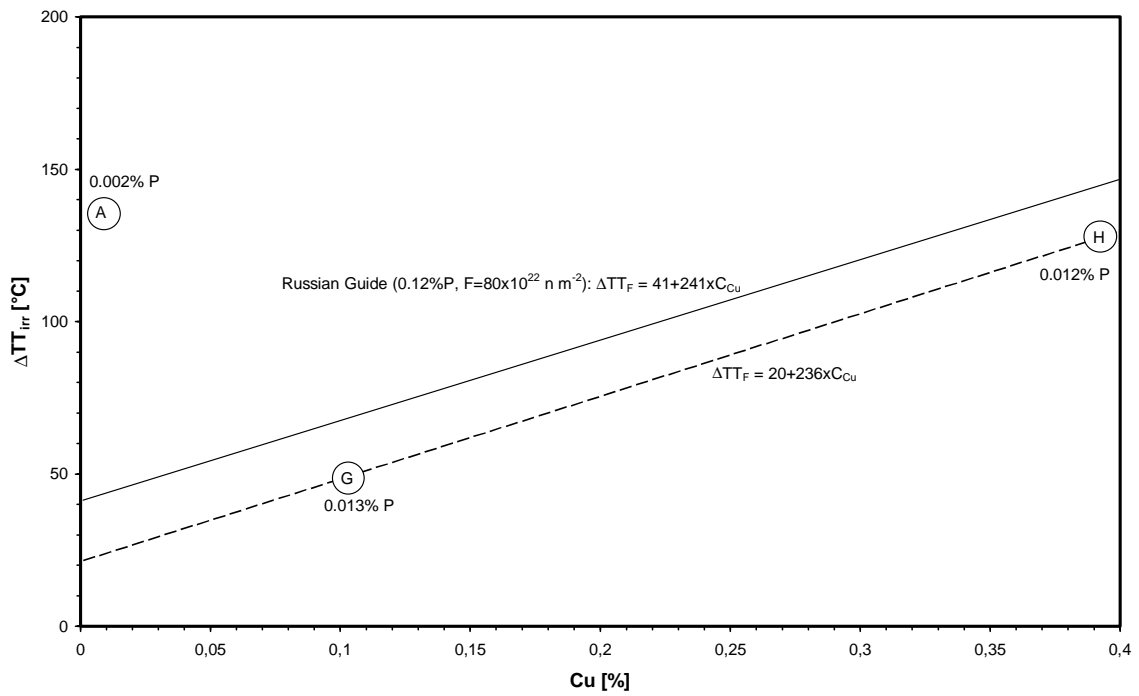


Fig. 4: Copper effect on the irradiation sensitivity for mock-up alloys with low phosphorus

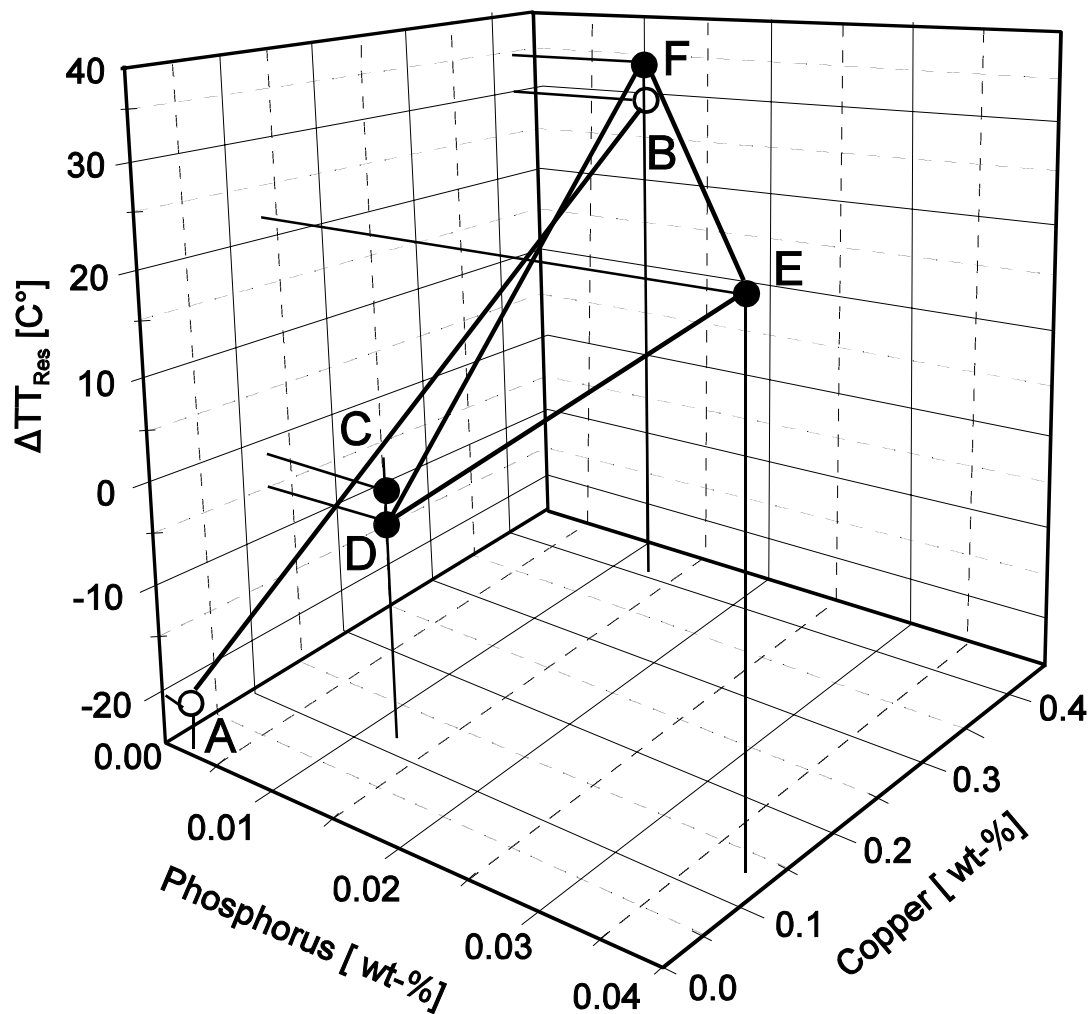


Fig. 5: Chemical composition effects on the residual shift  $\Delta T T_{Res}$  of the transition temperature (● high Ni, ○ low Ni)

## References

- [1] L.E. Steele (1970), Critical Aspects of Neutron Irradiation Embrittlement of Pressure Vessel Steels and Welds, Symposium on the Technology of Pressure Retaining Steel Components, Vail Village, 1970, M.S. Weckler (Ed.), Nuclear Metallurgy, 6, 270
- [2] P. Petrequin (1996), A Review of Formals for Predicting Irradiation Embrittlement of Reactor Vessel Materials, AMES-Report No. 6, Paris, EUR 16455
- [3] M. Brumovsky, C.Y. Rieg (1995), Problems in a Standard Surveillance Programme of WWER-1000 Reactor Pressure Vessels in Irradiation Embrittlement and Mitigation, Proc. of a IAEA Specialist's Meeting, Espoo (Finland), IWG-LMNPP 95/5, Vol. II
- [4] A.M. Kryukov (1998), The State of the Art of WWER-type RPV: Radiation embrittlement and Mitigation, Proc. of the Specialist's Meeting on Irradiation Effects and Mitigation, Vladimir (Russia)

# INCREASING THE ACCURACY OF NEUTRON LOAD DETERMINATION FOR WWER REACTOR COMPONENTS

**Bertram Böhmer, Gennady Borodkin<sup>1</sup>, Ernst Brodtkin<sup>2</sup>, Victor Gorbunov<sup>1</sup>,  
Gennadie Manturov<sup>3</sup>, Anatoli Tsiboulia<sup>3</sup>, Sergei Zaritsky<sup>2</sup>**

## 1. Introduction

The loss of ductility of the reactor pressure vessel (RPV) due to neutron irradiation and the possibly resulting brittle fracture of the vessel initiated by PTS is the most serious potential accident of WWER type reactors. In order to derive measures to reduce related risks a detailed knowledge of the neutron load is needed. Therefore, in the framework of the BMBF Reactor Safety Research Program (item "Component Safety and Quality Assurance") a project was financed aiming at an increase of the reliability of the determination of the neutron load of WWER reactor components. This project complemented the BMBF project "Development of an improved methodology for the determination of the neutron load of the pressure vessel steel of WWER-1000 type reactors" (1/1996 - 12/1997) [1]. The intention was to support powerful research groups working in Russia in the field of reactor safety and to strengthen existing cooperation. Three research groups were involved, each consisting of two Russian scientists, working in three Russian research centres, namely the Scientific and Engineering Centre for Nuclear and Radiation Safety of Russian GOSATOMNADZOR (SEC NRS) Moscow, the Russian Research Centre "Kurchatov Institute" (RRC) Moscow and the Institute of Physics and Power Engineering (IPPE) Obninsk. The objectives of the project were:

- the further development and testing of neutron data bases for fluence calculations
- providing reliable data for the evaluation of activation experiments at WWER reactors and formulation of the reactor models
- assessment and further development of methods for verifying and adjusting the calculations by means of experiments
- testing and further improvement of transport calculations with Russian data and codes
- proposals for a safer operation of WWER reactors.

In the following a short description of the obtained results will be presented. A detailed report is given in [2].

## 2. Further development and testing of data for neutron fluence calculations

Owing to advances of calculational methods and computer capacity nowadays the uncertainty of nuclear data remains as major obstacle to further increasing the accuracy of neutron fluence calculations. At the same time, scientific research capacities in the neutron data field have been reduced worldwide to a very low level although the knowledge about many neutron data is still unsatisfactory. Therefore, it seemed worthwhile to assess the neutron data libraries available for calculations in the outer region of the reactor, to improve existing data libraries by including new data and increasing their energy resolution, and to evaluate the covariances of the calculated

---

<sup>1</sup> SEC for Nuclear and Radiation Safety of Russian GOSATOMNADZOR, Moscow, Russia

<sup>2</sup> Russian Research Centre "Kurchatov Institute", Moscow, Russia

<sup>3</sup> Institute of Physics and Power Engineering, Obninsk, Russia

group fluences. These covariances are needed to get a more reliable basis for evaluating the uncertainties of calculational results and for the adjustment of calculated fluence spectra to experimental data.

The IPPE Obninsk is one of the leading institutes in nuclear data libraries. The ABBN data library is particularly well-known. It found worldwide application to fast reactors but is used now also for thermal reactor calculations in Russia and other countries. In the framework of this project an urgently necessary completion and testing of the ABBN/MULTIC data set with a tenfold increased number of neutron groups could be accomplished:

- For simple shielding benchmarks on iron spheres of different diameters (20, 30, 40, 50, 60 and 70 cm) around a  $^{252}\text{Cf}$ -source measured energy spectra of leakage neutrons and photons were compared with calculations done with 28 and 299 neutron groups and with 11 gamma groups. The found agreements between the two calculations and between experiment and calculations were reasonable.
- Neutron and gamma fluence spectra were calculated with the  $S_N$  transport code TWOTRAN at 4 different positions (core, downcomer, 1/4 thickness position of the pressure vessel and concrete shield) for a one-dimensional model of a typical pressure vessel. Results obtained from ABBN libraries with 28, 81 and 299 neutron groups were compared with each other and with results obtained from the ENDF/B-VI based VITAMIN-B6 199 group library. The ABBN 299 group spectra are very close to the VITAMIN-B6 spectra and also the spectra obtained with different ABBN group numbers are in good agreement. Differences are found in the low energy region, where probably the thermalization process is not properly described in the VITAMIN-B6 calculations. In the photon case the ABBN results are higher than the VITAMIN-B6 ones, because the ABBN-93 photon production group cross sections do not only include prompt but also delayed gamma yields. The photon spectra differ significantly for the 3 ABBN libraries, as only the 299-group library ensures the needed detailed representation of the thermal region.
- Cross section covariances calculated with the code NJOY91.91 from ENDF/B-VI nuclear data files have been compared for some important cases with covariances based on Obninsk evaluations. The agreement was reasonable. In cooperation with Forschungszentrum Rossendorf covariances of neutron fluence group spectra were calculated for the WWER-1000 pressure vessel using a one-dimensional reactor model and the Obninsk data system ABBN-93/INDECS. The fluence covariance matrix obtained for the outer boundary of the pressure vessel was compared with typical approximations used in spectrum adjustment procedures. The influence of these approximations on the adjustment results was evaluated.
- The data library ABBN/MULTIC has been extended by addition of new data, especially for the thermal region. Some errors were corrected in the data preparation code system CONSYST2 and new algorithms for calculations of  $P_N$  scattering matrices in the thermal region have been added. The library and CONSYST2 have been tested in international benchmarks by two-dimensional calculations with the code TWODANT and by three-dimensional Monte Carlo calculations with the code KENO-Va. In all considered cases the agreement with the experiments was similar or better as with ENDF/B-VI based libraries.

### **3. Development of reactor models for precise calculations of the neutron fluence at the pressure vessels of two WWER-1000 reactors**

Based on ex-vessel activation experiments at the reactors Rovno-3 (7th cycle) and Balakovo-3 (5th cycle) reactor models for neutron transport calculations have been prepared in the SEC NRS of the Russian GOZATOMNADZOR.

These models include:

- the description of the design of the reactors
- the description of the experiments
- the azimuthal-radial geometrical approximation of the reactor
- the axial-radial geometrical approximation
- material compositions and nuclear densities of model zones
- reactor operating data during the detector irradiation times (total power history, 2D assembly power distributions, coolant temperature variations)
- the description of time-dependent fission sources, including
  - 2D and 3D assembly power and burnup distributions
  - 3D pin-to-pin power and burnup distributions in the peripheral assemblies
  - heavy metal concentrations in the assemblies
  - the burnup dependence of the neutron emission.

The source data were based on neutron physical calculations of reactor cores, operational system measurements and other data compiled by the NPP staff and SEC NRS. For Balakovo-3 the data were given inside a 60° symmetry sector. For Rovno-3 a 30° sector proved sufficient. The formulated models allow three-dimensional Monte Carlo or  $S_N$  calculations as well as calculations with the method of 2D-1D synthesis.

The obtained data show the necessity of a pin-wise description of sources in the outer assemblies since the radial decline of the source strength over the peripheral assemblies approaches a factor 3. The computational models of the WWER-1000 reactors Rovno-3 (cycle 7) and Balakovo-3 (cycle 5) are the most comprehensive WWER reactor models ever made available and used for detailed 3D-neutron transport calculations in the ex-core region. The prepared data were used for  $S_N$  calculations and for Monte Carlo calculations with the FZR code TRAMO.

#### **4. Verification and Improvement of Methods of Neutron Fluence Calculations for the Pressure Vessel Region**

The calculational problem is characterized by the necessity

- to determine the neutron transport through thick layers of water and steel, whereas the neutron source is located in the core,
- to determine a detailed neutron spectrum above 0.1 MeV,
- to take into account the space and time dependence of the neutron source.

To solve this problem a 3-dimensional flux density function  $\varphi(r,\theta,z,E)$  was synthesized from two- and one-dimensional density functions in the following way:

$$\begin{aligned}\varphi(r, \theta, z, E) &= \varphi(r, \theta, E) K(r, z, E) \\ \text{with } K(r, z, E) &= \varphi(r, z, E) / \varphi(r, E),\end{aligned}$$

where  $\varphi(r, \theta, E)$  and  $\varphi(r, z, E)$  are results of two-dimensional calculations with the code DOT-3 and  $\varphi(r, E)$  is a one-dimensional solution obtained with the code ANISN. In first work steps an evaluation of the effect of different data libraries was made and the influence of different assumptions about the decrease of the source strength in the outer fuel elements on the calculated fluences was investigated. Finally, a special code was developed allowing the

transformation of the pin-wise source geometry to a fine  $(r, \theta)$ -grid. The obtained results for the 5th cycle of Balakovo-3 and the 7th cycle of Rovno-3 have been compared with experiments and results of different calculations. As example, Tab. 1 compares results from 2D-1D synthesis calculations of RRC, FRAMATOME/SEC NRS (FRAM) and results from high precision Monte Carlo calculations of FZR.

Table 1: Flux integrals above E [MeV] in n/cm<sup>2</sup>/s, spectral indices  $SI = \varphi_{>0.5\text{MeV}} / \varphi_{>3.0\text{MeV}}$  and relations between different results

$\theta$	Origin of data	E				SI
		0.1 MeV	0.5 MeV	1.0 MeV	3.0 MeV	
Max. Flux	RRC	$1.14 \cdot 10^{10}$	$5.08 \cdot 10^9$	$1.70 \cdot 10^9$	$2.29 \cdot 10^8$	22.2
	FRAM	$1.13 \cdot 10^{10}$	$4.92 \cdot 10^9$	$1.67 \cdot 10^9$	-	-
	FZR	$1.18 \cdot 10^{10}$	$4.90 \cdot 10^9$	$1.60 \cdot 10^9$	$2.12 \cdot 10^8$	23.1
	RRC / FRAM	1.01	1.03	1.02	-	-
	RRC / FZR	0.97	1.04	1.06	1.08	0.96
	FRAM / FZR	0.96	1.00	1.04	-	-
Min. Flux	RRC	$6.72 \cdot 10^9$	$2.68 \cdot 10^9$	$8.26 \cdot 10^8$	$1.06 \cdot 10^8$	25.3
	FRAM	$6.59 \cdot 10^9$	$2.50 \cdot 10^9$	$7.70 \cdot 10^8$	-	-
	FZR	$6.59 \cdot 10^9$	$2.61 \cdot 10^9$	$7.33 \cdot 10^8$	$9.41 \cdot 10^7$	27.7
	RRC/FRAM	1.02	1.07	1.07	-	-
	RRC / FZR	1.02	1.03	1.13	1.13	0.91
	FRAM/FZR	1.00	0.96	1.05	-	-

The presented calculation results agree well with each other, the maximum difference reaching 13%. In several cases it is convenient to calculate influence functions, defined as contributions of single assemblies to the neutron flux density at points of special interest at the pressure vessel. Whereas the source distribution is changing substantially due to different enrichment and burnup, the neutron transport properties of a given reactor remain practically unchanged. Obviously, once the contributions of different assemblies are calculated for a certain flux value, the flux value for any source distribution can be obtained as a simple sum of products (fuel assemblies contribution method).

Table 2: Relative contributions of 8 outer assemblies to the neutron fluence at  $E > 0.5$  MeV for equidistant angular positions  $\theta^\circ$  at the inner surface of a WWER-1000 pressure vessel

$\theta^\circ$	Number of assembly								Sum
	6	7	12	13	16	17	18	19	
0	0.005	0.103	0.039	0.786	0.005	0.053	0.0	0.003	0.994
5	0.005	0.079	0.037	0.789	0.005	0.075	0.001	0.006	0.997
10	0.004	0.045	0.035	0.723	0.009	0.161	0.001	0.018	0.996
15	0.003	0.026	0.035	0.532	0.016	0.311	0.003	0.068	0.994
20	0.002	0.013	0.030	0.275	0.026	0.418	0.010	0.222	0.996
25	0.001	0.005	0.019	0.102	0.035	0.325	0.021	0.490	0.998
30	0.001	0.003	0.012	0.042	0.037	0.221	0.027	0.56	0.999

## 5. Evaluation of the Experiments performed at Rovno-3 and Balakovo-3

Activation detectors of the SEC NRS using the reactions  $^{93}\text{Nb}(n,n')^{93m}\text{Nb}$ ,  $^{237}\text{Np}(n,f)$ ,  $^{238}\text{U}(n,f)$ ,  $^{58}\text{Ni}(n,p)^{58}\text{Co}$ ,  $^{54}\text{Fe}(n,p)^{54}\text{Mn}$ ,  $^{46}\text{Ti}(n,p)^{46}\text{Sc}$ ,  $^{63}\text{Cu}(n,\alpha)^{60}\text{Co}$ ,  $^{55}\text{Mn}(n,2n)^{54}\text{Mn}$  and  $^{59}\text{Co}(n,\gamma)^{60}\text{Co}$  were irradiated during the 7th cycle of unit 3 of the Rovno NPP and during the 5th cycle of unit 3 of the Balakovo NPP in cavities at the outer walls of the pressure vessels. Additionally, detectors of the FZR had been irradiated. In the case of Balakovo-3 also detectors of four further Russian institutes, of ECN Petten and SKODA Plzen had been applied. The irradiation and the comparison of the experimental results were done in the framework of the Balakovo-3 Interlaboratory Experiment [3]. This project covers a part of the evaluation of the Interlaboratory Experiment.

Reaction rates and spectral indices averaged over the time of irradiation were derived from the measured activities. The preliminary comparison during the Balakovo-3 Workshop in Rossendorf showed, that the independent measurement results of different participants agreed well for the  $^{54}\text{Fe}(n,p)$  monitor reaction and that there were greater differences for some other reactions and some radiation positions. A particularly interesting result of the SEC investigations was the azimuthal variation of the spectral index  $a = \text{RR}(^{237}\text{Np}(n,f)) / \text{RR}(^{54}\text{Fe}(n,p)^{54}\text{Mn})$ , indicating a substantial azimuthal variation of the neutron fluence spectrum.

## 6. Comparison of Experiments with Neutron Transport Calculations

A selection from the different comparisons described in [2] is given in tables 3 and 4.

Table 3: Comparison of RRC calculation results and SEC NRS experimental results for the azimuthal distribution of the  $^{54}\text{Fe}(n,p)$  -reaction rate at 149 cm above the core bottom

Data	$\theta^\circ$										
	6.8	9.4	15.6	23.4	32.0	37.0	47.0	50.8	55.8	58.4	62.1
$C_{\text{RRC}}/E_{\text{SEC}}$	1.14	1.15	1.17	1.18	1.14	1.13	1.08	1.07	1.08	1.10	1.11

Table 4: Comparison of calculated and measured results of RRC, SEC NRS and FZR for different azimuthal angles  $\theta$  at 149 cm above the core bottom

$\theta^\circ$	Data (C - Calcul. E - Exper.)	Detector reactions							
		$^{237}\text{Np}(n,f)$	$^{238}\text{U}(n,f)$	$^{93}\text{Nb}(n,n')$	$^{54}\text{Fe}(n,p)$	$^{58}\text{Ni}(n,p)$	$^{46}\text{Ti}(n,p)$	$^{60}\text{Ni}(n,p)$	$^{63}\text{Cu}(n,\alpha)$
9.4	$C_{\text{RRC}}/C_{\text{FZR}}$	-	-	1.02	1.02	1.02	1.06	-	0.97
	$C_{\text{FZR}}/E_{\text{FZR}}$	-	-	1.01	1.02	1.08	1.00	-	1.02
	$C_{\text{RRC}}/E_{\text{FZR}}$	-	-	1.03	1.04	1.10	1.06	-	0.99
	$C_{\text{RRC}}/E_{\text{SEC}}$	0.87	-	-	1.15	1.13	-	0.88	1.06
32	$C_{\text{RRC}}/C_{\text{FZR}}$	-	-	1.09	1.08	1.08	1.12	-	1.00
	$C_{\text{FZR}}/E_{\text{FZR}}$	-	-	0.85	0.97	1.00	0.91	-	0.96
	$C_{\text{RRC}}/E_{\text{FZR}}$	-	-	0.93	1.05	1.08	1.02	-	0.96
	$C_{\text{RRC}}/E_{\text{SEC}}$	0.85	0.99	-	1.14	1.14	-	0.84	1.05
55.8	$C_{\text{RRC}}/E_{\text{SEC}}$	0.83	0.91	-	1.08	1.08	-	0.85	1.04

The RRC calculations coincide within 10% with the FZR calculations and measurements, whereas their differences with the SEC NRS measurements are somewhat larger for some detector types and irradiation positions. The participants of the Balakovo-3 Workshop in Rossendorf recommended to define a benchmark for the verification of fluence calculation methods based on the results of the Balakovo-3 Interlaboratory Experiment.

## 7. Summary and Proposals

By formulating calculational models and providing data for the evaluation of ex-vessel neutron activation experiments a reliable basis has been established for the neutron load assessment of WWER-1000 reactors.

The leading Russian nuclear data library ABBN/MULTIC has been improved and tested. The uncertainties affecting the calculations of the fluence spectrum at the outer boundary of the pressure vessel have been analyzed and a spectrum covariance matrix has been derived.

The methodologies for the measurement of activation rates and for calculations of fluence spectra and activation rates have been further developed and tested by interlaboratory comparisons. It was demonstrated, that ex-vessel dosimetry in connection with advanced calculational methods can contribute substantially to a reliable determination of the pressure vessel neutron load.

To contribute to a safer operation of WWER type reactors it is proposed

- to create a full-scale 3D ex-vessel fluence benchmark for the standard WWER-1000 RPV on the basis of the Balakovo-3 Experiments results,
- to use ex-vessel dosimetry experiments to validate the calculational assessment of the RPV neutron load,
- to use routinely the method of fuel assemblies contributions (Greens' function method) for fuel cycle optimization in order to minimize the RPV neutron load.

## References

- [1] H.-U. Barz, B. Boehmer, J. Konheiser and I. Stephan (1998), Entwicklung einer fortgeschrittenen Methodik zur Bestimmung der Neutronenbelastung des Druckbehältermaterials vom Reaktor des Typs WWER-1000, Final Report BMBF Project 1501022, Report FZR-222
- [2] B. Böhmer, G. I. Borodkin, E. B. Brodtkin, V. P. Gorbunov, G. N. Manturov, A. M. Tsiboulia, S. M. Zaritsky (1998), Erhöhung der Zuverlässigkeit der Bestimmung der Neutronenbelastung von WWER-Reaktorkomponenten zwecks Ableitung von Vorschlägen für eine sicherere Betriebsführung von WWER-Reaktoren, Final Report BMBF Project 1501021, Report FZR-220
- [3] G. Borodkin, O. Kovalevich (1996), Interlaboratory VVER-1000 Ex-Vessel Experiment at Balakovo-3 NPP, Proceedings of the Ninth International Symposium on Reactor Dosimetry, Prag Sept. 2-6, 1996, Eds H. Ait Abderrahim, P. D'hondt, B. Osmera, World Scientific Publishing, Singapore (1998) ISBN 981-02-3346-9, pp 294-301

# INFLUENCE OF THE NUMBER OF ENERGY GROUPS ON THE ACCURACY OF NEUTRON FLUENCE CALCULATIONS

Hans-Ulrich Barz and Jörg Konheiser

## 1. Introduction

The question how many groups are necessary to obtain all needed integral quantities for the neutron load of pressure vessels and detector positions outside of the vessel with sufficient accuracy is of general interest. Until now, there are no systematic investigations on this question. In principle 3-dimensional consideration is required for such neutron load calculations. Therefore, an estimation of the needed number of groups can be of interest to minimize calculation time.

One general problem is the  $P_L$ -approximation of the angular distributions for the transfers between different groups. For elastic scattering this  $P_L$ -approximation becomes poorer with increasing number of groups. As deterministic methods generally use the  $P_L$ -approximation they cannot be used for investigations of the errors caused by the group approximation.

We have investigated this problem applying group Monte-Carlo but nearly exact representation of this elastic slowing down without  $P_L$ -approximation. The calculations were directed to assess the neutron fluence of a Russian WWER-1000 reactor. For that a simplified geometrical model of this reactor type has been used.

## 2. Methodical approach

The 3-d Monte Carlo code TRAMO has been especially developed for the investigation of the neutron load of reactor vessels [1-5]. First the elastic transfer  $f_{i \leftarrow j}(w)$  has been treated as for deterministic calculations by the  $P_L$ -approximation. This approximation can give negative contributions to the function  $f_{i \leftarrow j}(w)$  depending on the cosine of the scattering angle for a given transfer from group  $j$  to group  $i$ . This can be overcome in Monte Carlo calculations by changing the distribution  $f_{i \leftarrow j}(w)$  in such a way that the new distribution is positive and has (nearly) the same  $L+1$  moments as the  $P_L$ -approximation [7]. Another way is to use the normalized absolute part of  $f_{i \leftarrow j}(w_i)$  instead of  $f_{i \leftarrow j}(w)$  and then multiplying the neutron weight by the factor  $G$  (if  $w_i$  is randomly selected from  $f_{i \leftarrow j}(w)$ )

$$G = \frac{f_{i \leftarrow j}(w_1)}{|f_{i \leftarrow j}(w_1)|} * \int |f_{i \leftarrow j}(w)| d\omega \quad (1)$$

This factor can have a negative sign because of the first part. If negative parts of  $f_{i \leftarrow j}(w)$  occur the integral is greater than 1.

The calculation time is strongly increasing for increasing number of groups. The reason is that for elastic scattering and higher number of groups the function  $f$  becomes more and more similar to a delta function and the  $P_L$ -approximation gives more negative parts. Therefore, also the  $P_L$ -approximation itself is less justified because the representation of delta-functions by  $P_L$ -

expansion is very poor. This can be illustrated in Fig.1 where two different delta functions ( $f_0=d(w)$  and  $f_1=d(w-1)$ ) are represented by a  $P_5$ -approximation. It is obvious that both approximations are bad,  $f_0$  even extremely poor.

If the results obtained with a different number of groups are compared one must have in mind that the differences of results may not only be caused by the different group approximations. As mentioned above errors are also introduced by the not justified  $P_L$ -approximation of the elastic transition function. Nevertheless, as a first step such calculations have been performed [3,6].

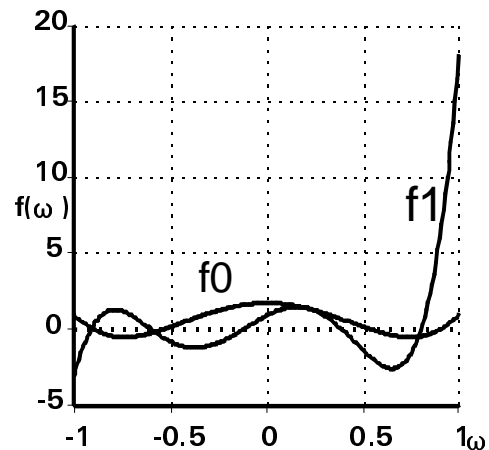


Fig. 1:  $P_5$ -approximation of delta functions

In the next step we have used within the Monte Carlo code another procedure to handle the elastic transitions. At first an angle is selected from the always positive function  $F(w,iso)$  which gives the angular distribution for elastic scattering at a certain isotope in general and not only for a particular transition between two groups. This function  $F(w,iso)$  is much smoother than the function  $f_{i \leftarrow j}$  and only depends on the neutron energy and the isotope but not on the number of groups. This elastic scattering angular distribution was represented by 32 equally probable cosine bins. This method is also used in the code MCNP [8].

The equally probable cosine bins can be determined by the code NJOY [9] for each single isotope and for a net of energy points. The Monte Carlo game has to be changed because now for each elastic scattering the responsible isotope must be selected. For a particle with an arbitrary energy we use these functions  $F(w,iso)$  of the two neighbouring energy points for interpolation. We can first select the scattering angle. Then, by the scattering laws in the cm-system, the energy loss of the neutron and in this way the new energy and energy group are calculated.

For the wanted comparison this way of calculation is not only much more accurate as the  $P_L$ -expansion method mentioned above but also independent on the group structure and the number of groups [3,6]. The calculation time was proved to be nearly independent of the number of groups. All the results presented further on are based on this method.

### 3. Model description

In Fig. 2 a top view of a symmetry sector of the WWER-1000 reactor Balakovo-3 is shown.

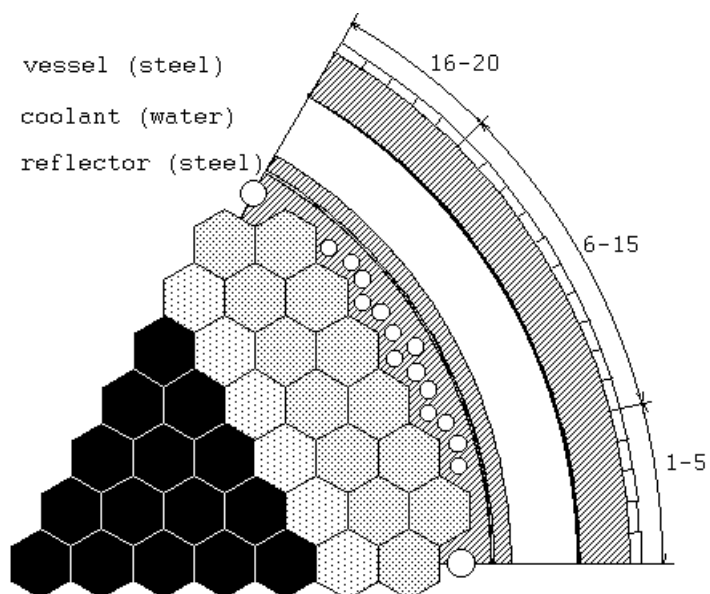


Fig. 2: Top view of the reactor Balakovo-3

As source regions only the two outer rows of fuel elements are taken into account. The next row is used as reflection region and the inner elements are assumed to be black. The real 3-dimensional source distributions are considered. For each fuel element 10 height layers of different sources are treated and each fuel element is horizontally divided into two parts to take into account the dependence of the source intensity over the cross section of the fuel element. The radial distances of the detector regions from the outer core boundary are approximately between 64 and 80 cm. The fluences are calculated at 20 angle sectors as illustrated in Fig. 2 in a given height interval (mid plane) of the outer boundary of the pressure vessel.

The representation of the results is restricted to some integral quantities as described in section 4. This model is a simplification in so far as it can not take into account the pin-wise structure of the sources. For a more detailed model with pinwise structure of sources 123-group calculations were performed. The results showed very good agreement with the activation detector measurements [3].

#### 4. Results

Using the described method to treat the elastic transition probability the results of calculations with different numbers of groups give the real differences due to the group approximation. The obtained differences between the different group numbers are remarkably smaller than the obtained differences with the  $P_L$ -approximation method mentioned above [3,4].

58 groups, 123 groups, 246 groups and 492 groups were used within an energy range above 20 keV on the base of the ENDF-B6 [10] data library. For representation purposes all results have been condensed to a coarse group structure of 29 groups. The differences of the following integral quantities are represented within the tables 1-3:

- The reaction rates obtained with the response functions of the detectors  $^{93}\text{Nb}$ ,  $^{54}\text{Fe}$ ,  $^{58}\text{Ni}$ ,  $^{46}\text{Ti}$ ,  $^{63}\text{Cu}$ , (columns 1 to 5)
- The dpa-values using group dependent dpa cross sections (column 6)
- Fluence integrals greater 0.1, 0.5 and 1.0 MeV( columns 7 to 9)

Table 1: Mean deviations of integral quantities in percent of different group calculation referring to 492 group calculation

Groups	Nb93	Fe54	Ni58	Ti46	Cu63	dpa	Fl>1.	Fl>.5	Fl>.1
246	-.61	-.34	-.41	-.36	-.44	-.41	-.88	-.54	-.34
123	-.80	-.75	-.80	-.77	-.94	-1.2	-.92	-.40	-1.0
58	-1.1	-1.0	-1.1	-1.4	-1.8	-1.7	-1.8	-.62	-1.3

Table 2: Difference of integral quantities at locations near and far from the core in percent near (1-5, 16-20, see fig. 2)

Groups	Nb93	Fe54	Ni58	Ti46	Cu63	dpa	Fl>1	Fl>.5	Fl>.1
246	-.57	-.24	-.32	-.26	-.36	-.39	-.86	-.46	-.39
123	-.83	-.68	-.73	-.73	-.91	-1.1	-.90	-.26	-.93
58	-1.1	-.92	-1.0	-1.3	-1.7	-1.7	-1.8	-.54	-1.3

far (6-15, see fig. 2)

Groups	Nb93	Fe54	Ni58	Ti46	Cu63	dpa	Fl>1	Fl>.5	Fl>.1
246	-.69	-.52	-.57	-.53	-.59	-.44	-.91	-.65	-.38
123	-1.1	-.88	-.93	-.83	-.99	-1.3	-.98	-.63	-1.1
58	-1.2	-1.2	-1.2	-1.6	-2.1	-1.7	-1.8	-.76	-1.3

Table 3: Maximum deviation of integral quantities in percent of different group calculation for 20 detector positions referring to 492 group calculation

Groups	Nb93	Fe54	Ni58	Ti46	Cu63	dpa	Fl>1	Fl>.5	Fl>.1
246	-.94	-1.3	-1.3	-1.4	-1.2	-.71	-1.5	-1.0	-1.6
123	-1.7	-1.8	-1.8	-1.7	-1.9	-1.7	-1.8	-1.1	-1.4
58	-1.5	-2.5	-2.3	-2.8	-2.9	-1.9	-2.4	-.97	-1.5

These deviations for different group numbers are represented not only for the mean values ( table 1), but also for intervals near and far from the core (table 2). Additionally ,the maximum deviations are given when all intervals are considered (table 3).

The statistical errors of the single results for different group number calculation were within the range of .02%-.07%. The errors of deviations given in table 1 and table 2 are smaller than 20%. For the values table 3 errors up to 35% are possible.

## 5. Conclusion

These results have quite general a meaning for shielding calculations. Therefore, if applying deterministic codes, it can be recommended not to use too many groups. The errors connected with the  $P_L$ -approximation could cause differences greater than those associated with the group number.

The calculation time is nearly independent from the used number of groups when specially treating the anisotropy of the elastic scattering in Monte Carlo calculations. After these investigations it can be stated that the effects of the number of groups on the calculated quantities is relatively small. This is in contradiction to assertions made in [11] based on pure  $P_L$ -approximation.

As expected the differences are slightly increasing with increasing distance source-detector as shown in Table 2. In general the results reveal the tendency that for increasing number of groups the shielding effect is decreasing. This shall be illustrated by means of a very simple example comparing the case of a given number of groups and the case, when each group is divided into 2 equal parts.

The probability  $p$  to overcome a shielding distance  $x$  from the source without further collisions can be expressed for a given group with the total cross section  $S$  as

$$p = \exp(-S \cdot x). \quad (2)$$

If this group is divided into two equal parts instead of  $p$  the quantity  $P$  provides the shielding probability

$$P = .5 \cdot \exp(-S_1 \cdot x) + .5 \cdot \exp(-S_2 \cdot x). \quad (3)$$

For the comparison the one group cross section  $S$  must be expressed as  $S = (S_1 + S_2) / 2$ .

If this is introduced into the expression for  $p$  it is easy to see that generally  $p$  is smaller than  $P$  because the arithmetic mean value is greater than the geometric mean value. The equality is only valid for  $S_1 = S_2 = S$ .

## References

- [1] H.-U. Barz (1990), TRAMO - a Flexible Multigroup Neutron Transport Code on the Basis of the Monte Carlo Method for Flux Calculations, Rossendorf, Report ZfK- 705
- [2] H.-U. Barz, G. Borodkin, B. Boehmer, J. Konheiser, I. Stephan (1996), Determination of Pressure Vessel Neutron Fluence Spectra for a Low Leakage Rovno-3 Reactor Core Using Three Dimensional Monte Carlo Neutron Transport Calculations and Ex-vessel Neutron Activation Data, in H.A. Abderrahim, P. D'hondt and B. Osmera (Ed.), Proceedings of the 9th International Symposium on Reactor Dosimetry, Prag (pp.58-66)
- [3] H.-U. Barz, B. Böhmer, J. Konheiser, I. Stephan (1998), Entwicklung einer fortgeschrittenen Methodik zur Bestimmung der Neutronenbelastung des Druckbehälter vom Reaktor des Typs WWER-1000, Rossendorf, Report FZR-222
- [4] H.-U. Barz, W. Bertram (1992), Calculation of neutron fluence in the region of the pressure vessel for the history of different reactors by using the Monte-Carlo Method, Nuclear Engineering and Design 137, 71
- [5] H.-U. Barz, B. Böhmer, J. Konheiser, I. Stephan (1995), Ermittlung der Neutronendosis von bestrahlten WWER-Reaktordruckbehältermaterialien, Report FZR-87
- [6] H.-U. Barz, W. Bertram, J. Konheiser, I. Stephan (1998), High-Precision Monte Carlo Calculations, Experimental Verification and Adjustment of Fluences in the Pressure Vessel Cavity of a VVER-1000, Proceedings ANS Radiation Protection and Shielding Division Topical Conference Technologies for the New Century, Nashville, Tennessee, USA, Vol. 1, p. 447-454

- [7] L.L. Carter, C.A. Forest (1976), Transfer Matrix Treatments for Multigroup Monte Carlo Calculations - The Elimination of Ray Effects, *Nuclear Science and Engineering* 57, 45
- [8] J.F. Briesmeister (1993), MCNP - a General Monte Carlo N-particle Transport Code (version 4A) Manuel, Los Alamos, LA-12625-M
- [9] R.E. MacFarlane, D.W. Muir (1994), The NJOY Nuclear Data Processing System (Version 91), Los Alamos, LA-12740-M
- [10] P.F. Rose, C.L. Dunford (1990), Data Formats and Procedures for the Evaluated Nuclear Data File ENDF-B6, Brookhaven, BNL-NCS-44945
- [11] B. Petrovic, A. Haghigat (1996), New Directional Theta-Weighted (DTW) Differencing Scheme and Reduction of Estimated Pressure Vessel Fluence Uncertainty, in H.A. Abderrahim, P. D'hondt and B. Osmera (Ed.), *Proceedings of the 9th International Symposium on Reactor Dosimetry, Prag* (pp.746-753)

# REACTIVE TRANSPORT MODELLING OF A MIXED EQUILIBRIUM-KINETIC SYSTEM

Roland K uchler and Klaus Noack

## 1. Introduction

A computer code was developed for the description of the reactive transport of chemicals in the unsaturated zone. The processes modelled by this code can be assigned to three categories: motion of water, chemical interactions, and species transport. Each part is a separate sub-model within the code. This contribution addresses the issue of the chemical weathering of pyrite, calcite and uraninite, and the transport of these weathering products downwards through a 10 m thick soil matrix. Transport equations can be derived for chemical species carried with the water. The solute transport system which is used to simulate this process incorporates the effects of hydrodynamic dispersion, non-linear reaction equations and kinetic chemical interaction between aqueous and solid phases (chemical weathering). At each time step, the Richards equation (sub-model water motion) and the transport equations are first solved by an implicit difference method. The chemical equilibrium sub-model is then called to calculate the distribution of chemical species. These two steps are repeated until the solution is obtained. The water motion is described in detail in the annual reports 1996,1997. For the annual motion of water through two soils, sandy silt (A) and silty sand (B), the transport system is solved numerically.

## 2. Transport of reacting solutes

In order to reach the aquifer, water from precipitation infiltrates through the ground surface and percolates downwards through the unsaturated zone. The same is true for chemical species carried with the water. These species may be already present in the water reaching the ground surface or they may be added and removed to/from the water by dissolution, adsorption, and chemical reactions along its path from the ground surface to the underlying aquifer. Simplified models for solute transport in the unsaturated zone lump the effects of several processes. This can be illustrated best in the one-dimensional convective-dispersive solute transport equation [1] written as,

$$w \frac{\partial C_i}{\partial t} = -v \frac{\partial C_i}{\partial z} + \frac{\partial}{\partial z} \left\{ \alpha_L |v| \frac{\partial C_i}{\partial z} \right\} + q_i(z, t, pH) + \sum_{j=1}^n S_{ij}(C_1, \dots, C_n), \quad i = 1, \dots, n \quad (1)$$

Here  $w$  is the volumetric water content of the soil and  $v$  is the water flow per unit area (Darcy-velocity)(m / h). For the flow through the unsaturated soil horizon  $w$  and  $v$  are not constants, but are functions of the negative pressure of matrix suction of soil.  $C_i(z, t)$  is the solute concentration (mol / L),  $q_i = q_i(z, t, pH)$  is a production function (mol / L / h), and  $\alpha_L$  is the dispersivity of the medium(m).  $\sum S_{ij}$  represents the chemical reactions, which take place in the water path and  $n$  is the number of components and species. This term can be viewed as the rate to maintain the reaction in equilibrium (see Table 1). The boundary conditions are as follows:

- At the ground surface a mixed von-Neumann / Dirichlet boundary condition is valid specifying the solute flux:  $v(0,t)C_i - \alpha_L |v(0,t)| \frac{\partial C_i}{\partial z} = v_0(0,t)C_i^{rain}$  (e. g.  $i = \text{CO}_2$ ).
- The free outflow at the outlet ( $z_0=10\text{m}$ ) is described by the boundary condition:  $\frac{\partial C_i(z \approx 1, 2z_0)}{\partial z} = 0$ .

## 2. 1. Simulation of a mixed equilibrium-kinetic system by kinetic formulation

The underlying model for representing the chemistry in waters is the assumption that the interactions between ions results in the formation of ion pairs through ion association. In other words, the model relies on being able to describe the association of any chemical species with a limited set of other species in solution, known as components, according to the general equation:



where capitals are used for the chemical entities and the  $\nu_k$  for their stoichiometric coefficients. For the formation of an ion pair, Guldberg and Waage's Law of Mass Action is valid:

$$a_A^{\nu_A} \cdot a_B^{\nu_B} = K \cdot a_C^{\nu_C},$$

where  $a_k$  is the thermodynamic activity of the  $k$ th component or specie and  $K$  is known as the equilibrium constant for the formation of species,  $C$ .

Table. 1: Aqueous reactions and their equilibrium conditions

Chemical Reaction	Mass action law
$\text{H}^+ + \text{OH}^- \Leftrightarrow \text{H}_2\text{O}$	$a_{\text{H}^+} a_{\text{OH}^-} = 10^{-7,99}$
$\text{H}^+ + \text{HSO}_4^- \Leftrightarrow \text{H}_2\text{SO}_4$	$a_{\text{H}^+} a_{\text{HSO}_4^-} = 10^6 a_{\text{H}_2\text{SO}_4}$
$\text{H}^+ + \text{SO}_4^{2-} \Leftrightarrow \text{HSO}_4^-$	$a_{\text{H}^+} a_{\text{SO}_4^{2-}} = 10^{1,08} a_{\text{HSO}_4^-}$
$\text{H}^+ + \text{CO}_3^{2-} \Leftrightarrow \text{HCO}_3^-$	$a_{\text{H}^+} a_{\text{CO}_3^{2-}} = 10^{-7,33} a_{\text{HCO}_3^-}$
$\text{H}^+ + \text{HCO}_3^- \Leftrightarrow \text{H}_2\text{CO}_3$	$a_{\text{H}^+} a_{\text{HCO}_3^-} = 10^{-3,35} a_{\text{H}_2\text{CO}_3}$
$\text{Ca}^{2+} + \text{SO}_4^{2-} \Leftrightarrow \text{CaSO}_4$	$a_{\text{Ca}^{2+}} a_{\text{SO}_4^{2-}} = 10^{0,69} a_{\text{CaSO}_4}$
$\text{Ca}^{2+} + \text{CO}_3^{2-} \Leftrightarrow \text{CaCO}_3$	$a_{\text{Ca}^{2+}} a_{\text{CO}_3^{2-}} = 10^{-0,15} a_{\text{CaCO}_3}$
$\text{UO}_2^{2+} + e^- \Leftrightarrow \text{UO}_2^-$	$a_{\text{UO}_2^{2+}} a_{e^-} = 10^{-0,58} a_{\text{UO}_2^-}$
$\text{UO}_2^{2+} + \text{SO}_4^{2-} \Leftrightarrow \text{UO}_2\text{SO}_4$	$a_{\text{UO}_2^{2+}} a_{\text{SO}_4^{2-}} = 10^{-0,15} a_{\text{UO}_2\text{SO}_4}$
$\text{UO}_2^{2+} + \text{CO}_3^{2-} \Leftrightarrow \text{UO}_2\text{CO}_3$	$a_{\text{UO}_2^{2+}} a_{\text{CO}_3^{2-}} = 10^{-7,09} a_{\text{UO}_2\text{CO}_3}$
$\text{Ca}^{2+} + \text{SO}_4^{2-} + \text{H}_2\text{O} \Leftrightarrow \text{CaSO}_4 \cdot \text{H}_2\text{O}$	$a_{\text{Ca}^{2+}} a_{\text{SO}_4^{2-}} = 10^{1,5}$

All  $a_k$  in mmol / L,  $k = \text{H}^+, \dots, \text{UO}_2^+$

To do the calculation it is assumed that the following homogeneous reactions assembled in Table 1 take place in the aqueous phase, and it is additionally assumed that the macroscopic flow processes are slow enough to allow local equilibrium to be achieved by the reactions. This assumption makes it possible to solve the transport equation and the set of equilibrium chemistry equations separately, with iterations in between. At each time step the Richards equation provides  $w$ ,  $v$  and the chemical transport equations are solved first by implicit difference methods described in [2]. The equilibrium chemistry calculations are then carried out to determine the chemical speciation and reaction mass transfer in each space element. The Newton-Raphson method is employed to solve the set of chemical non-linear algebraic equations (Table 1). Iterations between transport and chemistry yield the common solution. The iteration is continued until the errors are less than a prescribed limit. In order to eliminate the arbitrary initial conditions of the differential equations the calculation is repeated until the quasi steady state appears. Within this loop the initial condition is replaced by the distribution of the preceding step. In the case A the stationary state is achieved after 4 years and in case B after 3 years, respectively.

For aqueous species, activities and concentrations  $C$  are related to each other by means of an activity coefficient  $\gamma$ . The activity coefficients  $\gamma_k$  are functions of all aqueous concentrations. The Davies equation [3]

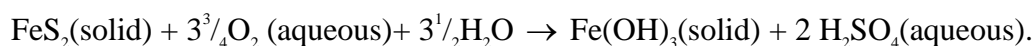
$$\lg \gamma_k = -\alpha \cdot z_k^2 \left( \frac{\sqrt{I}}{1 + \sqrt{I}} - 0,3 \cdot I \right) \quad (2)$$

is one possibility for such a function, but there are more. With this equation the  $\gamma_k$  were calculated. In (2)  $z_k$  is the charge of the  $k$ th aqueous chemical ion,  $\alpha$  is a constant depending on the dielectric constant of the solvent and temperature ( $\alpha = 0,5$  for  $T = 25^\circ\text{C}$ ), and  $I$  is the ionic strength, defined as

$$I = 0,5 \cdot \sum_{k=1}^{N_{\text{species}}} z_k^2 C_k. \quad (3)$$

Chemical reactions take place in heterogeneous systems, where different phases are in contact with each other. Thus, solutes often react with the surfaces of the water-conducting channels along which they are transported. The reaction may be for example in the form of mineral dissolution (chemical weathering) leading to changes of the reacting solutes. The results of these reactions are the sources of radio-elements and heavy metals. For these reactions chemical equilibrium cannot be assumed, and kinetic laws have to be applied to represent the real processes. Heterogeneous reactions involving minerals are generally slow compared to aqueous homogeneous reactions. Several options are available if a kinetic condition is specified. Almost all kinetic models are based on the assumption that the reaction rate depends on the surface area of the mineral.

The dissolution of pyrite (oxidation) involved in the chemical weathering is considered as:



That means, a dissolution of 1 mol of  $\text{FeS}_2(\text{solid})$  (needs  $3\frac{3}{4}$  mol dissolved oxygen) will supply 1 mol  $\text{Fe}(\text{OH})_3$  (ferrihydrite) and 2 mol  $\text{H}_2\text{SO}_4(\text{aqueous})$ . This reaction is extremely exothermic, releasing  $-1,468$  kJ of heat per mole of pyrite oxidized. The source term for  $\text{H}_2\text{SO}_4(\text{aq})$  by dissolution of pyrite can be expressed in the form [4]:

$$q_{H_2SO_4}^s = q_{H_2SO_4}^0 \cdot U(pH) \cdot \sqrt{p_{O_2}(z) / p_{O_2}(0)}, \quad q_{H_2SO_4}^0 = 8,3 \cdot 10^{-7} \text{ mmol} / \text{cm}^2 / \text{s},$$

$$U(pH) = 1,29 / (1 + 10^{2,5-pH} + 10^{pH-4,0}) + 0,048 = 1,29 / (1 + 0,316 \cdot a_{H^+} + 0,1 / a_{H^+}) + 0,048. \quad (4)$$

Here  $p_{O_2}$  is the partial oxygen pressure. It is assumed that the chemical and biological oxygen uptake can be described by a stationary diffusion profile of the partial pressure:

$$p_{O_2}(z) = 0,198(1+z)^{-3} - 0,524(1+z)^{-2} + 0,537(1+z)^{-1}. \quad (5)$$

$U(pH)$  has the shape of a Gaussian distribution the peak being at  $pH = 3,2$ . The rate of the pyrite oxidation (4) is catalysed by bacteria.

The dissolution rate for calcite is described in terms of the following rate law [4]

$$q_{CaCO_3}^s = q_{CaCO_3}^0 (a_{H^+} + \gamma_1 a_{H_2CO_3} + \gamma_2 (1 - a_{Ca^{2+}} a_{CO_3^{2-}})), \quad (6)$$

with  $q_{CaCO_3}^0 = \exp(0,456 - 1022 / T)$  mmol / cm<sup>2</sup> / s,  $\gamma_1 = \exp(6,083 - 3991 / T)$ .

The reaction for this process is:  $CaCO_3(\text{solid}) \rightarrow Ca^{2+}(\text{aqueous}) + CO_3^{2-}(\text{aqueous})$ .

Formula (6) is taken from Plummer et al [5] and is the most comprehensive one, as it is based on dissolution studies over a wide range of pH (2-7) and CO<sub>2</sub>-pressure (35 Pa –100 kPa). The last term in Eq. (5) is only important close to the carbonate equilibrium.

The kinetic rate law for the uraninite-water interaction is used as given by Bruno et al [6]:

$$q_{UO_2}^s = q_{UO_2}^0 (1,4 \cdot a_{H^+}^{0,53} + 10^{-4}), \quad q_{UO_2}^0 = 10^{-9} \text{ mmol} / \text{cm}^2 / \text{s}. \quad (7)$$

In order to get the production function  $q$  in (1),  $q^s$  has to be multiplied by the reactive surface area of mineral  $m$  per unit volume ( $q_m = S_m / V \cdot q_m^s = r_m \cdot q_m^s$ ).  $S_m / V (= r_m)$  can roughly be approximated by assuming the porous medium consist of equal-grain-sized spherical particles with radius  $r$  by  $r_m \approx 3r^{-1}(1-n)\zeta_m$  where  $n$  is the porosity and  $\zeta_m$  is the volume fraction of mineral  $m$  in the solid phase.

For the simulation the following rate constants were chosen:  $q_{tracer} = 10^{-3}$  mmol/L/h,  $q_{FeS_2}^0 \cdot r_{FeS_2} = 1,5 \cdot 10^{-3}$  mmol/L/h,  $q_{CaCO_3}^0 \cdot r_{CaCO_3} = 2 \cdot 10^{-3}$  mmol/L/h and  $q_{UO_2}^0 \cdot r_{UO_2} = 7 \cdot 10^{-5}$  mmol/L/h

### 3. Results and discussion

For the annual motion of water through the different soils, sandy silt (A) and silty sand (B), the above reactive transport system (1) is solved numerically.

Figures 1 (sandy silt) and 2 (silty sand) show the computed profiles of pyrite, calcite and uraninite (UO<sub>2</sub>) dissolution and the distribution of a tracer after 3, 6, 9 and 12 months. In the figures the red curves represent the case of a constant source:  $q_{tracer} = 0,001$  mmol / L / h. They show the strong dependence of the tracer concentration on the water content and water motion. With constant values  $w$  and  $v$  these curves would be straight lines. The faster motion of water in case B causes the stronger curvature of the tracer profiles.

In a depth of more than seven meters the concentration of  $\text{H}_2\text{CO}_3$  falls off in comparison to the tracer concentration. This is due to the decrease of oxygen with the depth whereby the source term (4) becomes weaker. Depending on the water motion the concentrations of  $\text{Ca}^{2+}$  and  $\text{SO}_4^{2-}$  achieve the solubility of gypsum in a depth from 0.5 to 2.5 meters so that gypsum precipitates. The straight lines therefore indicate also the presents of unsolved gypsum. The concentrations of  $\text{Ca}^{2+}$  and  $\text{SO}_4^{2-}$  do not differ (see Figures 1, 2). The reason for this identity is that the equations of the law of mass action adjust the pH-value in such a way that the source terms of  $\text{SO}_4^{2-}$  (Eq. (4)) and  $\text{Ca}^{2+}$  (Eq. (6)) become equal. In other words, an increase in the hydrogen and sulfate concentration will be immediately restricted by an increase solution of calcite. Therefore an nearly stable pH-value ( $\sim 3.2$ ) adjusts if all  $\text{H}^+$  ions of the pyrite source and  $\text{CO}_3^{2-}$  ions of the calcite source form carbonic acid. Thus no further  $\text{H}^+$  ions can increase the activity of the sources. Only if the volume fraction of pyrite reaches values which lead to a pH smaller than 2.5 it comes to a clear separation of both curves.

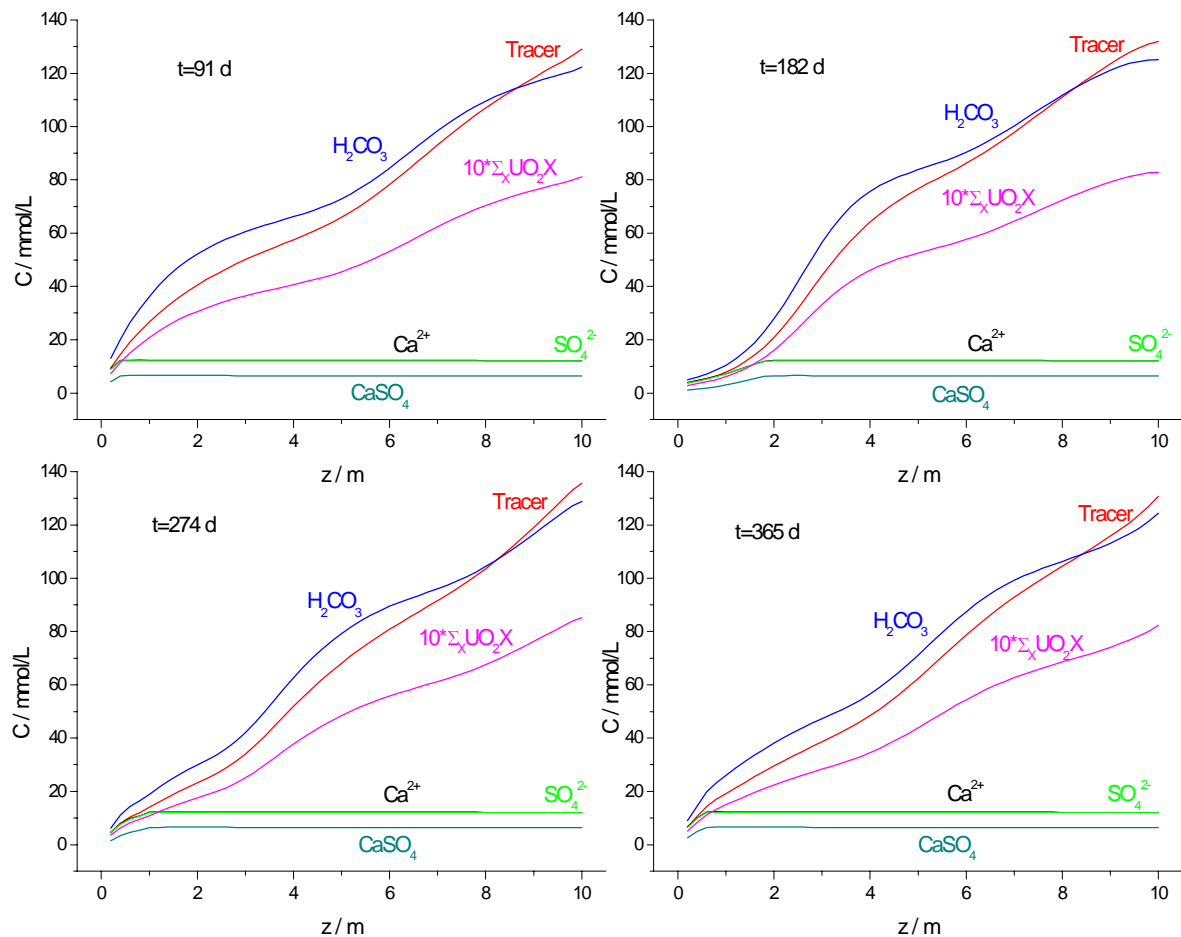


Fig. 1: Selected concentrations of the products of pyrite, calcite and uraninite dissolution for sandy silt at times 3, 6, 9 and 12 months.

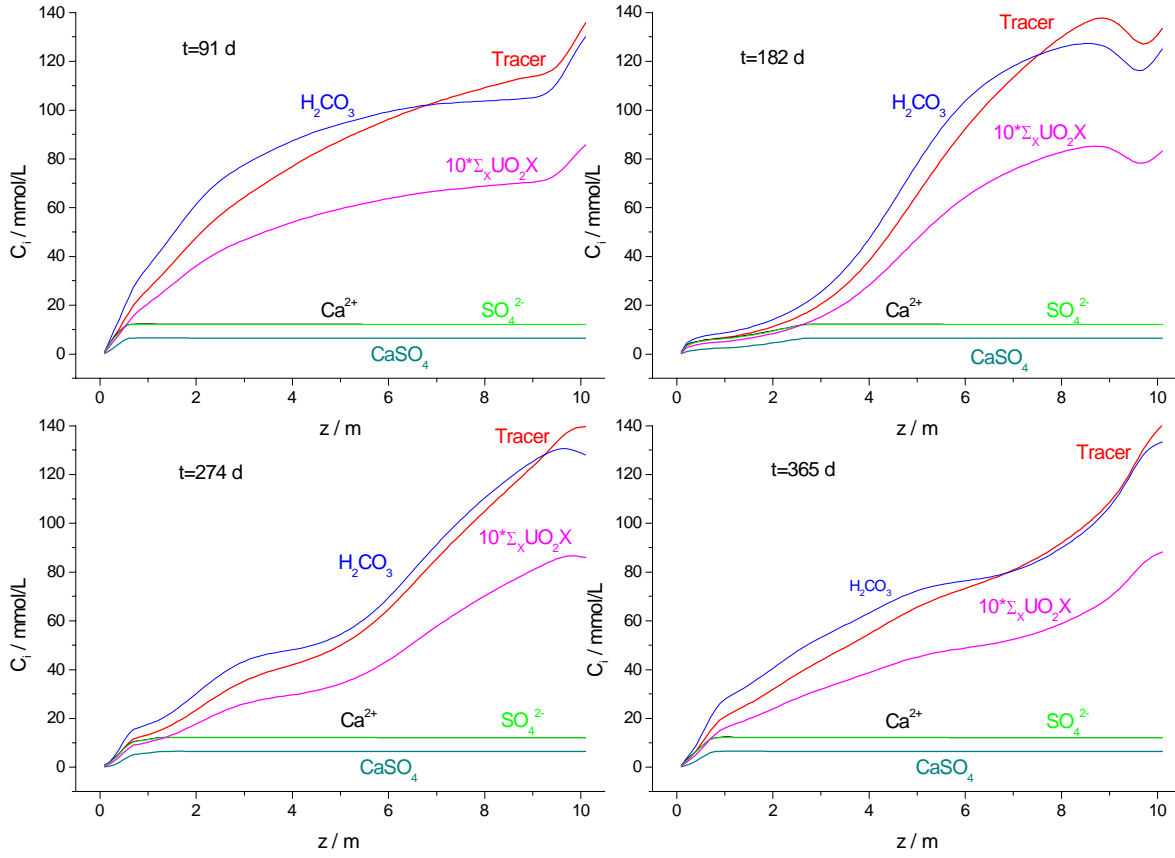


Fig. 2: Selected concentrations of the products of pyrite, calcite and uraninite dissolution for silty sand at times 3, 6, 9 and 12 months.

The time integral  $I_k = \int (vC_k - \alpha_L |v| \frac{\partial C_k}{\partial z})_{z=z_0} dt$ , which in the integration interval determines

the mass transfer per unit area into the groundwater is of more significance than the distribution of species. Results of these integrals are listed in Table 2. These values show much better the effects of the water motion than the species distribution, as well as the effects of the contributions of the source terms given by Eq.(4-7). The influence of water motion on the concentrations is seen from the quarterly integrals.

As expected, the fluctuation in the concentrations in case B is greater than in case A because the saturated hydraulic conductivity of silty sand is a factor of ten greater than for sandy silt. In case of a non-reactive tracer emitted by the constant source  $q_{Tracer}$  the integral must provide  $I_{Tracer} = 0,001 \text{ mmol} / \text{h} / \text{L} * 10 \text{ m} * 8760 \text{ h} (1 \text{ year}) = 87.6 \text{ mol} / \text{m}^2$  in the quasi steady state independently on  $w$  and  $v$  ( $w (w \neq 0, \min(w) = w_R)$ ). This is correct, as without sinks the number of particles per volume and unit time produced by the constant source is always identical. The deviation from this value yields the relative numerical error 2.2% for case A and

0.2% for case B, respectively. In both calculations the time step was 3 hours and the spatial step is 0.2 m in case A and 0.1 m in case B, respectively. It should be noted that the reason for the difference in the errors is not only determined by the difference in the spatial steps.

The comparison of both calculations shows no significant differences at the end of year (period). This means that a changes of water flow, water content, and in the dispersivity ( $\alpha_L = 0,1...1 m$ ), too, has no significant effect on the total release rate. This behaviour is plausible, because the nearly constant pH value also generates nearly constant sources .

Table. 2: Release rates per quarter (year)  $I_i$

Solid class	$\Delta t$ day	$I_{Tracer}$ mol/m <sup>2</sup>	$I_{H^+}$ mol/m <sup>2</sup>	$I_{SO_4^{2-}}$ mol/m <sup>2</sup>	$I_{Ca^{2+}}$ mol/m <sup>2</sup>	$I_{HSO_4^-}$ mol/m <sup>2</sup>	$I_{H_2CO_3}$ mol/m <sup>2</sup>	$\sum_X I_{UO_2X}$ mol/m <sup>2</sup>
Sandy Silt	91-0	21.74	0.060	2.07	2.07	0.028	20.70	1.37
	182-91	17.63	0.048	1.66	1.66	0.023	16.77	1.11
	274-182	24.51	0.065	2.21	2.22	0.03	23.29	1.54
	365-274	25.69	0.069	2.38	2.38	0.033	24.53	1.62
	$\sum I_{sp} =$	89.57	0.242	8.32	8.33	0.114	85.29	5.64
Silty Sand	91-0	16.71	0.044	1.52	1.52	0.021	16.22	1.06
	182-91	13.51	0.037	1.27	1.27	0.017	12.77	0.85
	274-182	34.56	0.092	3.11	3.12	0.043	31.66	2.13
	365-274	23.04	0.059	2.01	2.01	0.027	21.95	1.45
	$\sum I_{sp} =$	87.82	0.232	7.91	7.92	0.108	82.60	5.49

The obtained results also show that the time depending local fluctuating concentrations do not correlate with the release rates. That means for example, that concentration measurements in mining dumps do not result in values for the pollutant release into the ground water.

Further work will proceed along two broad lines: The first one is the validation of the models and numerical tools against well reproducible experiments. The second one is the model extension to consider temperature influences, so that the important temperature effect on the kinetic and equilibrium processes can also be taken into account.

## References

- [1] L. Luckner und W. M. Schestakow (1991), Migration Processes in the Soil and Groundwater Zone, Leipzig, Verlag für Grundstoffindustrie
- [2] R. Kuchler, K. Noack (1996), Migration of pollutants in mining dumps, FZ Rossendorf, Institute for Safety Research, Annual Report 1996
- [3] S. Pfeiffer, K. Pecher (1997), Experimentelle aquatische Chemie, Heidelberg, Berlin, Oxford, Spektrum, Akad. Verl.
- [4] R. Münze, B. Ullrich (1997), Beschreibung und Bewertung geochemischer Zustände, die eine Verringerung der Niederschlagsinfiltration in Halden erfordern, Vortrag zum Workshop Sanierung der Hinterlassenschaften des Uranbergbaus, 10 April 1997
- [5] D. L. Suarez and J. Simunek (1996), Solute Transport Modeling Under Variably Saturated Water Flow Conditions, in P. C. Lichtner, C. I. Steefel and E. H. Oelkers (Ed.),

- Reactive Transport in Porous Media, Reviews in Mineralogy Vol. 34
- [6] J. Bruno, I. Casas, and I. Puidoménech (1991), The kinetics of dissolution of  $\text{UO}_2$  under reducing condition and the influence of an oxidized surface layer ( $\text{UO}_{2+x}$ ), Application of a continuous flow-through reactor, *Geochimica et Cosmochimica Acta*, 55, 647-658

# ELECTROMAGNETIC CONTROL OF FLOW SEPARATION

Tom Weier, Gerd Mutschke, Uwe Fey, Vjatcheslav Avilov, Gunter Gerbeth

## 1. Introduction

The performance of fluid mechanical devices is often limited by flow separation. The form drag of cars, the efficiency of diffusers and the stall on airfoils are only some examples. Control of flow separation by suction was first demonstrated by Ludwig Prandtl [1] when he presented his boundary layer theory. Flow separation occurs when fluid decelerated by friction forces is exposed to an adverse pressure gradient which is stronger than the remaining kinetic energy of the fluid. Due to separation, form drag increases and possible lift decreases. To prevent separation, the momentum deficit of the boundary layer has to be overcome and the pressure gradient of the outer flow has to be balanced.

Numerous different techniques as, e.g. suction, blowing, and wall motion have been developed and many practical applications exist today e.g. in aerodynamics.

If the fluid is electrically conducting, an additional control possibility is given by the application of a Lorentz force  $\mathbf{f}$ . This electromagnetic body force results from the vector product of the magnetic induction  $\mathbf{B}$  and the current density  $\mathbf{j}$ :

$$\mathbf{F} = \mathbf{j} \times \mathbf{B} \quad (1)$$

The current density is given by Ohm's law

$$\mathbf{J} = \sigma(\mathbf{E} + \mathbf{U} \times \mathbf{B}); \quad (2)$$

where  $\mathbf{E}$  denotes the electric field,  $\mathbf{U}$  the velocity and  $\sigma$  the electrical conductivity, respectively. Depending on the conductivity of the fluid, different control strategies exist. In case of low-conducting fluids as electrolytes or seawater ( $\sigma \approx 10$  S/m), which will be considered in the following, induced currents  $\sigma(\mathbf{U} \times \mathbf{B})$  alone are too small, and external electric fields have to be applied in order to control the flow. Therefore, also time-dependent forces might easily be established by supplying AC-voltage feeding of the electrodes. However, electrochemical aspects like the production of electrolytic bubbles have to be considered.

The following paper gives an overview about recent experimental results on separation control at inclined plates and airfoils. For that a simple geometry of alternating stripwise electrodes and magnets attached to the surface of the body (see Fig. 1) was used. This arrangement generates a surface-parallel Lorentz force which is exponentially decreasing in wall-normal direction. Singularities at the corners of the electrodes and magnets additionally cause a slight spanwise variation of the Lorentz force in regions very close to the surface (see Fig. 2). The exact force distribution, integrated over the spanwise coordinate  $z$ , is

$$F = \frac{\pi}{8} j_0 M_0 e^{-\frac{\pi}{a} y} \quad (3)$$

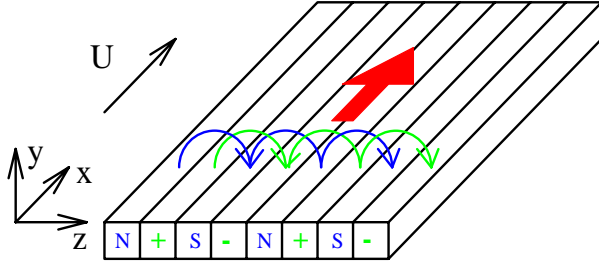


Fig.1: Sketch of the electric (green) and magnetic (blue) field lines and the resulting Lorentz force (red arrow) over a flat plate

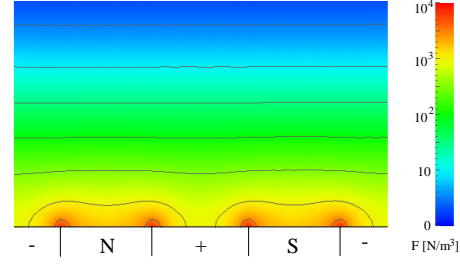


Fig. 2: Calculated Lorentz force distribution

where  $M_0$  denotes the magnetization of the magnets. Both electrodes and magnets are assumed to have the same width  $a$ .

The idea to influence the boundary layer flow of a low conducting fluid by electromagnetic forces dates back to the 1960s [2] and has recently attracted new attention for controlling turbulent boundary layers [3-6]. The first concept of Gailitis and Lielausis [2] used a streamwise Lorentz force for stabilizing a flat plate boundary layer. A tremendous reduction of skin friction will result from transition delay, since turbulent skin friction in general is orders of magnitude larger than laminar one. Following the approach of Tsinober and Shtern [8], the non-dimensional parameter

$$Z = \frac{1}{8\pi} \frac{j_0 M_0 a^2}{\rho U_0 \nu} \quad (4)$$

is obtained (“Tsinober-Shtern” parameter) by normalizing the boundary layer equations with the electromagnetic force term (3).  $Z$  describes the ratio of electromagnetic to viscous forces.  $\nu$ ,  $\rho$  and  $U_0$  denote the kinematic viscosity, density and freestream velocity of the fluid, respectively. For the canonical case of a flat plate boundary layer, the streamwise pressure gradient  $dp/dx$  vanishes. Provided  $Z = 1$ , the boundary layer thickness reaches an asymptotic value. That means, the momentum loss due to the wall friction is just balanced by the momentum gain caused by the electromagnetic force. As consequence, an exponential boundary layer profile develops

$$\frac{u}{U_0} = 1 - e^{-\frac{\pi}{a}y} \quad (5)$$

comparable to the asymptotic suction profile. This profile has a critical Reynolds number which is two orders of magnitude higher than the one for the Blasius profile, i.e. transition will be delayed considerably.

The normalization of the Navier-Stokes equation leads to an additional non-dimensional parameter

$$N = \frac{j_0 B_0 L}{\rho U_0^2} \quad (6)$$

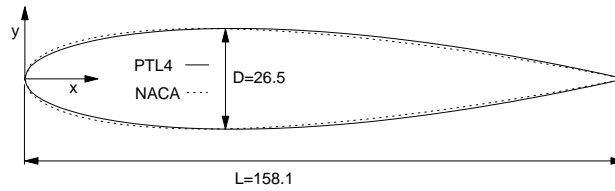


Fig.3: PTL-IV hydrofoil in comparison to a NACA-0017 airfoil

$N$  is the so-called interaction parameter defining the ratio of electromagnetic to inertial forces.  $B_0$  is the surface magnetization of the permanent magnets and  $L$  is a characteristic length. Obviously,  $N$  and  $Z$  are not independent, since  $Z/N \sim Re$ .

## 2. Experimental Apparatus

Flat plate boundary layer measurements and the investigation of the flow around a hydrofoil were carried out in a closed loop filled with the sodium chloride electrolyte at the Hamburg Ship Model Basin (HSVA). LDA measurements at the flat plate were performed on the upper plate side because of the electrolytic bubble production, but both sides of the plate were equipped with electrodes and magnets. The plate has 25 electrodes and 25 magnet strips, each 10 mm in width. The magnet/electrode array starts at 100 mm from the leading edge of the plate and has a length of 400 mm. The whole plate is 500mm×590mm in size and 18mm thick. Leading edge and trailing edge are rounded. The magnets generate an induction of 0.35T at their surface and consist of neodymium-iron-boron (NdFeB). The electrodes are made from stainless steel.

Separation prevention by electromagnetic forces has been studied on an additional small flat plate and two hydrofoils at different angles of attack.

The small flat plate is 130mm×140mm and 6mm thick. Electrodes and magnets cover the plate at 3mm from the leading edge and extend up to 37mm from the trailing edge. The width of the electrodes and magnets is  $a=10$ mm. Stainless steel has been used as electrode material in combination with a sodium hydroxide solution in the open channel. The permanent NdFeB magnets surface induction is  $B_0 = 0.4$ T. The hydrogen bubble technique has been applied to visualize the flow.

To verify the influence of separation prevention on the lift and the drag of a body, force measurements on two hydrofoils have been carried out at HSVA's Arctic Environmental Test Basin. Fig. 3 shows the geometry of the hydrofoil PTL-IV in comparison to a NACA 0017 airfoil. The hydrofoils with a span  $s$  of 360mm and additional end plates were mounted on a Kempf&Remmers force balance. All signals (drag, lift, angle of attack, pitching moment) were recorded by a standard PC.

The Arctic Environmental Test Basin is an open channel 30m long and 1.2m deep filled with the same aqueous sodium chloride. The maximum speed is about 1m/s. The two hydrofoils differ in their electromagnetic system. One has an electrode spacing of  $a = 5$ mm, the other of  $a=10$ mm. The magnets of the first hydrofoil have a surface induction of  $B_0 = 0.2$ T, those of the second one  $B_0 = 0.4$ T.

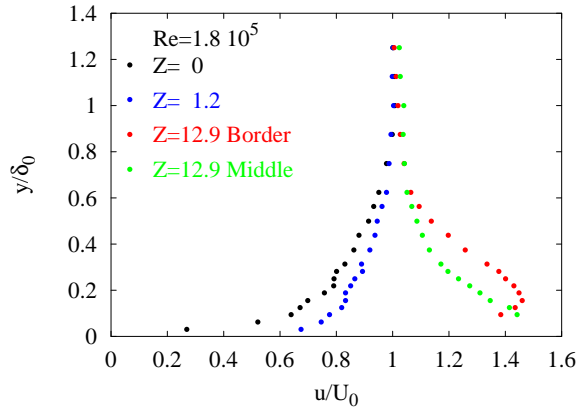


Fig. 4: Mean velocity profiles for the flat plate boundary layer in parallel flow

### 3. Results

#### 3.1. Flat Plate

The effect of a streamwise Lorentz force on the mean velocity profile of a flat plate boundary layer is shown in Fig. 4. This profile was measured at the end of the electrode/magnet array, i.e. at  $x=500\text{mm}$  measured from the leading edge. A Reynolds number  $Re=U_\infty x/\nu$  of  $1.8 \cdot 10^5$  slightly below the theoretical transition value characterizes the flow. As can be seen from the fluctuating velocities without the Lorentz force ( $Z=0$ ), the boundary layer flow is not laminar as it could be expected for such non-optimized conditions. A similar conclusion can be drawn by looking closer at the mean velocity profile. It is an intermediate profile between a Blasius and a logarithmic one. This early transition of the boundary layer is probably caused by the high turbulence level of 2% in the cavitation tunnel.

Thus the streamwise Lorentz force is, in contrast to the theory, applied to a turbulent boundary layer. For  $Z=1.2$  the influence of the force on the flow consists in a moderate acceleration of the near wall fluid. The velocity profile becomes more convex near the wall, but its shape is not an exponential one. Mainly three reasons could be responsible for this behavior. At first, the early transition of the boundary layer causes conditions not considered in the theory. Second, in order to establish the asymptotic profile, a certain evolution length has to be covered. A rough estimate can be given by looking at the definition of the dimensionless streamwise coordinate  $x' = \nu \pi^2 / (a^2 U_\infty)$  which should at least be in the order of one to allow the asymptotic profile to develop. An integration of the boundary layer equations shows that at  $x'=7$  the boundary layer profile for  $Z=1$  has still a mean deviation of 1% from the exponential shape. The profiles in Fig. 4 are taken at  $x'=0.13$ , i.e. at a position far from the required one. Third, the real force distribution differs from the ideal one. Their  $z$  modulations could have a destabilizing effect instead of the desired stabilizing one by possibly triggering transition due to secondary instabilities.

At a Tsinober-Shtern parameter of  $Z=12.9$  the mean velocity profile shows the form of a wall jet, demonstrating the strong accelerating effect of the Lorentz-force. Fig. 4 gives the flow profile at two distinct positions in the spanwise coordinate  $z$ , at the border of a magnet and an

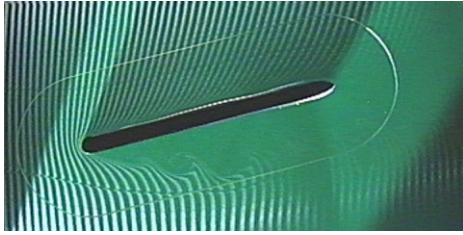


Fig. 5: Inclined plate: Lorentz force off

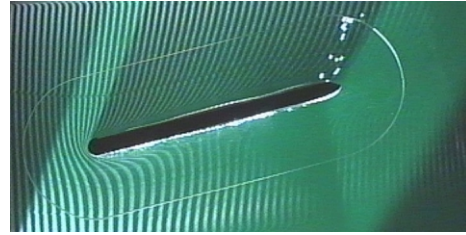


Fig. 6: Inclined plate: Lorentz force on

electrode and over the middle of a magnet. The result of the spanwise modulations on the velocity distribution is clearly to be seen. The flow is stronger accelerated at the force maxima, i.e. at the borders between electrodes and magnets (see Fig.2), than at the minima.

The wall jet in Fig.4 at  $Z=12.9$  indicates the strong momentum increase in the boundary layer due to the Lorentz force. Since boundary layer separation occurs owing to an energy deficit of the near wall fluid, the streamwise Lorentz force should be able to counteract separation.

### 3.2. Inclined flat plate and hydrofoils

Visualizations of the flow around an inclined flat plate are given in Figs. 5 and 6. The electrolyte flows from the left to the right. Fig. 5 shows the flow around the plate without Lorentz force at an angle of attack  $\alpha=15^\circ$ . Since the Reynolds number based on the plate length is small ( $Re=1.24 \cdot 10^4$ ), the flow separates laminar at the leading edge without reattachment. Because of the leading edge separation, the flow should be influenced already at the nose of the plate. Consequently the magnet/electrode-array is placed just behind the half cylinder forming the leading edge of the plate.

The flow situation under the influence of a Lorentz force of  $N=6.87$  is shown in Fig. 6. As the bubble strips indicate, the boundary layer is attached over the whole length of the plate. Due to the pressure rise in the outer flow, the boundary layer fluid is strongly decelerated at the leading edge. By the Lorentz force, the near wall fluid is subjected to an acceleration while passing the plate. This can be seen by looking at the shape of the hydrogen bubble stripes near the plate.

Separation of flow causes a form or pressure drag on the moving body simply due to the pressure difference between forward and backward stagnation point. This form drag determines practically the total drag of bluff bodies at higher Reynolds numbers. Separation prevention can reduce the form drag to zero. The application of a streamwise Lorentz force for separation prevention has two additional consequences on the drag. On the one hand due to the exponential force distribution the velocity gradient at the wall and therefore wall friction is increased. On the other hand the force exerts thrust on the body. At high enough forcing parameters a configuration is possible, where thrust overcomes drag.

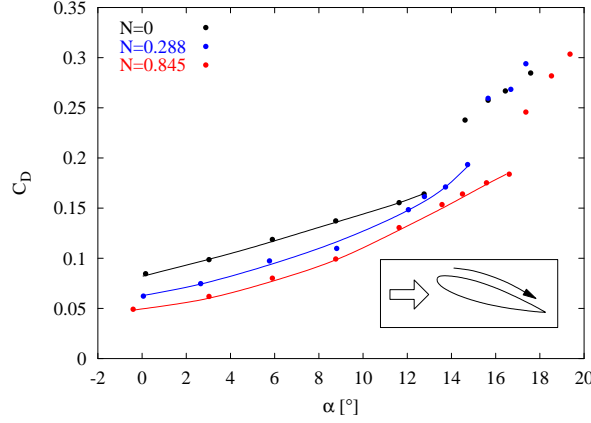


Fig. 7:  $C_D$  versus  $\alpha$  for  $Re=4 \cdot 10^4$ ,  $a/L=0.03$  and different interaction parameter

In Fig. 7 drag values of the PTL-IV hydrofoil with  $a/L=0.03$  are presented for a Reynolds number  $Re=4 \cdot 10^4$  and different values of  $N$  versus the angle of attack  $\alpha$ . The drag coefficient is defined in the usual way as

$$C_D = \frac{F_D}{\frac{\rho}{2} U_0^2 A} \quad (7)$$

with  $F_D$  denoting the total force in streamwise direction as obtained directly from the force balance measurements and  $A$  giving the wing area. The Lorentz force in Fig. 7 acts on the suction side of the hydrofoil only. At the low Reynolds number considered here, separation occurs for  $N=0$  like at the flat plate as leading edge separation but at a higher inclination angle of  $13^\circ$ . Since the separation occurs abruptly a sudden increase of the drag coefficient is obtained. The application of the Lorentz force at the suction side results at small angles of attack, i.e. in a situation without separation, in a decrease of the drag coefficient due to the momentum gain caused by the force. The drag reduction is relatively moderate ( $\Delta C_D=0.024$  at  $N=0.288$  and  $\Delta C_D=0.037$  at  $N=0.845$ ). A larger effect on the drag results from the separation delay. At  $N=0.288$  separation is delayed to  $\alpha=14.7^\circ$ , thereby reducing drag by  $\Delta C_D=0.044$ . At  $N=0.845$  separation occurs first at  $\alpha=16.6^\circ$ , resulting in a  $\Delta C_D=0.084$ . The actual drag values are always compared to the values of the natural flow at the same angle of attack.

Thinking about drag reduction implies, of course, the question about the overall energetical balance. The small conductivity of typical electrolytes leads to large losses caused by Joule heating. It is clear that the drag reduction should overcompensate at least these Joule losses. Some hopes and estimates still exist for that based on the stabilization of a laminar boundary layer [2]; but to the best of the authors knowledge, no energetically efficient electromagnetic drag reduction has been demonstrated up to now.

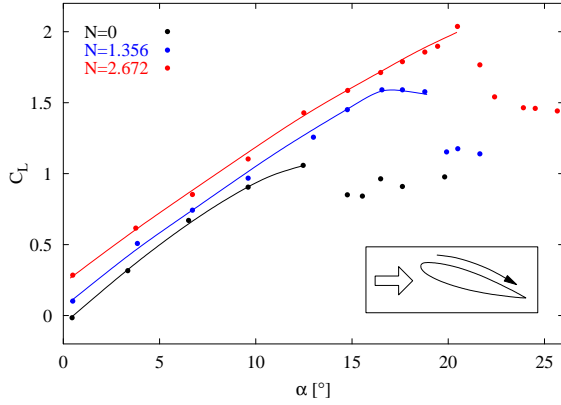


Fig. 8:  $C_L$  versus  $\alpha$  for  $Re=2.9 \cdot 10^4$ ,  $a/L=0.06$  and different interaction parameter

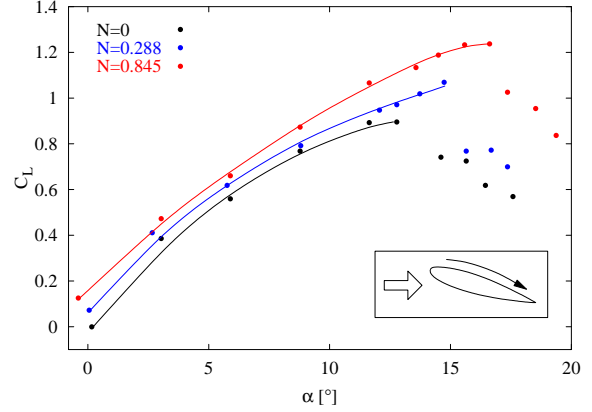


Fig. 9:  $C_L$  versus  $\alpha$  for  $Re=4 \cdot 10^4$ ,  $a/L=0.03$  and different interaction parameter

Especially on a hydrofoil, separation doesn't influence the drag alone, but also the lift. Figs. 8 and 9 show the lift development with the angle of attack at different  $N$  for the two hydrofoils. The lift coefficient is defined in analogy to the drag coefficient as

$$C_L = \frac{F_L}{\frac{\rho}{2} U_0^2 A} \quad (8)$$

Here  $F_L$  denotes the force on the hydrofoil in the direction normal to the liquid flow. Fig. 8 gives experimental values obtained at  $Re=2.9 \cdot 10^4$  and  $a/L=0.06$ , Fig. 10 for  $Re=4 \cdot 10^4$  and  $a/L=0.03$ . As in Fig. 7, the Lorentz force is applied at the suction side only. At  $N=0$  separation takes place at  $\alpha=13^\circ$  leading to an abrupt lift decrease. If the Lorentz force is switched on, already at small angles of attack a lift increase can be seen. This lift increase results from the additional circulation caused by the acceleration of the suction side flow. Corresponding to the drag reduction at small angles of attack, also the lift increase due to enhanced circulation is of moderate size. Nevertheless it is possible to obtain a lift force even without an inclination of the hydrofoil.

A much larger lift increase results from the delayed separation of the suction side flow at high angles of attack. The lift coefficient increases further monotonically with the angle of attack up to a point, where the Lorentz-force cannot any longer withstand the pressure gradient of the outer flow. From Fig. 8 one can detect, that for the hydrofoil with  $a/L=0.06$  at  $Re=2.9 \cdot 10^4$  and  $N=2.67$  stall can be delayed up to  $\alpha=21^\circ$ . This results in an increase of the lift coefficient by 92% in comparison to the unforced flow. The same scenario is shown in Fig. 9 but for the hydrofoil with  $a/L=0.03$  at  $Re=4 \cdot 10^4$  and  $N=0.84$ . Due to the lower interaction parameter, the hydrofoil stalls at  $\alpha=17^\circ$ , the maximum lift increases by 43%.

#### 4. Conclusions

Experimental demonstration of separation prevention on a circular cylinder by means of a streamwise Lorentz force with accompanying numerical simulations have been given in [9].

The influence of a streamwise Lorentz force on the flow along a flat plate has been studied in a saltwater flow. The experiments show a strong acceleration of the near wall flow if electromagnetic forces of sufficient strength are applied. The application of the streamwise force to the control of separation at an inclined plate and two hydrofoils has been successfully demonstrated. Stall is delayed to higher angles of attack resulting in an increase of maximum lift and a decrease of total drag of the hydrofoils.

### Acknowledgments

Financial support from VDI under Grant NLD-FKZ 13N7134/1 is gratefully acknowledged. We would also like to thank the measuring crew from HSVA and Prof. Lielausis from IoP Riga for preparing a plate and an airfoil.

### References

- [1] L. Prandtl (1904), Über Flüssigkeitsbewegung bei sehr kleiner Reibung, Verhandlg. III. Intern. Math. Kongr. (pp.484-491), Heidelberg
- [2] A. Gailitis and O. Lielausis (1961), On a possibility to reduce the hydrodynamical resistance of a plate in an electrolyte, Applied Magnetohydrodynamics. Reports of the Physics Institute 12 (pp. 143-146), Riga (in Russian)
- [3] C. Henoeh and J. Stace (1995), Experimental investigation of a salt water turbulent boundary layer modified by an applied streamwise magnetohydrodynamic body force, Phys. Fluids, 7, 1371
- [4] C.H. Crawford and G.E. Karniadakis (1997), Reynolds stress analysis of EMHD-controlled wall turbulence. Part I. Streamwise forcing, Phys. Fluids, 9, 788
- [5] J.C.S. Meng (1994), Seawater Electromagnetics: A new Frontier, Magnetohydrodynamics, 30, 401
- [6] D.M. Nosenchuck and G. Brown (1993), Discrete spatial control of wall shear stress in a turbulent boundary layer, in R.M.C. So, C.G. Speziale and B.E. Launder (Ed.), Near-Wall Turbulent Flows (pp.689-698), Elsevier
- [7] E. Grienberg (1961), On determination of properties of some potential fields, Applied Magnetohydrodynamics. Reports of the Physics Institute 12 (pp. 147-154), Riga (in Russian)
- [8] A.B. Tsinober and A.G. Shtern (1967), On the possibility to increase the stability of the flow in the boundary layer by means of crossed electric and magnetic fields, Magnitnaya Gidrodinamica, 152
- [9] T. Weier, G. Gerbeth, G. Mutschke, E. Platacis, O. Lielausis (1998), Experiments on cylinder wake stabilization in an electrolyte solution by means of electromagnetic forces localized on the cylinder surface. Experimental Thermal and Fluid Science, 16, 84

# SI-CZOCHELSKI CRYSTAL GROWTH MELT FLOW CONTROL BY MEANS OF MAGNETIC FIELDS

Vladimir Galindo and Gunter Gerbeth

## 1. Introduction

A contact-less melt flow control is important for the convective motions in many crystal growth technologies. Typically steady magnetic fields are used to damp such flows. Surprisingly, active flow driving forces due to alternating magnetic fields can be of stabilising character, too. We present numerical results for the combined action of steady and alternating magnetic fields for the Czochralski growth process of silicon crystals. Not only the thermal convection and rotation of crystal and crucible are taken into account, but also the influence of driving and/or damping electromagnetic forces, the effects related to the induced electrical current in the melt and the thermo-capillary driven flow at the free melt surface. We apply a two equations low Reynolds number turbulence model since a weak turbulence slightly above the transition values is characteristic for the melt motion.

## 2. Geometry

The geometry used to compute the flow is shown in Fig. 1. The dimensions are given in mm and were taken according to a Czochralski single crystal growth furnace with a crucible having a diameter of 14 inches. The problem is assumed to exhibit symmetry about the  $z$ -axis – that is, all field quantities are supposed to be independent of the polar angle  $\theta$ . That makes possible to consider the problem as axis-symmetric and to reduce the computation mesh to the meridional plane  $r - z$ .

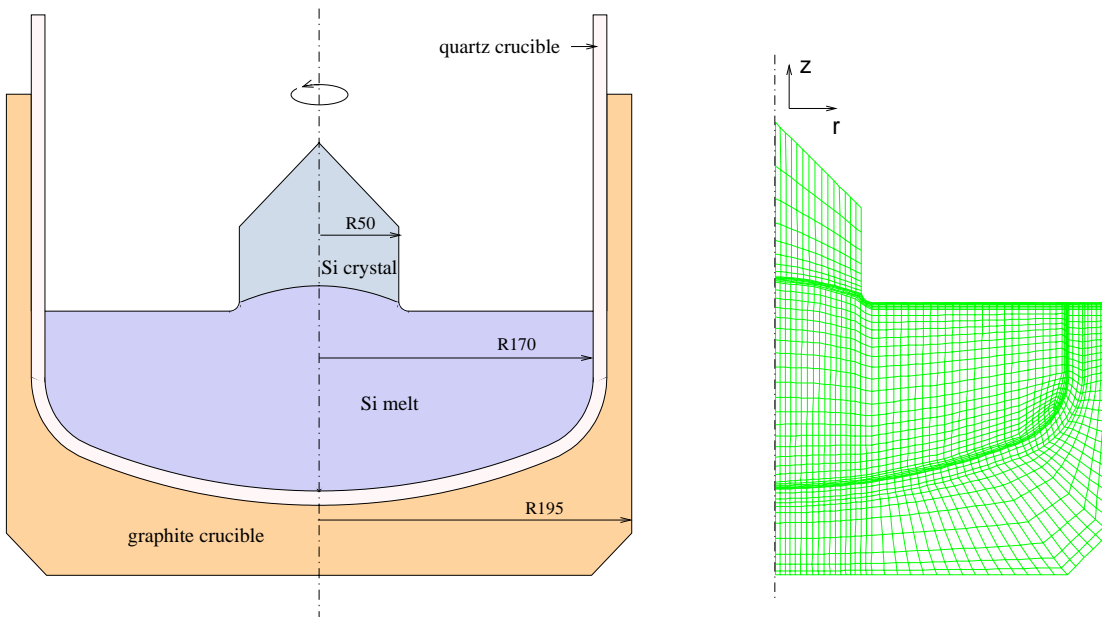


Fig. 1: Sketch of the geometry (left) and coarse computation mesh (right)

### 3. Governing equations and boundary conditions

With reference to Fig. 1, we consider axi-symmetric, steady, buoyancy-, thermo-capillary-, and electromagnetically induced flow and heat transfer within a crucible that is heated from the sides and from the bottom. Assuming that the fluid is incompressible and that the Boussinesq approximation is valid, the time averaged momentum, continuity, and energy equations are as follows:

Navier-Stokes (momentum) equation with electromagnetic force term:

$$\rho \left( \frac{\partial \vec{v}}{\partial t} + (\vec{v} \cdot \nabla) \vec{v} \right) = -\nabla p + \eta \nabla^2 \vec{v} - \rho \vec{g} \beta (T - T_0) + \vec{j} \times \vec{B} \quad (1)$$

where  $\vec{v}$  is the velocity vector field,  $p$  the pressure,  $\rho$  the reference density,  $\eta$  the dynamic viscosity,  $\beta$  the coefficient of volume expansion,  $g$  the gravity acceleration constant,  $\vec{j}$  the electric current density and  $\vec{B}$  is the magnetic field induction. For its specification see chapter 5.

Mass conservation and energy transport equations:

$$\nabla \cdot \vec{v} = 0 \quad (2)$$

$$\rho c_p \left( \frac{\partial T}{\partial t} + (\vec{v} \cdot \nabla) T \right) = \nabla \cdot (k \nabla T) \quad (3)$$

where  $T$  is the temperature and  $c_p$  is the specific heat. The heat conductivity is designated as  $k$ .

Boundary conditions:

- no-slip at the crucible walls and interface crystal/melt
- melting temperature at the interface crystal/melt
- fixed heat flux distribution at the external graphite crucible walls (taken from a thermal global modelling)
- thermo-capillary conditions at the free melt surface
- gray body radiation condition at the melt surface and crystal side (with an "effective" emissivity  $\epsilon(\vec{r})$  distribution computed from the thermal global modelling, where  $\sigma_S$  denotes the Stefan-Boltzmann constant)

$$-k \frac{\partial T}{\partial n} = \epsilon \sigma_S (T^4 - T_0^4) = \epsilon(\vec{r}) \sigma_S T^4$$

In order to define a smooth heat boundary condition at the external graphite crucible walls, we made a polynomial fit of the values provided by the thermal global modelling.

#### 4. Numerical method

The governing equations for the computation of the flow, the temperature and the electrical stream function were solved numerically by a finite element method. We applied the commercial code FIDAP. Because the characteristic numbers (like the Reynolds and Grashof numbers) are near critical values (but not so large, that a fully developed turbulence exists) we used the Wilcox's Low-Reynolds turbulence model (see [1]). This model belongs to the so-called two-equation group of turbulence models and is therefore closely related to the  $k-\epsilon$  type models. An important advantage of this model is that it can be used to directly predict low- $Re$  ( $Re \leq 10^5$ ) effects on the turbulence field in the near wall regions and does not need any (artificial) wall functions.

The two dimensional computational domain, contained in the plane  $r-z$ , has been discretized into a mesh of quadrilateral finite elements, with a finer spacing near the melt boundaries, but specially near the interface melt/crystal.

A typical velocity vector plot is shown in Fig. 2. It shows the predominance of the crucible and crystal rotation.

It is worth to assert that the Ekman layer (depth:  $\delta_E \approx 0.7mm$ ) caused by the crystal rotation at the interface is very thin and it turns out to be crucial for gridding of the computational domain. A very high grid refinement is necessary in this region. It is necessary to find a compromise between memory usage, computational time and the need to find a grid independent solution. After the analysis of the grid dependency of the solution, we decided to use a grid with 22300 elements for all further calculations. Within this grid resolution, a complete converged flow and heat transfer simulation needs approximately 20h cpu time on a SGI Origin 2000 workstation.

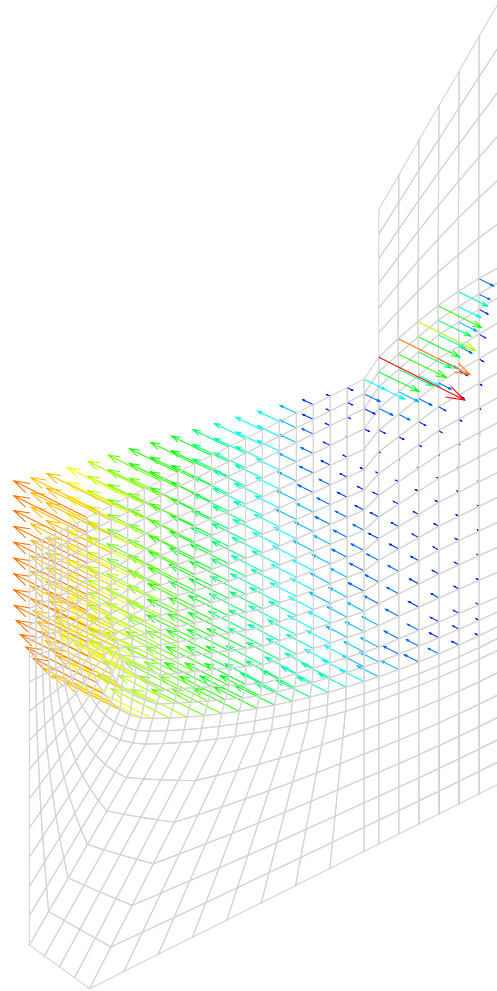


Fig. 2: Typical velocity vector plot.

#### 5. Magnetic fields

The magnetic induction field distribution and, in the case of non-steady magnetic fields, the distribution of the electromagnetic force density  $\vec{f}_L = \vec{j} \times \vec{B}$  were computed using the electromagnetic commercial solver OPERA. The geometry is assumed to be axi-symmetric.

## 5.1. Steady magnetic field

In the case of a steady magnetic field, the induction law reduces to  $\nabla \times \vec{E} = 0$ . It means that an electrical potential can be introduced:  $\vec{E} = -\nabla\Phi$

Taking into account the Ohm's law ( where  $\sigma$  denotes the electrical conductivity)

$$\vec{j} = \sigma \left( -\nabla\Phi + \vec{v} \times \vec{B} \right)$$

and the Kirchoff's law  $\nabla \cdot \vec{j} = 0$  we obtain the following equation for the electric potential:

$$\Delta\Phi = \text{div} \left( \vec{v} \times \vec{B} \right) = \vec{B} \cdot (\nabla \times \vec{v})$$

This relation shows that in vorticity regions potential differences exist creating a local electric field which can balance the electromotive field and allow the electric current lines to close. The relation above couples the electric potential, the magnetic induction and the vorticity distribution. This equation is solved numerically in order to determine how the DC magnetic fields act.

In this paper, results for numerical studies are presented concerning 2 types of steady magnetic fields: an axial homogeneous and a cusp field.

In order to generate a *homogeneous axial magnetic field* which has a main component in the direction of the symmetry axis, we presumed to have 2 direct current coils in the way connected, that the electric current is flowing in the same direction. For the calculations with OPERA we assumed a current density flowing through the coil of approximately  $10^7 \text{ A/m}^2$  what provides a maximum magnetic induction of  $400 \text{ mT}$ .

The so called *cusp magnetic field* can be generated by means of two coil systems carrying electric currents in opposite direction. The distribution of the field in the region containing the melt is very inhomogeneous. The cusp magnetic field induction distribution shows (see Fig. 3) that the field strength grows in the melt from zero at the symmetry axis up to approximately 1/30 of the maximal value of the corresponding axial field strength at the crucible walls.

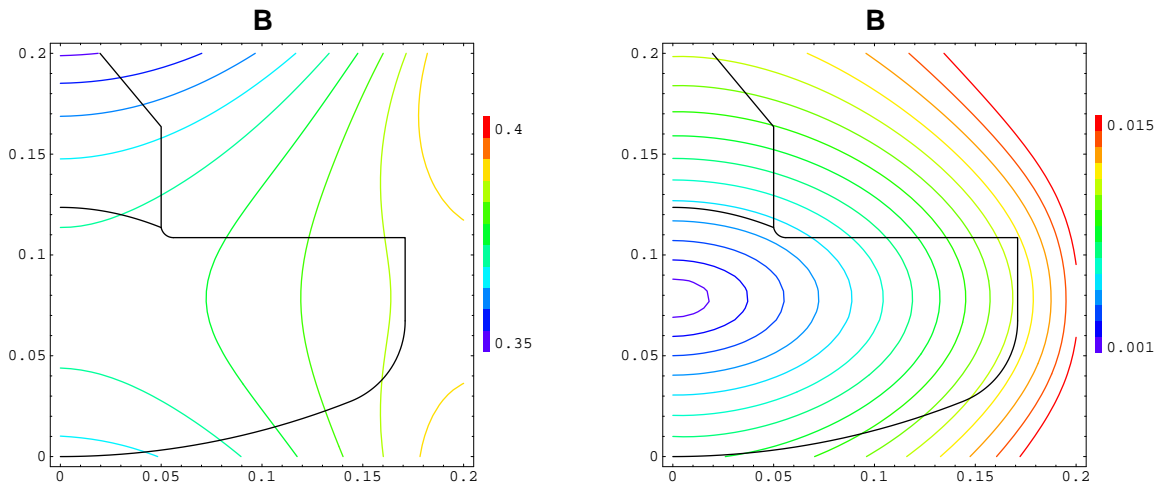


Fig. 3: Homogeneous (left) and cusp (right) steady magnetic induction distribution in Tesla.

## 5.2. Alternating magnetic field

The alternating magnetic field is induced using a set of windings fed by an external power supply with an alternating current (AC). This time dependent magnetic field induces an electric current in the conducting melt. Because of the skin effect, the magnetic lines penetrate into the conducting material up to a skin depth of the order  $\delta = (\mu \sigma \omega)^{-1/2}$ , where  $\mu$  is the magnetic permeability, and  $\omega$  the frequency of the pulsating field.

The Lorentz force  $f_L = \vec{j} \times \vec{B}$  averaged over one period has a time-independent component since both  $\vec{j}$  and  $\vec{B}$  vary harmonically in time with the same frequency.

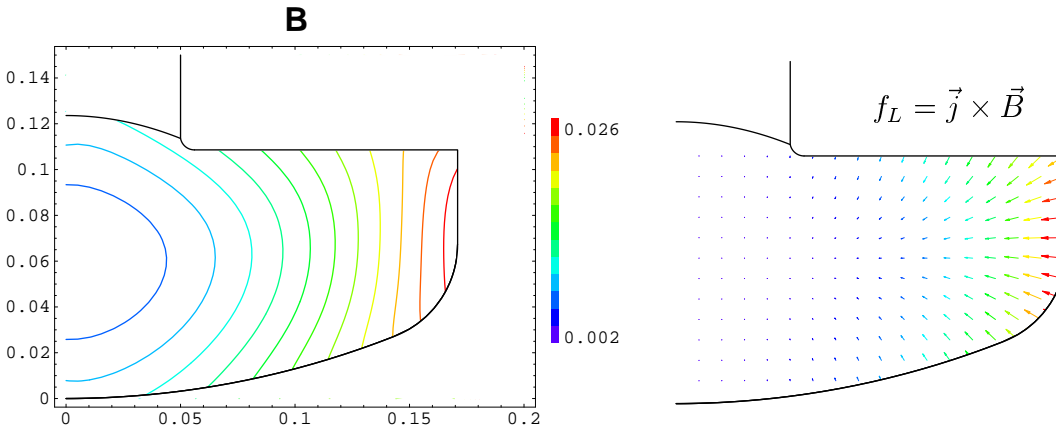


Fig. 4: Alternating magnet field distribution (left) and Lorentz force vector plot (right).

## 6. Results

Typical results of the magnetic field actions are shown in Fig. 5. The main action of the AC-field consists in a flow driving mechanism which may superimpose the buoyancy convection in the meridional plane. This can lead to an opposite flow direction at the free melt surface if the AC-field amplitude is sufficiently strong. Without magnetic fields the meridional flow is mainly determined by buoyancy with a strong vortex resulting in a melt flow direction from the crucible to the crystal at the free surface of the melt (not shown in Fig. 5). The AC-field primarily creates a jet at mid-height of the crucible as can be seen from the Lorentz force distribution in Fig. 4. This Lorentz force creates a double vortex structure in the melt causing the melt at the free surface to flow from the crystal to the crucible wall, i.e. against the basic buoyant flow direction. Depending on the strength of the AC field this may change drastically the heat- and mass transport in the meridional plane. The DC-fields have in general a stabilising influence on the melt flow. It results in a general weakening of the convective velocities, and (not shown in Fig. 5) in a reduction of the turbulent velocity and temperature fluctuations. A better homogeneous damping effect is found for the cusp magnetic field since it provides no preferred direction to the flow field. In case of a vertical homogeneous magnetic field additional instabilities may arise due to the fact that vorticity parallel to the preferred magnetic field direction is not influenced by such type of DC-fields.

The different magnetic fields offer a large variety of control possibilities for a contact-less optimization of the heat and mass transfer processes in the silicon melt.

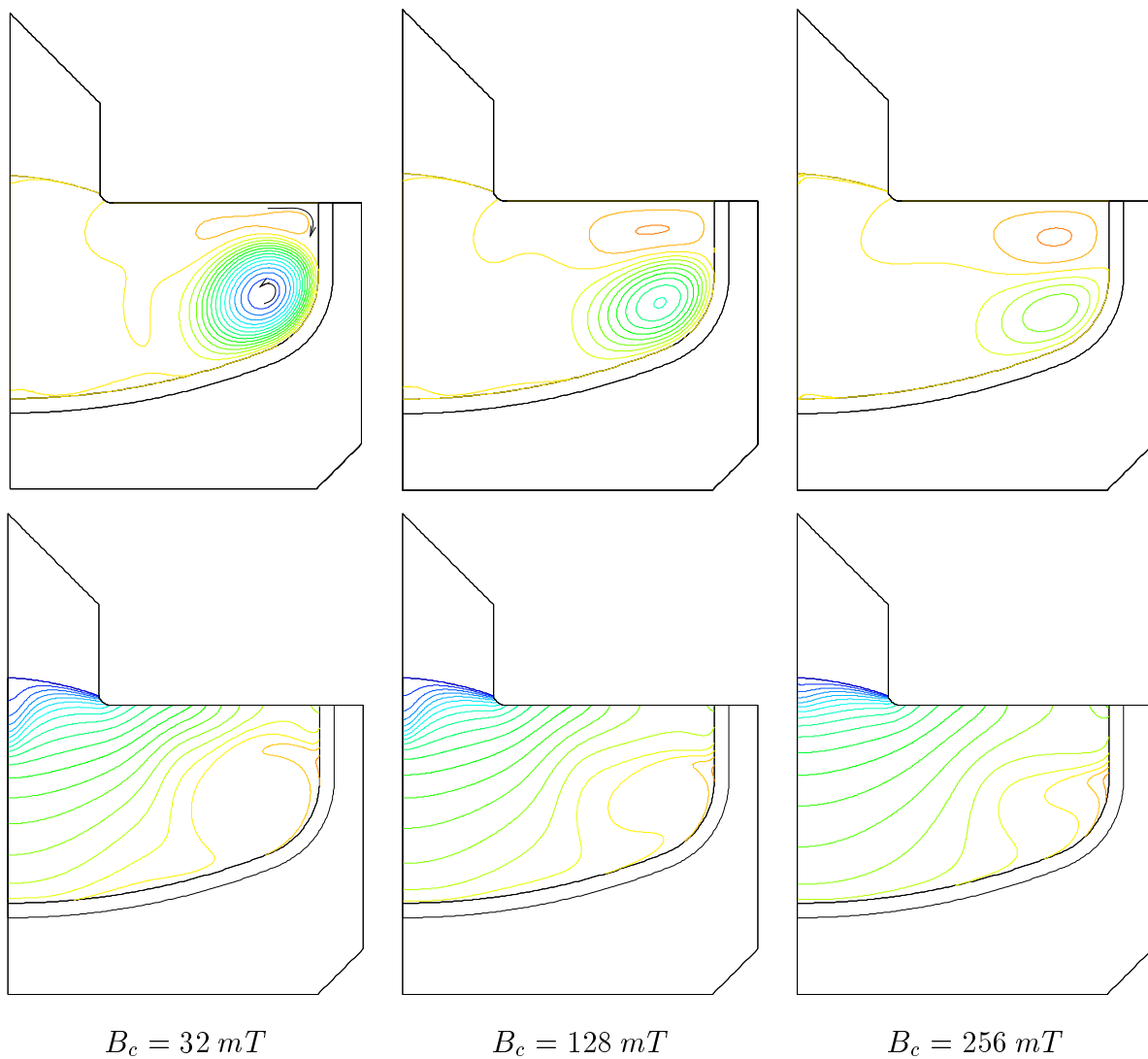


Fig. 5: Flow streamlines (above) and isotherm distribution (below) by the combined action of alternating ( $B_{ac} = 12 \text{ mT}$ ) and cusp ( $B_c = 32, 128$  and  $256 \text{ mT}$ ) magnetic fields.

## References

- [1] D. C. Wilcox (1993), Turbulence Modelling for CFD, DCW Industries, Inc.

# CONTRIBUTIONS TO THE RIGA DYNAMO EXPERIMENT

Frank Stefani and Gunter Gerbeth

## 1. Introduction

Nowadays, it is widely accepted that the magnetic fields of planets, stars, and galaxies are generated by motion of electrically conducting fluids. The underlying physical processes are explained in dynamo theory. Recalling the technical realization of magnetic field self-excitation in a technical dynamo by means of well-separated parts (rotor, coils, etc.) one might be surprised how self-excitation can result from the movement of a nearly homogeneous medium. The last decades saw an enormous progress in the theoretical understanding of this old question of physics. This was, not at least, also due to growing numerical investigations culminating in the famous simulations of the outer earth core giving impressive numerical evidence for polarity reversals [1].

Quite contrary to the success of dynamo theory, an experimental verification of magnetic field self-excitation in conducting fluids is still missing. A first liquid metal experiment undertaken in Riga in 1987, a forerunner of the present experiment, had to be stopped for mechanical stability reasons before self-excitation was reached [2]. Apart from Riga, there are at present five places in the world where dynamo experiments are under construction or planned. The first international workshop devoted mainly to dynamo experiments was organized by the authors in collaboration with the Riga Institute of Physics in June 1998 [3].

The present paper is intended to give a short overview about the authors contribution to the Riga dynamo experiment which laid, to the most part, on the numerical side. The optimization of the velocity profiles will be sketched and some numerical prognoses for the real experiment will be given.

## 2. Velocity profile optimization

The basic idea of the Riga dynamo experiment goes back to a paper of Ponomarenko in 1973 [4] where it was shown that a screw motion of a solid rod through a fixed medium can lead to a dynamo effect. The Riga dynamo is, in a way, a hydrodynamic analogue of the Ponomarenko dynamo, the main difference being (for obvious reasons) the finite length of the system and a counterflow of the fluid. Figure 1 shows the main parts of the facility. Driven by 2 motors (55 kW each) a propeller generates a helical flow of liquid sodium through a central channel surrounded by a back-flow channel where the fluid motion is supposed to be purely axial. A third outer channel with sodium at rest accomplishes the „heart“ of the set-up. Of course, for the real experiment much more components, like sodium storage tanks, heaters, kick-field coils, magnetometers etc. are needed. Figure 1 gives also an impression of the dimensions of the facility. The active part has a length of around 3 m and a diameter of 0.8 m. The velocity of the sodium will be of the order 10 m/s. Notwithstanding the security questions arising when handling sodium, it is also the pure dimension of the facility which explains the fact that experimental attempts to dynamos are still rare. From the physical point of view this

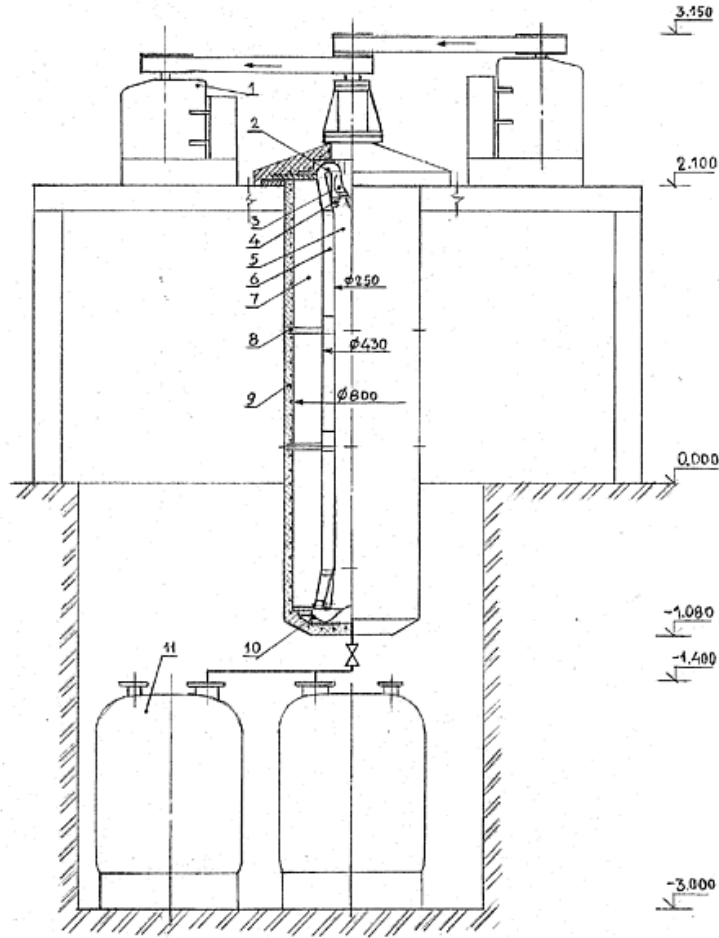


Fig. 1: The experiment: 1-DC motors, 2-pre-propellor vanes, 3-propeller, 4-post-propeller vanes, 5-principal channel with helical fluid motion, 6-channel with straight counterflow, 7-sodium at rest, 8-supports with field sensors, 9-heaters with thermo-isolation, 10-flow reversing guides, 11-sodium tanks

is due to the fact that for self-excitation of a magnetic field the product of electrical conductivity  $\sigma$ , a typical length  $L$ , and a typical velocity scale  $v$  must exceed a certain value. Actually, it is the magnetic Reynolds number  $Rm = \mu_0 \sigma L v$  which governs the stability of the system with respect to magnetic excitations. This can easily be deduced from the so-called induction equation

$$\frac{\partial \vec{B}}{\partial t} = \text{curl}(\vec{v} \times \vec{B}) + \frac{1}{\mu_0 \sigma} \Delta \vec{B} \quad (1)$$

which can be derived from Ampere's law, Faraday's law, and Ohm's law. The trivial solution  $\vec{B} = 0$  of (1) is stable only below a critical value  $Rm_c$  above which a bifurcation to a non-zero solution occurs. For all dynamos theoretically studied until now  $Rm_c$  is greater than 1, although for practically realizable flows  $Rm_c$  is in the order of  $10^1 \dots 10^3$ .

For the Ponemarenko flow with a solid body rotation (i.e. a rigid rod screwing through a fixed medium) and its experimental modification  $Rm_c$  is of the order of 15. However, our numeri-

cal investigations [5] proved that the precise value of  $Rm_c$  depends sensitively on the radial dependence of the axial and the azimuthal components of the velocity. Whereas the technically achievable  $Rm$  for the Riga dynamo facility is around 23 the computed  $Rm_c$  for the velocity profiles measured in a first water pre-experiment turned out to be 31. Thus, two problems had to be solved. At first, it was indicated to search for a velocity profile yielding minimal  $Rm_c$ . At second, it was necessary to look for technical means by which such an optimal velocity profile could be realized.

Concerning the first problem, we found that a so-called Bessel functions profile was able to decrease the critical  $Rm$  by about 20 per cent compared to the value of the solid body rotation profile. The test of this Bessel function profile was inspired by the heuristical argument that helicity maximizing flows are suitable for dynamo action. For the computations various numerical codes were used. There was a one-dimensional eigenvalue solver available from the partners in Riga. A second one-dimensional code was developed by the authors in order to treat arbitrary velocity profiles. Additionally, a two-dimensional code was written to study the effects of the finite length of the system and of axial variations of the velocity profiles in detail.

Concerning the second problem, it was possible in close collaboration with the Institute of Physics in Riga and the University of Technology in Dresden to improve the velocity profiles. Technically, this was realized by installing appropriate pre- and post-propeller vanes in order to „form“ the sodium flow. The iterative velocity optimization process is documented in more detail in [5]. Although the Bessel functions profiles could not be achieved a certain „technical optimum“ seems to be realized now.

### 3. Prognoses for the experiment

After optimizing the velocity profiles in a water dummy the sodium facility was put up in Riga in spring 1998. There, the velocity profiles were measured again showing a reasonable correspondence with those of the last water dummy pre-experiment. One important point to note is a certain decrease of the azimuthal velocity component in axial direction. Thus, the two-dimensional code was necessary in order to get realistic prognoses for self-excitation. Figure 2 represents a snapshot of the magnetic field at a certain time. The computed growth rates and frequencies of field rotation are depicted in Figure 3. The green crosses are numerical results for the actually measured velocities. The blue lines are interpolations between these points. The differences to the red lines which represent numerical results for a simple down-scaling of the velocity fields at 2000 rpm give an indication for a slight changing of the velocity profiles with growing pump rates. According to our computations, self-excitation should appear at  $Rm \approx 18.5$  (where the growth rate reaches zero). Hence, there seem to be sufficient resources for a successful experiment.

### 4. Conclusions

The sodium experiment is expected for autumn 1999. Meanwhile, special magnetic field sensors have been developed and tested in our group in order to document the magnetic field behaviour during the run. In case of a successful experiment, a lot of new questions will appear,

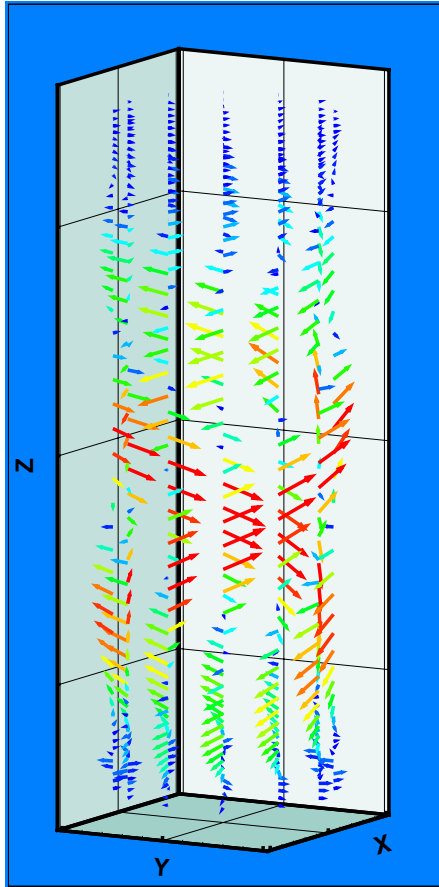


Fig. 2: Impression of the expected magnetic field structure close to the innermost wall.

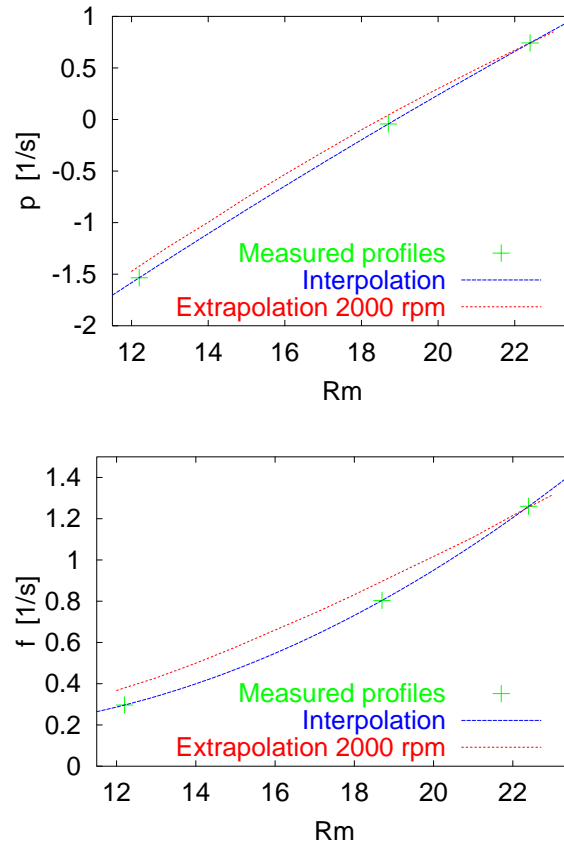


Fig. 3: Computed growth rates (above) and frequencies (below) for measured (at 1000, 1600, and 2000 rpm) and interpolated velocity profiles.

especially with respect to the complicated problem of non-linear back-reaction of the magnetic field on the velocity.

## References

- [1] G. A. Glatzmaier and P. H. Roberts (1995), A three-dimensional self-consistent computer simulation of a geomagnetic field reversal, *Nature*, 377, 203
- [2] A. Gailitis (1993), Experimental aspects of a laboratory scale liquid sodium dynamo model, in M. R. E. Proctor, P. C. Matthews and A. M. Rucklidge (Eds.), *Theory of Solar and Planetary Dynamos* (pp. 91-98), Cambridge, CUP
- [3] G. Gerbeth, F. Stefani, A. Gailitis, O. Lielausis (Eds.) (1998), Laboratory experiments on dynamo action, *Workshop Proceedings, Riga, June 1998*
- [4] Yu. B. Ponomarenko (1973), On the theory of hydrodynamic dynamo, *Zh. Prikl. Mekh. Tekhn. Fiz.*, 6, 47
- [5] F. Stefani, G. Gerbeth and A. Gailitis (1999), Velocity profile optimization for the Riga dynamo experiment, in A. Alemany, Ph. Marty and J. P. Thibault (Eds.), *Transfer phenomena in magnetohydrodynamic and electroconducting flows* (pp. 31-44), Dordrecht, Kluwer

## **Short Contributions**



## Plant models for accident analysis

*U. Grundmann,  
S. Kliem,  
S. Mittag,  
U. Rohde,  
A. Seidel,  
as guest  
scientist:  
I. Reiche*

### **Development, Validation and Application of the Code Complex DYN3D - ATHLET**

Concerning the validation of the coupled 3D neutron kinetics/thermohydraulic code complex DYN3D-ATHLET, a new quality was reached by participation in international benchmarks and comparison of calculations with measurement data from real transients in NPPs. The benchmarks comprise the analyses of 2 main steam line break scenarios. Due to the overcooling of the reactor connected with positive reactivity insertion, recriticality and return to power of the shut down reactor can occur. 5 organisations from 5 countries participated in the benchmark exercise for VVER-440 type reactors, which was defined by FZR. The other exercise for a Western PWR is organized by OECD/CSNI.

In the framework of an EU PHARE project under the leadership of FZR in which institutions from 3 EU member states and 5 East European countries take part, measurement data on transients in nuclear power plants with VVER type reactors have been collected and documented. Two transients, the power drop of one generator down to house load level at NPP Loviisa (VVER-440) and turning off one of two working feedwater pumps at NPP Balakovo (VVER-1000), were selected for the analysis using different coupled code systems. It is the first international validation of coupled codes against measuring data from NPPs.

A new, original nodal expansion method was developed leading to enhanced accuracy of the neutron flux calculation in DYN3D. In cooperation with IPPE Obninsk (Russia), DYN3D is going to be coupled to the internationally widely used thermohydraulic system code RELAP.

Using the 2D neutron transport code HELIOS, effective macroscopic cross sections for the absorber elements of VVER-440 type reactors were generated. A methodology has been developed to ensure the equivalence of the neutron diffusion theory which is applied in DYN3D to transport calculations.

*supported by  
BMBF, BMU,  
and EU*

*E. Krepper,  
F. Schäfer*

### **Validation of thermohydraulic system codes**

The activities were focused on the validation of the thermohydraulic code ATHLET (developed by Gesellschaft für Anlagen- und Reaktorsicherheit) against experiments performed at thermohydraulic integral test facilities. Post test analysis calculations of two experiments were carried out, which were performed at the french integral test facility BETHSY. In the experiment 5.2c, the accident management procedure was investigated in case of the total loss of steam generator feedwater. The experiment should show the possibility of emergency core cooling by primary bleed and feed. In the test 9.3, the consequences of the failure of the emergency feedwater and high pressure safety injection systems after

a steam generator tube rupture were investigated. Primary and secondary side depressurization to activate the low pressure emergency core cooling system was shown to be an appropriate accident management measure.

Calculations were started for two large break LOCA experiments with cold and hot leg safety injection into the primary circuit. The tests were performed at the Japanese test facility CCTF. Significant counter current flow of steam and water occurred during these experiments. The analyses aim at the validation of an improved ATHLET model for phase interaction.

*funded by  
BMBF*

*E. Krepper,  
A. Krüßenberg,  
T. Höhne,  
M. Kliem*

### **Computational fluid dynamics simulations of one and two-phase flow**

At the Rossendorf coolant mixing test facility ROCOM, first experiments were performed on the mixing of a plug of salt water simulating a temperature or boron concentration perturbation in one of the loops. CFD calculations show a good agreement of the velocity distribution in the downcomer with data obtained in the experiment by laser Doppler anemometry. Comparative numerical studies on the flow field in the downcomer of KONVOI and VVER-440 type reactors were done confirming a simplified mixing model for VVER-440 as it is used in the code DYN3D.

Experiments on the convection in externally heated storage tanks were done together with VKTA Rossendorf. The temperature and void fraction were measured at different locations in the tank. The formation of stable temperature layers during the heat-up of the tank was observed in the case of heating from the side, while in the case of heating from the bottom the fluid is homogeneously mixed. The measurement data will be taken for the validation of CFD codes.

*partially funded  
by BMBF  
(know how  
conservation  
program)*

*D. Lucas,  
H.-M. Prasser*

Using the code CFX-4, experiments carried out at the Rossendorf two-phase flow test loop were numerically simulated. Velocity and void fraction profiles of water and air flows were measured with different gas and liquid superficial velocities in the tube using high resolution two-phase instrumentation (wire mesh sensor). Taking into account different forces acting on the bubbles in a two-phase flow, typical radial velocity and void fraction profiles were simulated.

### **Pressure relief of chemical reactions**

The programme BRICK, which was developed for the simulation of depressurisation processes in batch reactors with consideration of the chemical reactions, was validated against experimental data. A large number of different experiments was used, among them experiments at an own 2 litre autoclave with and without chemical reaction. In charge of an industrial partner, BRICK was used for the assessment of a pressure relief system.

*supported by  
VW Stiftung*

## Separate effects in two-phase flows

*A. Böttger  
G. Grunwald  
T. Höhne  
H.-M. Prasser  
K.-H. Richter  
J. Zschau*

### **Coolant mixing in pressurised water reactors**

The mixing test facility ROCOM modelling the German KONVOI type pressurised water reactor in the scale of 1:5 was constructed and put into operation. It is aimed at studying the mixing during boron dilution and steam line break transients. The main purpose is the generation of high-resolution data for the validation of 3D CFD codes. The facility disposes of four individually controllable loops. It is equipped with several mesh-sensors used for the measurement of the tracer salt concentration in the downcomer and at the core entrance.

*A. Böttger  
H.-M. Prasser  
J. Zschau  
C. Zippe  
W. Zippe*

### **Development and calibration of two-phase flow measurement techniques**

The qualification of the diversified level indication system for boiling water reactors developed by FZR was started according to the German reactor safety regulations. The qualification procedure and the series production will be accomplished by an industrial supplier of measurement instrumentation. FZR contributes as a scientific consultant.

An extensive calibration of different kinds of two-phase flow instrumentation was performed at the two-phase test loop in Rossendorf. A gamma-densitometer was used as reference measurement. Void fractions obtained by the wire-mesh sensor and the needle probes developed by FZR are in good agreement with the readings of the gamma-densitometer in the entire void range between 0 and 100 %.

In co-operation with the Technical University of Nishny Novgorod (Russia) a new ultrasonic mesh sensor was developed. The work is part of a TRANSFORM project financed by the BMBF. The sensor is based on a system of crossing ultrasonic wave-guides. It is complementary to the electrical wire-mesh sensors of FZR, because it can be applied to non-conducting fluids. The sensor was tested at the Rossendorf two-phase flow test loop.

For the investigation of transport processes in bubble columns and foam layers, a PET detector is under construction. The scanner will allow to measure the distribution of a tracer marked by a positron emitting nuclide with a time resolution of better than 1 s. It consists of 8 axial layers with 16 BGO detectors each. The spatial resolution will be in the range of a centimetre.

*T. Kern  
D. Lucas  
H.-M. Prasser*

### **Basic studies of two-phase flows with foam production**

The thermal decomposition of hydrogen peroxide was used as a model reaction for a runaway in a batch reactor. Experiments were carried out at a 2 l autoclave. The strong exothermal reaction leads to a combined degassing-evaporation process, which is very valuable for the validation of computer models, like the code BRICK, developed by FZR.

*A. Grahn*

### **Thermoconvection and instabilities at the boundary layer of two non-miscible liquid reacting components**

During the neutralisation of carbonic acids dissolved in the organic phase with sodium hydroxide in the aqueous phase, a double-diffusive convection flow regime was discovered. In a capillary gap the regime is characterised by fingering in the heavier aqueous phase. Characteristic wave lengths and the time behaviour of the growth of the fingers were studied as a function of the reacting species and the gap width.

*E. Krepper,  
H.-M. Prasser,  
A. Schaffrath,  
C. Zippe,  
W. Zippe*

### **Transient two-phase flows in pipelines**

The wire-mesh sensor for fast gas fraction measurements in two-phase flows was used to study the transient flow pattern in an air-water flow in a vertical pipe. Experiments were carried out by varying the superficial velocities of both phases in a wide range, so that bubble, slug and annular flow regimes were covered.

Besides the high-speed flow visualisation and the analysis of gas fraction profiles, the sensor data were used to get bubble size distributions. For this purpose, a special signal evaluation algorithm was developed. In the transition region between bubble and slug flow, a change from a monomodal to a bimodal bubble size distribution was found at growing superficial liquid velocity, which can be taken as a quantitative criterion for the onset of bubble coalescence. When the maximum bubble diameter exceeds the inner diameter of the pipe this is an indication that bubble-to-slug transition has occurred. Several flow maps from the literature were compared to the new criterion. The best agreement was found with the flow map after Taitel, Bornea & Dukler.

In the next step, the evolution of the flow pattern along the vertical pipeline is studied. In a series of experiments, the axial distance between the air injection and the wire-mesh sensor is successively increased. Additionally, three different air injection modes are used. The experiments are not yet finished.

*A. Schaffrath*

### **Condensation models for horizontal pipelines**

In co-operation with the HTWS Zittau/Görlitz the condensation models KONWAR (FZJ) and HOTKON (HTWS) were validated by cross-checking against experimental data from the HORUS test facility. Despite the fact, that the models were developed for different working parameters, both models implemented in ATHLET, describe the condensation process in horizontal steam generator tubes of VVER type reactors very well, while ATHLET with the standard condensation model is not able to reproduce the measurements.

## Materials safety

*H.-W. Viehrig,  
H. Richter,  
J. Böhmert*

*supported by  
BMW*

*H.-W. Viehrig,  
H. Richter,  
J. Böhmert*

*supported by  
BMW*

*M. Große,  
A. Ulbricht,  
J. Böhmert*

### **Mechanical tests of reactor pressure vessel steel from the irradiation programme Rheinsberg**

After the licence for the operation of the radionuclide material testing laboratory became valid at the end of 1997, a comprehensive test programme was performed with unirradiated materials to prove the practicable, correct and reliable operation of the equipment. The programme proved that the installed devices and used techniques meet the requirements. In the laboratory both conventional mechanical and fracture mechanics parameters can be measured. It has been used for the specimens from the irradiation programme Rheinsberg, which is part of the German Russian scientific cooperation. The programme comprised instrumented Charpy impact tests and quasi-static 3-point bending tests. The shift of the Charpy transition temperature due to irradiation and the recovery by annealing were determined. Additionally, the fracture toughness  $K_{IC}$  was measured and evaluated using the master curve concept. In general, the results were consistent with the prediction according to the Russian guides. In the case of a VVER 1000-type weld metal a surprisingly high embrittlement was detected.

### **Correlation between mechanical and fracture mechanics parameter for irradiated reactor pressure vessel steels**

In order to gain a broad data base, unirradiated materials were additionally investigated. For that purpose a heat of ASTM A533 B cl 1 pressure vessel steel was selected which is often used as IAEA reference material. The correlation between the Charpy transition temperature and the reference temperature according to the master curve concept is significant but scatters considerably. The large variations result from material inhomogeneities (segregations). As consequence of this scattering, neither the Charpy transition temperature nor the reference temperature could be determined with satisfactory accuracy if the tests were done according to the standards. New testing concepts are designed and examined. They include tests at different temperatures and an increased number of specimens.

### **Microstructural analyses of irradiated VVER pressure vessel steels**

Microstructural analyses of irradiated reactor pressure vessel steels were carried out using different techniques, such as transmission electron microscopy and small angle scattering with neutrons and X-rays. Transmission electron microscopy is not suitable to detect and characterize the weakly structured nano-defects produced by irradiation. Small angle neutron scattering clearly indicated irradiation-induced effects. Unfortunately, the interpretation of the measuring effects is difficult for a such highly complex material system like the pressure vessel steel. Therefore, additional techniques were applied to gain information about the type and composition of the irradiation defects.

*supported by  
BMW*

The method of contrast variation (anomalous X-ray scattering, ratio between magnetic and nuclear small angle neutron scattering) was combined with annealing experiments and model calculations of the scattering intensity of hypothetical defect structures. In this way, it could be shown that the irradiation defects can be interpreted as clusters from vacancies, iron and solute atoms. Their volume fraction but not their size depends on the fluence. By annealing the defects can almost entirely be annihilated.

## **Mechanical behaviour of components under accident loads**

*T. Repp,  
E. Altstadt*

### **Calculation of the loads in pipelines due to waterhammers**

The pressure waves induced by a sudden slow down of the fluid flow in a pipeline are modelled on the base of the finite element method. Special attention is put on the influence of fluid-structure interaction if the pipe diameter is relatively large in comparison with the wall thickness. The FE-code ADINA is used for modelling. The transient velocity and pressure distribution was calculated in a straight pipe and in a 90° elbow assuming a slightly compressible fluid. The coupling between the elastic pipe wall and the fluid is realized by boundary elements. It is shown that there are local stresses in the elbow which are higher than those calculated with the conventional uncoupled calculations.

*supported by  
VDEW*

*E. Altstadt*

### **Structural dynamic modelling of BWR components**

During a hypothetical break of a BWR feed water line, the feed water distributor (FWD) inside the RPV is subjected to a high pressure load for a short time (10 ms). Due to the sudden coolant release from the inner volume of the FWD there is a pressure difference between the inner and outer surface. It is conservatively assumed that the pressure difference can nearly reach the operating pressure. The distributor box and the ring line of the feed water distributor are modelled with shell and volume elements that can be used for large strain analyses with elastic-plastic material behaviour. By non-linear static calculations (without consideration of the inertia of the material) it is demonstrated that a buckling instability occurs at about 60% to 80% of the maximum pressure load. The arc-length method is used for the numerical solution to overcome these points of instability. To evaluate the influence of the dynamics of the process a non-linear transient analysis was done showing that the maximum strain occurs with a time delay to the pressure peak. The maximum plastic strain differs only insignificantly between static and transient solution. In spite of the large strains the mechanical integrity is maintained during the hypothetical event.

## Simulation of particle and radiation fields

*R. Kuchler,  
K. Noack*

### **Transport of Reacting Solutes Through Unsaturated Soil**

Unsaturated flows within subsurface regions control many large-scaled hydrological and environmental processes. It is the goal of the development of a transport code for the migration of various radionuclides to model these phenomena in sufficient detail. The present code was used to compute the water flow and the reactive transport of several chemical species produced by the weathering of pyrite, calcite and uraninite through a soil matrix. The water motion was calculated for three different soil classes and for a typical annual precipitation. The code module which calculates the transport of the species incorporates the effect of hydrodynamic dispersion, nonlinear reaction equations and kinetic chemical interactions between aqueous and solid phases. The obtained results have already demonstrated that the code system can produce results which are of practical significance.

*H.-U. Barz,  
B. Böhmer,  
J. Konheiser*

### **Neutron Dosimetry of Reactor Pressure Vessels**

The BMBF project "Development of an Advanced Method for Determination of the Neutron Load on VVER-1000 Reactor Pressure Vessel Material" was completed. The developed methodology allows to calculate pressure vessel fluences for VVER-1000 type reactors with high accuracy. By covariance analyses and spectral adjustment of the calculated fluence spectra, the theoretical results could be further improved in accuracy and consistency with the measurements.

The EU TACIS project "Development of Advanced Methods for the Evaluation of Irradiation Embrittlement of VVER-1000/320 Type RPVs" was started with the FZR as member of the leading consortium. Within the scope of this EU project, measurements and calculations for an international dosimetry experiment at the Russian irradiation facility KORPUS in Dimitroffgrad have been done. A calculational model was developed including all details about geometry, material composition of the facility, and the experiment. First TRAMO test calculations were performed with this model.

The Rossendorf Monte Carlo code TRAMO, so far intended only for neutron transport, is now being extended to allow also gamma transport calculations coupled to the neutron transport by neutron-gamma reactions. The needed additional nuclear data files have been generated. The adjustment code COSA2 was extended to allow simultaneous adjustment of several correlated spectra with activation detectors at different positions.

*supported by  
BMBF and EU*

*H. Kumpf*

### **Recriticality Calculations for Uraniumdioxide-Water System**

An important question of reactor safety is whether recritical constellations of fuel and moderator might appear in the course of a core melt accident. In this connection, some fundamental aspects of the recriti

cality of water-uraniumdioxide mixtures were elucidated. Stochastic geometric arrangements of fuel and water were modeled and their neutron multiplication was determined by MCNP. It turned out, that these arrangements can be characterised globally by two parameters, the fuel chord length and the fuel/moderator volume ratio. The worst case with respect to recriticality has been identified still exhibiting mechanical stability.

*H.-U. Barz,  
B. Böhmer*

#### **Transport of High Energy Ions and of Fragmentation Products**

The development of the Monto Carlo Code IONTRA allowing the simulation of the transport of ions with initial energies from some ten to some hundred MeV/nucleon and of their daughter products has been completed. A Russian code based on different nuclear reaction models that treats the fragmentation as a stochastic process can now be used alternatively to a description of the reaction cross sections by phenomenological formula adjusted to the experiments. A comparison of both approaches with measured cross sections showed considerable differences. The agreement with experiments is better if the phenomenological approach is used, but there is a potential to improve the microscopic approach by adjusting selected input parameters of the nuclear reaction models.

### **Process and plant monitoring**

*M. Werner,  
S. Perov,  
E. Altstadt*

#### **Vibration modelling of VVER-1000 light water reactors**

The work is to contribute to the efficient early failure of VVER-1000 primary circuit components. For that purpose, a finite element model for the simulation of mechanical vibrations of all primary circuit components of the VVER-1000 was established. With the adjusted model it is possible to clarify how hypothetical damages of reactor internals influence the vibration signature of the primary circuit. For a better recognition and analysis of damages at VVER-1000 reactors it is intended to integrate the simulation results into a catalogue of spectral signatures. Moreover, damage simulation is an appropriate means to find sensitive measuring positions for on-line monitoring and to define physically based threshold values for frequency shifts and amplitude changes.

The influence of fluid-structure interaction (FSI) on vibration modes was especially investigated. The method of modelling FSI was verified comparing the results obtained by finite-element calculations with the exact analytical solution of a simple fluid-shell test system. It was shown that the method of coupling between structural and fluid elements is important for the exact simulation of the eigenfrequencies. The vibration modes were calculated of the reactor pressure vessel and its internals. The FSI causes a considerable down shift of the shell mode frequencies of the pressure vessel, core barrel and thermal shield. Some bending modes which exhibit a relative displacement

*support by BMBF*

*G. Hessel,  
W. Schmitt,  
N. Tefera,  
K. van der Vorst,  
F.-P. Weiß*

between pressure vessel and core barrel or between core barrel and thermal shield are significantly affected, too.

#### **Early detection of dangerous operation states in chemical plants**

The research project "Application of new computer-aided diagnostic methods to identify dangerous operational states in chemical plants" was completed. The catalytic esterification of acetic anhydride and methanol was chosen as prototypical exothermal reaction. In the lab scale, it was shown that neural networks are capable of reliably identifying dangerous states in reactors operating in the batch or semibatch mode.

Further, to increase the operational safety of batch and semibatch reactions, on-line concentration measurements were accomplished in the reaction calorimeter RC1 using a Fourier-Transform Infrared-Spectrometer. In case of the hydrogenation of an aromatic nitro compound the in-situ measured concentration profiles of reactant, intermediates, by-products, and products could not only be used to clarify the reaction mechanisms, but allowed also to provide more accurate kinetic data of this strongly exothermic reaction. For example, it was possible not only to determine the formal kinetics, but also the kinetic data of partial reactions.

*supported by  
BMBF*

*G. Hessel,  
H. Kryk,  
W. Schmitt,  
T. Seiler,  
F.-P. Weiß*

#### **Environmentally safe process control and state diagnostics in chemical plants using neural networks**

In this interdisciplinary project, the Fraunhofer Institute for Environmental, Safety, and Energy Technology UMSICHT, the Arzneimittelwerk Dresden (AWD) and the Institute of Safety Research of Forschungszentrum Rossendorf have collaborated since August 1998. The project aims at the development of neural networks for the diagnosis of discontinuous chemical processes and their test application in a production plant. It is the goal to achieve an early detection of deviations from the optimum, environmentally safe operation of a chemical plant. Besides the conception of the state-identification method and the process data interface, detailed studies of the kinetics and the mass transfer in heterogeneous, exothermal hydrogenation reactions (hydrogenation of nitro-aromatics) were accomplished. These reactions were chosen as a model reaction for the prototype test in a real production plant of AWD. In co-operation with AWD, the necessary input parameters for a process simulation tool (UMSICHT) were obtained. With the help of the simulator, data will be generated for training the neural networks with operational states beyond normal operation. Further, the investigation of the mass transfer in the AWD plant was started to enable scalable disturbance and runaway tests in the laboratory reactors of FZR, which can be used to train neural networks.

*supported by  
BMBF*

## Liquid metal Magneto hydrodynamics

W. Witke,  
S. Eckert,  
G. Gerbeth,  
V. Kolevzon,  
T. Weier,  
U. Fey

### Measuring techniques for liquid metal test facilities

Liquid metals are non-transparent, typically hot and aggressive. There is almost no commercial measuring technique available for the determination of local velocities or pressure. A mechano-optical velocity probe was developed which is able to measure two components of the local velocity. It is calibrated and tested in different melts like InGaSn, SnPb, SnBi, and PbBi. The measuring principle consists in the velocity induced elongation of a glass rod which is encapsulated in a glass capillary. This elongation is then measured by optical means using an endoscope and a camera. Due to its measuring principle the probe is independent of any electromagnetic fields. It is now developed and tested up to temperatures of about 700°C.

supported by  
DFG, BMBF, GIF

A laser light scattering technique was applied in order to investigate the phenomena at free liquid metal surfaces. The experiments with molten gallium show that the observed frequencies and damping constants differ strongly from the classical description of the gallium surface as that of a normal liquid. The results are explained in terms of surface layering possessing visco-elastic properties.

J. Priede,  
G. Gerbeth

### Theoretical studies on Marangoni flows in a magnetic field

The model configuration of a plane liquid metal layer exposed to a horizontal temperature gradient and a vertical steady magnetic field has been studied. The basic two-dimensional flow due to the thermo-capillary effect (Marangoni convection) becomes oscillatory in a three-dimensional way if the applied temperature gradient increases. The magnetic field provokes a basic boundary layer type flow and an efficient suppression of the first instabilities. The threshold of instability increases as square of the magnetic field strength.

supported by  
DARA

V. Galindo,  
G. Gerbeth,  
R. Mößner,  
Th. Jung,  
E. Zienicke

### Numerical simulation of flow and heat transfer in crystal growth

Numerical codes have been developed and used for melt flow and heat transport calculations of crystal growth problems. For the Czochralski growth of silicon commercial codes were used in order to simulate the melt control by means of different magnetic fields. The calculations were compared with model experiments and real growth experiments of silicon single crystals. Parameter regions have been identified where the growth process and the grown crystal show clear improvements. Meanwhile the corresponding magnetic systems are successfully introduced into industrial growth facilities. For simulations of transport phenomena and magnetic field influences on growth processes in ampulla, an own spectral code was developed. These results are compared with InAs growth experiments performed at Bergakademie Freiberg where a rotating magnetic field is installed in order to enhance the convective transport within the melt.

supported by  
DFG, SMWK and  
industry

*F. Stefani,  
A. Gailitis,  
G. Gerbeth*

*supported by DFG*

*T. Weier,  
G. Mutschke,  
U. Fey,  
G. Gerbeth*

*supported by VDI  
and DFG*

*J. Priede,  
G. Gerbeth*

*supported by  
DARA*

*S. Eckert,  
G. Gerbeth,  
C. Guttek,  
H. Stechemesser*

*supported by FZ  
Jülich*

### **Participation at the Riga Dynamo experiment**

The experimental verification of a magnetic field selfexcitation at the IoP in Riga was supported by numerical investigations. The measured water experiment profiles have been checked with respect to their critical magnetic Reynolds numbers. In an iterative procedure between the pump designers and the Riga water experiments the profiles have finally been adjusted in such a way that selfexcitation should be possible. As a particular result of the magnetic field calculations, additional pre- and post-propeller blades were installed at the Riga facility in order to improve the velocity profiles. Moreover, optimum measuring sites for the excited magnetic field have been fixed on the basis of the computer simulations.

### **Electromagnetic boundary layer control for saltwater**

The flow of saltwater around bodies can be controlled by electromagnetic forces localized directly on the surface of the body even though the electromagnetic forces penetrate only slightly into the low-conducting fluid. With suitable arrangements of electrodes and permanent magnets Lorentz forces can be produced which for instance accelerate the fluid motion parallel to the body surface. This results in a stabilized flow, drag reduction of the body, and prevention of flow separation. All these effects have been convincingly demonstrated during a set of plate experiments performed at the Shipbuilding Test Basin Hamburg in a saltwater flow. A significant drag reduction of about 80% was measured.

### **Levitation of metallic samples**

Electromagnetic levitation is a well-known method in order to support and fix metallic samples without any contact to wall. However, these samples typically show a strong tendency to instabilities resulting in rotation or oscillation of the body. The physical reason of such instabilities has been analysed. A frequency dependent threshold has been identified as main result of the theoretical investigations. Model experiments were performed clearly confirming the theoretical results.

Based on these investigations a method to stabilize the levitated samples by means of steady magnetic fields is developed.

### **Experiments on gas injection for the liquid metal target of a spallation source**

The next generation of spallation sources will require a mercury target instead of solid targets being used today. The strong energy input due to the proton beam pulses will cause shock waves in the target which may lead to serious structure problems. These shock waves shall be suppressed by adding of gas bubbles to the mercury, thus making the fluid slightly compressible. Basic experimental studies have been performed in order to analyse the possibilities of gas bubbles injection and their measurement. X-ray visualizations of gas bubble motions in liquid metals show the strong influence of wetting and surface tension

phenomena. A homogeneous distribution of tiny bubbles was obtained by injecting the gas through a wetted porous body.

## **Publications in scientific and technical journals and in conference proceedings**

Altstadt, E., F.-P. Weiß, M. Werner, H.-G. Willschütz  
Finite Element Based Stress Analysis of BWR Internals Exposed to Accident Loads  
Proceedings of the 6<sup>th</sup> International Conference on Nuclear Engineering (ICONE-6)  
San Diego, May 10-15, 1998

Altstadt, E., F.-P. Weiss, M. Werner, H.-G. Willschütz  
Stress Analysis of BWR Components Under Accident Loads Using Finite Elements  
Proceedings of TOPSAFE '98  
Valencia (Spain), April 15-17, 1998

Altstadt, E. and F.-P. Weiss  
Finite Element Based Vibration Analysis of WWER-440 Reactors  
Proceedings of the 6<sup>th</sup> International Conference on Nuclear Engineering (ICONE-6)  
San Diego, May 10-15, 1998

Barz, H.-U., B. Böhmer, J. Konheiser, I. Stephan  
High-Precision Monte Carlo Calculations, Experimental Verification and Adjustment of Flu-  
ences in the Pressure Vessel Cavity of a VVER-1000  
Proc. of the ANS Radiation Protection and Shielding Division Topical Conference  
Vol. 1, p. 447-454  
Nashville, Tennessee (USA), April 19-23, 1998

Bergner, F., M. Schaper, U. Bergmann  
Analyse von Rißschließvorgängen mit Ultraschallverfahren  
30. Tagung des DVM-Arbeitskreises Bruchvorgänge  
DVM-Bericht 230, S. 151-160  
Dresden, 17.-18.02.1998

Beyer, M., H. Carl, P. Schumann, A. Seidel, F.-P. Weiß, J. Zschau, K. Nowak  
Ein modernes technisches System zur verbesserten betrieblichen Überwachung des ukraini-  
schen Kernkraftwerkes Saporoshje  
atomwirtschaft-atomtechnik atw 43 (1998), Heft 4, Seite 230

Böhmer, B., G. Manturov  
Neutron Spectrum Covariances and Their Influence on Results of Pressure Vessel Neutron  
Spectrum Adjustments  
Voprosy Atomnoi Nauki i Techniki, Seriya Jadernye Konstanty, 1998  
Vypusk 1, p. 28-34, Ed. ZNIIatominform, Moscow

Böhmert, J., M. Große  
Nanoscale Precipitates in Russian Reactor Pressure Vessel Steel After Irradiation and Annea-  
ling  
Jahrestagung Kerntechnik 1998, Tagungsbericht S. 631  
München, 26.-28. Mai 1998

Cramer, A., A. Bojarevics, G. Gerbeth, Yu. Gelfgat  
Stabilisation of the Melt Extraction Process with a Magnetic Field  
accepted at: El-Kaddah (Ed.): Fluid Flow Phenomena in Metals Processing, San Diego (USA)

Eckert, S., G. Gerbeth, B. Guttek, H. Stechemesser  
Bubble formation heavy liquid metals: Evaluation of conventional gas injection methods with respect to a suitability under ESS relevant conditions, (ESS-European Spallation Source)  
ESS 98-72-T, August 1998

Eckert, S., G. Gerbeth, O. Lielausis  
The behaviour of gas bubbles in a turbulent liquid metal MHD flow - Part I: Dispersion in quasi-two-dimensional MHD turbulence  
accepted at: Int. Journal of Multiphase Flow, Elsevier, Dec. 1998

Erge, Th., V. U. Hoffmann, K. Kiefer, E. Rössler, U. Rindelhardt, G. Teichmann, B. Decker, J. Grochowski, G. Heilscher, M. Schneider, G. Blaesser, H. Osserbrink, H. Becker, W. Vaaßen, B. Genennig, H. Rieß, P. Sprau  
The German 1000-Roofs-PV-Programme - a Resume of the 5 Years Pioneer Project for Small Grid-Connected PV-Systems  
Proc. of the 2nd World Conference and Exhibition on Photovoltaic Solar Energy Conversion  
Vol. III, p. 2648  
Vienna (Austria), 6 - 10 July 1998

Fethke, M., A. Schaffrath, L. Rossner, H. Jaegers, E. F. Hicken  
Experimental Investigation of the Operation Mode of Passive Safety Systems  
ENS Bern (Ed.): Transactions of the ENC '98 World Nuclear Congress, Vol. III, S. 403-407  
Nizza, (France) 25-28 Oct. 1998

Fey, U., T. Weier, G. Gerbeth, G. Mutschke, M. Gad-el-Hak  
Separation control using Lorentz forces: recent experimental and numerical results  
51th APS Meeting Philadelphia, 22.-24.11.98  
Bulletin of the American Physical Society 43 (1998) 2024

Franke, K., U. Rindelhardt  
Die räumliche und zeitliche Korrelation der Globalstrahlung auf beliebig orientierten Flächen in Sachsen  
11. Internationales Sonnenforum 1998, Tagungsband S. 881  
Köln, 26.-30. Juli 1998

Futterschneider, H., U. Rindelhardt, G. Teichmann  
Modul-Untersuchungen im FZR-Testfeld  
SONNENENERGIE 5/1998, S. 36

Große, M., J. Böhmert  
Irradiation Damage Structure in VVER-440 Steels After Irradiation at Different Temperatures and Post-Irradiation Annealing  
19<sup>th</sup> International Symposium "Effects of Radiation on Materials", Seattle (USA), June 1998  
American Society of Testing and Materials STP 1366, Seattle, June 1998

Große, M., J. Böhmert, Ch. Riekell  
Investigations of the Structural Changes Ahead of a Crack Tip in Ductile Aluminium Using  
Scanning Micro-Beam Small Angle X-Ray Scattering  
J. Material Science Letters 17 (1998) 1631

Große, M., J. Böhmert, R. Gilles  
Small Angle Neutron Scattering Investigations of the Microstructure of VVER 440-type Re-  
actor Pressure Vessel Steel after Irradiation at 60 °C  
Journal of Nuclear Materials, 254 (1998) 143-150

Große, M.  
Additional Information about the Chemistry of Precipitates by Variation of the Scattering  
Contrast in the SANS and SAXS Experiment  
Proc. International School and Symposium on Small-Angle Scattering  
Matrahaza (Hungary), Oct. 1998

Große, M.  
SAXS Experiments with High Lateral Resolution by Using of an X-ray Micro Beam  
Proc. International School and Symposium on Small-Angle Scattering,  
Matrahaza (Hungary), Oct. 1998

Große, M., A. Hempel, R. Gilles  
SANS Investigations of the Irradiation and Annealing Behaviour of the VVER-type Reactor  
Pressure Vessel Steel 15Xh2MFA  
BENSC Experimental Reports 1997, Berichte des HMI Berlin, HMI-B552, (1998), S. 244

Große, M., V. Denner, J. Böhmert, G. Goerigk  
ASAXS-Investigations of the Structural Changes in the Reactor Pressure Vessel Steel  
15Kh2MFA after Electron Irradiation  
Jahresbericht HASYLAB 1997, Hamburg (1998)

Hackstein, G., J. Riedel, U. Rindelhardt, M. Schwanitz  
Die Nutzung erneuerbarer Energiequellen in Sachsen  
Wirtschaftsdienst IHK Dresden 9/1998, S. 33

Hensel, F., U. Rohde  
Measurement and Simulation of the Turbulent Dispersion of a Radioactive Tracer in a Two-  
Phase Flow System  
M. Rahman, C. A. Brebbia, G. Comini (Hrsg.) Advances in Fluid Mechanics II  
Conference held in Udine (Italy), Computational Mechanics Publications, Southampton 1998  
ISBN 1-853-12589-X, S. 283-294

Heilscher, G., M. Schneider, H. Becker, U. Rindelhardt  
Ermittlung der Fehlertoleranz bei Kennlinienmessungen in Vorortuntersuchungen  
13. Symposium Photovoltaische Solarenergie, Tagungsband S. 323  
Staffelstein, 11. - 13. März 1998

Hessel, G., W. Schmitt, N. Tefera, K. v.d. Vorst, F.-P. Weiß, J. Neumann, S. Schlüter  
Identifying Dangerous States in Chemical Plants Using Neural Networks  
6th European Congress on Intelligent Techniques and Soft Computing EUFIT'98  
Aachen, Sept.- 7-10, 1998

Kern, T.  
Gasgehaltsmessung mit nadelförmigen Leitfähigkeitssonden in schäumenden Medien  
DECHEMA Jahrestagung 1998, Fachtreffen Sicherheitstechnik, Tagungsband II, S. 163-164  
Wiesbaden, 26.-28. Mai 1998

Kern, T.  
Quantifizierung der hydrodynamischen Parameter in kurzlebigen Schäumen  
4. Fachtagung „Anlagen-, Arbeits- und Umweltsicherheit“, Preprint P10  
Köthen, 5./6. November 1998

Kliem, S.  
Analysis and Calculation of an Accident with Delayed Scram at NPP Greifswald using the  
Coupled Code DYN3D/ATHLET  
1998 International Conference on the Physics of Nuclear Science and Technology  
Proceedings pp. 486-491, ANS  
La Grange Park, IL (1998)

Kliem, S.  
Solution of the Fifth Dynamic AER Benchmark using the Coupled Code DYN3D/ATHLET  
Proceeding of the 8th AER-Symposium, pp. 357-367  
KFKI Atomic Energy Research Institute, Budapest (1998)

Kliem, S.  
Comparison of the Results of the Fifth Dynamic AER Benchmark-a Benchmark for Coupled  
Thermohydraulic System/Three-Dimensional Hexagonal Neutron Kinetic Core Models  
Proceeding of the 8th AER-Symposium, pp. 429-469  
KFKI Atomic Energy Research Institute, Budapest (1998)

Kliem, S., U.Grundmann, U. Rohde  
Main Steam Line Break Analysis of a NPP with VVER by Means of the Coupled Code  
DYN3D/ATHLET  
Tagungsbericht Jahrestagung Kerntechnik '98, pp. 15-19  
München, 26. - 28. Mai 1998

Kliem, S., U.Grundmann, U. Rohde  
Main Steam Line Break Analysis of a NPP with VVER by Means of the Coupled code  
DYN3D/ATHLET  
Proc. TOPSAFE '98, Session TSC-1a, ENS  
Valencia (Spain), 1998

Krepper, E.  
Natural circulation experiments at the ISB-VVER Integral Test Facility and Calculations us-  
ing the Code ATHLET  
Proceedings of TOPSAFE '98  
Valencia (Spain), April 15-17, 1998

Kruber, St., H. Schöne  
The application of decision analysis in the remediation sector  
Environmental Engineering and Policy

Krüssenberg, A.-K., E. F. Hicken  
Neue Rechnungen zu Lufteinbruchstörfällen bei Fusionsreaktoren mit einer Beschichtung des Reaktorraums aus CFC-Material  
Jahrestagung Kerntechnik, Tagungsbericht S. 573-576  
München, 26. - 28. Mai 1998

Krüssenberg, A.-K., R. Moormann, H. K. Hinssen, M. Hofmann, C. H. Wu  
Investigation of Oxidation Resistance of Carbon Based First-Wall Liner Material Aerosol AO5  
Journal of Nuclear Materials 258-263 (1998) 770-776

Lucas, D., H.-M. Prasser  
Einfluß der Abblaseleitung auf die Notentspannung von Reaktoren  
DECHEMA Jahrestagung '98, Tagungsband S. 158-159  
Wiesbaden, 26. - 28.05.1998

Lucas, D.  
BRICK - ein Simulationstool für Mehrphasenströmungen in Behältern auf der Basis einer Partikelmethode  
GVC-Jahrestagung '98, Kurzfassung in Chemie-Ingenieur-Technik 70 (1998) 1139  
Freiburg, 30.09. -02.10.1998

Lucas, D., H.-M. Prasser, T. Kern  
Die thermische Zersetzung von Wasserstoffperoxid als Modellreaktion für die Druckentlastung  
4. Fachtagung Anlagen, Arbeits- und Umweltsicherheit, Preprint P 9  
Köthen, 5./6. Nov. 1998

Moormann, R., S. Alberici, H.-K. Hinssen, A.-K. Krüssenberg, C. H. Wu  
Oxidation behaviour of carbon-based materials used for high-temperature gas-cooled reactors and fusion reactors  
Proceedings of 9th CIMTEC  
Florence, June 1998

Mößner, R., G. Gerbeth  
Bouyant Melt Flows Under the Influence of Steady and Rotating Magnetic Fields  
Journal of Crystal Growth, Elsevier Netherlands, acceptet: September 1998

Mutschke, G., V. Shatrov, G. Gerbeth  
Cylinder wake control by magnetics fields in liquid metals flows  
Experimental Thermal and Fluid Science 16 (1998) 92-99

Prasser, H.-M., A. Böttger, J. Zschau  
A new electrode-mesh tomograph for gas-liquid flows  
Journal Flow Measurement & Instrumentation 9 (1998) 111-119

Priede, J., G. Gerbeth  
Spin-up instability of electromagnetically levitated shperical bodies  
accepted at: Journal IEEE Transactions on Magnetics  
Washington (USA), Oct. 1998

Priede, J., G. Gerbeth  
Oscillatory instability of electromagnetically levitated solid bodies  
submitted to: IEEE Transactions of Magnetics  
Washington (USA), Oct. 1998

Priede, J., G. Gerbeth  
Hydrothermal wave instability of thermocapillary-driven convection in a transverse magnetic field  
submittet to: Journal of Fluid Mechanics  
Cambridge (UK), June 1998

Priede, J., G. Gerbeth  
Oscillatory and rotational instabilities in electromagnetic levitation  
accepted at: El-Kaddah (Ed.): Fluid-Flow Phenomena in Metals Processing,  
TMS, San Diego (USA)

Priede, J., A. Cramer, A.Y. Gelfgat, P.Z. Bar-Yuseph, A.L. Yari, G. Gerbeth  
Experimental and numerical study of an anomalous thermocapillary convection in liquid gallium  
submitted to: Physics of Fluids, American Institute of Physics  
New York (USA), September 1998

Rindelhardt, U., G. Teichmann  
Netzgekoppelte Photovoltaik-Anlagen: Erfahrungen und Perspektiven  
Elektrizitätswirtschaft 24 (1998), S. 36

Rohde, U.  
The modeling of Fuel Behaviour under RIA Conditions in the Code DYN3D  
Proceedings of the 8th AER-Symposium, S. 721-740  
KFKI Atomic Energy Research Institute, Budapest (1998)

Schaffrath, A., H.-M. Prasser  
Meßtechnik für stationäre und transiente Mehrphasenströmungen  
atomwirtschaft-atomtechnik atw 43 (1998), Heft 11, S. 706-708

Schaffrath, A., H.-M. Prasser  
Workshop on „Measuring techniques for steady state and transient multiphase flows“  
Kerntechnik 63 (1998), Heft 5-6, S. 300-302

Schaffrath, A., P. Dumaz  
Post test calculations of NOKO Experiments within the Framework of a European Research Programm  
Kerntechnik 63 (1998), Nr. 3, S. 113-119

Schaffrath, A., E. F. Hicken, H. Jaegers, H.-M. Prasser  
Results of Experimente at the NOKO Pilot Plant  
VGB-Power Tech 78 (1998), Nr. 5, S. 79-84

Schaffrath, A., E. F. Hicken, H. Jaegers, H.-M. Prasser  
Experimentelle Ergebnisse mit der NOKO-Versuchsanlage  
VGB-Kraftwerkstechnik 78 (1998), Nr. 5, S. 90-96

Schaffrath, A., P. Dumaz  
Calculation of the NOKO-Test B6-4  
Jahrestagung Kerntechnik '98, Tagungsbericht S. 87-90  
München, 26. - 28. Mai 1998

Schaffrath, A.  
Post Test Calculations of NOKO Bundle Experiments  
Proceedings TOPSAFE 98, Beitrag TSC4-b  
Valencia (Spain), 15.-17. April 1998

Schaffrath, A., P. Dumaz  
Post Test Calculations of NOKO Emergency Condenser Experiments  
Proceedings of the 6<sup>th</sup> International Conference on Nuclear Engineering (ICONE-6)  
San Diego, May 10-15, 1998

Schaffrath, A., H.-M. Prasser, A. Böttger  
Sonderuntersuchungen zu Strömungsformen am NOKO Einzelrohr  
Jahrestagung Kerntechnik '98, Tagungsbericht S. 83-86  
München, 26. - 28. Mai 1998

Stephan, I., D. Gawlik, W. Gatschke  
Bestimmung der Neutronenflußdichten in den Bestrahlungseinrichtungen des BER II bei der  
HEU-LEU-Umstellung  
Jahrestagung Kerntechnik 1998, Tagungsbericht, S. 631  
München, 26.-28. Mai 1998

Stefani, F., G. Gerbeth  
Velocity reconstruction in conducting fluids from magnetic field and electric potential measurements  
accepted at: „Inverse Problems“  
London, Dec. 1998

Stefani, F., G. Gerbeth, A. Galitis  
Velocity Profile Optimization for the Riga Dynamo Experiment  
A. Alemany, Ph. Marty, J.P. Thibault (Eds.): Transfer Phenomena in Magnetohydrodynamic  
and Electroconducting Flows, Kluwer, 1998, pp. 31-44

Thess, A., G. Gerbeth  
Magnetohydrodynamik  
Physikalische Blätter 54, S. 125  
Februar 1998

Viehrig, H.-W., J. Böhmert  
Specimen Reconstitution Technique and Verification Testing for Charpy Size SENB Specimens, Small Specimen Test Techniques,  
ASTM STP 1329, W.R. Corwin, S.T. Rosinski, E. van Walle, (Eds.),  
American Society for Testing and Materials, July 1998, pp. 420

Viehrig, H.-W., J. Böhmert

Anwendung des Master-Curve-Konzeptes zur bruchmechanischen Charakterisierung von Reaktordruckbehälterstählen,  
Deutscher Verband für Materialforschung und -prüfung e.V., Tagungsberichte "Werkstoffprüfung 1998", S. 353

Weier, T., G. Gerbeth, G. Muschke, U. Fey, O. Posdziech, O. Lielausis, E.

Some results on electromagnetic control of flow around bodies

Proc. of the International Symposium on SEAWATER DRAG REDUCTION, pp. 395-400  
Newport, Rhode Island (USA), 22.-24. Juli 1998

Weier, T., G. Gerbeth, G. Mutschke, E. Platacis, O. Lielausis

Experiments on cylinder wake stabilization in an electrolyte by means of electromagnetic forces localized on the cylinder surface

Experimental Thermal and Fluid Science 16 (1998) 84-91

## Oral Conference Contributions

Aszodi, A., E. Krepper

Simulation of the single phase natural circulation at the secondary side of an emergency condenser (NOKO facility) using the CFD-code CFX-4

ENC-Konferenz

Nizza, Oktober 1998

Bojarevics, A., Yu. Gelfgat, G. Gerbeth, A. Cramer

The effect of a superimposed steady magnetic field on nonstationary flow driven by a high frequency AC magnetic in an open cavity

Workshop „The Use of Magnetic Fields in Crystal Growth and Metals Casting“

Frankfurt a. M., 1.-2. April 1998

Cramer, A., A. Bojarevics, G. Gerbeth, Y. Gelfgat

Stabilisation of the Melt Extraction Progress with a Magnetic Field

Fluid Flow Phenomena in Metals Processing, TMS Annual Meeting

San Diego (USA), March 1998

Dudlik, A., H.-M. Prasser, S. Schlüter

Verhinderung des Kavitationsschlages beim schnellen Absperren einer Flüssigkeitsleitung

Vortrag 4. VDI-Fachtagung „Anlagen-, Arbeits- und Umweltsicherheit“

Köthen, 5.-6. Nov. 1998

Dumaz, P., A. Schaffrath

Analysis of the NOKO Emergency Condenser Experiments

Vortrag, Seminare Systemes REP No 2

Cadarache, 19. März 1998

Galindo, V., G. Gerbeth

Numerical studies on crystal growth melt flow control using different magnetic fields

SIAM Annual Meeting

University of Toronto (Canada), July 13-17, 1998

Galindo, V., G. Gerbeth

Crystal Growth Melt Flow Control by Means of Magnetic Fields

Workshop SOLFIDAP, IKZ Berlin

Berlin-Adlershof, 25.-27. Mai 1998

Gerbeth, G., V. Galindo

Einsatz von Magnetfeldern bei der Silizium-Czochalski-Kristallzucht

Berg und Hüttenmännischer Tag

TU Bergakademie Freiberg, 18.06.1998

Gerbeth, G.

Fundamentals of technical applications of MHD

Workshop "The use of Magnetic Fields in Crystal Growth and Metals Casting"

Frankfurt a. M., 1.-2. April 1998

Gerbeth, G.

Influence of magnetic fields on surface driven flows

Workshop "Applications of magnetic fields in materials processing under microgravity conditions"

Erlangen, Nov. 11-12, 1998

Große, M.

Type and Annealing Behaviour of Irradiation Defects in Surveillance Materials of the VVER-type Weld Metal Sv-10KhMFT

Table Ronde LLB

Saclay (Frankreich), Nov.1998

Grundmann, U., F. Hollstein

HEXNEM2 - a New Nodal Method for Hexagonal Geometry

AER Working Group D Meeting

Rez (Czech Republic), May 18-20, 1998

Grundmann, U., S. Mittag, U. Rohde

The 3-Dimensional Core Model DYN3D

Safety Analysis for NPPs of VVER and RBMK Type

Obninsk, 26.-30. October 1998

Höhne, T., G. Grunwald, U. Rohde

Coolant mixing in pressurized water reactors

8th Symposium of AER

Oct. 1998

Kliem, S.

Fifth Dynamic AER Benchmark - A Benchmark for Coupled Thermohydraulic System/3D

Hexagonal Neutron Kinetic Core Models - Comparison of Results - Level 1

AER Working Group D Meeting

Rez (Czech Republic), May 18-20, 1998

Kliem, S.

OECD PWR MSLB Benchmark - Dependence of the Results from Several Parameters

2<sup>nd</sup> PWR MSLB Workshop CIEMAT

Madrid (Spain), June 22-23, 1998

Lindau, B.

Anwendung wissenschaftlicher Methoden auf der Grundlage von Insitu-Messung und Online Modellierung zur Optimierung von Schüttgutbehandlungstechniken am Beispiel des Dosierens

FA „Agglomerations- und Schüttguttechnik“ der VDI-Gesellschaft

Magdeburg 30.03. - 01.04.1998

Lindau, B.

Anwendung wissenschaftlicher Methoden auf der Grundlage von Insitu-Messung und qualitativer Modellierung zur Optimierung von Schüttgutbehandlungstechniken am Beispiel des Dosierens

49. Berg- und Hüttenmännischer Tag 1998

TU Bergakademie Freiberg, 18.06.1998

Lucas, D.  
BRICK - ein Simulationstool für Mehrphasenströmungen in Behältern auf der Basis einer Partikelmethode

1. Chemnitzer Verfahrenstechnisches Kolloquium  
TU Chemnitz, 25.-26.11.1998

Lucas, D., H.-M. Prasser, T. Kern  
Einfluß von Zusätzen niedermolekularer oberflächenaktiver Stoffe auf den Massenaustrag bei der Druckentlastung eines verdampfenden Stoffsystems  
GVC-Fachauschuß-Sitzung "Mehrphasenströmungen"  
Aachen, 02.-06.03.98

Mutschke, G., G. Gerbeth, V. Shatrov  
Bluff body wake control by magnetic fields  
SIAM Annual Meeting  
University of Toronto (Canada), July 13-17, 1998

Prasser, H.-M.  
Messung von Gasgehalt, Gasgeschwindigkeit und Volumenstrom mit Gittersensoren  
1. Chemnitzer Verfahrenstechnisches Kolloquium  
TU Chemnitz, 25.-26.11.1998

Rindelhardt, U.  
Use of Renewable Energies in Saxony  
International Forum "Alternative Energy Sources"  
Lubawka (Poland), 28-29<sup>th</sup> May 1998

Rindelhardt, U.  
Netzgekoppelte Photovoltaik-Anlagen - Ergebnisse des 1000-Dächer-Langzeitmeßprogramms in Sachsen  
2. Merseburger Solartag, 09.06.1998

Rindelhardt, U.  
Solarenergie - Photovoltaik  
Tagung der Evangelischen Akademie Meißen, 12. - 14. Juni 1998

Stefani, F., G. Gerbeth, A. Gailitis  
Numerical Simulation for the Riga Dynamo  
Workshop „Laboratory Experiments on Dynamo Action“  
Jurmala (Latvia), June 13-16, 1998

Stefani, F., G. Gerbeth, A. Gailitis  
Numerical Simulation of the Riga Dynamo Experiment  
SIAM Annual Meeting  
University of Toronto (Canada), July 13-17, 1998

Stefani, F., Gerbeth, G., A. Gailitis, Lielausis, O.  
Laboratory Experiments on Dynamo Action  
SIAM Annual Meeting  
University of Toronto (Canada), 13.-17. July 1998

Stefani, F., G. Gerbeth, A. Gailitis  
Numerical Simulation of the Riga Dynamo Experiment  
SIAM Annual Meeting  
University of Toronto (Canada), 13.-17. July 1998

Stefani, F., G. Gerbeth, A. Gailitis  
Numerical Simulation for the Riga Dynamo  
Workshop / Laboratory Experiments on Dynamo Action  
Riga, 14.-16. June 1998

## **FZR-Reports and other publications**

Gerbeth, G., A. Alemany, V. Shatrov, E. Krasilnikov

Magneto-hydrodynamic flow around bluff bodies

Final Report: Januar 1995 – Dezember 1997

Dresden, September 1998, Reference number: INTAS-94-1504

Barz, H.-U., J. Konheiser

Monte-Carlo Programm TRAMO - Möglichkeiten und Anleitung zur Nutzung

FZR-245, Dezember 1998

Barz, H.-U., B. Böhmer, J. Konheiser, I. Stephan

Entwicklung einer fortgeschrittenen Methodik zur Bestimmung der Neutronenbelastung des Druckbehältermaterials vom Reaktor des Typs WWER-1000,

Final Report BMBF-Projekt 1501022

FZR-222, Mai 1998

Böhmert, J., M. Große

Anwendung von Kleinwinkelstreuverfahren zum Nachweis verformungsbedingter Strukturschädigung

FZR-229, Juli 1998

Eckert, S.

Experimentelle Untersuchung turbulenter Flüssigmetall- und Flüssigmetall-Gas-Strömungen in einem äußeren Magnetfeld

FZR-219, April 1998

Fiorini, G. L., E. Friesen, T. v. D. Hagen, J. Lopez Jimenez, P. Meloni, U. Rindelhardt

BWR Physics and Thermalhydraulic Complementary Actions to the IPSS-BWR R&D Cluster

Final report, CEA Cadarache: RT DER/SIS/LSS 98/32-1, Februar 1998

Gerbeth, G.

Marangoni-Konvektion in einer seitlich beheizten ebenen Flüssigmetallschicht unter dem Einfluß eines Magnetfeldes

Schlussbericht, Juli 1998

Große, M., A. Ulbricht

SANS-Investigation of the Irradiation-Induced Changes in Reactor Pressure Vessel Steels

Rapport de Experience 1998, LLB Saclay

Grundmann, U., S. Kliem, E. Krepper, S. Mittag, U. Rohde, F. Schäfer, A. Seidel

Qualifizierung des Kernmodells DYN3D im Komplex mit dem Störfallcode ATHLET als fortgeschrittenes Werkzeug für die Störfallanalyse von WWER-Reaktoren

FZR-216, März 1998

Hessel, G., D. Hoppe, W. Schmitt, N. Tefera, K. van der Vorst, F.-P. Weiß

Anwendungsmöglichkeiten neuartiger EDV-gestützter Erkennungsmethoden zur Identifizierung gefährlicher Betriebszustände in Chemieanlagen (I)

FZR-223, Juni 1998

- Hoppe, D.  
Nutzung der statischen Informationstheorie und eines tensororientierten Klassifikationsverfahrens zur Signalerkennung an einem chemischen Prozeß  
FZR-225, Juni 1998
- Hoppe, D.  
Modellbildung durch Auswertung von Fehlerdimensionen  
FZR-244, Dezember 1998
- Höhne, T.  
Vergleich von Kühlmittelströmungen und -vermischung in einem skalierten Modell des DWR Konvoi mit den Vorgängen im Originalreaktor  
FZR-210, Februar 1998
- Höhne, T., G. Grunwald, U. Rohde  
Coolant Mixing in Pressurized Water Reactor  
FZR-237, Oktober 1998
- Krepper, E., F. Schäfer  
Verifikation des ATHLET-Rechenprogramms im Rahmen der externen Verifikationsgruppe ATHLET BETHSY Test 5.2c - Totalverlust des Speisewassers  
FZR-231, August 1998
- Krepper, E., F. Schäfer  
Verifikation des ATHLET-Rechenprogramms im Rahmen der externen Verifikationsgruppe ATHLET BETHSY Test 9.3c - Heizrohrbruch mit Versagen der Hochdruck-Noteinspeisung  
FZR-232, August 1998
- Meyer, K., F. Hollstein  
Analytisches Modell zur Berechnung der Übertragungsfunktionen für das Neutronenflussrauschen in WWER-440-Reaktoren bei stochastischen Schwingungen der Regelelementunterteile  
FZR-205, Januar 1998
- Prasser, H.-M. (Ed.)  
Workshop „Meßtechnik für stationäre und transiente Mehrphasenströmungen“  
24.-25. September 1998 in Rossendorf  
FZR-241, November 1998
- Prigarin, S. M., K. Noack  
About the Influence of Randomness of Hydraulic Conductivity on Solute Transport in Saturated Soil: Numerical Experiments  
FZR-243, Dezember 1998
- Richter, H., J. Böhmert, M. Valo, H.-W. Viehrig  
Detektion von duktiler Rißinitiierung durch Schallemission  
FZR-230, August 1998
- Rindelhardt, U., G. Teichmann, H. Fatterschneider  
Langzeituntersuchungen an netzgekoppelten Photovoltaikanlagen in Sachsen  
FZR-221, Mai 1998

Schaffrath, A., H.-M. Prasser  
Theoretical support to the NOKO Experiments  
FZR-224, Juni 1998

Walle, E. van, M. Valo, H.-W. Viehrig, G. Gage, M. Wootton, E. Keim, L. Debarberis,  
M. Horsten  
Reconstitution Techniques Qualification & Evaluation to Study Ageing Phenomena of  
Nuclear Pressure Vessel Materials - Resque, Contract FI4SCT960038,  
Yearly Progress Report 1997, European Commission, Euratom Research Framework Pro-  
gramme 1994-1998 "Nuclear Fission Safety", June 1998, AGE-Resque(98)-P003

## **Meetings and Workshops**

Composition Effects on Neutron Embrittlement  
Rossendorf, 20.-21. Januar 1998

Laboratory Experiments on Dynamo Action (LEDA)  
International Workshop  
Jurmala (Lettland), June 14-16, 1998

2. Workshop  
Messtechnik für stationäre und transiente Mehrphasenströmungen  
Rossendorf, 24.-25. September 1998

FE-Modelling of VVER-type reactors  
Project in the frame of WTZ Deutschland-Rußland with DIAPROM (Rußland)  
Rossendorf, October 26-28, 1998

## Patents

1. B. Lindau  
Verfahren zur Bestimmung der Festigkeit von dispersem Material  
Patent DE 198 13 065.1  
Anmeldung 25.03.1998
2. H.-M. Prasser, J. Zschau, A. Böttger  
Anordnung zur Verhinderung eines Kavitationsschlages beim schnellen Absperren einer zum Transport von Flüssigkeiten genutzten Rohrleitung  
Patent DE 198 15 232.6  
Anmeldung 04.04.1998
3. D. Hoppe, H.-D. Giera  
Anordnung und Verfahren zur akustischen Volumenbestimmung  
Patent DE 198 30 442.0  
Anmeldung 08.07.1998
4. H.-M. Prasser, S. Schlüter, A. Dudlik  
Anordnung zum druckstoßfreien Absperren einer flüssigkeitsfördernden Rohrleitung  
Patent DE 198 40 961.3  
Anmeldung 08.09.1998
5. B. Lindau  
Vorrichtung zum Fördern von Schüttgut mittel Vibrationsförderung  
Patent DE 198 35 530.0  
Anmeldung 06.08.1998

## SEMINARS 1998

1. Dr. A. Polte  
Modellierung und Bewertung von Störfallauswirkungen technischer Anlagen in urbanen Gebieten im Rahmen der Entscheidungsanalyse für öffentliche Entscheidungen  
15.01.1998
2. T. Reitz  
Visuelle Ansätze der Wissensrepräsentation im Altlastenbewertungssystem XUMA/GEFA  
22.01.1998
3. Dr. R. Koch  
Programme zur Berechnung von Neutronenfeldern  
12.02.1998
4. Dr. R. Kuchler  
Migration von Schadstoffen in Bergbauhalden  
26.02.1998
5. Dr. A. Schaffrath  
Stand der Arbeiten zu TOPFLOW  
12.03.1998
6. Dr. E. Altstadt  
Nichtlineare Finite-Elemente-Analyse von Schalenstrukturen  
26.03.1998
7. Dr. J. Böhmert, Holger Richter  
Nachweis der dynamischen Reißinitiierung - eine kritische Methodenbewertung  
09.04.1998
8. PD Dr. U. Rindelhardt, G. Teichmann  
Netzgekoppelte Photovoltaikanlagen in Sachsen  
- Ergebnisse des 1000-Dächer-Programmes -  
14.05.1998
9. Dr. Unholzer (TU Dresden)  
Neutronen- und Photonenflußspektren in einem ITER-Mockup  
19.05.1998
10. Dr. S. Eckert, Dr. G. Gerbeth  
Flüssigmetall-Zwei-Phasen-Untersuchungen für das Target einer Neutronen-Spallationsquelle  
04.06.1998
11. R. Beck (Siemens KWU)  
Modellierung der Fluidkräfte bei der Erdbebenauslegung von Kompaktlagerstellen  
19.06.1998

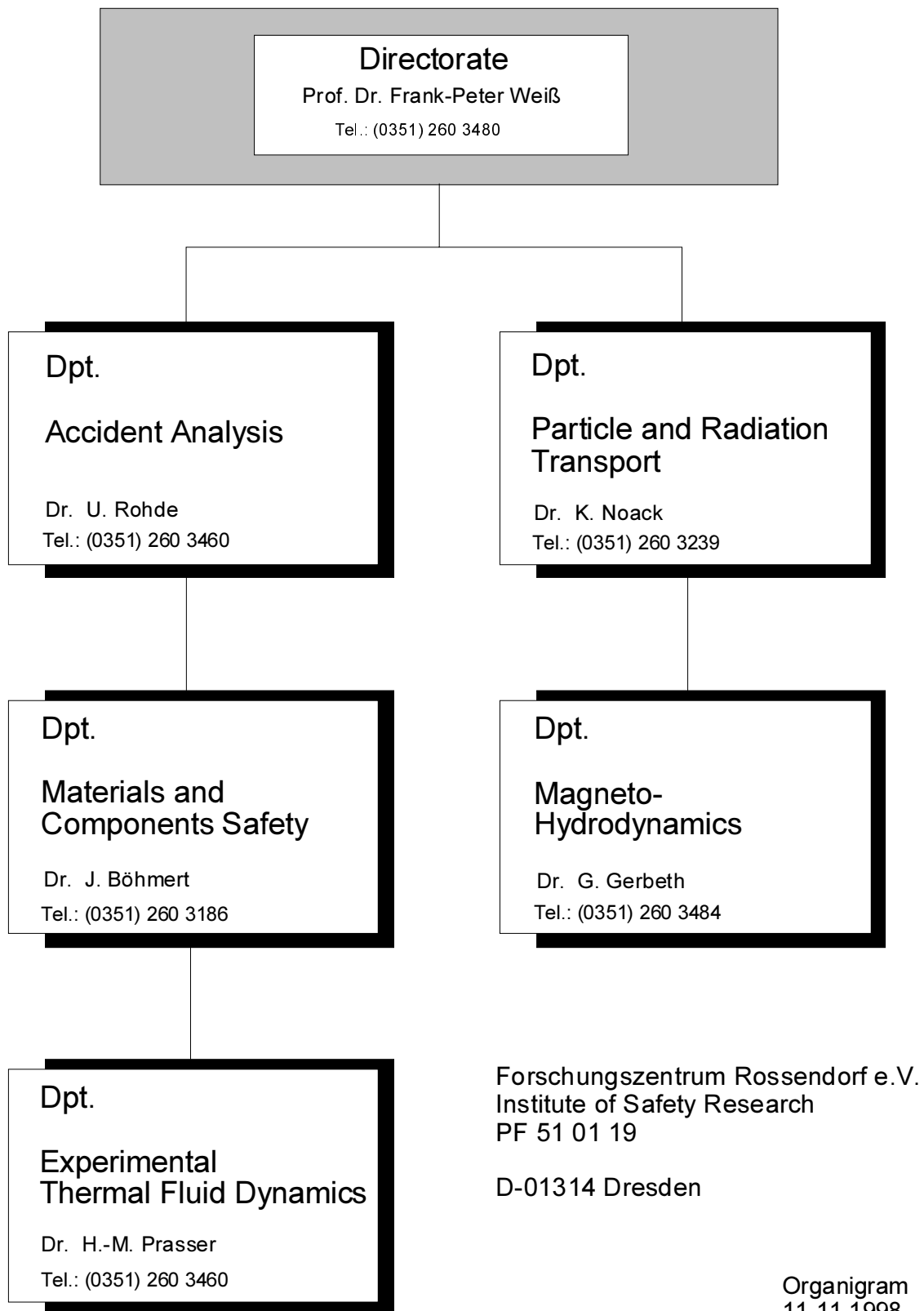
12. Prof. Dr. J. Wagschal (Hebrew University of Jerusalem)  
Cross Section Adjustment Revisited  
08.07.1998
13. Dr. A. Polte  
Wertesystem bei der Beurteilung störfallrelevanter technischer Anlagen  
23.07.1998
14. Prof. Gokhmann (Universität Odessa)  
Interpretation of small angle curves of neutron-irradiation Cr-Mo-V-steels  
27.08.1998
15. Dr. B. Lindau  
Prozeßführung beim Feststoffdosieren  
03.09.1998
16. Dr. H.-M. Prasser  
Visualisierung von Kavitation in Rohrleitungen mit Gittersensor  
11.09.1998
17. Dr. V. Galindo  
Einsatz von Magnetfeldern in der SI-Einkristallzüchtung  
01.10.1998
18. Dr. E. Krepper, F. Schäfer  
Verifikation des Programmes ATHLET anhand der Nachrechnungen von BETHSY-  
Experimenten  
08.10.1998
19. Dr. W. Schmitt, G.Hessel  
Identifizierung gefährlicher Betriebszustände in Chemieanlagen  
22.10.1998
20. M. Fethke (FZ Jülich)  
Berechnung des Gebäudekondensators des SWR-1000 mit RALOC  
29.10.1998
21. Dr. W. Ferse  
Angewandte Entscheidungsanalyse  
- Ein Überblick der Arbeiten im FZR -  
30.10.1998
22. Dr. M. Werner  
WWR-1000-Schwingungsmodellierung mittels finiter Elemente  
05.11.1998
23. Dr. K. Noack  
Stand und Perspektiven des Themas "Reaktordosimetrie" in der Abteilung FWST  
19.11.1998

24. Dr. F. Stefani  
Ergebnisse zum Rigaer Dynamoexperiment  
10.12.1998
25. Dr. N. Tefera  
Reaktions- und sicherheitstechnische Untersuchungen von exothermen chemischen  
Reaktionen  
16.12.1998

## Lectures

1. F.-P. Weiß  
Zuverlässigkeit und Sicherheit technischer Systeme  
TU Dresden, Fakultät Maschinenwesen  
SS 98 und WS 98
2. U. Rindelhardt  
Erneuerbare Energien I und II  
Universität Leipzig, Fakultät für Physik und Geowissenschaften  
SS 98 und WS 98

# Institute of Safety Research



**Director:**

Prof. Dr. F.-P. Weiß

**Scientific Staff**

Altstadt, Eberhard Dr.  
Barz, Hansulrich Dr.  
Beyer, Matthias  
Böhmer, Bertram  
Böhmert, Jürgen Dr.  
Böttger, Arnd  
Carl, Helmar Dr.  
Cramer, Andreas Dr.  
Eckert, Sven Dr.  
Erlebach, Stephan  
Ferse, Wolfgang Dr.  
Fey, Uwe, Dr.  
Fietz, Jürgen Dr.  
Galindo, Vladimir Dr.  
Gerbeth, Günter Dr.  
Grants, Ilmars Dr.  
Große, Mirco  
Grundmann, Ulrich Dr.  
Grunwald, Gerhard Dr.  
Hessel, Günter  
Hirsch, Werner Dr.  
Hoppe, Dietrich Dr.  
Hüller, Jürgen Dr.  
Jung, Thomas Dr.  
Kliem, Margarita  
Kliem, Sören  
Koch, Reinhard Dr.  
Konheiser, Jörg  
Krepper, Eckhard Dr.  
Kruber, Stefan Dr.  
Krüssenberg, A.-Kathrin Dr.  
Kryk, Holger Dr.  
Kumpf, Hermann Dr.  
Küchler, Roland Dr.  
Lindau, Bernd Dr.  
Lucas, Dirk Dr.  
Mittag, Siegfried Dr.  
Mößner, Ralph, Dr.  
Mössner, Thomas  
Müller, Gudrun, Dr.  
Mutschke, Gerd  
Noack, Klaus Dr.  
Prasser, Horst-Michael Dr.  
Priede, Janis Dr.

Reitz, Thomas  
Rindelhardt, Udo PD Dr.  
Rohde, Ulrich Dr.  
Schaffrath, Andreas Dr.  
Schmitt, Wilfried Dr.  
Scholz, Thomas  
Schütz, Peter  
Schumann, Peter Dr.  
Seidel, Andre  
Stephan, Ingrid Dr.  
Stephani, Frank Dr.  
Teichmann, Günther  
Tefera, Nurelegne Dr.  
Viehrig, Hans-Werner Dr.  
Werner, Matthias Dr.  
Willschütz, Hans-Georg  
Witke, Willy  
Zschau, Jochen Dr.  
Zienicke, Egbert Dr.  
Zippe, Winfried Dr.  
Zippe, Cornelius Dr.

**PhD Students**

Beckert, Carsten  
Eckert, Sven  
Grahn, Alexander  
Hensel, Frank  
Höhne, Thomas  
Kern, Tommy  
Ramisch, Kai  
Repp, Thomas  
Richter, Holger  
Schäfer, Frank  
Schneider, Carola  
Ulbricht, Andreas  
Weier, Tom

**Technical Staff**

Baldauf, Dieter  
Behrens, Sieglinde  
Blumentritt, Thea  
Bombis, Doris  
Borchardt, Steffen  
Eichhorn, Christine  
Forker, Klaus  
Futterschneider, Hein  
Gundrum, Thomas  
Heinze, Gerda  
Kaule, Christian  
Kunadt, Heiko  
Leonhardt, Wolf-Dietrich  
Leuner, Bernd  
Losinski, Claudia  
Mansel, Catrin  
Möller, Falk  
Nowak, Bernd  
Opitz, Ruth  
Otto, Gerlind  
Pietzsch, Jens  
Richter, Annett  
Richter, Henry  
Richter, Joachim  
Richter, Karl-Heinz  
Richter, Petra  
Rott, Sonja  
Russig, Heiko  
Schleißiger, Heike  
Schneider, Gisela  
Seidler, Christa  
Seiler, Torsten  
Skorupa, Ulrich  
Tamme, Marko  
Tamme, Günther  
Trepte, Manuel  
Webersinke, Steffen  
Weiß, Rainer  
Zimmermann, Wilfried